



POLITECNICO DI MILANO  
DEPARTMENT OF ELECTRONICS, INFORMATION AND BIOMEDICAL  
ENGINEERING  
DOCTORAL PROGRAMME IN INFORMATION TECHNOLOGY

---

DEVELOPMENT OF A GAMMA-RAY DETECTION  
MODULE FOR MULTIMODAL SPECT/MR  
IMAGING

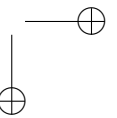
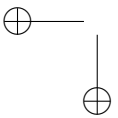
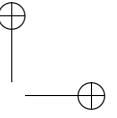
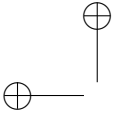
Doctoral Dissertation of:  
**Michele Occhipinti**

Supervisor:  
**Prof. Carlo E. Fiorini**

Tutor:  
**Prof. Angelo Geraci**

The Chair of the Doctoral Program:  
**Prof. Carlo E. Fiorini**

2015 – XXVIII





## Acknowledgments

I would like to express my appreciation and thanks to my advisor Professor Carlo Fiorini for encouraging my research and for allowing me to grow as a research engineer and scientist. Your advice on both research as well as on my career have been priceless.

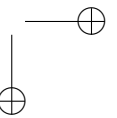
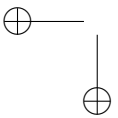
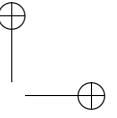
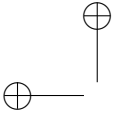
I would also like to thank my friends and colleagues who shared with me the last three years of PhD work, in particular Dr. Paolo Busca, who has been a tremendous mentor for me.

My thanks are also addressed to the members and colleagues of the INSERT project consortium: I am really thankful of the professional and human relationship we built during these years of work together.

Words cannot express how grateful I am to my family: you always know how to love and support me. It is not rhetoric to affirm that my PhD is also made of your sustain and affection.

I have not mentioned in the acknowledgments my friends, with whom I shared laughs and tears in the last years: they just have to be considered and included as part of the family I have arbitrarily built along my life. They have shared with me the joys and pains of the work I have carried on.

For this reason, in the hope that my work will eventually be helpful to the people, I dedicate to them the present thesis.



---

---

## Abstract

---

**M**ULTIMODAL imaging techniques have been representing one of the main and most focused research and development topic in the field of medical diagnostic of the last thirty years. The best solution to achieve consistency in time and space is obtained by the synchronous image acquisition, that is the combination of two or more modalities simultaneously recording images from the same object.

In the present work the design and development of a compact SPECT insert for hybrid SPECT/MR is discussed. The range of possible applications extends from in vivo studies for physiological and pathological studies and drug delivery to cardiovascular functionality and diagnosis, oncology, neuro-imaging and neuro-oncology. The synchronous combination of SPECT and MR is rather unexplored in literature mainly due to the major technical constrains related to mutual compatibility of the scanners. The SPECT insert is required to be compact, do not interfere with the MR acquisition, present no significant susceptibility to magnetic field and RF signal from MR coils and also to detect multiple radiotracers within the same imaging session.

The design and development of the gamma-cameras that compose the SPECT ring is presented together with the main methodology adopted to fulfill a detector with adequate imaging and spectroscopic performance: analytical and custom simulation tools implementing montecarlo algorithms have been exploited, but also scaled experimental measurements for the validation of the parameters adopted in the overall system.

---

The planar image quality has been optimized through the implementation of statistical based reconstruction algorithm which profit of a new and practical method for Light Response Function (LRF) retrieval. Tests with a preliminary gamma-camera prototype have produced the first experimental results: the intrinsic spatial resolution in the center of a  $50 \text{ mm} \times 50 \text{ mm}$  field of view has been measured around 1.4 mm FWHM, with an energy resolution of 16.6 % at 140 keV ( $^{99m}\text{Tc}$ ). The simulated outcomes present good correspondence with the experimental ones, thus providing a reliable tool for the prediction of the final system performance: approximately 1 mm FWHM of intrinsic spatial resolution and an energy resolution slightly higher than 12 % at 140 keV.

---

---

## Summary

---

INSERT is the name of the European project (7<sup>th</sup> framework program of UE commission) aiming to the realization of an integrated SPECT/MRI for enhanced stratification of brain tumors (more specifically gliomas). The objective of the multimodal medical device is to combine the anatomical and versatile information from MRI with the high sensitivity of SPECT systems to track radiolabeled biological processes, with the final purpose to provide higher quantity and quality information for the diagnosis, patient-specific radio/chemo-therapy and early assessment of treatment efficacy.

The SPECT insert, composed by a population of gamma cameras organized in a ring shape, is going to be realized in two versions: a *preclinical* system for biological research on small animals and a *clinical* one for the human brain/neck region imaging.

The overall work is shared by a community of European partners and Politecnico di Milano represents the project leader and responsible for the design and development of the basic gamma camera composing the SPECT ring.

My doctoral thesis concerns the design, development, qualification and optimization of the detection module, with a particular focus on the conversion block of the device and on the signal elaboration for planar image reconstruction. I also participated in the electronic and mechanic design and gave a contribute in the exploitation of a cooling strategy necessary to aim towards the required system performance.

The detection module has been build following an Anger architecture (a monolithic inorganic scintillator optically coupled to a photodetectors ma-

trix), balancing good imaging performance with a limited number of electronic readout channels which represents a fundamental aspect for the realization of a large clinical SPECT with a plurality of gamma cameras.

The presence of high magnetic fields in the commercial available MR scanners has prevented the project to adopt conventional photomultiplier tubes (PMTs) in an integrated SPECT architecture, due to their high sensibility to the EM fields and to their bulky dimensions. This issue required the study and selection of an adequate photodetector among the family of the solid-state detectors, which are insensitive to magnetic fields and typically present a compact structure.

Another important requirement for the SPECT insert is to permit multiple radiotracers detection for a better stratification of the biological processes in only one diagnostic acquisition. This implies that good energy resolution capability is needed together with the commonly required imaging performance. The design of the gamma camera was supported by analytical and statistical models to forecast the possible system outcomes and to monitor the implications of the project decisions on the final spectroscopic and imaging performance.

In order to improve image quality and to better address the initial requirements, a sophisticate and practicable statistical reconstruction method has been developed and implemented.

The state of the art picture for the INSERT project depicts the realization of a first gamma detection module prototype, characterized in its imaging and energy capabilities. The very next step in the development is the assessment of the MR compatibility of the device.

The overall discussion has been organized in five chapters.

In the first chapter a general overview on the multimodality imaging combining nuclear medicine and radiology is provided. The motivations for multimodality and, more specifically, hybrid SPECT/MR development are explored. The dissertation is particularly focused on the differences between PET and SPECT capabilities, since the PET/MR systems have known a research golden age in the recent years, while the SPECT/MR prototypes realized up to now are in a number of few exemplars. For this reason a brief description of possible SPECT/MR contribution to scientific research and medical practice is reported.

The second chapter presents the INSERT project, its objectives and requirements and briefly reports the present state of the art of the research and development of the components for the SPECT insert. In an initial section, a limited quantity of preliminary definitions is provided for discussion sup-

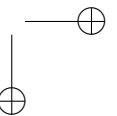
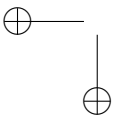
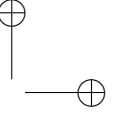
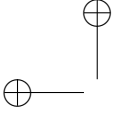
port.

The design and development of the gamma-detection module, representing the basic unit for the SPECT ring, is debated in the third chapter. The content is divided in three main sections:

1. Description of the main components in an Anger camera and definition of the main parameters for the characterization of inorganic scintillators and photodetectors. Particular emphasis is given to the Silicon Photomultipliers (SiPMs), that are insensitive to high magnetic fields and, for this and other reasons, have been chosen as photodetectors for the project. Then, the main electronic strategies for SiPM readout are briefly described.
2. Exposition of the analytical and stochastic model employed for the design optimization of the gamma-detection module.
3. Report of the state of the art in the development of the INSERT detection module. The design choices and the technical motivations are described with detail for each component of the gamma camera.

In the fourth chapter the issues in scintigraphy image reconstruction are debated: the center of gravity method, widely diffused in general practice, presents intrinsic limitations that prevent the recovery of the entire field of view of the imaging camera and produce uniformity and linearity distortions, mainly at the edges of the reconstructed image. The achievement of the project requirement has stimulated the study and development of a statistical reconstruction algorithm based on maximum likelihood, with better output performance. The most original characteristic of the method implemented is that the light response function (LRF), required from the statistical method for reconstruction, is retrieved from a calibration dataset obtained directly from the acquisition of an experimental uniform irradiation of the gamma camera.

The energy and imaging performance of the INSERT prototype are presented in the fifth chapter. The experimental measurements are compared to the analytical and stochastic models to assess the forecast quality of the design methods adopted. A prevision on the possible outcomes from the next detection module version is then retrieved and presented.





---

---

## Contents

---

<b>1</b>	<b>Multimodality in medical imaging</b>	<b>1</b>
1.1	Introduction . . . . .	1
1.2	Historical notes on medical imaging . . . . .	2
1.3	Multimodality techniques . . . . .	2
1.3.1	Hardware architectures . . . . .	3
1.3.2	Multimodality advantages and drawbacks . . . . .	5
1.3.3	SPECT/CT and PET/CT . . . . .	6
1.4	Multimodality with Magnetic Resonance . . . . .	7
1.4.1	PET/MR . . . . .	9
1.4.2	SPECT/MR . . . . .	12
1.5	Rationale for SPECT/MR systems . . . . .	16
1.5.1	Preclinical SPECT/MR rationale . . . . .	18
1.5.2	Clinical SPECT/MR rationale . . . . .	20
<b>2</b>	<b>INSERT project</b>	<b>21</b>
2.1	Objective and motivations . . . . .	21
2.2	Technological and technical principles on SPECT systems . . . . .	23
2.2.1	SPECT principles . . . . .	23
2.2.2	Collimation in SPECT . . . . .	31
2.2.3	Tomographic image reconstruction . . . . .	34
2.3	Magnetic Resonance Imaging basics . . . . .	37
2.3.1	MR hardware . . . . .	38
2.4	Project requirements . . . . .	41
2.4.1	Preclinical requirements . . . . .	42

**Contents**

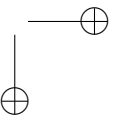
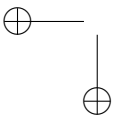
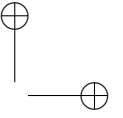
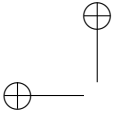
---

2.4.2	Clinical requirements . . . . .	43
2.4.3	Gamma-detection module requirements . . . . .	44
2.5	Architectures of the SPECT insert . . . . .	45
2.5.1	State of the art of the gamma-detection module . . . . .	46
2.5.2	Preclinical architecture . . . . .	47
2.5.3	Clinical architecture . . . . .	49
<b>3</b>	<b>Gamma-detection module design</b>	<b>57</b>
3.1	Gamma-ray detection with scintillators . . . . .	57
3.1.1	Inorganic scintillators . . . . .	58
3.1.2	Photodetectors . . . . .	65
3.1.3	Silicon PhotoMultiplier - SiPM . . . . .	69
3.1.4	Signal elaboration . . . . .	81
3.2	Design tools . . . . .	85
3.2.1	Energy resolution theoretical model . . . . .	85
3.2.2	Montecarlo simulator . . . . .	89
3.3	Detection module design . . . . .	99
3.3.1	Crystal design . . . . .	99
3.3.2	Crystal wrapping and optical coupling media . . . . .	106
3.3.3	Photodetector selection . . . . .	107
3.3.4	SiPMs array design . . . . .	112
3.3.5	Readout electronics . . . . .	115
3.3.6	Structure of the gamma-detection module and cooling strategy. . . . .	118
3.3.7	Compatibility issues and strategies. . . . .	126
<b>4</b>	<b>Reconstruction algorithms</b>	<b>131</b>
4.1	Centroid methods . . . . .	132
4.1.1	Modified centroid method . . . . .	137
4.2	Statistical methods . . . . .	138
4.2.1	Light Response Function - LRF . . . . .	139
4.2.2	Maximum likelihood method . . . . .	143
4.3	Implementation of the statistical method . . . . .	144
4.3.1	Light Response Function generator . . . . .	145
4.3.2	Maximum Likelihood algorithm optimization . . . . .	147
4.3.3	Reconstruction performance . . . . .	149
<b>5</b>	<b>Detection module performance and results</b>	<b>153</b>
5.1	Introduction . . . . .	153
5.2	Theoretical and simulated expectations . . . . .	154
5.2.1	Model parameters . . . . .	154

**Contents**

---

5.2.2 Energy resolution from analytical model . . . . .	157
5.2.3 Simulation results . . . . .	161
5.3 Experimental setup: INSERT detection module prototype . .	171
5.4 Experimental results . . . . .	173
5.5 Final discussion . . . . .	189
<b>6 Conclusions</b>	<b>195</b>
<b>Bibliography</b>	<b>199</b>



---

# CHAPTER *1*

---

## Multimodality in medical imaging

---

### 1.1 Introduction

---

Nowadays biological and medical research, as well as clinical practice, deeply relies on the integration of several information layers such as anatomy, physiology, molecular behavior and genomic expression of the organic structure under analysis. Specifically for medical application, this combination of knowledge is required for accurate disease diagnosis, prediction of treatment response and development of highly specific and sensitive drugs and imaging agents. Today’s medical imaging technologies are expected to furnish an adequate grade of correlated information between anatomical structure and functional processes. This paradigm found its historical actualization in the development of technological systems or computational techniques that allow to merge images from different medical modalities and registered in space and time, taking the name of *multimodality imaging*.

## Chapter 1. Multimodality in medical imaging

---

### 1.2 Historical notes on medical imaging

---

Historically, medical and scientific devices to image either anatomical structure or functional processes have developed along independent paths. The first x-ray computed tomography (CT) prototype was realized in the early 1970s by Hounsfield, initially for brain imaging and later for whole body. The CT can generate high resolution and 3D reconstruction of patient anatomy using x-ray imaging and image reconstruction algorithms. Improvements in camera technology such as helical and multi-detector CT (MDCT) have brought to ever higher spatial resolution with shorter scan times [1]. Despite the good anatomic details provided by CT, it gives very low information regarding functional or metabolic activity of tissues.

The 1980s witnessed the appearance of first clinical magnetic resonances (MR), a technique of particular importance for imaging patients because it does not require the use of ionizing radiation. These two techniques, CT and MR, came to dominate the imaging of human anatomy. However, in diagnosis and staging diseases or monitoring response to therapy, anatomical imaging does not always provide the complete picture. Functional or metabolic changes occur even in the absence of a corresponding anatomical correlate.

On the other side, nuclear medicine techniques, initiated in the late 1940s, image functional processes by using radioactive tracers and photon detectors (gamma-cameras). Tomographic imaging with radionuclides actually predates CT (early attempts were in 1963). The first human tomographic images with positron-emitting isotopes were presented in 1972 [2], to be joined by single photon emission tomography (SPECT) approximately one year later. Instrumentation for tomographic imaging of function (SPECT, PET) evolved along a path distinct from that of anatomical imaging devices (CT and MR), and the corresponding clinical studies were performed and interpreted separately in the different medical departments, respectively of nuclear medicine and radiology. Despite this segregation, the usefulness of combining anatomical and functional planar images was evident to physicians even in the 1960s [3].

### 1.3 Multimodality techniques

---

Prior to the advent of the first commercial SPECT/CT and PET/CT scanners in the early 2000s, multimodality was accomplished exclusively through

### 1.3. Multimodality techniques

retrospective *software registration* of the volumetric datasets [4]. First images, obtained through software fusion, started from late 1980s [5]. For tissues with limited motion, such as the brain, these approaches worked very well. At the contrary, in many other parts of the body, image registration was challenging because of changes in the patient position on the two separate imaging devices, organs motion, temporal changes between the two scans that may have been acquired days or even weeks apart, and limited information in the image datasets (especially the PET or SPECT datasets) to drive the algorithms to accurate registration. Nevertheless, these techniques were important to demonstrate the validity of the multimodality imaging approach. Moreover, they are still widely used for registering modalities for which multimodality instrumentation does not commonly exist.

An attempt to overcome the problems introduced by the software registration was addressed by combining different imaging devices in one single registration system, an approach referred to with the term *hardware fusion*. The main idea is to physically combine two or more equipments, typically one dedicated to anatomic definition (e.g. CT or MR) and one to functional and metabolic analysis (e.g. SPECT, PET, optical imaging) in order to enhance the co-registration and optimize the quality of the fused images.

#### 1.3.1 Hardware architectures

The architectures for the available commercial multimodal system can be separated in three main categories [6].

***Separate system approach*** - The imaging scanners have separate gantries positioned in different rooms. An example of this configuration is the system proposed by GE Healthcare in late 2010: the design is based on a combination of a dual modality PET/CT and a 3 T MR system that are operated side-by-side in separate adjacent rooms. Patients are shuttled from one system to the other without getting off the bed. This approach permits the acquisition with more than two modalities with limited time interval between different registration; moreover the two scanner can be used in parallel and each one of them can be replaced independently in case of malfunction or if the technology is outdated. The devices need no particular redesign since they are separated and the performance of the respective images is preserved. The only design limit that has to be considered is the architecture of the facilities in the building that hosts the systems. The main drawback for this approach is that synchronous acquisition of the images is

## Chapter 1. Multimodality in medical imaging

not feasible and the transfer of the patient bed from one room to the other is a critical phase since it can introduce variation in the position and geometry of the subject.

**Sequential approach** - The two imaging device are arranged with the gantries in the direction of the main scanner axis with a patient handling system (usually placed on a track) mounted in between (Figure 1.1). Most of the commercial SPECT/CT and PET/CT scanners adopt this architecture and also many PET/MR and few SPECT/MR have followed this scheme in order either to limit mutual compatibility issues and to maintain the two tools as close as possible. The redesign of the devices is quite limited for SPECT/CT and PET/CT systems since they just need to be aligned and avoid interferences from one another radiation sources. In the case of systems coupled with an MR, an higher level of redesign is required. As for the separate system approach, there is no possibility for synchronous acquisition, even if the transfer procedure is faster and more accurate and reliable.



**Figure 1.1:** Schematic view of a sequential, or “tandem”, design for combined nuclear medicine and radiology scanners (in this example a PET/MR). The two imaging device are arranged with the gantries in the direction of the main scanner axis with a patient handling system (usually placed on a track) mounted in between. [7]

**Integrated approach** - The two modalities are fused together in a combined volume or integrated one inside the other, providing a simultaneous acquisition multimodality scanner (Figure 1.2). This approach is one of the most challenging from a technical point of view since it requires to adapt



### 1.3. Multimodality techniques

the design of the two systems in order to avoid mutual interferences between different modalities and the volumes dedicated to one or both the scanners are constrained by several factors, like manoeuvrability of the patient into the gantry, geometry dependence of some imaging performance, etc. The simultaneous acquisition is of particular interest for following fast dynamic events with more than one modality and for reducing the overall time of an imaging session, with a direct increase in patient throughput.



**Figure 1.2:** Schematic views of a synchronous, or integrated, design for combined nuclear medicine and radiology scanners. The two imaging device are integrated one inside the other. On the left, a combined PET/MRI for head/neck acquisition. On the right, a whole-body PET/MRI scanner. [7]

#### 1.3.2 Multimodality advantages and drawbacks

The guiding principle that has been giving success to the multimodality imaging techniques, in particular to the systems relying on hardware fusion, is due to the added value they provide with respect to the single modality approach. Integrated combination of modalities proved to possess the ability to address scientific or clinical questions that would be impossible on separate systems (i.e. studies that require simultaneous imaging, or very good spatial registration that cannot be achieved using registration algorithms). With respect to single modality, multimodality improved quantitative accuracy of functional/molecular imaging studies, with benefits not only in clinical practice, but most of all in biological and scientific studies. It has already been mentioned that multimodality improved throughput for clinical or preclinical studies: this is not only a great advantage for the single patient who spend less time in annoying and stressing diagnosis procedures, but also for the overall organization of the hospital patients waiting

## Chapter 1. Multimodality in medical imaging

---

list or for the time schedule of a scientific study with a big amount of specimens or test subjects to be analyzed.

However, multimodality systems typically come with trade-offs that have to be balanced against the perceived added value. First, because of compatibility or geometrical constrains, the redesign of the systems brings to non-optimal configurations compared with stand-alone scanners. Thus, the imaging performance are often affected and decrease in quality. Second, the overall cost of the multimodality system is -except in few circumstances- greater than the individual components. Another consideration is that multimodality systems requires typically a large space to be installed, especially for the *separate* and the *sequential* systems. Integrated systems are more compact, but usually need for bulky ancillary systems. As last general drawback, multimodality introduces additional operational complexity, with necessity for the final user to form an expertise across diverse modalities. This element has somehow limited an explosive implementation of multimodal system in the clinical and preclinical practice as described by Townsend [5].

### 1.3.3 SPECT/CT and PET/CT

In 1990, the pioneering work of Hasegawa et al. [8], paved the way for the realization of the first hybrid systems, more precisely for the first prototypes of SPECT/CT scanners. He was the first who proposed using an x-ray tube rather than a radionuclide source for transmission scanning. Moreover, it was clear that the great advantage in coupling a CT with a nuclear medicine scanner like SPECT came from the possibility to easily calculate attenuation maps with the CT in order to correct the absorption non homogeneities given by different tissues that can affect SPECT images. Following this new technical approach also PET/CT systems were developed in the next years, then in 1998 the first commercial scanners were introduced and from that moment on, the use of these equipments has grown exponentially [4, 8].

Current hybrid PET/CT and SPECT/CT systems represent an important, but only partial step towards full multimodality integration. They enable sequential functional and anatomic imaging, without moving the patient off the couch; and there is a fixed and known coordinate transformation between the images produced from the two systems, eliminating the need for image registration algorithms. However, to all intents and purposes, the hardware of the two imaging systems remains separate and the patient moves sequentially through two independent devices that are bolted

---

#### 1.4. Multimodality with Magnetic Resonance

---

together in a tandem configuration. The integration or hybrid imaging occurs at the software level. Nonetheless, this method is extremely effective, leading to considerably improved spatial registration over software registration for many parts of the body, and improved temporal registration with only a few minutes separating the PET or SPECT scan and the CT scan.

SPECT/CT and PET/CT find a wide range of applications in either pre-clinical studies with little animals and clinical diagnosis, where human-body size scanners are already available, in particular for studies in oncology and cardiology, but also musculoskeletal imaging and endocrinology (SPECT/CT) and neurology (PET/CT).

SPECT/CT has currently a more limited clinical use than PET/CT, due in part to longer scan times.

---

#### 1.4 Multimodality with Magnetic Resonance

---

One of the most active area of research and development in multimodality imaging at the present time is the integration of MRI with PET or SPECT. The motivation for combining nuclear medicine techniques with MRI is to address clinical applications where the latter is the preferred anatomic imaging modality with respect to CT (e.g. many neuroimaging applications and cancers in the pelvic area) mainly because it provides superior soft-tissue contrast. But perhaps more interestingly, this combination would allow correlation of radiotracer assays with other types of more functional MR measurements, for example dynamic contrast-enhanced MRI, diffusion-weighted MRI, functional MRI, pharmacologic MRI and MR spectroscopy [9]. This opens up a wealth of interesting research opportunities, and with these advanced MR techniques finding increased clinical utility, there likely will be range of clinical applications that combine anatomic MR, some form of functional MR measurement and molecular imaging with PET or SPECT [4].

Another recognized advantage of MR over CT is that the radiation dose in the former case is significantly inferior than in the latter. Thus provides a crucial improvement for studies that are monitoring disease progression and response to therapy, where multiple scans have to be repeated along time.

On the other hand, there is one significant drawback of MR that must be acknowledge: it does not directly provide the information required for attenuation correction of the nuclear medicine studies. Instead of measuring the photon attenuation as with CT, MR images a map for proton density (whereas photon attenuation is proportional to electron density). The dis-

## Chapter 1. Multimodality in medical imaging

---

inction is clearly demonstrated by the fact that both air and cortical bone give no measurable MR signal, while there is an extremely high difference (around 2500 HU) in their photon attenuation properties. A first approach to solve the lack of attenuation maps in MR is based on a multi-component segmentation of the MR images, using atlas information to correlate known attenuation values to segmented anatomical structures. The disadvantage of this procedure is that atlases do not reflect inter- and intra-subject anatomic variability [8]. Another possibility for MRI-based attenuation is a combination of atlas registration obtained with CT and local pattern recognition based on patient-specific MR images in order to generate a pseudo CT scan of the SPECT/MR or PET/MR study from which the attenuation map can be derived [5].

Additional drawbacks include increased imaging times of MR compared to CT. Moreover, the inability to image patients with contraindications to MR (pacemakers, metal prothesis, etc.) or of wide girth due to a smaller field of view further limits this modality.

The integration of nuclear medicine scanners with magnetic resonance requires the resolution of constrained technical issues, above all the mutual electromagnetic interference between different devices.

The SPECT or PET system must operate inside or in proximity of a high magnetic field environment, which precludes the use of conventional photomultiplier-tube based equipments in the vicinity of the magnet. Different solutions have been proposed: optical transmission of the scintillation signal through optical fibers (see more in section 1.4.1); the implementation of magnetic field insensitive solid state light detectors such as avalanche photodiodes (APDs) [10, 11] and Silicon Photomultipliers (SiPMs) [12]; direct conversion of the gamma photons through sub-millimeter pixelated solid state detectors based on Cadmium Telluride (CdTe) or Cadmium-Zinc Telluride (CZT) [13, 14]; alternatively, traditional PMTs have been implemented in a sequential PET/MR, placing the detectors outside of the magnet, in an area where the fringe field is low enough that they can be effectively shielded [12, 15].

Another aspect in mutual compatibility is given by the fact that the MR systems require an high level of magnetic field uniformity, typically 1 ppm or better, and foreign elements, placed inside or around the magnet gantry, introduce perturbations in the field due to their magnetic permeability.

The last issue related to mutual electromagnetic interference between equipments: an MR system generates high power radiofrequency pulses through its coils, as well as rapidly switching gradient magnetic fields. The

## 1.4. Multimodality with Magnetic Resonance

strong variations in the EM field can be easily picked up by the SPECT or PET electronics, with correlated interference on the signal produced by the gamma-ray detectors. The other way round, components from the SPECT or PET electronics (such as power supplies or preamplifier electronics) radiate electromagnetic waves that can interfere with the MR signal.

In the next sections, the state of the art for PET/MR and SPECT/MR systems is reported. A comparison of the two modalities is provided, underlining advantages and drawbacks for both the modalities.

### 1.4.1 PET/MR

Hammer and co-workers represent one of the first groups to address the issue of integrating PET and MR scanners in the mid 1990s [16, 17]. Their design was based on placing PET detectors inside a clinical MR scanner and extracting the information from the scintillator over light guides that transported the signals to photomultiplier tubes positioned outside the magnetic field. In the meanwhile, a small ring of PET detectors for small animal imaging was developed by Shao, Cherry and co-workers [18, 19]. However, in contrast to the SPECT/CT and PET/CT developments, MR/PET was destined to remain in the pre-clinical field for another decade: progresses were hampered mainly by the substantial difficulties posed by operating PET and MR in close proximity, and in part due to initial lack of industry interest and concerns over the cost of such a combined device [4]. In 2006, the first simultaneous MR and PET images of the human brain were acquired demonstrated successfully [20, 21].

Table 1.1 provides an overview over the development of prototypes and commercial PET/MR scanners in the last two decades. The number of clinical systems is still limited by several technical difficulties that make combining the two modalities challenging. It requires a careful design of both modalities to achieve performance and specifications similar to their stand-alone imaging counterparts.

PET is intrinsically a 3D imaging methodology, replacing physical collimation required for single-photon imaging with the electronic collimation of coincidence detection [5]. Recent developments aim to the production of time of flight (TOF) systems, capable to reduce the uncertainty in the positrons absorption position reconstruction, with an increase of the signal on noise ratio (SNR) and reduction of image artifacts. Thus paving the way to imaging systems that reconstruct high quality images in a relatively short amount of time. PET/MR scanning time is then defined by the slower

<sup>1</sup>P: Preclinical, C: Clinical; R: Research, Co: Commercial; Seq: Sequential, Sim: Simultaneous.

## Chapter 1. Multimodality in medical imaging

**Table 1.1:** Overview of PET/MR systems described in literature

Company or university	Year	Usage <sup>1</sup>	MR field strength (T)	Scintillator, detector	Crystal rings	Blocks/ring
University of California Los Angeles, CA (US)	1997	P-R-Sim	0.2	LSO MC PMT + fibers	1	48
University of California Los Angeles, CA (US)	1997	P-R-Sim	0.2 and 9.4	LSO MC PMT + fibers	1	72
Kings College Londo (UK)	2005	P-R-Sim	3	LSO PS PMT + fibers	1	8
University of Cambridge Cambridge (UK)	2006	P-R-Sim	1 (split magnet)	LSO PS PMT + fibers	48	24
West Virginia University Morgantown, WV (US)	2007	P-R-Sim	3	LSO PS PMT + fibers	20	2
Kobe City College of Technology, Kobe (JP)	2009	P-R-Sim	0.15	MLS PS PMT + fibers	3	32
Western Ontario London, ON (CA)	2009	P-R-Seq	0.3 (field cycled)	BGO PS PMT + fibers	8	2
Kobe City College of Technology, Kobe (JP)	2010	P-R-Sim	0.3	LGSO PS PMT + fibers	11	16
Nagoya University Nagoya (JP)	2012	P-R-Sim	0.3	LGSO PS PMT + fibers	13	16
Mediso Ltd. Budapest (HU)	2013	P-Co-Seq	1	LYSO PS PMT	81	12
University of California Davis, CA (US)	2006	P-R-Sim	7	LSO PS APD + fibers	8	16
University of Tübingen Tübingen (DE)	2007	P-R-Sim	7	LSO APD	12	10
Brookhaven National Laboratory, Upton, NY (US)	2011	P-R-Sim	9.4	LSO APD	8	12
University of Tübingen Tübingen (DE)	2013	P-R-Sim	7	LSO APD	45	16
Sogang University Seoul (KR)	2011	P-R-Sim	3	LYSO SiPM	4	16
Seoul National University Seoul (KR)	2012	P-R-Sim	3	LGSO SiPM	20	12
RWTH Aachen Aachen (DE)	2012	P-R-Sim	3	LYSO Digital SiPM	22	10
Eulji University Gyeonggi (KR)	2012	P-R-Sim	3	LYSO SiPM + fibers	6	12
Kobe City College of Technology, Kobe (JP)	2012	P-R-Sim	0.15	LGSO SiPM phoswich	11	16
Sogang University Seoul (KR)	2013	P-R-Sim	3	LYSO SiPM	4	72
Koninklijke Philips NV Eindhoven (NL)	2011	C-Co-Seq	3	- PMT	44	28
Siemens AG München (DE)	2008	C-R-Sim	3 and 9.4	- APD	72	32
Siemens AG München (DE)	2012	C-Co-Sim	3	- APD	64	56
GE Healthcare Waukesha, WI (US)	2014	C-Co-Sim	3	SiPM	45	112

#### 1.4. Multimodality with Magnetic Resonance

---

process, defined by the MR protocols. It is important also to underline that the PET/MR acquisition is still slower rather than in a PET/CT one. As general consideration, the implementation of simultaneous multimodal scanners has a crucial impact on the patient scanning time.

Although technical optimization of PET/MR systems still presents open points, nowadays the research and development has reached a quite mature level, with a number of scanners dedicate to clinical whole-body registration.

The combination of picomolar sensitivity to tracers of the PET (information about cell metabolism and receptor status) and the superb soft-tissue contrast and functional information on perfusion, diffusion, or metabolism from the MR opened the way to a wide range of clinical applications, mainly in the fields of cardiology, neurology and monitoring different cellular processes. Neuroreceptors and neurotransmitters kinetic studies, together with activation studies, will play a key role in preclinical research and neuro-psychiatry.

It is feasible with current prototypes and future generation systems to simultaneously study brain function, metabolism, oxygen consumption, and perfusion. The exact spatial and temporal co-registration of data will allow the attribution of functional and molecular information to even anatomically small brain structures. For the first time, it may become possible to study the correlation of local radiotracer uptake and brain perfusion. Time-dependent processes such as perfusion changes in stroke patients may rely on simultaneous diffusion-weighted imaging and detection of PET perfusion to determine the optimal therapy procedure. In neuro-oncology, an accurate spatial match between PET and MRI data is mandatory for both radiation therapy planning and biopsy guidance [22].

In parallel with the development of multimodal systems and the discussion on their possible fields of application, big effort has been dedicated in the research of new multimodality imaging/contrast agents. The PET/MR will certainly benefit from these discoveries, even though SPECT based systems will be the most boosted since the big number of radiotracers available. For this reason, a more detailed discussion on imaging/contrast agents is presented in section 1.5. Table 1.2 reports the list of isotopes used in PET imaging: the first four are of particular note with regard to imaging biological systems.

Carbon, nitrogen, and oxygen are key elements for biological systems and they are binded to specific molecules after their production in cyclotrones.

## Chapter 1. Multimodality in medical imaging

**Table 1.2:** *PET radiotracers*

<b>Isotope</b>	$^{11}\text{C}$	$^{13}\text{N}$	$^{15}\text{O}$	$^{18}\text{F}$	$^{38}\text{K}$	$^{62}\text{Cu}$	$^{64}\text{Cu}$	$^{68}\text{Ga}$	$^{82}\text{Rb}$	$^{124}\text{I}$
<b>Half-life</b>	20.4 m	10 m	122 s	110 m	7.6 m	9.7 m	12.7 h	68.1 h	75 s	4.2 d

Fluorine (also created in cyclotron), the fourth entry in the table, is not a normal element in biological systems, but fluorine can often replace either a hydrogen atom. One of the most evident limitation in the employment of PET radiotracers is their short half-lives. Oxygen has and approximately two minutes half-life, which means that it needs to be pumped directly from a cyclotron to the scan room. Nitrogen and carbon isotopes have a relatively longer half life and can be managed more easily, even if they allow a very limited time window for the entire injection and acquisition protocol [PET radiotracers]. For logistical reasons, the isotope which is most commonly used in clinical practice is  $^{18}\text{F}$  because of its long half-life (110 minutes) allowing transportation to distant places from its production origin.

Although the potentiality of this multimodality systems makes it extremely attractive for both preclinical studies and clinical practice, there are still some properties that are hampering its fast diffusion. The major limitations of the PET/MR are the restricted availability and the high costs of the equipments, since most of the solutions proposed in literature foresee the design of a completely new integrated scanners. Another major challenge is the relative lack of technologists who are trained in both modalities: this aspect could somehow enhance the the diffidence with such complex apparatus and slow down its diffusion in clinical practice.

### 1.4.2 SPECT/MR

The same technical complexity that has affected the development of PET/MR multimodal systems, is also the primary cause of lateness in a mature research dedicated to SPECT/MR prototypes. Mutual compatibility between the two instruments has to be provided and, at the same time, the performance of both the systems together should not be compromised with respect to that of the independent stand-alone ones. In addition to the issues already identified in section 1.4.1), the SPECT introduces other complications in the design of the multimodal scanner. The first one is related to the fact that most stand-alone SPECT systems implement a motorized rotation around the field of view (FOV). The presence of a stationary magnetic field and the activation of gradient fields during the MR acquisition make extremely difficult the engineerization of such movement. Thus only sta-



#### 1.4. Multimodality with Magnetic Resonance

tionary SPECT rings can be integrated in MR scanners. As second level of complication is introduced by the presence of tungsten collimators, which are fundamental to provide spatial coherence to the SPECT reconstructed image. Bulky metal materials introduced in MR gantries are likely to have eddy currents generated in their volumes, with extreme consequences for the compatibility. Moreover collimators limits the possibility to have a compact design of the whole SPECT in the very limited space inside the magnet.

In the effort made by the scientific community to combine a nuclear medicine imaging device with magnetic resonance, PET has definitely been preferred with respect to SPECT. Since PET is intrinsically a 3D imaging methodology, it does not need the implementation of physical collimation, avoiding compatibility issues and improving considerably the sensitivity of the system. In order to achieve the same range of sensitivity, SPECT’s collimator have to be redesigned, considering an unavoidable tradeoff between spatial resolution and sensitivity.

As like the PET, SPECT systems have proven to be useful molecular imaging techniques due to their higher detection sensitivity compared to CT or MRI. However, one of the major limitations of clinical SPECT scanners is the poor spatial resolution (in the order of several millimeters with parallel-hole collimators) with respect to PET. The limitation could be improved by pinhole collimation and image magnification. Unfortunately this is only possible at the expense of a loss in detection sensitivity and increased imaging time to retain a good signal-to-noise ratio (SNR) in the images. One obvious way to increase the detection sensitivity while obtaining high spatial resolution is to use multi-pinhole collimators [23]. A further disadvantage of increasing the image magnification is related to the necessity of using larger detectors resulting in increased system costs [24].

Although clinical SPECT scanners can provide a tomographic resolution of about 10 mm, some preclinical SPECT ones can provide a submillimeter spatial resolution pushing down to sub-half millimeters using a specialized dedicated multipinhole geometry [25] and thanks to the development of high resolution gamma cameras [26, 27]. This situation is different in clinical and preclinical PET imaging where the spatial resolution of preclinical PET scanners is about 1-2 mm while that of clinical PET scanners lies in the range of 4-6 mm (Figure 1.3). These resolution differences are mainly due to the fact that SPECT systems are not affected by some physical and fundamental limits that hinder the PET camera to reach sub-millimeter ranges.

Many factors serve to impact the final reconstructed images of data acquired from a PET scanner. These are crystal size, positron range, photon

## Chapter 1. Multimodality in medical imaging

8–12 mm	4–6 mm	1–2 mm	≤1 mm
Clinical SPECT	Clinical PET	Preclinical PET	Preclinical SPECT

**Figure 1.3:** *Spatial resolution across the clinical and preclinical SPECT and PET imaging scanners. [28]*

non-collinearity, inter-crystal interaction and scatter, depth of interaction and the reconstruction algorithm. In preclinical PET machines, positron range appears to be the most important challenge that needs to be tackled to improve the spatial resolution of the PET images. However, the current generation of clinical PET scanners is slightly affected by the positron range, but the presence of a static magnetic field from MR induced a reduction in positron free path, with direct reduction of the uncertainty on the emission position and better spatial resolution [29]. These issues are obviously absent in clinical as well as preclinical SPECT systems. The gamma camera relies on hardware collimators to determine the photons trajectory and hence able to localize the emission site by analyzing the electronic signal detected by the imaging detector. This hardware collimation plays a significant role in reducing the overall system sensitivity as well as the spatial resolution.

The intrinsic resolution of gamma camera is about 3–4 mm and tomographic SPECT acquisition reveals a spatial resolution, as mentioned above, not better than 10 mm. However, a new trend of semiconductor-based systems is emerging in the field, providing a significant improvement in spatial resolution, and other performance measures [30–32].

Table 1.3 reports the radioactive isotopes of widest diffusion in SPECT imaging. The radiolabeling of specific molecular agents (Radiolabeled Molecular Imaging Probes - RMIPs) can follow different design strategies, exhaustively described in [28]. The labeling operation represents a chemical linking of the radionuclide in the specific structure of a molecule, then the functional and biological behavior of the molecule itself can be altered. Although this limitation, a very high number of RMIPs is today available for SPECT diagnosis. Another factor of strength is related to the half-life range of this isotopes, since it is set in a tradeoff region between radionuclides with too short half life, for which patient preparation and scanning

## 1.4. Multimodality with Magnetic Resonance

**Table 1.3:** *SPECT radionuclides*

Radionuclide	Half-life	Principal $\gamma$ emission [keV]
$^{99m}\text{Tc}$	6.01 h	140.5
$^{123m}\text{I}$	13.27 h	159.0
$^{131}\text{I}$	8.02 d	364.5
$^{67}\text{Ga}$	3.261 d	93.3 / 184.6
$^{111}\text{In}$	2.805 d	171.3 / 245.4
$^{201}\text{Tl}$	3.038 d	167.4

can become unpractical, and those with long decay time. In this last case a very high dose has to be delivered to assess a regular acquisition in a reasonable time lapse.

Although SPECT/MR co-registration images through software merging were studied since the mid 1990s [33, 34], the technological limitations previously analyzed limited the development of hardware systems up to the end on the 2000s.

A first solution for multimodal hardware imaging of small animals with SPECT and MR was explored in 2008 by placing a PMT-based SPECT in tandem with a low-field (0.1 T) MR scanner [35].

Following in 2009, a prototype of simultaneous SPECT/MR scanner for preclinical studies has been developed by Tsui and colleagues [24, 36, 37]. The first version of the prototype consisted in a non-rotating, 16 cm diameter SPECT system based on Cadmium Zinc Telluride (CZT) detectors to be inserted in a commercial MR scanner. It demonstrated the feasibility of simultaneous SPECT/MR imaging using a multiple detector ring system. However, the system exhibited some limitations, such as relatively poor spatial resolution (3-5 mm). To address some of these issues, a second-generation SPECT/MR prototype was produced, comprising five rings of 19 CZT detectors (each containing a  $16 \times 16$  array of 1.6 mm pixels) and a variety of cylindrical multipinhole collimators. The new device has an outer diameter of 20 cm, enabling it to fit inside a mid-sized preclinical MRI scanner. A 36-pinhole design for the collimator, with three rows of 12 pinhole inserts, offered a resolution of 1.5 mm within a 30 mm FOV.

In the same period, Meng and colleagues developed and optimized an high resolution SPECT/MR for small animals imaging based on cadmium Telluride (CdTe) detectors [14, 38–40]. The overall system diameter for the SPECT insert is of 248 mm and it is composed by 10 gamma detection

## Chapter 1. Multimodality in medical imaging

---

modules. Each module consists of CdTe detectors having an overall size of  $22.5 \times 11.2 \times 2 \text{ mm}^3$ , divided into  $64 \times 32$  pixels of  $350 \mu\text{m}$  in size. The stationary system has sub $500 \mu\text{m}$  spatial resolution.

CdTe and CZT detectors have paved the way for preclinical SPECT systems combined with MR imaging because of their compactness and the high performances in terms of spatial and energy resolution. However, high performances come with a tradeoff with the number of detector channels to be read by the electronics and with the cost of the crystals when composed in large field of view (FOV) detection modules. Moreover, it has been pointed out a shift of the signal charge inside the detector volume, caused by Lorentz forces when it is located inside the MR magnetic field. This effect is undesirable and requires detector-specific corrections.

Other projects are in an earlier stage of development of SPECT/MR systems, typically in the designing and characterizing phase of the MR-compatible gamma modules: the department of electronics and information systems from Ghent university designed and manufactured a compact gamma camera with a thin (2 mm) LYSO crystal coupled to an array of  $8 \times 8$  digital SiPMs ( $3.2 \times 3.2 \text{ mm}^2$  each) [41]. They obtained very good resolution around 0.5 mm in an approximately  $32 \times 32 \text{ mm}^2$  FOV and an energy resolution above 28 % (at 140 keV).

A group from Laboratory of linear accelerator (Orsay, France) has tested a gamma camera with  $\text{LaBr}_3$  coupled to an array of  $16 \times 16$  SiPMs ( $3 \times 3 \text{ mm}^2$  each) [42]. The spatial resolution they estimated is 1 mm in the center of the  $54 \times 53 \text{ mm}^2$  FOV and a 9.8 % energy resolution (at 122 keV) was also estimated.

In 2015, Yamamoto and colleagues presented the preliminary results regarding a MR-compatible SPECT module, in which a bundle of optical fibers are coupled to a YSO scintillator crystal [43]. The light signal is then transported to a PSPMT. The energy resolution was 38 % and the system resolution was 1.7 mm FWHM, 1.5 mm from the collimator surface.

### 1.5 Rationale for SPECT/MR systems

---

The hereafter discussion of the thesis is based on the design, development and characterization of a gamma module for the population of a MR-compatible SPECT insert. A global overview on multimodal imaging systems has been provided as well as a brief description of the state of the art for SPECT/MR systems with advantages and drawbacks, mostly when compared with the competitive PET/MR systems. In the present section,

## 1.5. Rationale for SPECT/MR systems

the technological, scientific and clinical motivations for a combined SPECT and MR scanner are discussed.

The multimodality approach has proved to increase the possibilities related to analysis and diagnostic by combining two or more imaging tools. The outcome image from two medical devices merged contains richer information rather than the sum of the independent images of the stand alone systems. This aspect impacts not only on diagnostic, but also on patient treatment or research on pharmacologic agents.

Another direct consequence of multimodality is the optimization of the procedures time. When a patient or a laboratory animal is to be imaged with both modalities, the two studies have to be done in distinct imaging sessions, in different rooms and often in different departments or building within a medical facility. Hybrid SPECT/MR would reduce the time employed in performing the two (time-consuming) scanning with independent systems and this would have tremendous consequences in the case of a series of repeated scanning sessions (e.g. patients that need to be followed up periodically during a recovery treatment). On this purpose, the non-ionizing capability of the MR scanner represents a crucial added value.

Combined SPECT/MRI imaging is important since non-invasive probing of intact, living biological organisms bridges the gap between exponentially growing understanding of molecular and genetic mechanisms and the phenotypical embodiments of diseases and their response to treatments. SPECT is a radionuclide-based technique with relatively poor resolution, but really sensitive to picomolar tracer concentration. MRI suffers from much lower sensitivity to concentration of contrast agents, but it provides high soft-tissue contrast and spatial resolution. Moreover, the SPECT images can benefit from other functional MR measurements, already seen in section 1.4.1 (dynamic contrast-enhanced MRI, diffusion-weighted MRI, functional MRI, pharmacologic MRI and MR spectroscopy). Moreover, there are studies for the enhancement of SPECT image reconstruction, starting from the coregistered SPECT-MR tomography.

SPECT/MR systems make feasible the simultaneous and dynamic imaging of both structure and function even using multiple tracers during the same registration, further reducing total scan time and providing valuable and accurate information with regards to different metabolic paths within only one scanning session [44, 45]. With PET systems, on the contrary, multi-tracing it is not feasible, since all the positrons produce a couple of 511 keV gamma photons during the decay. Thus energy is fixed and there is no possibility to distinguish different tracers.

## Chapter 1. Multimodality in medical imaging

---

Unlike PET, single photon emitting radiopharmaceuticals have several features in the context of molecular imaging such as cost and wide availability of the radioligands as well as relative ease of labeling [28].

The development of combined SPECT/MR system is still in a preliminary phase, with only few prototypes realized and/or commercialized. Nevertheless, the current interest in such system has incited the quest for novel dual-modality agents, but also for new SPECT molecular ligands. A number of large biomolecules (e.g. peptides and proteins) and particles (e.g. liposomes and nanoparticles) offer appropriate platforms for building imaging agents that can provide contrast for both SPECT and MRI. One motivation for developing these hybrid agents is that they enable the study of the same labeled target on different technological platforms and at different scales [4]. For example, the high sensitivity of the SPECT could be employed to determine areas of focal uptake of a targeted agent in the body, followed by very high resolution MR imaging of the same agent, but with the MR images only being acquired in the localized regions where PET signal was seen.

It is important to consider that the application of radiolabelled MRI probes using a suitable chemical reporter group for hybrid SPECT/MR imaging is limited due to the required alteration of the molecular structure and thus changing and compromising their in vivo properties. One alternative solution is given by radiolabelling of existing MRI contrast agents with SPECT isotopes of paramagnetic elements, such as  $^{147}\text{Ga}$ ,  $^{149}\text{Ga}$  or  $^{52g}\text{Mn}$  [46] or supermagnetic ones like  $^{59}\text{F}$  [47]. Considering the latter example, supermagnetic iron oxide nano-particles (SPIONs) are used as MRI agents in clinical practice and they have also been radiolabelled with  $^{99m}\text{Tc}$  to evaluate a possible implementation in preclinical studies [48].

### 1.5.1 Preclinical SPECT/MR rationale

The application of imaging modalities to preclinical models (immunodepressed animal hosts for human disease cell lines) has scope for noninvasively studying dynamic biological processes at the molecular and cellular level. The noninvasive nature of SPECT and MR imaging provides advantages in investigating the onset and the progression of disease, assessing the biological effects of experimental drugs and assisting in the development of disease biomarkers and monitoring the therapeutic effectiveness of new treatment and/or pharmaceuticals. This technology plays a key role in bonding studies of disease modeled in vitro to their implementation in animal models (in vivo) for their translation into the clinical practice. In

## 1.5. Rationale for SPECT/MR systems

fact, the implementation of imaging in rodents has a great relevance because of the widespread use of genetically modified mice in biomedical research and the need to characterize the in vivo anatomical and functional characteristics of animal disease models [28].

Due to its high sensitivity, SPECT has preeminent capability to monitor and quantify dynamic processes at a molecular level in vivo. Unique SPECT capabilities include: the ability to image ligands such as peptides and antibodies with  $^{99m}\text{Tc}$ ,  $^{111}\text{In}$  or iodine isotopes ( $^{123}\text{I}$ ,  $^{125}\text{I}$ ), the possibility to measure slow kinetic processes due to the long half-life (compared to most PET tracers) of some of the commonly used radionuclides, and the capability to probe multiple molecular pathways simultaneously by detecting radionuclides with different gamma energies [49].

For SPECT, pinhole and multi-pinholes collimation techniques are capable of submillimeter and millimeter spatial resolution for acquisition time shorter than 1 hour [50], while preclinical PET is intrinsically limited to a 2-3 mm resolution. For MRI, high magnetic fields up to 11.3 T are considered mandatory for high-resolution imaging, leading also to acquisition times in the order of 1 hour.

On the other hand, the drawbacks of SPECT include its lower sensitivity compared to PET, especially when high-resolution SPECT is desired. Moreover, as already mentioned, SPECT tracer molecules may differ in functionality with regard to their biological properties since the introduction of a radionuclide in the chemical structure, which is not the case for several PET tracers in which endogenous atoms (such as hydrogen, carbon and oxygen) can be replaced by their radioactive isotopes. In addition, the dynamic capabilities of SPECT, although recently greatly improved, are often limited compared to those of PET.

The most evident motivation for the development of hybrid SPECT/MR systems is the wide range of possible preclinical applications, described in detail by [28, 49], with direct implication also in clinical practice. The research field of interest are:

- Cardiovascular functionality and disease diagnosis.
- Oncology, particularly through the monitoring of interstitial hypertension, hypoxia, acidosis, metabolic activity and proteolytic activity.
- Drugs discovery and delivery.
- Cell migration and tracking.
- Neuroimaging and neuro-oncology applications.

## Chapter 1. Multimodality in medical imaging

---

### 1.5.2 Clinical SPECT/MR rationale

The interest into an hybrid SPECT/MR for human patients have been already covered by the discussion on preclinical applications, since the research on animals is intended for the translation towards clinical practice. The specific applications intended for the clinical SPECT/MR system discussed in the present work and related to the INSERT project will be presented in a separated section (2.1).

The potential of multimodal imaging with SPECT and MRI in the clinical routine has been addressed by Zaidi [51]. The applications for such multimodal instrument can be deduced from the uprising trend of each independent modality into new fields. As an example, Dynamic Contrast Enhanced (DCE) breast imaging is rapidly growing in the field of MRI. At the same time, Molecular Breast Imaging (MBI) using  $^{99m}\text{Tc}$ -sestamibi is giving promising results in the definition of small breast lesions. Thus, the two modalities can measure different and complementary biological processes connected to the same anatomical compartment, for a richer information that benefits diagnosis accuracy.

Another important example of effective application is related to prostate cancer imaging, for which the PET systems are poorly sensitive because of the limited uptake of  $^{18}\text{F}$ -FDG (Fluorodeoxyglucose - a RMIP largely employed in PET for oncology) in this relatively non-aggressive cancer. Many works also underline the interest into combining  $^{123}\text{I}$ -IMP (or others RMIPs) cerebral blood flow dynamic acquisition (SPECT) together with measurements of arterial concentration of Gd-DTPA (MRI) [52–54].



---

## CHAPTER 2

---

### INSERT project

---

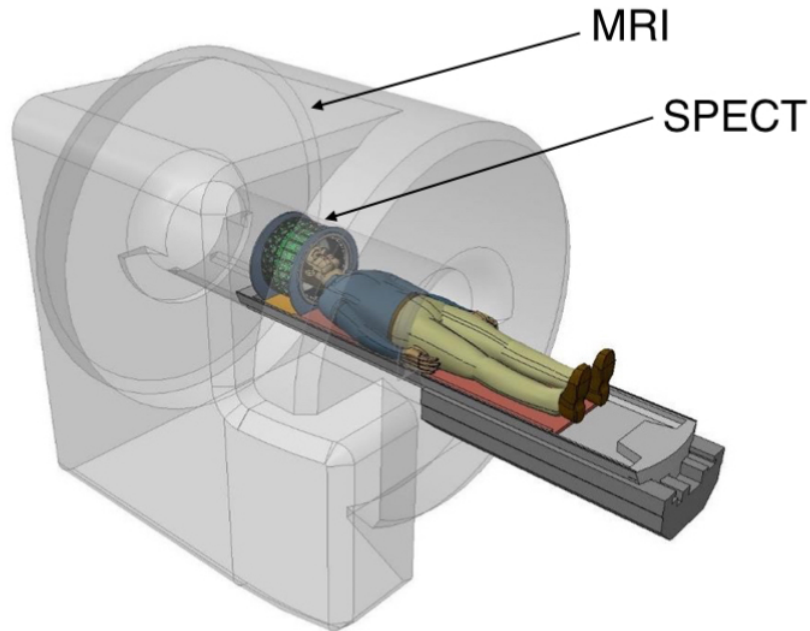
#### 2.1 Objective and motivations

---

INSERT is a research project funded by the Seventh Framework Program of the European Commission and started on March 1<sup>st</sup>, 2013. *INSERT* acronym stands for "Development of an integrated SPECT/MRI system for enhanced stratification of brain tumor patients prior to patient-specific radio-chemo therapy and early assessment of treatment efficacy". The aim of the project is to develop a MR compatible and compact SPECT insert to be fit inside commercial MR scanners. The combination of the two systems will enable the simultaneous acquisition of images from both the modalities (Figure 2.1).

The design concept of a insertable SPECT rises many technical and logistic challenges, but it represents the most flexible typology of hardware fusion with MR system: it permits either multimodal, simultaneous registration for the two imaging techniques and, at the same time, keeps the hardware costs low, since the two systems are independent and only the SPECT ring has to be redesigned for MR compatibility (with the only exception of the RF coils).

## Chapter 2. INSERT project



**Figure 2.1:** *Conceptual draw of the MR-compatible, clinical SPECT insert under development, dedicated to human neck/head sector tomography. Courtesy of Mediso Kft., Hungary.*

The motivation of the INSERT project lays in the wide range of possible applications both for biological research and for clinical diagnosis and therapy monitoring described in section 1.5. Nevertheless, the project needed a more defined and specific motivation to address a manageable program and specific technological requirements. The INSERT project is then dedicated to the research of a more powerful tool for the diagnosis and therapy of gliomas. A glioma is a common type of brain (and spine) tumor that occurs in the 33 % of the overall central nervous system tumors and represents the 80 % of all malignant brain tumors. Gliomas originate in the glial cells in the brain, which compose the tissue that surrounds and supports neurons in the brain. There is no obvious cause of glioma. This type of brain tumor affects all ages, but is more common in adults [55] and it presents an high mortality rate. Unfortunately the management of these patients, both adults and in pediatric age, is still a challenge since the life expectancy given by this pathology is very low and the traditional surgery does not represent a definitive solution in all cases, given the nature of these tumors. One of the most interesting techniques that is producing outstanding results in terms of brain cancer treatment is radiotherapy. It consist in the modification of

## 2.2. Technological and technical principles on SPECT systems

---

the malignant tissue conditions and environment through the delivery of energy provided by ionizing radiation. The final aim of radiotherapy is the destruction of the tumoral cells and, at the same time, prevent the surrounding healthy tissues to be compromised by the ionized radiation which is part of the therapy itself. Starting from this principle statement, it is evident that a precise identification and localization of the tumor and its environment is a key element in efficient radiotherapy protocols. In such a contest, the INSERT system would give the possibility to obtain multiple parameters to better define not only the tumor position inside the patient-specific anatomy, but also its biological characteristics. The final aim of the multimodality instrument is to give rich and detail information for a personalized treatment, with a considerable impact on the efficacy of the therapy.

The system will be validated at the pre-clinical level thanks to the creation of animal models, and to the clinical level, thanks to a pilot study which will involve patients affected by glioma.

## 2.2 Technological and technical principles on SPECT systems

---

The present section summarizes the basic elements that compose both the SPECT and MRI system, with also a description of the functional principles that allow the instruments to properly operate. The portrait given is not all-embracing, but takes into consideration only those characteristics that are fundamental for the following discussion.

### 2.2.1 SPECT principles

With scintigraphy and positron emission tomography (PET), single photon emission computed-tomography (SPECT) completes the list of the equipments employed in nuclear medicine for diagnostic purposes. Differently from the radiology approach, in which the radiation is generated by external sources (e.g. X-ray tubes) and delivered to the patient, SPECT imaging is *radiology done inside out* or *endoradiology* because it records radiation emitting from within the body. As already described in Chapter 1, radioactive isotopes or radionuclides are bond to molecular probes that are likely to interact with specific biological processes that can involve different scales of the living being: molecular and proteins activity, DNA replication, cellular metabolism, tissues and organs structure functionality or also system of organs activity. The radiolabeled substance will then be distributed in the host body depending on the activation of the biological process described above. A SPECT system is a combination of devices that together are capable to catch the radiation emitted from inside the patient body and retrieve

## Chapter 2. INSERT project

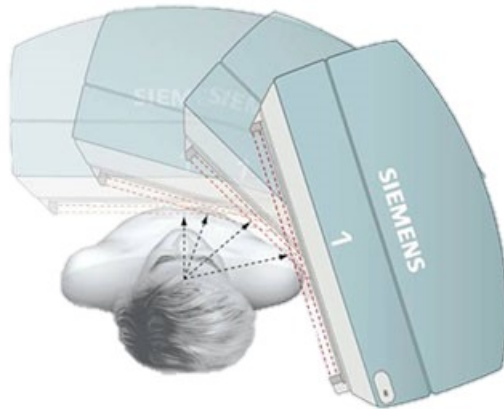
---

the information regarding the spatial distribution of the of the radioactive substance inside the body. Furthermore, SPECT is a 3D tomographic technique in the sense that uses distribution data from many projections, acquired with several planar imaging systems, in order to obtain reconstructed cross-sectional slices of the radiomolecule distribution in different planes of the patient body.

### Structure

SPECT imaging is performed by acquiring the radiation projected from inside the patient body on several external detection planes. These planes have a transverse positioning with respect to the tomographic slices that will be finally reconstructed. The planar detection on a single plane is performed by a gamma-camera which will be better described later. The exploration of different projection planes is performed through two possible approaches:

**Rotational approach** - In this case the SPECT system is composed by a limited number of gamma-cameras (typically 1-4) that are positioned around the region to be imaged. The cameras are mechanically connected to a rotational engine that changes the angular position of the devices around the region, in order to change the projection plane to be imaged (Figure 2.2).



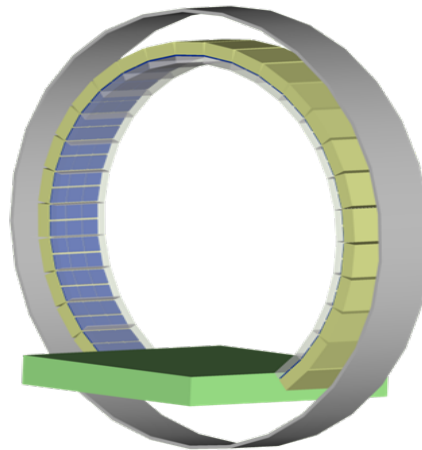
**Figure 2.2:** *Single gamma-camera pivoting around patients head: rotational approach for SPECT systems (www.siemens.com/press).*

Adopting a limited number of gamma-cameras gives the advantage of larger planar image acquisitions and of limited cost for the system (also depending on the rotational engine). Moreover the number of projections that

## 2.2. Technological and technical principles on SPECT systems

can be retrieved is virtually infinite and this is beneficial to the reconstruction methods that will be later described. On the other hand, the registration from different angles is sequential and not synchronous, representing an obstacle to dynamic imaging, and the acquisition duration in different projections has to be scaled considering the source activity variation. Considering hybrid SPECT/MR scanners, the rotational systems definitely introduce a very high level of design complexity, mostly because of the eddy currents induced in the matter when it moves in a high-magnitude static field and also because the engines and the transmission and structural components that support rotation are often made with material incompatible with MR.

**Ring approach** - The SPECT system is composed by a multitude of gamma-cameras that cover an equivalent number of projections around a circular trajectory. The final geometry of the apparatus is a closed or open ring populated with the gamma-cameras (Figure 2.3).



**Figure 2.3:** Conceptual draw - numerous, identical gamma-cameras populating a ring SPECT system.

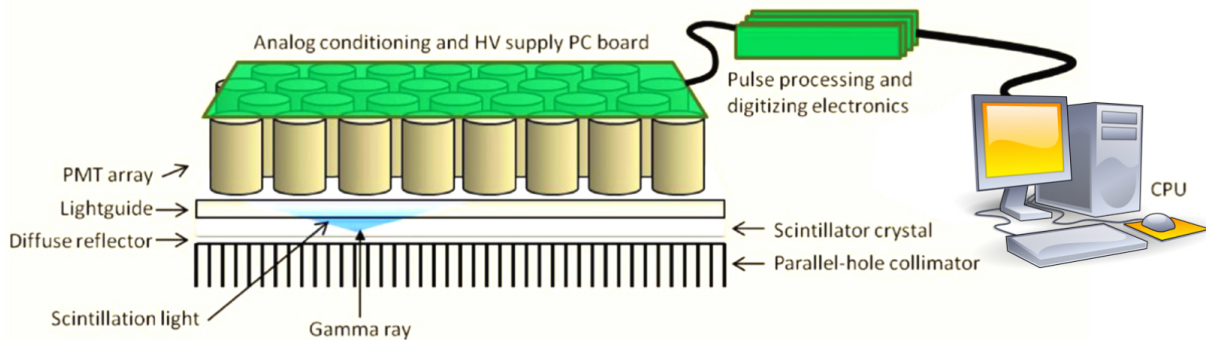
This paradigm has a higher cost and can provide only a limited number of projected images (the total number of gamma-cameras) with typically a reduced field of view with respect to the rotational case. Nevertheless, the images are recorded in the same time interval, opening the possibility for dynamic tracking of the radionuclides. As an additional note, rotational and ring approaches are not mutually exclusive, which means that rotational ring SPECT are feasible and lead to very challenging performance,

## Chapter 2. INSERT project

as demonstrated in an important work from Genna and Smith [56].

### The gamma-camera

The main component of a SPECT is the gamma-camera (Figure 2.4): it is a device that converts single gamma-rays into an electronic signal to be filtered and elaborated.



**Figure 2.4:** Description of a gamma-camera system. The collimated gamma-ray is absorbed in the scintillator volume, then a flash of photons is generated and read by an array of photodetectors. The electronic signal from each device is amplified, filtered and then elaborated for image reconstruction.

The incoming radiation is filtered by the collimator and only the gamma-rays with a direction parallel to the collimator holes can pass through. The percentage of gamma radiation that “survives” the collimation, can be absorbed by the gamma-ray detector positioned beyond the collimator. The detection of the gamma-rays can be either direct or indirect. In the former case, the device is able to convert the radiation directly into an amount of charged carriers (typically electrons) and their number is proportional to the energy of the impinging gamma ray. As example, direct conversion is provided by Germanium-based detectors which provide impressive performances, but require severe cooling with liquid Nitrogen (approximately at 77 K) to reduce thermal excitation. The approach that is mostly implemented in nuclear medicine is the indirect detection through the adoption of inorganic scintillators. These are dense crystals composed of atoms with high atomic number, thus with a better chance to absorb impinging radiation with respect to direct conversion devices. Scintillators are so called since they are material that exhibits scintillation: when excited by ionizing radiation, scintillators absorb all or part of the energy and re-emit it in the form of a isotropic beam of photons (typically in the visible wavelength range). The crystal absorption spectrum is very low for the re-emitted pho-

## 2.2. Technological and technical principles on SPECT systems

tons, practically transparent, then the scintillator can be optically coupled to a photo-detector (see Section 3.1.2) to record the scintillation light emitted. The photodetector (i.e. the PMT - Photo-Multiplier Tube) converts the scintillation photons into carriers that are read by electronics circuits.

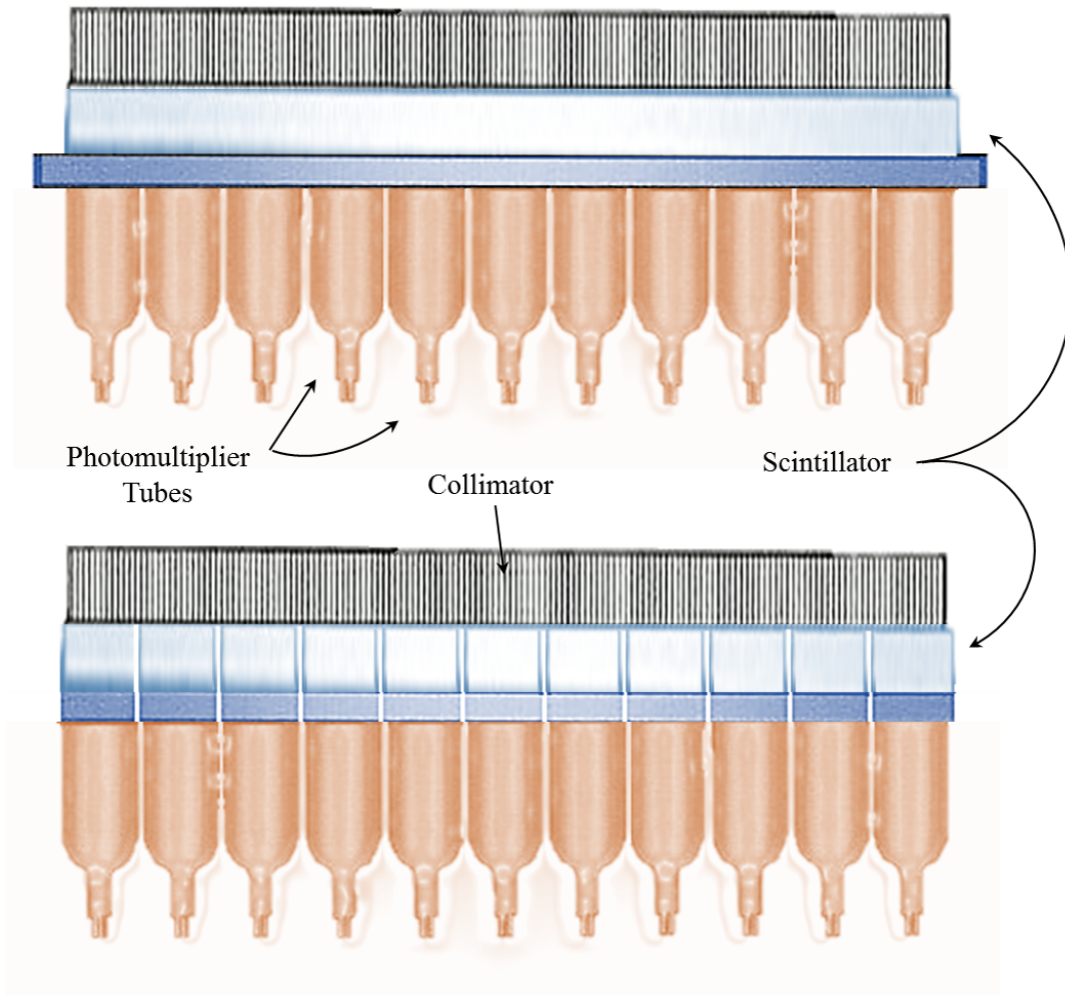
Even if the indirect method exhibits an higher detection efficiency with respect to direct detection, the implementation of a two-steps process for the conversion of the radiation (from gamma-ray to scintillation photons and then to charged carriers) introduces more sources for the signal fluctuation, with an augmented error on the final outcome. Nevertheless, the indirect approach has led to the development of systems that can be used in more practical context and for this reason they are the most spread in nuclear medicine practice.

The formation of an image requires the encoding of spatial information incorporated in the detection process. There are different possible methods to accomplish this task. Originally, a single detector element was translated across the field of view to collect many pieces that were than composed together into the final image. An example for this approach is the rectilinear scanner [57]. Nowadays, the systems implement a bidimensional array of detectors. The gamma-detectors that implement inorganic scintillators and multiple photo-detectors can present two main kind of architectures. In a first case, each photo-detector is optically coupled to a single scintillator that has typically the same dimensions of the photo-detector, for what concern the coupling surface. Since each scintillator and photo-detector form an independent detection element, they are defined as pixels and their dimension define the spatial resolution of the camera. For this reason, this type of gamma-detectors are referred to as *pixelated*.

The second architecture is that proposed by Hal Anger in 1952 and for this reason they are called *Anger camera*. A continuous, monolithic scintillator is coupled to an array of photo-detectors.

Compared with the pixelated camera (Figure 2.5), an Anger camera with the same detection surface can employ a lower number of larger photo-detectors while providing the same spatial resolution. In the former case the resolution is ruled by the dimension of the pixel, then a big number of detectors with their related readout electronics channels has to be implemented. On the opposite side, the spatial resolution in the Anger camera is governed mainly by the distribution of the scintillation light on the detection array plane: the correlated light information collected by multiple pixels is elaborated by algorithms that retrieve the original point of interaction of the gamma-ray in the scintillator. In such a way, the resolution of the camera can be even ten times (thumb rule) inferior with respect to

## Chapter 2. INSERT project



**Figure 2.5:** (top) Anger camera, with collimator, monolithic scintillator and array of photodetectors. (bottom) Pixelated camera architecture, with collimator and one scintillator couples to each photodetector.

the lateral dimension of the single pixel (photo-detector). The number of readout channels is notably reduced with respect to the pixelated approach, thus also the complexity and cost of the system is reduced.

### Gamma-camera parameters

In chapters 3 and 4 a detailed discussion on the conversion and elaboration procedure for the gamma signal is developed. The present section briefly



## 2.2. Technological and technical principles on SPECT systems

summarizes the main output parameters of a gamma-camera, for support to the following discussion.

The imaging quality of a gamma-detection system is mainly related to the intrinsic spatial resolution and to the dimension of the useful Field of View (FOV).

**Spatial resolution** - Intrinsic spatial resolution of the gamma-camera image is defined as the minimum distance required between two point gamma-sources (emitting only gamma-rays perpendicular to the main scintillator plane) to visualize them as distinct objects on the output image. The overall resolution of a gamma-camera with collimator (required for spatial coherence of the gamma distribution on the camera) can be defined as:

$$R_{extrinsic} = \sqrt{R_{intrinsic}^2 + R_{collimator}^2} \quad (2.1)$$

where  $R_{collimator}^2$  represents the collimator contribute to spatial resolution and is related to geometrical dimensions and shape of the collimator components.

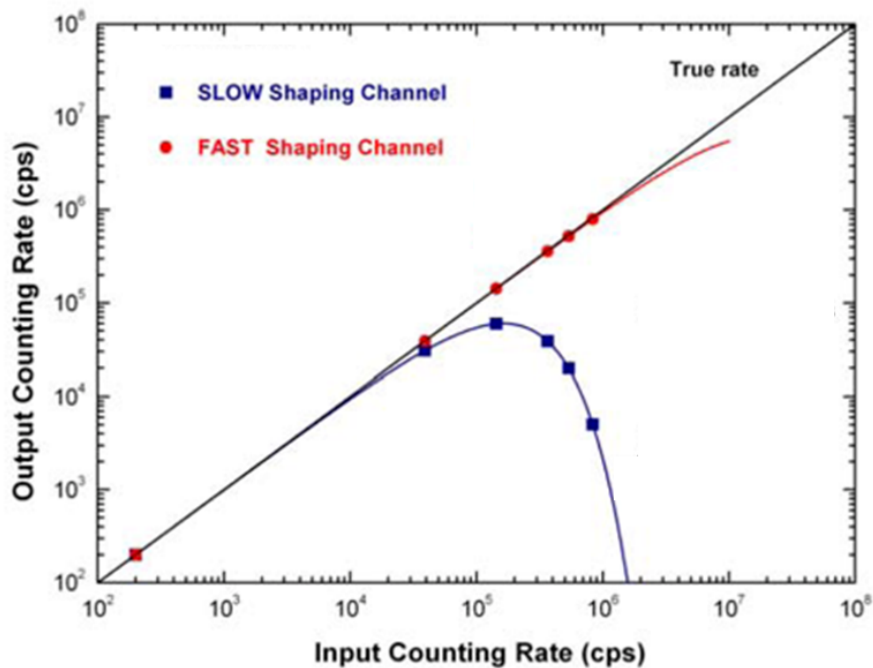
Spatial resolution is associated to the concept of Point Spread Function (PSF), representing the spatial response of the gamma imaging system to the point source: spatial resolution is frequently measured as the full width at half maximum (FWHM) of the PSF that defines the imaging tool.

**Field of view** - The field of view (FOV) represents the extent of the detectable radiation seen by the detector. The FOV can be defined as the active detection surface of the detector (e.g. the scintillator). In the case of a gamma-camera, there are two more detailed definitions for the FOV: the useful field of view (UFOV) of the gamma camera is essentially the entire reconstructed detector area, while the central field of view (CFOV) corresponds to the central area of the crystal (typically 3/4 of the total crystal) and, by definition, is that portion of the FOV where the image present no particular linearity artifacts and the spatial resolution is equal or inferior to the maximal required one.

**Count rate** - Count rate represent the temporal capability of the system to detect gamma-events without distortions on the output (imaging quality or energy spectrum). Count rate is generally represented as the number of events read by the detection system per time unit and is measured

## Chapter 2. INSERT project

in  $[\text{counts}\cdot\text{s}^{-1}]$ . Pulse pile-up is the main issue that limits the ability of a gamma camera to have satisfactory performance at high count rates. A more detailed characterization of the count rates is described in Figure 2.6 for a generic gamma-detector: the number of measured counts depends on that of the expected ones, which means the number of gamma-rays that are converted by the gamma-detector.



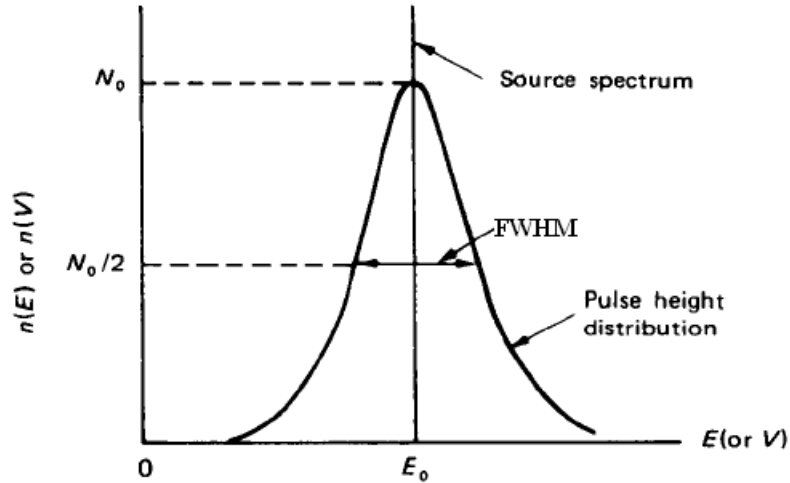
**Figure 2.6:** Measured count rate as function of the input count rate for a generic gamma-detector. Depending on the electronics shaping time, output count rate can be tremendously affected at high frequencies. [58]

The curve presents a linear behavior at low count rates, while for higher ones it becomes non-linear. This is related mainly to crystal afterglow that produces pulse pile-up effects and depends also on the electronics readout strategy.

**Energy resolution** - Energy resolution is defined as the minimum energy gap between two gamma-sources to be distinguished by the detection system.

A monoenergetic source radiation produces a number of events in the gamma-detection module and, ideally, the energy measured for each event should be always the same. Because of stochastic and intrinsic processes

## 2.2. Technological and technical principles on SPECT systems



**Figure 2.7:** Main parameters of a Gaussian curve, approximating the energy peak distribution on a radioactive source spectrum. [59]

(for details the reader can refer to section 3.2), the measured energy spectra of monoenergetic sources present broaden distributions in correspondence of the emission peaks. The distribution can be approximated to a Gaussian curve 2.7, for which energy resolution is defined as:

$$R_{en} = \frac{\Delta E}{E_0} = \frac{FWHM}{E_0} \quad (2.2)$$

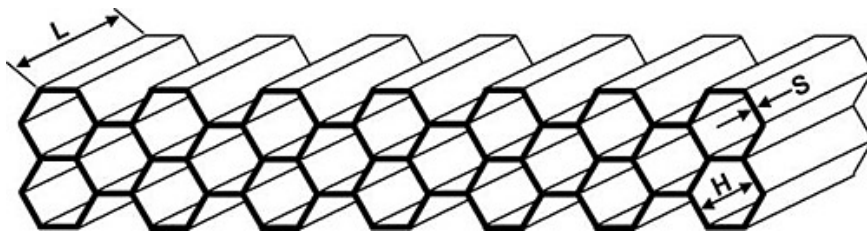
### 2.2.2 Collimation in SPECT

The collimator is a device composed by high density material, typically made of Lead (Tungsten is also employed, but less frequently because of higher machining costs), an designed in such a way to stop the gamma radiation that does not proceed along a well-defined range of paths with respect to the detection plane of the gamma-camera, depending on the geometry of the collimator itself. The collimator can be described as a solid plate presenting one or more holes and such a geometry works as a mechanical filter: only the gamma-photons that pass through the holes can reach the detector. The collimation of the gamma-rays heavily reduces the sensitivity of the detection system and set up a limit to the spatial resolution,

## Chapter 2. INSERT project

but it is necessary to provide spatial coherence in the reconstructed image. Different geometries of collimators are available, with distinct consequent outcome in terms of spatial resolution and sensitivity.

**Parallel-Hole Collimator** - It can be visualized as a pack of parallel lead straws (Figure 2.8). Only the radiation with a direction transverse with respect to the collimator plane can pass through. Parallel hole collimators produce no image distortion and provide a constant field of view.



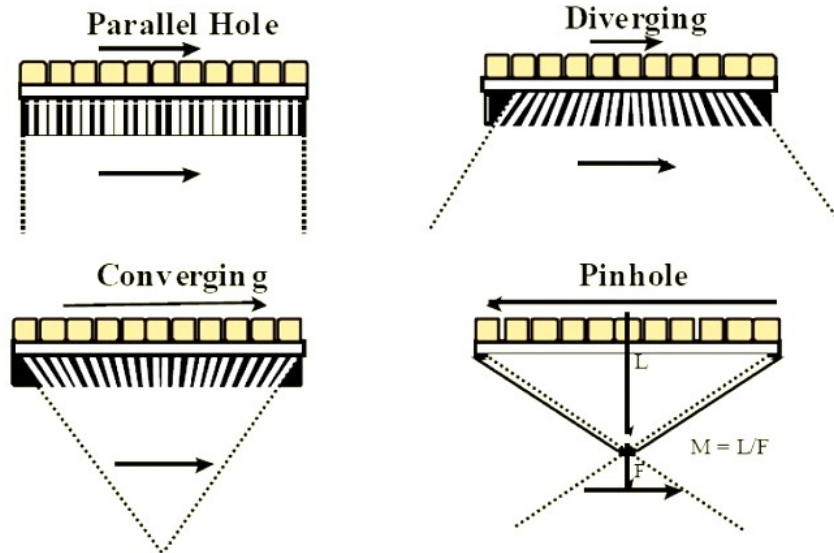
**Figure 2.8:** Parallel straws composing a collimator.  $L$  = hole length,  $W$  = hole diameter,  $S$  = septa thickness. Courtesy of Nuclear Fields, The Netherlands.

The best spatial resolution is obtained when the object is placed against the collimator, then decreases with distance from the camera surface. The magnitude of the loss of resolution is directly proportional to the width of the collimator hole and inversely proportional to the hole length. Septa penetration by photons is another cause of decreased resolution for a parallel hole collimator and is related to the thickness of the septa. The sensitivity of a parallel hole collimator is independent of distance from the collimator [60].

Before introducing other collimation architectures, we introduce here the concept of converging and diverging collimation, that refers to the direction of the holes. Precisely, converging and diverging collimators are named by observing the holes from the scintillator perspective. Converging collimators project an object onto a larger portion of the crystal and thus magnify the image (Figure 2.9).

A *converging collimator* may actually allow detection of structures smaller than the cameras intrinsic resolution (increase system resolution). Unfortunately converging collimators introduce image distortion as magnification varies based upon the depth of the object. The collimators sensitivity increases with distance from the collimator, but this will decrease resolution. A *diverging collimator* minifies the image and degrades both sensitivity and resolution, which will worsen with increasing distance from the collimator. It is useful only when it is necessary to image a structure larger than the

## 2.2. Technological and technical principles on SPECT systems



**Figure 2.9:** Architecture typologies for the collimator: (top-left) Parallel holes, which maintains the dimensions of the object to image; (top-right) Diverging holes, produce minification; (bottom-left) Converging holes, which magnifies the viewed object; (bottom-right) Pinhole collimator, which inverts and usually magnifies the object. [61]

size of the detector.

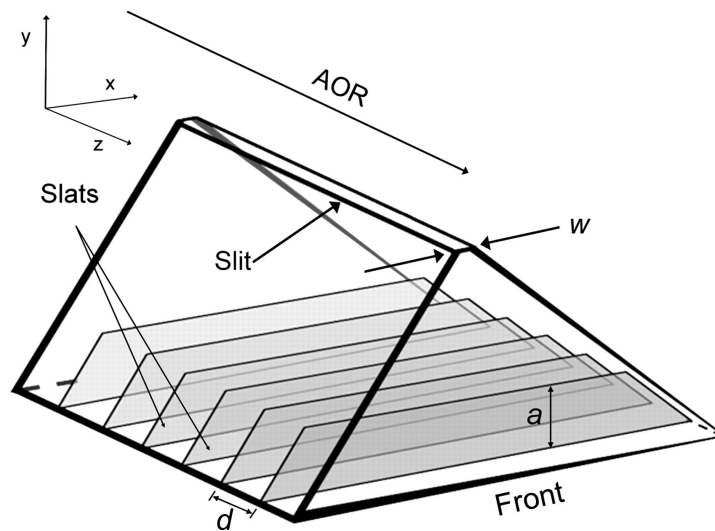
**Pinhole Collimator** - It is a cone-shaped collimator with a single hole. A pinhole generates magnified images of a small organ with high spatial resolution. Maximal magnification is reached when the collimator is closest to the object and decreases as the pinhole is moved further away. Since magnification is determined by distance from the aperture, a bulky object contains layers that will be imaged at different magnifications, with a consequent image distortion (greatest at high magnification). Pinhole images also increase the spatial resolution of the camera system. Resolution is related to the size of the aperture, however, small apertures which produce the best resolution limit the number of accepted counts (sensitivity). It is one of the collimation mostly diffused in preclinical SPECT imaging.

**Multi-Pinhole Collimator** - Intuitively, it is a collimator designed with multiple pinholes that can be parallel, converging or diverging depending on the function they have to fulfill. Multi-pinhole collimators, with respect to single pinhole ones, do increase the sensitivity and FOV with a preserved spatial resolution [62]. Multiple projections through different pinholes pro-

## Chapter 2. INSERT project

vide relatively efficient coverage of the detector area while multiplexing effect can make a problem for image reconstruction. If the projections from different apertures overlap, then the multiplexing artifacts occur.

**Slit-Slat Collimator** - Slit-slat collimation may be well described as a hybrid of pinhole and parallel/fan-beam collimation (Figure 2.10). The fan-beam collimator is practically like a parallel hole ones, but with converging septa. Also the performance of this kind of collimator are a combination of that of the pinhole and parallel/fan-beam. The of the slit-slat resolution is described well by the pinhole resolution in the transaxial direction, while axial resolution is consistent with the parallel-beam formula. The sensitivity falls between pinhole and parallel/fan-beam [63].



**Figure 2.10:** *Slit-slat collimator with reference coordinates and axis of rotation (AOR). The slit is parallel to the AOR and works similarly to pinhole, but limited to the transaxial view of the object. Slats are transverse to the AOR and works similarly to parallel holes collimators in the sagittal dimension. [64]*

### 2.2.3 Tomographic image reconstruction

The aim of reconstruction algorithms is to retrieve through calculations a virtual 3D distribution of the radioactivity from the recorded projections. The overall quality of the SPECT image is then dependent on the nature of the planar projections, thus on total counts, on the system configuration (collimator geometry, detector parameters, geometry of the SPECT ring,

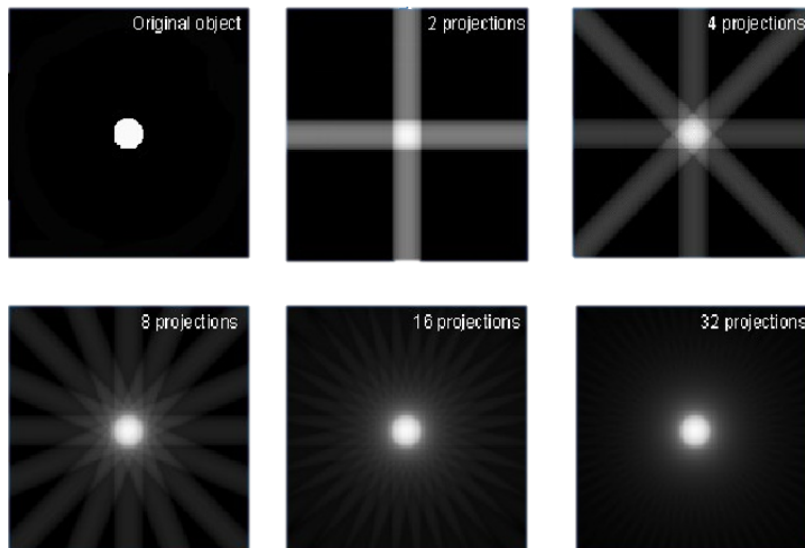
## 2.2. Technological and technical principles on SPECT systems

etc.) but is also related to tomographic reconstruction method [65].

There are two main families of methods to reconstruct SPECT images, either through Filtered Backprojected technique (FBP) or iterative methods.

**Filtered Backprojection** - FBP is an analytical method and represent the reconstruction algorithm most widely used in clinical SPECT because of its simplicity, speed, and computational efficiency. The method implements two steps: filtering of the planar image followed by a back projection of the filtered data.

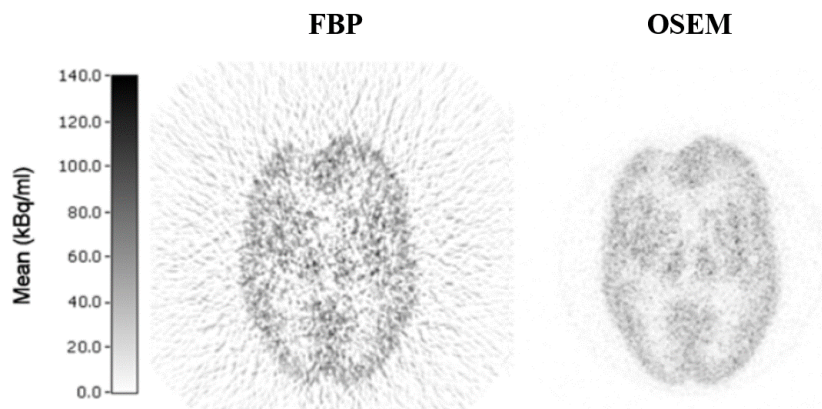
In the planar image acquired by the gamma-camera, each pixel of the reconstructed image represents the sum of all counts along a perpendicular projection line that moves through the depth of the object being imaged. Back projection technique virtually redistributes the number of counts at each particular position back along a line from which they were originally detected. The method is repeated for all pixels and all projection angles. Since the number of projection sets is limited by the geometry of the SPECT and by each single gamma-camera, the resulting image is affected by star artifact and the blurring. This issue can be mitigated by filtering the projections before back-project them onto the image matrix (Figure 2.11).



**Figure 2.11:** Reconstruction of a simple image through Filtered BackProjection (FBP) algorithm. The image definition is proportional to the number of iterations (number of projections) implemented.

## Chapter 2. INSERT project

**Iterative Reconstruction** - Iterative reconstruction is performed by obtaining a first, approximated, estimate of the image. Usually, the initial estimate is very simple, for example a uniform activity distribution. Then a set of virtual projection data is estimated from the initial tomographic estimate using a mathematical process called forward projection. The virtual projections are compared with the recorded projections and the differences between the two are used to update the estimated image. The process is repeated iteratively until a stop condition in the algorithm is reached, for example the differences between the calculated and measured data are smaller than a specified preselected value. The iterative reconstruction methods include algebraic methods like the algebraic reconstruction technique (ART) and statistical algorithms like maximum likelihood expectation maximization (MLEM) or ordered-subsets expectation maximization (OSEM). Figure 2.12 compares the same object reconstruction (Hoffman phantom) with FPB method and OSEM algorithm [66].



**Figure 2.12:** Reconstruction of a Hoffman phantom with Filtered BackProjection method (left) and with Ordered Subset Expectation Maximization algorithm (left).

Both the methods need to consider not only the dimensions of the projection plane, but most of all the geometry of the collimator, since the projection line are directly affected by the type of collimation implemented. On this purpose, it is worthy to stress the importance of precise reconstruction of the gamma-ray absorption site in the crystal: this allow to better distinguish the projection line from which the gamma-ray originated. For this reason, even if the projected images are planar, then defined in a X-Y plane, interest has been raised towards methods that can retrieve also the Z coordinate of interaction of the gamma radiation in the crystal. This kind



## 2.3. Magnetic Resonance Imaging basics

of analysis is better known as *Depth of Interaction (DOI) discrimination*.

### 2.3 Magnetic Resonance Imaging basics

This section is meant to procure only the most essential elements regarding the Magnetic Resonance Imaging (MRI) which will support the discussion in the following sections and chapters of the present work.

MRI is a tomographic imaging technique that produces 3D images of internal physical and chemical characteristics of a body or an object from external Nuclear Magnetic Resonance (NMR) signal measurement. NMR is a physical phenomenon in which nuclei of isotopes, that possess an intrinsic magnetic moment, can absorb and re-emit electromagnetic radiation (in the radiofrequency range, between 60-1000 MHz) on the assumption that they are placed inside a magnetic field. The emitted radiation has a specific resonance frequency which depends on the strength of the magnetic field and the magnetic properties of the isotope of the atoms. Only the isotopes that contain an odd number of protons and/or of neutrons have an intrinsic magnetic momentum (non-zero spin) and can therefore be imaged by NMR based techniques. Among all the nuclei studied,  $^1\text{H}$  and  $^{13}\text{C}$  are the most common, especially in medical applications, since they represent an abundant part of the atoms constituting the living being.

Imaging techniques with NMR exploit the feature that the resonance frequency of a particular substance is directly proportional to the strength of the applied magnetic field. By modulating the magnetic field in the space, it is than possible to make the isotope nuclei resonate at different frequencies, depending on where they are located. The principle of imaging formation with NMR involves the following sequential steps:

- The alignment (polarization) of the magnetic nuclear spins of the nuclei in an applied, constant magnetic field  $B_0$ .
- The perturbation of this alignment of the nuclear spins by employing an electro-magnetic, usually radio frequency (RF) pulse. The required perturbing frequency is dependent upon the static magnetic field ( $H_0$ ) and the nuclei of observation.
- The re-emitted signal from all the nuclei in the interested space or volume, is collected under the form of a frequency spectrum and can be elaborated in order to obtain bidimensional information.

Since the resolution of the imaging technique depends on the magnitude of magnetic field gradient, many efforts are made to develop increased field

## Chapter 2. INSERT project

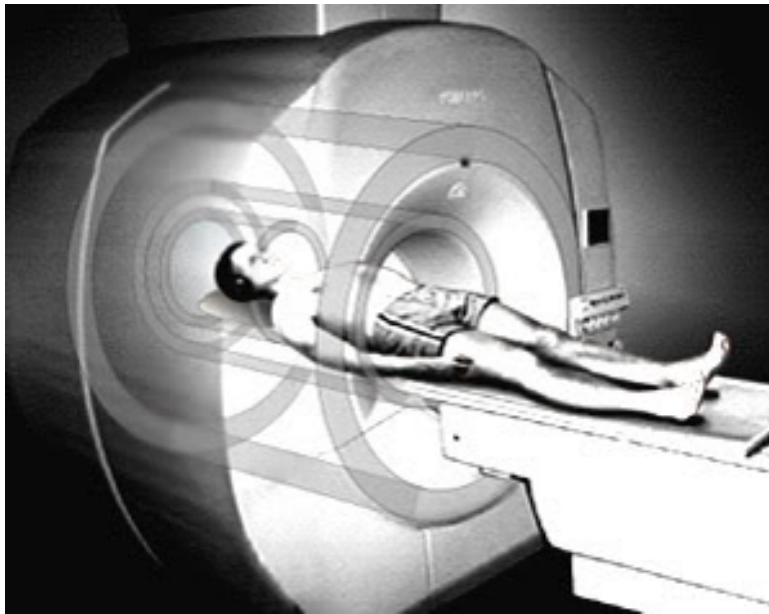
---

strength, often using superconductors.

As already mentioned in the previous chapter, MR images are extremely rich in information content. The procedures that can be applied to stimulated NMR signal are numerous and every one of them can retrieve data regarding different intrinsic parameters of the object under analysis. Above all, the most important ones are nuclear spin density  $\rho$ , the spin-lattice relaxation time  $T_1$ , the spin-spin relaxation time  $T_2$ , molecular motions (such as diffusion and perfusion), susceptibility effects and chemical shift differences [67]. A more detailed delineation of these parameters is out of the purposes of the present work.

### 2.3.1 MR hardware

An MR scanner (Figure 2.13) consists of three main components: a main magnet, a magnetic field gradient system, and an RF system. This section briefly describes their functional characteristics.



**Figure 2.13:** *Illustration of a scanner for Magnetic Resonance Imaging (MRI). [68]*

**Main Magnet** - The chief function of the main magnet is to generate a strong uniform static field, referred to as the  $B_0$  field, for polarization of nuclear spins in the analyzed volume. It can be either a resistive, a permanent, or a superconducting magnet. Resistive magnets are generally used at

### 2.3. Magnetic Resonance Imaging basics

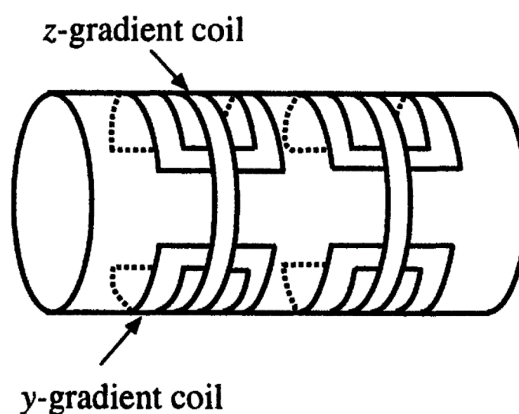
low field ( $< 0.15$  T); permanent magnets can operate at field strengths up to 0.3 T; superconducting magnets are normally used for generating higher field strengths and are the most diffused in preclinical and clinical practice. Advantages of high fields are better signal-to-noise ratio and spectral resolution. Disadvantages include RF penetration problems and higher costs. An approximately 3 T field strength is commonly employed in clinical whole-body systems.

The primary parameter for the static field is its spatial homogeneity, defined as the maximum relative excursion of the field over a given volume, inside the interest region:

$$Homogeneity = \frac{(B_{0,max}) - (B_{0,min})}{(B_{0,mean})} \quad (2.3)$$

Good image quality can be achieved only if moderate homogeneity over a large volume is provided (typically 10 to 50 parts per million (ppm) over a 30 to 50 cm diameter spherical volume, for human scanning). In practice, the main magnet alone is not capable of generating such a highly homogeneous field. This issue is commonly overcome by the employment of a secondary compensating magnetic field generated by a set of *shim coils* to correct the field inhomogeneities.

**Magnetic Gradient System** - The magnetic field gradient system consists of three orthogonal gradient coils, an example of which is shown in Figure 2.14.



**Figure 2.14:** Schematic representation of the Maxwell coil pair and the y-saddle coil set used to establish the z- and y-gradient, respectively.

## Chapter 2. INSERT project

---

Gradient coils are designed to generate time-varying magnetic fields with also a controlled spatial non-uniformity of the magnetic polarization within the interest region. The gradient system is a crucial component of an MRI scanner because it provides the spatial information encode through the modulation of the transient response of a spin system relaxation upon RF excitation. Important specifications for a gradient system include maximum gradient strength and the rate at which this maximum gradient strength can be obtained. Gradient strength is normally measured in units of millitesla per meter (mT/m). Most clinical imaging systems can provide a maximum gradient strength of approximately 30-45 mT/m. The lower limit of the gradient strength required is determined by the criterion that the gradient field must be stronger than the main field inhomogeneity.

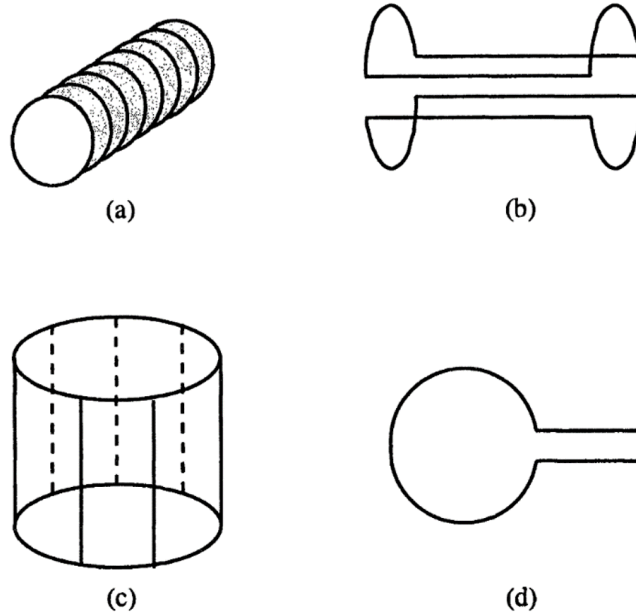
The time interval for a gradient to ramp up to its full strength is called the rise time. It is measured in milliseconds, and is typically in the range of 0.1-0.3 msec for most scanners. For some fast imaging methods a shorter rise time is needed.

The most significant parameter for a gradient system is the slew rate, defined as maximum gradient strength over rise time and measured in tesla per meter, per second [T/(m·s)]. Generally, the higher the slew rate, the shorter is the overall scanning session.

**Radio-frequency System** - The RF system consists of a transmitter coil that is capable of generating a rotating magnetic field, often referred to as the  $B_1$  field, for excitation of a spin system, and a receiver coil that converts a precessing magnetization into an electrical signal. Sometimes, a single coil can be used as both a transmitter and receiver coil, thus the name transceiver coil. Both the transmitter and receiver coils are usually called RF coils because they resonate at a radio frequency, as required by spin excitation and signal detection.

A desirable characteristic of the RF coils is to provide a uniform  $B_1$  field and high detection sensitivity. In order to accomplish this function, an MR system is often equipped with RF coils of different shapes and sizes for different applications. Some common examples are solenoidal coils, saddle coils, birdcage coils, and surface coils, as shown in Figure 2.15. A long solenoidal coil consists of many closely spaced turns on a cylindrical form with a diameter much less than its length. It can produce a uniform  $B_1$  field in its interior. A saddle coil has a pair of coils wound on a cylindrical surface and is able to generate a relatively homogeneous field near its center. A birdcage coil consists of a series of identical loops connected together and located on the surface of a cylinder giving the appearance of a birdcage. It

## 2.4. Project requirements



**Figure 2.15:** Some examples of RF coils: (a) solenoidal coil; (b) saddle coil; (c) birdcage coil; (d) surface coil.

provides the best RF field homogeneity of all the RF coils currently in use.

## 2.4 Project requirements

The INSERT project, presented in section 2.1, is constituted by a consortium of research groups and industrial entities and has been conceived to cover the necessary skills and expertise for instrument development, pre-clinical and clinical experimentation, and for the project support activities such as dissemination and management.

In the project framework, Politecnico di Milano group is responsible for the development of the gamma-ray detection modules, equipped with scintillator crystal, SiPM photo-detectors, electronics, cooling and other ancillary systems where needed. The detection modules should then populate two SPECT rings: a preclinical one for small animals imaging and a clinical one for human head/neck imaging. The design of the detection system has been addressed towards constrained requirements that are defined by the final performance expected from the two systems (preclinical and clinical). The collaboration of a biological and medical group with the partner responsible for the design of the SPECT ring and the collimator has

## Chapter 2. INSERT project

---

produced a document that summarizes the technological outcomes required from the SPECT system in order to obtain proper images for the preclinical and clinical applications mentioned in previous sections.

The requirements on the detection module have been inferred by SPECT system simulations. Once the tomographic imaging performance have been defined, the output parameters from the planar projected images needed to achieve those performance have been deduced by taking into account the reconstruction algorithm for the SPECT image.

In the following sections the requirements for the preclinical and clinical SPECT systems are listed.

### 2.4.1 Preclinical requirements

A representative model for the glioma behavior can be obtained by the analysis of the evolution of human derived cell lines that grow in immune-compromised rodent hosts. For this purpose, mice and rats have been chosen as small animal target for preclinical studies with INSERT. Their anatomical dimensions have provided a reference for the definition of the bore size and of the field of view to be visualized consider. The animal would need to be positioned on a heated pad or other system to maintain body temperature. An estimated bore diameter of 4 cm is required to allow positioning of the animal with anesthetic nose cone and tubing. The necessary field of view would be 16 mm transaxially  $\times$  11 mm axially for the mouse brain or 20 mm  $\times$  20 mm for rat brain. The restricted space available in the MRI bore make the system unsuitable for imaging the whole animal body. Additional space is required to accommodate MRI coils which surround the host.

For the collimator, a pinhole geometry have been elected. This is a standard in small animal imaging and would allow high spatial resolution and magnification. For mouse brain imaging using  $^{99m}\text{Tc}$  an expected spatial resolution of 0.8-1.0 mm<sup>3</sup> should be achieved with the highest possible sensitivity. This suggests that resolution of 1.0 mm (based on visible separation of hot rods should be reached for mouse brain at a sensitivity greater than 2000 cps/MBq (with  $^{99m}\text{Tc}$  source).

The maximal injected activity is likely to be in the region of 300 MBq and maximum activity in the brain have been estimated around 60 MBq; the overall count rate capability required will depend on the system sensitivity but a conservative estimate suggested an gamma-detection module count rate capability of less than 15000 cps. An ideal minimum acquisi-

## 2.4. Project requirements

tion time during dynamic acquisition would be 10 seconds per time frame; acquisition time of 30 seconds is probably more realistic given the likely sensitivity.

No rotation of the preclinical system appeared necessary for carrying out mouse and rat brain imaging.

A list of tracers have been selected in order to give relevant biological information (also of interest for clinical use) and to fulfill the aim of contributing to multi-parametric data. The preclinical system is likely to use the radionuclides defined in table 2.1

**Table 2.1:** *Preclinical radionuclides*

Radionuclide	<sup>99m</sup> Tc	<sup>123</sup> I	<sup>111</sup> In	<sup>177</sup> Lu	<sup>131</sup> I
Peaks energy [keV]	140	159	171/245	113/208	365

Proceeding from this list, very important informations can be inferred. First, crystal thickness will need to ensure reasonable efficiency for photons up to 365 keV in energy. Second, that simultaneous imaging of <sup>99m</sup>Tc and <sup>123</sup>I is the most challenging due to the proximity of their photo-peak energies. As consequence, requirement to image multiple radionuclides places priority in achieving the best possible energy resolution. In order to distinguish the sources with lower energy (<sup>99m</sup>Tc and <sup>123</sup>I) at least 159 keV - 140 keV = 19 keV of FWHM are required to both the peak energy distributions. Considering <sup>99m</sup>Tc, this brings to a required energy resolution of at least  $R_{en} = 19 \text{ keV} / 140 \text{ keV} = 13.75 \%$  (from equation 2.2) and preferably close to 10 % as conservative strategy.

### 2.4.2 Clinical requirements

The aim of the clinical INSERT is to image distribution of radioactive probes in whole human brain, with the intention to eliminate need for prior knowledge of tumor location from other modalities.

The SPECT system is to be inserted in a 59 cm aperture 3T PET/MRI system (Siemens), which is also a standard dimension for commercial available MR scanner. The required patient aperture has been estimated as 35 cm diameter to accommodate head support and a volume head RF coil placed close to the head.

The necessary field of view (FOV), to image the whole brain, would be 200 mm transaxially × 150 mm axially.

For the collimator geometry chosen, the reader can refer to the state of the art report for the clinical system in section 2.5.3.

## Chapter 2. INSERT project

---

The clinical preference for the intended application is to maximize sensitivity with a spatial resolution similar to the one achieved with conventional gamma camera based SPECT (8-10 mm). Preliminary simulations have been performed for a slit-slat collimator system and, with this configuration, spatial resolution of 10 mm is achievable with a system geometric-efficiency of around 380 cps/MBq. Maximum count rate for the clinical is estimated to be around 5000 cps (considering a detection area of  $5 \times 5 \text{ mm}^2$ ).

No rotation of the clinical system appears necessary for the geometry tested and considering the implementation of an iterative reconstruction algorithm.

In the clinical system the choice of radionuclide is restricted to  $^{99m}\text{Tc}$ ,  $^{123}\text{I}$  and  $^{177}\text{Lu}$ . In the interest of limiting weight, shielding will be designed for a maximum emission energy of 210 keV which may permit imaging of  $^{177}\text{Lu}$ . Crystal thickness should be chosen so as to optimize the tradeoff between detection efficiency at 140 keV and spatial intrinsic resolution. The former takes advantage from thicker crystals, while the latter from thinner.

The requirement for best possible energy resolution is equally relevant to the clinical system in order to facilitate multiple radionuclide acquisition (in particular  $^{99m}\text{Tc}$  and  $^{123}\text{I}$ ).

### 2.4.3 Gamma-detection module requirements

The requirements for the single gamma-detection module, that is going to populate the SPECT rings, have been inferred from the evaluation on the preclinical and clinical requirements.

***Spatial resolution*** - Intrinsic spatial resolution of the detection system, not considering the contribution of the collimator, is required to be better than 1 mm FWHM.

***Field of view*** - The UFOV for the gamma-detection module is expected to be  $50 \text{ mm} \times 50 \text{ mm}$  for the preclinical and  $100 \text{ mm (transaxial)} \times 50 \text{ mm}$  for the clinical system. The CFOV should be wider than or equal to  $40 \text{ mm} \times 40 \text{ mm}$  (preclinical) and  $90 \text{ mm} \times 40 \text{ mm}$  (clinical), considering a limit spatial resolution of 1 mm FWHM.

***Count rate*** - The requirements of the previous two sections underlined that a count rate of at least 15000 cps should be achieved for the preclinical, while 10000 cps is required for the clinical.



## 2.5. Architectures of the SPECT insert

---

**Energy resolution** - Dual-tracer discrimination of  $^{99m}\text{Tc}$  and  $^{123}\text{I}$  requires an energy resolution of at most 10-12 %.

**Mechanical and technical requirements** - The gamma-detection module and all its parts should be chosen and designed in order to follow electromagnetic compatibility with MR. For example, no ferromagnetic material should be chosen; MR magnets can induce eddy currents in close conductive loops; electronic devices from the detector and RF signal from the MR coils can mutually interfere.

The whole SPECT insert should fit constrained MR bore and leave space for the collimator, the RF coils and the object to be imaged, either the small animal from the preclinical or the patient head in the clinical. The requirement for compactness of the system is then mandatory to achieve integration of the systems.

As described in chapter 3, the most suited alternatives to (MR not-compatible) photo-multiplier tubes are solid state photo-detectors that provide quite good detection performance, but also exhibit high level of intrinsic thermal noise at room temperature. Cooling up to moderate temperatures (in a range between  $-20\text{ }^{\circ}\text{C}$  to  $0\text{ }^{\circ}\text{C}$ ) it is mandatory to have a favorable signal on noise ratio on each photo-detection channel. Thus, a system for temperature cooling and stabilization has to be provided.

The last point is more a remark rather than a requirement: since two systems (preclinical and clinical) have to be populated with the same type of gamma imaging detector, a criteria of efficiency should be considered in the design of the gamma camera either of the preclinical and clinical. Practically speaking, the plan for the two detector should start from a common design and only minor changes to the structure and to the electronic should be needed to pass from one configuration to the other. These approach has been followed in the developing of the instrument and has given a benefit to the project work flow.

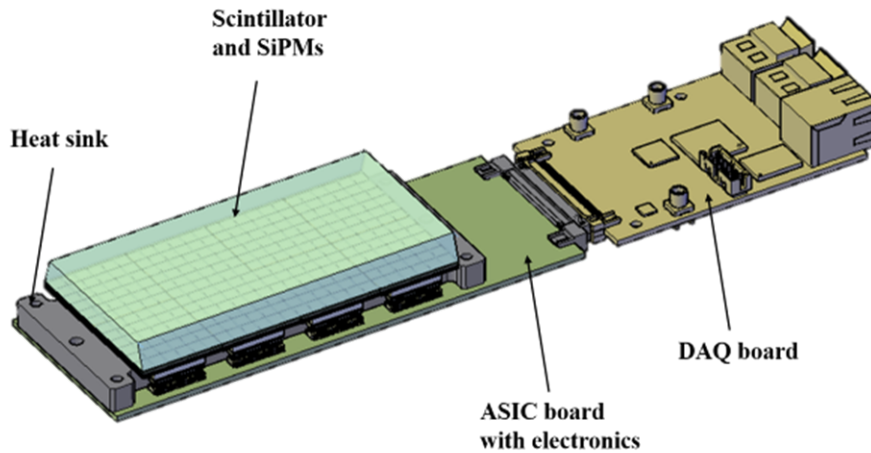
## 2.5 Architectures of the SPECT insert

---

A state of the art of the architecture of the SPECT insert for both preclinical and clinical configurations is here reported. The discussion starts from the description of the fundamental element, the gamma-detection module, and than rapidly evolves into the synthetic geometrical description of the SPECT rings with their collimators.

## Chapter 2. INSERT project

### 2.5.1 State of the art of the gamma-detection module



**Figure 2.16:** Drawing of the clinical gamma-detection module for the INSERT project. For the preclinical system, the axial length of the sensor area (scintillator and SiPMs) is halved.

The gamma-camera for the INSERT project (a design draw is depicted in Figure 2.16) is a compact, indirect gamma-rays detector based on the well-established Anger architecture: the conversion from high energy photons into carriers is provided by optical coupling of a monolithic, inorganic scintillator with an array of solid-state photodetectors. The architecture of the module in the preclinical and clinical configuration differ only in the dimension of the scintillator and, consequently, in the surface of the photo-detection matrix. A CsI(Tl) (Tallium doped Cesium Iodide) scintillation crystal has been elected with base dimensions  $50\text{ mm} \times 50\text{ mm}$  (preclinical) and  $100\text{ mm} \times 50\text{ mm}$  (clinical). Crystal thickness is set to 8 mm. Two edges of the scintillator are slanted in order to fix the module in the final SPECT architecture in a ring shape.

The photodetector array is populated by silicon photomultipliers (SiPMs), each one with an active area of  $4\text{ mm} \times 4\text{ mm}$ , covering the entire lower surface of the crystal.

The signal from the SiPMs is read by an electronics readout board (ASIC board -  $150\text{ mm} \times 53\text{ mm}$ ) which implement an application specific integrated circuit (ASIC) for the filtering and shaping of each imaging channel. The signals are then carried to a second board (DAQ board -  $80\text{ mm} \times 55\text{ mm}$ ) to be digitized and transmitted to a calculator through optical fiber cables.

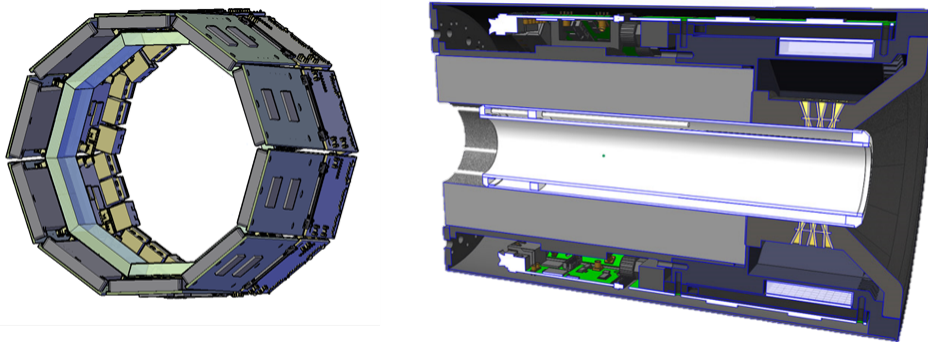
## 2.5. Architectures of the SPECT insert

A thermoplastic, MR compatible heat sink (8 mm thick) is placed in between the photodetection array and the ASIC board, composing a compact “sandwich” geometry. The purpose of the heat sink is to provide a stable and moderate cooling (0 - 10 °C) for the reduction of the thermal noise on the SiPMs.

The design and development of this module, and the protocol for signal filtering and elaboration, are the main core of the present thesis and will be better discussed in the next chapters.

### 2.5.2 Preclinical architecture

The geometry of the preclinical SPECT is a stationary, full ring composed by 10 gamma-cameras (Figure 2.17) supported by a plastic structure that provides mechanical stability and a close environment for the detector (Figure 2.18): moisture and temperature inside the structure can be kept under control and the mechanic also provides light shielding to avoid external photons to interfere with the photodetectors acquisition. Because of the MRI compatibility considerations the choice of the material for the 3D printed support structure has fallen on the Accura Bluestone material.

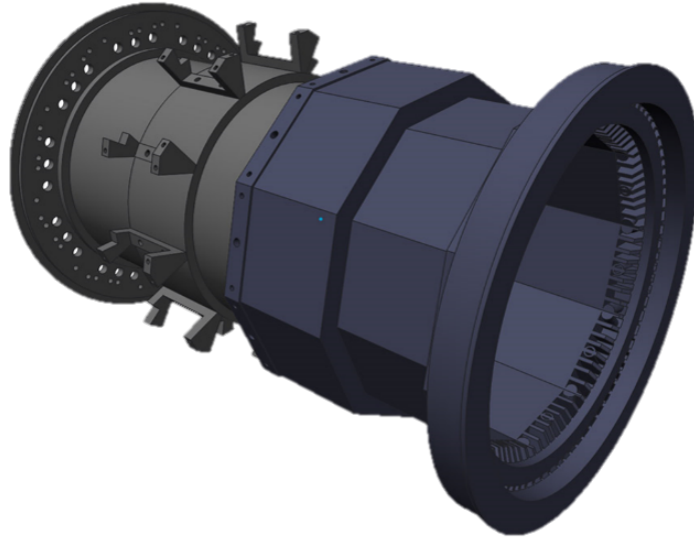


**Figure 2.17:** Preclinical SPECT ring. (left) Disposition of 10 gamma-detection modules composing a full ring geometry. (right) Cross-section of the SPECT with detail on the detection module, the multi-pinhole collimator and the RF coils. Courtesy of Mediso Kft., Hungary.

The external diameter of the ring is 198 mm. The inner volume is sufficiently large to host the collimator and the pad module for small animal support.

## Chapter 2. INSERT project

---



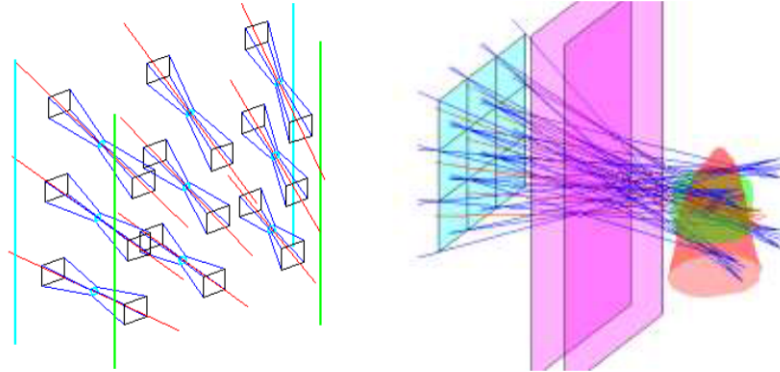
**Figure 2.18:** *Preclinical plastic (Accura Bluestone) support system. The mechanical structure humidity and light protection for the gamma-detection modules. Courtesy of Mediso Kft., Hungary.*

### Preclinical Collimator

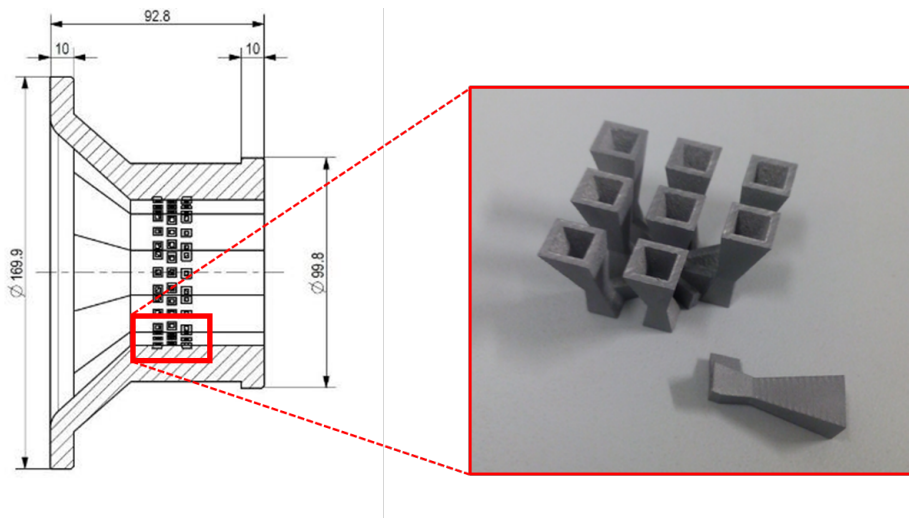
Preliminary studies on the collimator design have underlined that the UFOV of the gamma-detectors (conservative estimation:  $4\text{ cm} \times 4\text{ cm}$ ) is bigger in both transaxial and axial direction with respect to the size of the object to be imaged (see preclinical requirements in section 2.4.1). Thus, divergent projection seems the most suitable solution for preclinical imaging, therefore a multi-pinhole architecture for the collimator was chosen. TeraTomo<sup>TM</sup>-SPECT, a simulation and reconstruction software tool, has been employed to evaluate the likely performance of the SPECT system as function of the geometrical parameters of the multi-pinhole collimator. A simulation of the aperture model is depicted on Figure 2.19.

The design for the complete ring collimator and shielding structure is depicted in Figure 2.20. The multi-pinhole collimator is made in pure Tungsten, while the volume of the shielding structure is composed by a mixture of adhesive glues and Tungsten powder, in order to minimize eddy-currents proliferation.

## 2.5. Architectures of the SPECT insert



**Figure 2.19:** (left) Simulation study of a multi-pinhole construction for mouse brain imaging, with 9 holes per aperture. Green and cyan lines indicate the border of the aperture regarding the 10 headed preclinical gantry. (right) Projections of the holes: green cylinder is the imaging FOV, red shape represents the head of the mouse, purple planes are the gamma incoming and outgoing surfaces of the body of the aperture. Courtesy of University College London, UK.



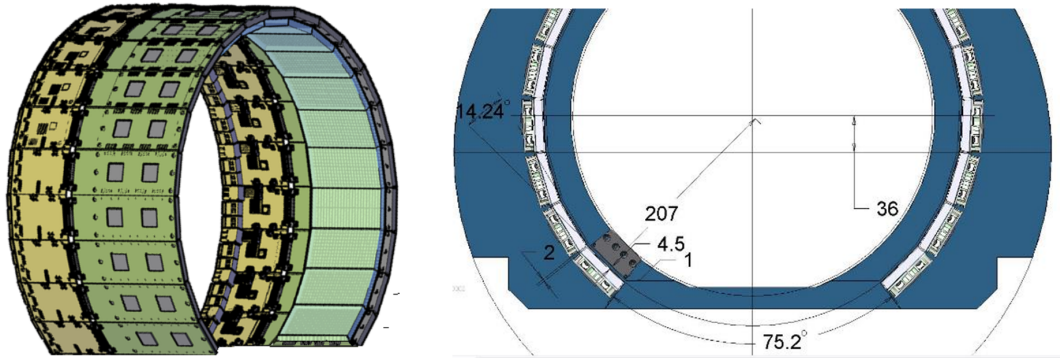
**Figure 2.20:** (left) Conceptual and mechanical draw of the preclinical collimator. The structure volume is mainly composed by Tungsten powder. (right) Pure Tungsten pinholes for the collimator prototype. Courtesy of Mediso Kft., Hungary.

### 2.5.3 Clinical architecture

The geometry of the clinical SPECT is a stationary, open ring composed by 20 gamma-cameras (Figure 2.21). The expected outer diameter of the

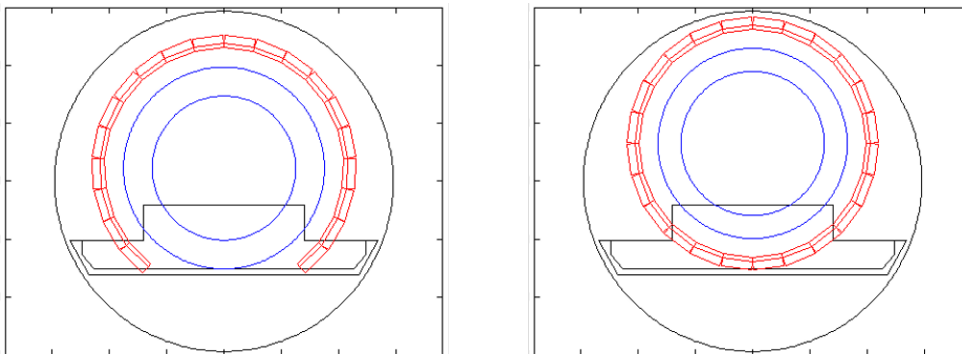
## Chapter 2. INSERT project

system is 414 mm.



**Figure 2.21:** Clinical SPECT ring. (left) Disposition of 20 gamma-detection modules composing an open ring geometry. (right) Technical draw of the SPECT with detail on geometry dimensions and constrains. The arrangement of one collimator module is depicted on bottom left. Courtesy of Mediso Kft., Hungary.

The detection modules are organized in a partial ring architecture because of spatial constrains inside the MR bore: an equivalent full ring SPECT (with the same number of detection elements) would raise the head of the patient significantly and it would also imply limitations to SPECT imaging due to the reduced diameter (Figure 2.22).



**Figure 2.22:** Different architectures for the clinical SPECT. (left) Open ring solution requires complex solutions for the mechanical stability, but provides a larger entrance for the patient head. (right) Closed ring configuration is more compact and reliable, but requires a net reduction of the internal volume for collimator, RF coil and patient head. Courtesy of University College London, UK.

## 2.5. Architectures of the SPECT insert

The open ring solution is required for practical reasons, but it has been estimated that the new configuration will have also an impact on the tomographic image quality. In fact, simulation studies have underlined that the imaging system should lose *penetration efficiency* in the backward part of the head, that is the region most proximal to the ring section not covered with gamma-detectors.

The design of the case structure have taken into consideration also a gamma-rays shielding for that radiation that originates from body districts (i.e feet, bladder, etc.) different from that interested in INSERT studies. Moreover, for practical reasons the first INSERT prototype for the clinical SPECT will be tested into a Siemens mMR Integrated Whole-Body PET/MR Scanner: the PET ring implements LSO scintillators have intrinsic activity due to  $^{176}\text{Lu}$  (peaks of emission at 88.4, 201.8 and 306.8 keV). A 2.5 mm thick shielding cover made of Tungsten powder is then required to minimize the interference of such extrinsic radiosources on the gamma-detectors.

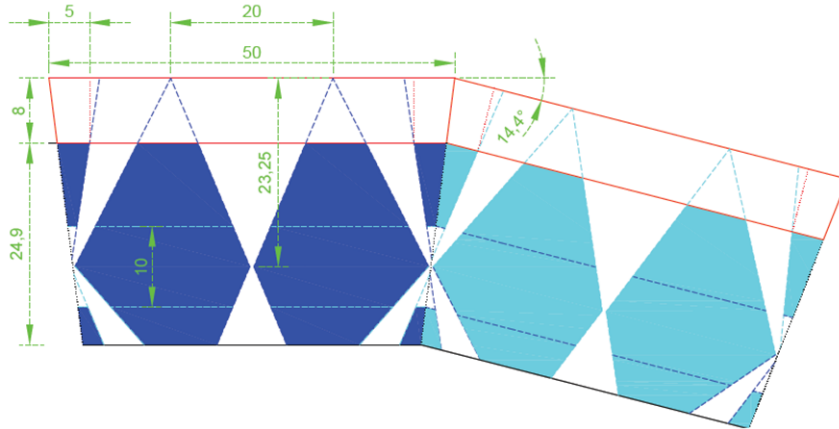
### Clinical Collimator

The optimization process for the collimator design focused on the trade-off between sensitivity, spatial resolution and the space constraints. As defined in section 2.4.2, effort should be made to improve sensitivity while maintaining a spatial resolution close to that of a standard clinical SPECT camera (approximately 10 mm in the center of the FOV). In a first approach, the slit-slat collimator was selected due to its suitability for brain imaging [69]. This collimator provides two different types of collimation in the transaxial and axial directions. For a conventional SPECT system, the transaxial direction (governed by the slit) produces a magnification, while, for the INSERT clinical case, the detector is small compared to the projected FOV and the available volume for the collimator is limited, resulting in a small focal length. Therefore minification will occur in the projections space; however the system can benefit from the detector’s high resolution to compensate for this effect.

In addition, multi-pinhole and multi-slit slit-slat configurations were also evaluated. These use new collimation concepts like half-slit (Figure 2.23) or half-pinhole, i.e. slits or pinholes that are shared between adjacent detectors in a detector ring, and interior slit in the slat component of a slit-slat collimator .



## Chapter 2. INSERT project



**Figure 2.23:** *Technical draw of a mini-slit slit-slat (MSS) collimator and scintillation crystal in a ring configuration. Two half slits are shared with neighbor collimators. Each slat is represented with filled in color and its internal slit highlighted by the dashed lines. Dimensions are given in mm. Courtesy of University College London, UK.*

Moreover a new collimation method was proposed, which uses mini-slit slit-slat arrays to obtain improved angular sampling of the object - the MSS collimator (Figure 2.24).

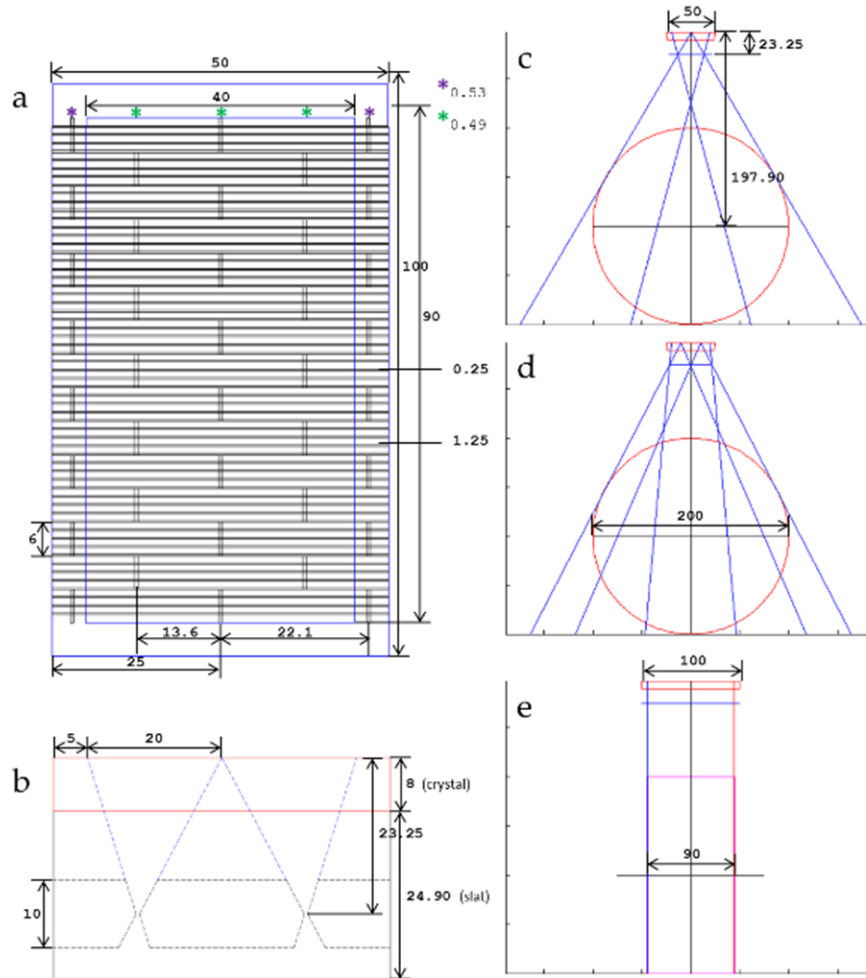
In all calculations, the pinhole/slit aperture is obtained for a fixed target resolution and the collimator material is assumed to be tungsten. The focal length of the collimator is calculated as the distance between the aperture and the face of the crystal coupled to the photodetectors in order to obtain the correct geometry of the collimator and minimize overlapping effects with adjacent apertures, and then is corrected with the DOI information for the sensitivity calculations. For DOI it is assumed that the crystal’s first and second half can be differentiated.

Simulated reconstructed data were used to further assess the different collimator designs: in the study, different geometric phantoms have been used, uniform, Derenzo and DeFrise, and the Zubal brain phantom (Figure 2.25). For the latter, simulations were performed only for two designs of choice.

The proposed MSS design demonstrates good performance characteristics when compared to other collimator configurations, and is therefore the design of choice for the SPECT/MRI insert. A similar design but with pinhole collimation would be a possible alternative. Prototypes of these collimators will be manufactured and further assessed to make a final decision for the SPECT insert [70].



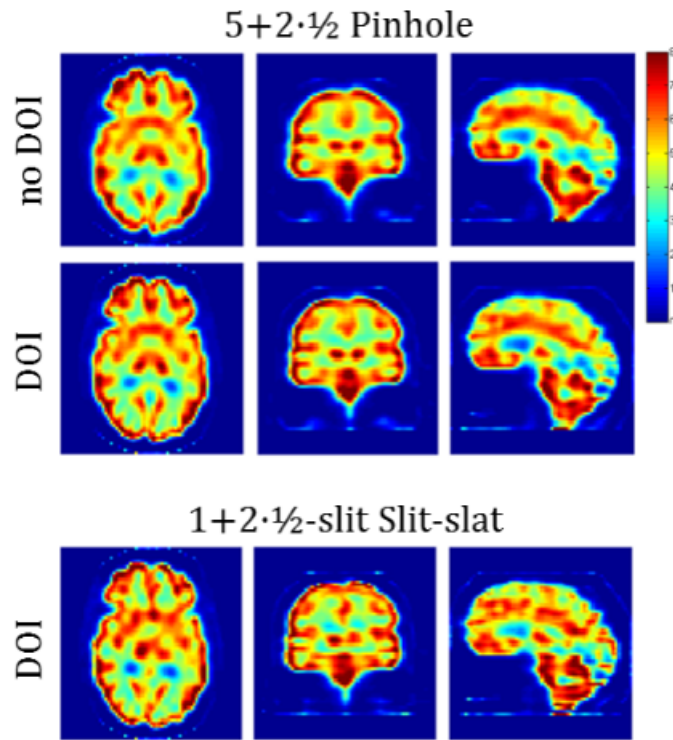
## 2.5. Architectures of the SPECT insert



**Figure 2.24:** Diagrams of the configuration of the MSS collimator and its coverage of the FOV: (a) top view; (b) side view (slat detail); (c) transaxial view through a 2-slit-array plane; (d) transaxial view through a 3-slit-array plane; (e) axial view. Dimensions are given in mm. Courtesy of University College London, UK.

The bulky volume of the Tungsten collimator could represent a major issue for MR compatibility, mainly because of the eddy currents generated in the metal loops. With regard to this limitation, three main strategies have been adopted: the first one, is more an inference to the practical decision to open the SPECT ring. In such a way also the collimator ring, following the detectors trajectory, is open and does not form big closed loop where

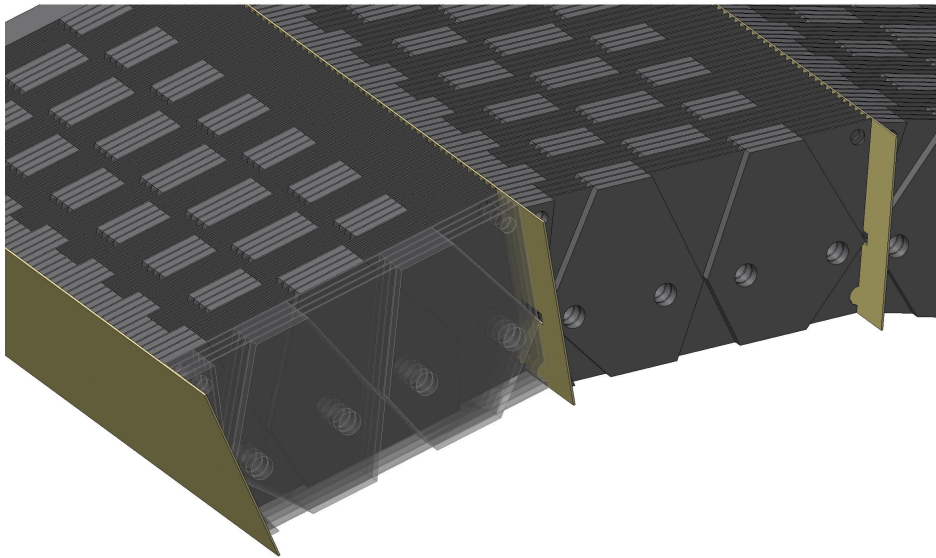
Chapter 2. INSERT project



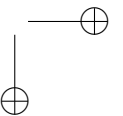
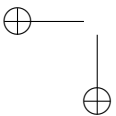
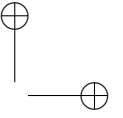
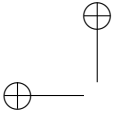
**Figure 2.25:** Reconstructed images for the Zubal brain phantom simulated with the  $5+2\cdot\frac{1}{2}$ -pinhole collimator, with (middle row) and without (top row) DOI information, and with the  $1+2\cdot\frac{1}{2}$ -slit slit-slat collimator with DOI information (bottom row): transaxial (1<sup>st</sup> column), coronal (2<sup>nd</sup> column) and sagittal (3<sup>rd</sup> column). [70]

magnetic field variations can produce induced currents. As second action, the material that compose the bulky part of the collimator is a mixture of Tungsten powder and glue, to reduce the metal continuity in the volume and limit the possible loop circuits for induced currents. Finally, adjacent collimators are separated by a thin layer of electric insulating foil (Figure 2.26).

## 2.5. Architectures of the SPECT insert



**Figure 2.26:** *Technical 3D draw of part of the ring collimator for the clinical INSERT. The overall collimator is composed by a fundamental unit which is the collimator for the single gamma-detectors. Thin layers of electrically insulating material are foreseen between adjacent elements with the objective to limit the possible conductive paths and loops, which could affect system compatibility with MR. Courtesy of Nuclear Fields, The Netherlands.*



---

## CHAPTER 3

---

### Gamma-detection module design

---

The aim of the present work is to describe the design and development process of the gamma-ray detection module for INSERT and report the resulting performance. The current chapter describes the gamma-camera components, gives a better understanding on the design procedure and discusses the investigations made to assess an optimal configuration for the overall detector. The development of the detector was always focused on the direction paved by the requirements listed in section 2.4.3.

In a first section, a brief discussion on the family of components (scintillator and photodetectors), with also readout electronics is reported. The main parameters of the elements that compose a gamma-camera are analyzed.

In a second section, we discuss the statistical methods employed for the detector design.

Finally, the resulting gamma-camera is presented in all its part and an estimation on its likely performance is calculated.

#### 3.1 Gamma-ray detection with scintillators

---

As already described in chapter 2, gamma-ray detection with inorganic scintillators is a indirect conversion modality that implies the optical cou-

## Chapter 3. Gamma-detection module design

pling of a scintillation crystal to one or more photodetectors. In the case of imaging systems, there are multiple photodetectors, typically organized in a rectangular array that covers one of the faces of the scintillator.

The coupling is optically and mechanically provided by some sort of transparent media: optical grease or glue (typically a resin) that has the function to facilitate the transmission of the scintillation photons from the crystal to the photodetectors.

### 3.1.1 Inorganic scintillators

The scintillator is the component designated to the absorption of the gamma-ray energy and convert it into a bundle of lower energy photons (typically in the UltraViolet (UV) or visible range). The inorganic scintillators are solid crystal composed of two or more atoms with high atomic number, thus providing very dense material, with an high absorption probability. Beer-Lambert law describes (indirectly) the probability for a certain material to absorb radiation at a fixed energy, with dependence to the depth of penetration:

$$I(x) = I_0 e^{-\mu x} \quad (3.1)$$

where  $x$  is the depth of penetration,  $I_0$  is the intensity of the radiation beam at depth of penetration zero, and  $\mu$  is the attenuation coefficient, expressed in  $[\text{m}^{-1}]$ . The attenuation is related to the material (e.g. the composition of the scintillator) and, in principle, is considered as a constant. In real condition, it is a linear combination of components that are  $x$ -dependent. For gamma radiation, we can write:

$$\mu = \mu(x) = \mu_{Photoelectric} + \mu_{Compton} + \mu_{Pairs} \quad (3.2)$$

which refers to the three most important processes that involve gamma-ray absorption in matter (Photoelectric effect, Compton scattering and pairs production). For ease of discussion, no extended description is given for these phenomena. Equation 3.1 tells (considering  $\mu$  as a constant) that the absorption of gamma radiation is more probable in the first millimeters of entrance into the crystal.

#### Physical principles of scintillation

Inorganic scintillation material exhibits the behavior of an insulator or semiconductor, with a large forbidden band between the valence and the conduc-

### 3.1. Gamma-ray detection with scintillators

tion ones. When a gamma-ray energy is absorbed by mean of photoelectric interaction, an inner shell electron gain enough energy to be extracted from the orbital and produces a cascade of events that, for the majority of te cases, conclude with the generation of a number of electron-hole pairs. In the pure crystal, the return of the electron to the valence band with the emission of a photon is an inefficient process. To enhance the probability of visible photons re-emission during the de-excitation process, inorganic scintillator are often doped with impurities, called emphactivators. The activated sites in the lattice interfere with the normal band structure and modify it in such away that intermediate states become available. Electron-hole pairs have higher probability to recombine in this region of the crystal and the de-excitation of one pair produces one visible photon. Other processes compete with the one just described, with the effect to delay the scintillation process or quench it.

One important consequence of luminescence through activator sites is the fact that the crystal can be transparent to the scintillation light. In pure crystals the emission and absorption spectra would almost overlap and there would be substantial self-absorption. The emission at an activator site, instead, occurs at an energy transition substantially lower than the one needed for the creation of the electron-hole pair. As a result, the emission spectrum is shifted to longer wavelengths with respect to the absorption one, resulting in no self-absorption of the scintillation light by the crystal [57].

#### Crystal physical and geometric parameters

The design of a gamma-detection system can not disregard the choice of a suitable scintillator. The main physical parameters for scintillation

- **Density ( $\delta$ )** - It is proportional to the atomic number of the species that compose the crystal and gives an indication of the gamma radiation absorption capability of the scintillator. The higher the density, the more probable is the interaction of high-energy photons with the lattice. Photoelectric absorption follows the ensuing proportion:

$$\tau_{ph} \propto \frac{Z^n}{E_\gamma^{3.5}} \quad (3.3)$$

where the exponential  $n$  varies between 4 and 5 over the gamma-ray energy region of interest.

- **Yield (Y)** - Parameters that defines the average number of photons

### Chapter 3. Gamma-detection module design

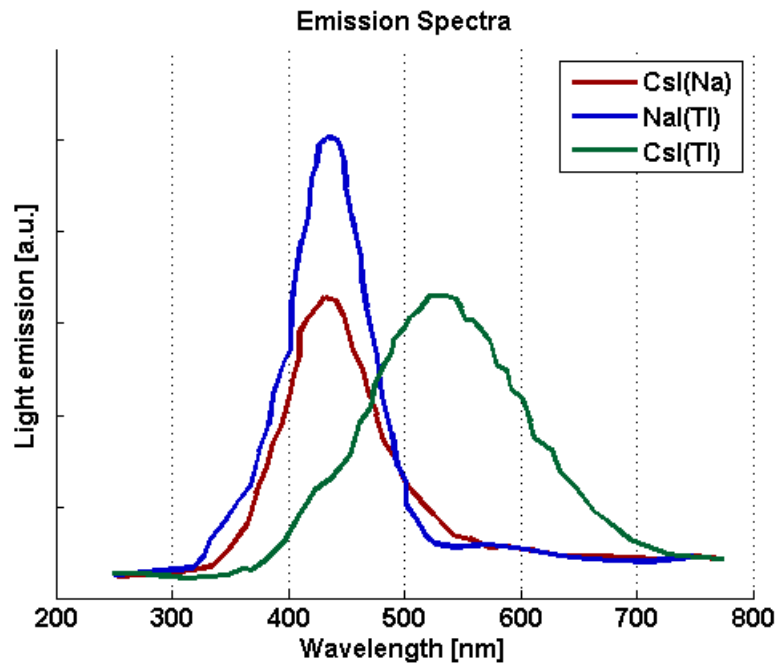
generated in a scintillation process as function of the gamma-ray energy: it is the conversion efficiency of the crystal. The unit of measure is number of photons over electronVolt [ph/MeV]. Scintillation light yield is temperature and energy dependent and non-linear behavior is observed in many scintillators [71, 72]

- **Refractive index ( $n$ )** - Optical characteristic of the medium. It is a dimensionless complex number that describes the way an electromagnetic wave propagates in a medium. The real component defines the speed of the EM radiation in the matter, while the imaginary part describes the attenuation to the electromagnetic flux provided by the material. Considering the interface of two objects with different refractive indexes, it is possible to calculate the reflection probability of an impinging photon, knowing its energy and its incidence angle with respect to the interface plane, by means of Fresnell’s equations (here not reported for ease of discussion). For what concern scintillators, ideally, one would like the refractive index to be as close as possible to the value of  $n$  of the material which are optically coupled with the scintillator itself (see next sections). In such a way that collection of light from the crystal to the photodetector array is not affected by reflection phenomena.
- **Scintillation decay time ( $\tau$ )** - Generation of photons in the activation sites exhibits a time distribution, which is related to the cascade of processes involved in scintillation. As seen, competitive phenomena can delay the de-excitation of electron-hole pairs, leading to longer emission time. The temporal distribution of generated photons follow an exponential decay, fully described by the *scintillation decay time* parameter.  $\tau$  is typically in the order of tens or hundreds of nanoseconds (ns), but some scintillators can be even slower( $\mu s$ ). In some cases the time distribution is better described by a combination of two or more exponential, with an equivalent number of time decay constants. Since the signal is later filtered and elaborated by an electronics that implements time constant in the order of  $\mu s$ , slow scintillation signals can incur into incomplete charge collection issues.
- **Maximum wavelength ( $\lambda$ )** - These parameter resumes a more complex characteristic of the scintillators that is the light emission spectrum. Visible photons generated in the scintillation process are not monoenergetic, since the activators introduce multiple state levels for the de-excitation. As consequence, the energy (or wavelength) of the



### 3.1. Gamma-ray detection with scintillators

photons generated is continuously distributed in the wavelength domain, around a value where the maximum probability of emission is set (Figure 3.1).



**Figure 3.1:** Scintillation emission spectra for three crystal materials (*CsI(Na)*, *CsI(Tl)* and *NaI(Tl)*).

This value is defined *maximum wavelength* or *peak wavelength*. When developing a gamma-camera, emission spectrum of the scintillator has to be matched with the absorption spectrum of the photodetectors employed to optimize the detection efficiency.

The ideal scintillator would have very high light yield (independent from energy and temperature) and very short scintillation decay time, in order to completely collect an high signal over noise. The denser material, the better to absorb the majority of the radiation in only few millimeters of crystal section. Moreover, the emission spectrum of the scintillation light should match as much as possible the absorption range of the photodetector. Table 3.1 reports a limited list of inorganic scintillation material and their main properties.

The quest for an ideal scintillator is nowadays far from its more ambitious

### Chapter 3. Gamma-detection module design

**Table 3.1:** *Inorganic scintillators*

	NaI(Tl)	CsI(Tl)	GaGG	LaBr <sub>3</sub> (Ce)	LSO
<b>Density [g/cm<sup>3</sup>]</b>	3.67	4.51	6.63	5.08	7.40
<b>Wavelength of Max. Emission [nm]</b>	415	540	520	380	420
<b>Refractive Index</b>	1.85	1.80	n.a.	1.9	1.82
<b>Decay Time [<math>\mu</math>s]</b>	0.20	0.68 (64 %) 3.34 (36 %)	0.088 (91 %) 0.258 (9 %)	0.016	0.047
<b>Abs. Light Yield [photons/keV]</b>	38	65	57	63	25
<b>Note</b>	Hygroscopic	Slightly Hygroscopic	-	Hygroscopic	Radioactive Background
<b>Reference</b>	[57]	[57]	[73]	[74]	[57]

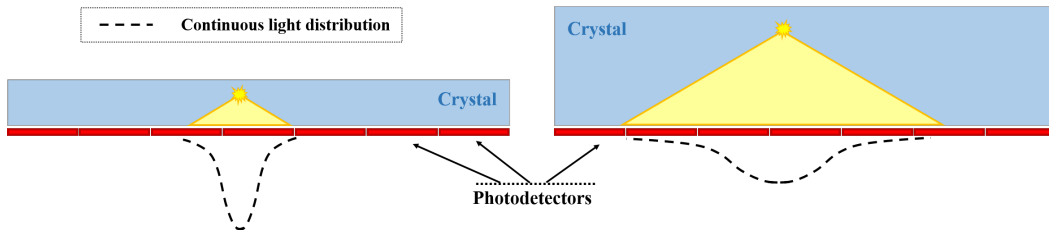
target: more realistically, the choice on the material requires a tradeoff between advantages and drawbacks that need to be balanced to reach the requirements. For example, CsI(Tl) crystals have very high conversion efficiency (yield), but the time distribution of the photons generated is described by a slow bi-exponential function.

Beyond physical considerations, there are also practical aspects to be considered: for example, the NaI(Tl) is a material that present very good parameters, but it requires to be sealed in a moisture-proof box, since it is hygroscopic and humidity compromises its performance.

For what concern the geometry of the crystal, most of them are bulky monolithic blocks realized in either cylindrical or parallelepiped shape. In Anger cameras, the width and length of the geometry define the FOV of the detection system, while the thickness, or height, its a parameter to be optimized: on one side a thick section is suitable to stop most of the incoming radiation. Thus, the higher the crystal, the better the absorption efficiency of the system. On the other side, imaging detectors do often implement thin scintillators (few millimeters in thickness) since they provide better spatial resolution. The reasons are related to the distribution of scintillation light on the photodetection plane. As described by Beer-Lambert equation (3.1), scintillation light is likely generated in the first millimeters of the material, then it is seen by the photodetector through a solid angle. The distribution of light on the detection plane its sharper when the crystal is thin, while

### 3.1. Gamma-ray detection with scintillators

thicker scintillators the distribution becomes spreader(Figure 3.2).



**Figure 3.2:** Light distribution for a generic gamma-event in a thin crystal (left) and in a thicker one (right).

The light distribution on the photodetector matrix has a direct impact on the point reconstruction error, consequently on spatial resolution. By the way, resolution is also dependent from the size of the detectors employed (see section 3.1.2).

As a general consideration, the choice of the geometry and material for the scintillator is a non-trivial task and can not be independent by the decision taken on the specific photodetector for the system.

#### Reflective coverings and coatings

The amount of scintillation light collected on photodetectors is a crucial parameter for both imaging and spectroscopic performance, since it represent the information carrier, the signal to be read. Light produced in a scintillation spreads in all directions inside the crystal from the gamma interaction site: the dispersion of this photons bundle is isotropic and only a percentage of them aims towards the photodetection array and it can be roughly be estimated through a solid angle calculation. The optimization of the gamma-detector requires to enhance the light collection also for those photons with an initial trajectory which is not directed to the photodetection plane. For this reason, reflective materials that are employed, with the objective to redirect photons towards the sensitive array.

The most important parameters for reflectors are:

- the **refractive index (n)** - As mentioned in previous section, it is a fundamental parameter to calculate the amount of reflected light at an interface between two media and as function of the incident angle.
- the **reflectivity (R)** - It is the average percentage of light reflected by a material, given a light bundle with uniform angular impact direction. Can be derived from the refractive index and depends on the optical

### Chapter 3. Gamma-detection module design

---

properties of the media at the interface. For light collection applications in scintillators, an high value of reflectivity is required from the covering materials.

Depending on the material optical properties and on its structure (on different scales), reflectors can exhibit different behavior in the way they bounce the electromagnetic waves. Pure reflectors, or specular reflectors, are mirror-like materials that throw back the radiation with a specular angle equal to the impinging one. Examples of this family of coatings are aluminum foils, enhanced specular reflectors (ESR) and so on.

Diffuse reflection, on the other hand, can be exhibited by materials (like white papers) that scatters back the incoming radiation in all directions, with no regards to the impinging angle. This behavior is related to the molecular structure and properties of diffusive materials: as shown in Figure 3.3, the light, transmitted in the first atomic/molecular layers of the material crystal or matrix, undergoes multiple optical interactions at different interfaces, following a complex trajectory and with an high probability to re-emerge from the material surface. Among the most used diffuser there is Teflon, Titanium oxide paint, Millipore, etc.

Realistic specular behavior from material is most of the time a combination of both mirror-like and diffuse reflection [76].

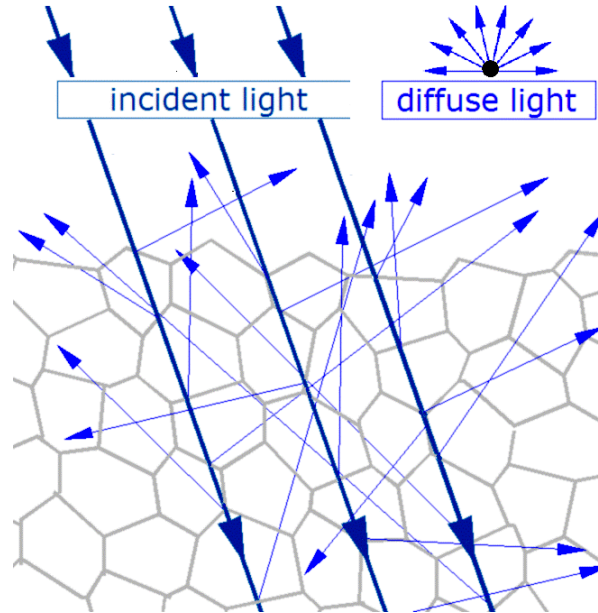
Specular reflectors cover scintillation crystal mostly implemented in imaging systems, since they provide high spatial coherence. Indeed, the light path from the scintillation site to the photodetectors is less subjected to random variations.

At the contrary, in spectrographic measurements (where the number of collected photons is the most crucial parameter) diffuse reflectors are preferred, because they typically exhibit the highest reflectivity values.

#### Optical media

Scintillator and photodetectors are typically coupled by mean of an optical material. Some systems present quartz windows (like the capsules for hygroscopic crystals). In most of the cases, optical coupling is performed by particular transparent greases or glues (resins). The parameter that characterizes these media is the refraction index and it has to be matched with those of the scintillation crystal and the photodetector entrance window in such a way to minimize the amount of light reflected from the detectors.

### 3.1. Gamma-ray detection with scintillators



**Figure 3.3:** Mechanisms of diffuse reflection include surface scattering from roughness and subsurface scattering from internal irregularities such as fiber boundaries in polymers or grains in crystalline solids. [75]

It can be proven that the optimization of the light transmission from a material **A** to a material **C** and passing through medium **B** is performed by choosing a refraction index for **B** equal to the geometric mean of the other two:

$$n_B = \sqrt{n_A n_C} \quad (3.4)$$

#### 3.1.2 Photodetectors

The photodetectors are devices that convert IR and visible photons into carriers to be read by the electronics exploiting a voltage difference between an anode and a cathode. All the detectors are characterized by a conversion efficiency, often referred to as quantum efficiency (QE), which is the percentage of photons that manage to convert into carriers. Quantum efficiency depends on the physical process laying for the specific photodetector and it is strongly dependent from the wavelength of the impinging photon. Temperature can affect it too.

### Chapter 3. Gamma-detection module design

Some photodetectors present internal processes capable to multiply the primary generated carrier into a cascade of secondaries. This property is commonly defined *multiplication* and the number of generated carriers follow a stochastic probability with related uncertainty.

Typical plain geometries for the photodetectors are square, circular or, sometimes, exagonal. The sensitive surface, also called *active area* and in antagonism with *dead area*, is a fundamental parameter: in the final gamma-camera, light collection from one of the crystal faces requires the latter to be completely populated by an array of photodetectors and the surface of each one of them needs to be optimized considering a tradeoff among different aspects. We would like the surface to be wide in order to reduce the number of detectors, then channels, needed to read all the light from the crystal. Moreover the ratio between dead and active area with large surfaces is typically lower than in little detectors and this is positive for light collection.

On the other side, the photodetectors usually include in their electrical model a capacitor and its value is proportional to the area dimension of a detector: a large surface brings to higher capacitance, with drawbacks in term of readout circuit noise optimization and stability. In addition, smaller detectors can lead to better spatial resolution performance for the imaging.

Another characteristic to consider when dealing with photodetectors is its time pulse function: the photons/carriers conversion and the following collection of charges on the electrode present a time development depending on the physics and geometry of the detector. The ideal detector would have a very short pulse duration, practically a Dirac’s delta impulse response.

Hereafter the principal photodetectors usually employed in scintillator-based gamma cameras are reported. For different reasons, they have not been chosen for the INSERT project and the motivations are here analyzed. In a separate, following section, silicon photomultipliers (SiPMs) - the photodetectors elected for INSERT - are discussed in detail.

#### Photomultiplier Tube

Photomultiplier tubes (PMTs) present very high internal gain (multiplication of approximately  $10^6$ ) with the consequence of a limited influence from the following elaboration stages on signal. The main limitation of such devices is the moderate quantum efficiency, around 20-30 % and their bulky structure (Figure 3.4).

Still the most mature and diffused photodetector for nuclear medicine, the PMT is employed also in multimodal scanners, such as PET/CT and SPECT/CT [77, 78], but also SPECT or PET in combination with MR, de-

### 3.1. Gamma-ray detection with scintillators



**Figure 3.4:** *Different shapes of photomultiplier tubes (PMTs, Hamamatsu - All rights reserved to Laurin Publishing Co.).*

spite the magnetic compatibility issues. Some of the solutions proposed are to place the PMT-based device in tandem with the magnetic scanner and optionally reduce the magnetic field magnitude to limit PMT shielding [35, 79]; otherwise works suggest to place the PMTs far from the MR scanner and couple it with optical fibers [43, 80, 81]. Nevertheless, the drawbacks of these approaches have limited the diffusion of PMT in multimodality with nuclear medicine devices combined with MR: tandem acquisition prevent synchronous recording, while lowering the magnetic field makes the MR imaging resolution and contrast poorer. The optical fiber coupling its still a limited method, since light transmission represents an additional stochastic process that contributes to signal to noise ratio (SNR) worsening.

#### **Avalanche Photo-Diodes**

Avalanche photo-diode (APD), like PMT, are designed to have an internal multiplication (order of  $10^3$ ) and QE around 80 % (higher than in PMTs). Moreover, as like most of the solid-state detectors based on silicon, APDs have shown good compatibility in presence of high magnetic fields and present a compact structure. APDs have been already implemented in gamma-cameras for combined PET/MR imaging [82, 83].

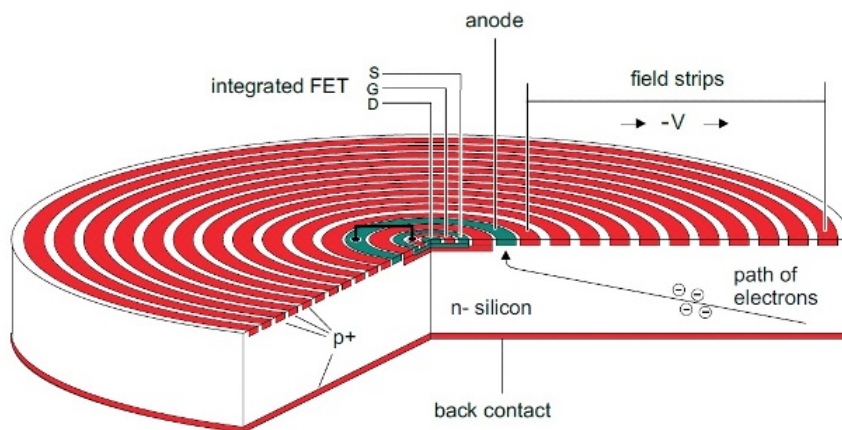
Unfortunately, a great limitations for this photodetectors comes from the high variability on the multiplication process. Moreover, APDs show a

### Chapter 3. Gamma-detection module design

high sensitivity of the gain to temperature and bias variations as well as the need to be operated at high voltages with the additional difficulty to fabricate arrays of uniform units.

#### Silicon Drift Detectors

Silicon drift detectors (SDDs, Figure 3.5) present very high quantum efficiency (higher than 80 %) and are biased at moderate biasing voltages (around -140 V).



**Figure 3.5:** Schematic architecture and working principle of a Silicon Drift Detector (SDD). [84]

This device, unlike PMTs and APDs, does not provide any internal gain, which means that the noise and variabilities on the electronics stage coupled to the device can introduce substantial worsening on the SNR. The electronic noise is dependent on the leakage current of the device and on the total anode capacitance, which is the sum of the detector capacitance and of the preamplifier input capacitance. For this reason, a careful design of the preamplifier is required to reduce the noise of the readout electronics. SDD-based gamma-cameras have demonstrated high performance in terms of imaging resolution [32] and their behavior in magnetic fields has been tested to be coherent with regular working conditions [85]. Nevertheless, this kind of photodetector present limited studies in nuclear medicine with respect to other fields and no works on multimodal imaging with MR scanner have been promoted up to the present day (on our knowledge).

The SDDs have been considered as INSERT photodetectors: the following sections will present the performance foreseen for the SDD-based gamma-



### 3.1. Gamma-ray detection with scintillators

detection module in INSERT and their comparison with SiPMs. As general consideration, the main motivation for dismissing the SDDs from the INSERT project has been the difficulty to obtain uniform and low noise units from production and the relatively high fragility of the upper silicon layer of the devices (the one in optical contact with the scintillator).

#### 3.1.3 Silicon PhotoMultiplier - SiPM

The photon detection technology elected for the INSERT project is the Silicon Photomultiplier (SiPM). In sections 1.4.1 and 1.4.2 we have explored the state of the art for the PET and SPECT systems combined with MR and many works appears to implement SiPMs coupled to scintillators for their gamma-detection modules. SiPM-based modules aiming for PET systems have been diffusely proposed [86, 87], while a less extended literature implements SiPMs [88] or digital SiPMs [41] in SPECT systems for multimodal systems. Other works implement SiPM in compact gamma-cameras with no direct interest in multimodal integration [42].

Not only the interest on SiPM is boosted by the wide number of applications in literature, but also by the fact that it is a relatively new technology and we can anticipate that more research and development in the next years will push the performances of this kind of device that has not reached its maturity yet.

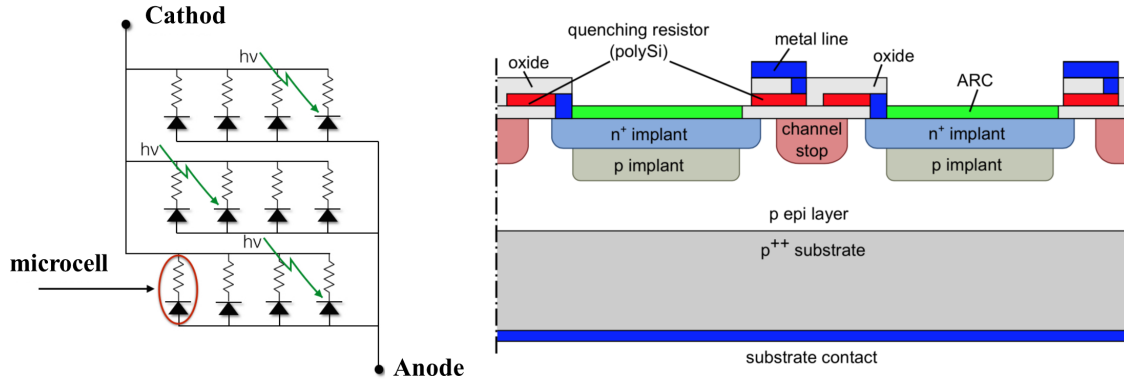
#### Structure and Principles

A SiPM is a bidimensional array of photodiodes (also called *microcell*) operated in Geiger mode and hosted on a common Silicon substrate (Figure 3.6). Every microcell is coupled with all the others by mean of a polysilicon quenching resistor. The active area of each photodiode can vary from 15 to 100  $\mu\text{m}$  and the density can reach 4000 microcells per square millimeter.

The total active area of the SiPM is equal to the sum of all the photodiodes active areas. Because of design constrains for the microcell, the active area of the single photodiode is inferior to its overall surface: the remaining area is dead area. The ratio between active area and overall area is called *fill factor* (FF) and it is an important geometric parameter of the SiPM.

All the parallel photodiodes are operated in the Geiger mode: they are reverse-biased slightly above their breakdown voltage. When a ionizing radiation impact in the volume of the device, an electron-hole pair is generated in the depleted region across the p-n junction and suddenly the carri-

### Chapter 3. Gamma-detection module design



**Figure 3.6:** (left) Schematic structure of a SiPM: a bidimensional array of Geiger mode photodiodes commonly biased and with all the anodes connected together. Each microcell presents a quenching resistor to stop the self-sustained avalanche current after a photon has been absorbed. (right) cross-section of two microcells in a SiPM; the p implantation defines the microcell active area; The Anti-Reflective Coating (ARC) is a passivation layer that optimize light transmission for a limited wavelength range. Quenching resistor is realized in polysilicon.

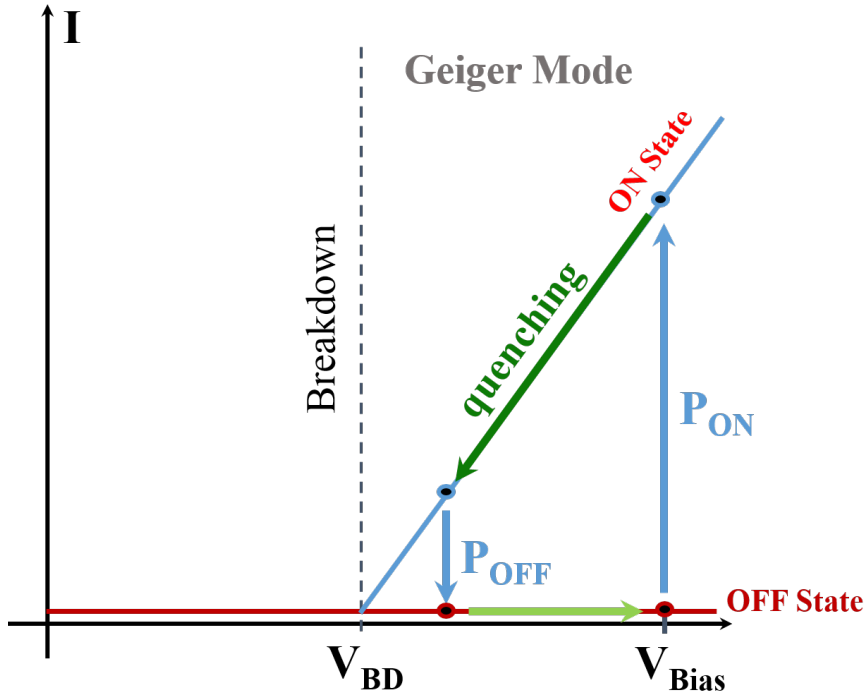
ers are accelerated towards the cathode and the anode. The device present a region with particular abundance of dopant inclusions and the electric field is here augmented. The energy of the carriers in this region is sufficient to trigger a cascade generation of electron-holes, forming an avalanche of carriers. When the voltage is above the breakdown, the kinetic energy of both electrons and holes is sufficient to trigger new avalanches (while regular photodiodes works only with the electrons trigger), thus producing a self-sustained process. The quenching resistor has the function to limit and then extinguish the avalanche.

Figure 3.7 describes and simplifies the I-V characteristic of a photodiode operated in Gaiger mode: in the initial condition the cell is in "OFF" state, with no current generated and a voltage difference across the device equal to:

$$V_{Bias} = V_{BD} + V_{OV} \tag{3.5}$$

where  $V_{BD}$  is the breakdown voltage and  $V_{OV}$  is defined as *Over Voltage*. The passage to the "ON" state is triggered by either ionizing radiation (an incoming photon), a spontaneous thermal generation of an electron-hole

### 3.1. Gamma-ray detection with scintillators



**Figure 3.7:** *I-V characteristic of a SiPM microcell operating in Geiger mode: initially is set on a OFF state and no current flows. An incoming photon can trigger an avalanche with probability  $P_{ON}$  and the characteristic passes to the ON state. Quenching and  $P_{OFF}$  stop the avalanche and return to the starting condition.*

pair or other processes better described later in the discussion. The activation of the avalanche gives suddenly rise to an high flow of charges. This current would self-sustain, but the presence of the quenching resistor causes a passive voltage drop on the microcell and blocks the avalanche, passing back to the "OFF" state. After the quench, the voltage across the microcell is gradually recovered to the  $V_{Bias}$  value.

Thus, the single microcell exhibits a digital behavior (ON/OFF), with the following characteristic:

- The total amount of charge collected for one avalanche "event" is always the same. Given the equivalent capacitance for the depletion region of the photodiode ( $C_D$  and the  $V_{OV}$  applied, one can calculate the microcell gain ( $M$ ) as:

$$M = \frac{C_D \cdot V_{OV}}{q_{e^-}} \quad (3.6)$$

### Chapter 3. Gamma-detection module design

with  $q_{e^-}$  equal to the single electron charge. A considerable drawback of SiPM is the high gain variation in dependence to the temperature:  $\Delta T$  is approximately 0.3 °C for a  $\Delta G/G = 1 \%$ . The gain is also proportional to the  $V_{OV}$ .

- One microcell can read only one photon during the "ON" phase, which is also called *absolute refractory time*. The arrival of a second photon in this time interval would be masked by the avalanche process. There is a second phase, defined as *relative refractory time*, when the voltage is recovering from  $V_{BD}$  to  $V_{Bias}$  in which the microcell can detect a new photon arrival, but the effective Over Voltage is reduce, then also the gain will be inferior and the current amplitude of the output signal will result affected.

The charge output from all the microcell are cumulated into a common line which represent the overall SiPM output. Although the single microcell works in digital/switching mode, the SiPM is an analog device because all the microcells are read in parallel making it possible to generate signals within a dynamic range from a single photon to a number  $N_{microcells}$  of photons for just a single square millimeter area device.

For fast distributed photon signals, the *relative refractory time* represent a limit that involves also the spatial dimension: if more than one photon impinges on the same microcell, the system will detect only one photon. Then, if the light distribution on the SiPM is too focused on few cells or too many photons are hitting the overall SiPM area, the risk to miss the acquisition of a number of photons is really high. This limit is referred to as *saturation effect* for the SiPMs. In case of uniform irradiation over a SiPM, one can write:

$$N_{FiredCells} = N_{Total} \cdot (1 - e^{-\frac{N_{Triggers}}{N_{Total}}}) \quad (3.7)$$

where  $N_{FiredCells}$  is the effective number of microcell activated,  $N_{Total}$  is the total number of microcells composing the SiPM and  $N_{Triggers}$  is the number of photons absorbed that can trigger an avalanche. The system we are going to present implements a large area array of SiPMs, a slow scintillation decay time from the CsI(Tl) crystal and a number of scintillation photons limited to few thousands. Starting from these hypothesis, saturation effect can be neglected in the case of the gamma-modules for INSERT.

### 3.1. Gamma-ray detection with scintillators

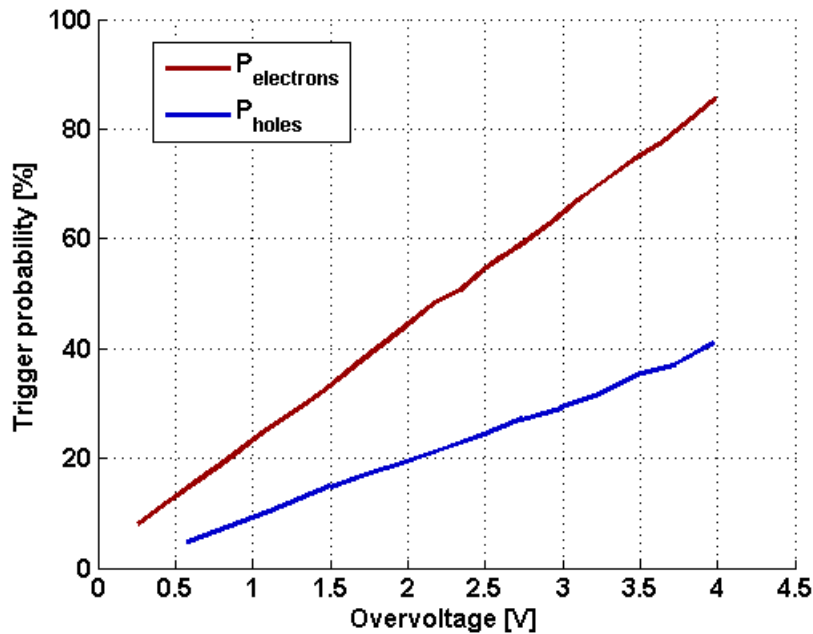
#### SiPM figures of merit

Hereafter the most important parameters and effects of interest for a SiPM are described.

**Photodetection Efficiency** - Due to the geometry and to the intrinsic processes of a SiPM, the mere Silicon quantum efficiency value is not sufficient to describe the conversion factor from impinging photons to electrons. PhotoDetection Efficiency (PDE) is used instead and it is defined as:

$$PDE = FF \cdot QE \cdot P_{ON} \quad (3.8)$$

where  $FF$  is the fill factor for the SiPM described above and varies depending on the microcells design and dimension;  $QE$  is the quantum efficiency of the material, typically around 80 % or higher and is wavelength of the photons and temperature dependent;  $P_{ON}$  is the probability that the primary electron-hole pair triggers an avalanche.



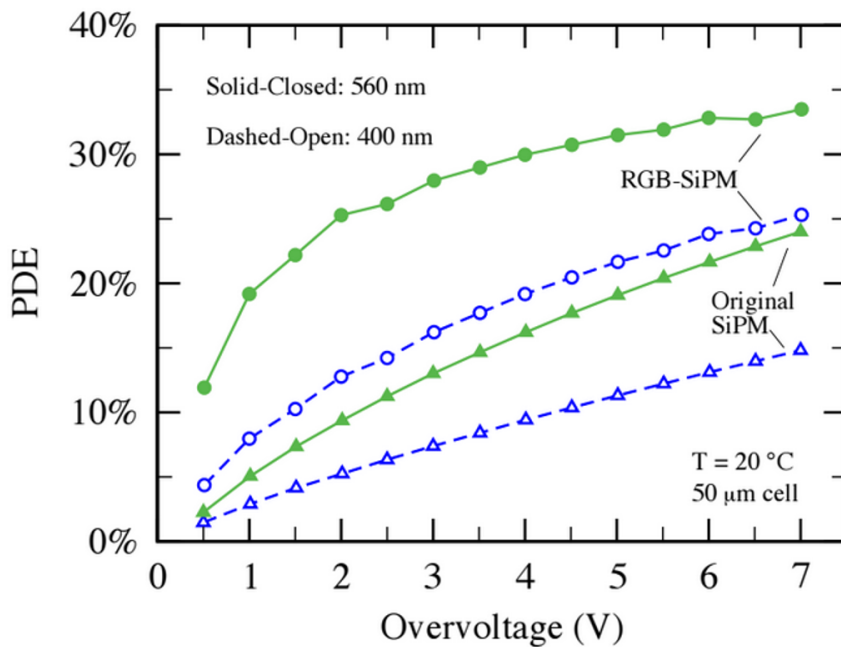
**Figure 3.8:** Avalanche trigger probability as function of the overvoltage ( $V_{OV}$ ). The electrons have more probability to activate a process than the holes because of their higher mean kinetic energy.

$P_{ON}$  has a dependence with temperature, wavelength of the absorbed

### Chapter 3. Gamma-detection module design

photons and  $V_{OV}$ .  $V_{OV}$  influences the electric field in the microcell and then the kinetic energy on the carriers (which is higher in electrons rather than in holes for a fixed EM field) [89]. For low values of  $V_{OV}$ , trigger probability is almost linear as depicted in Figure 3.8.

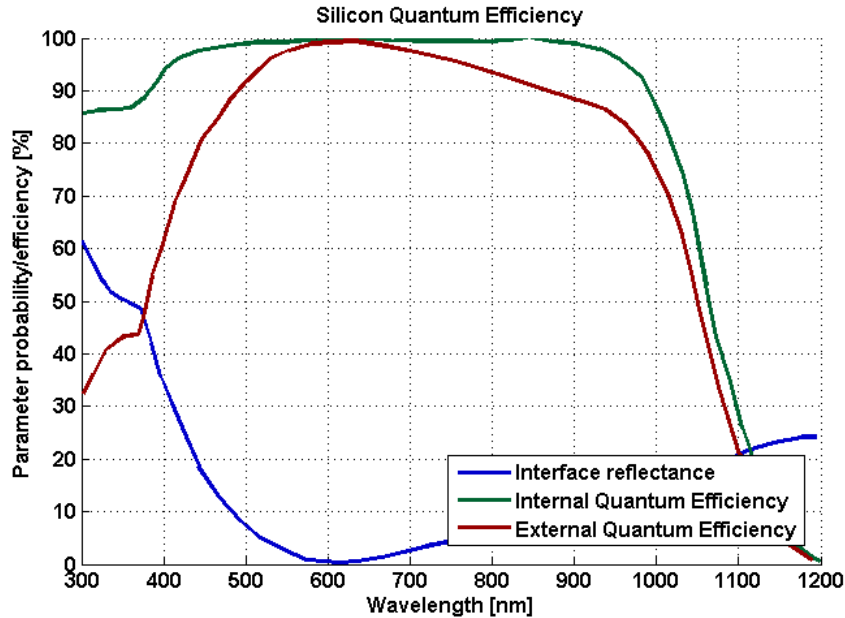
In general, it is possible to state that  $PDE = PDE(T, V_{OV}, \lambda)$ . The detection efficiency behavior as function of  $V_{OV}$  is mostly related to the above mentioned  $P_{ON}$  variation (Figure 3.9).



**Figure 3.9:** PDE at 400 and 560 nm as a function of overvoltage in RGB (circles) and an older device (triangles) SiPMs. The electric field engineering made it possible to have a faster increment with bias of the PDE in RGB-SiPMs than in the original technology [90].

Dependence from  $\lambda$  is related to  $QE(\lambda)$  characteristic for Silicon: Figure 3.10 shows a general characteristic of the QE as function of wavelength. The probability of absorption and generation of primaries is related mainly to the entrance window reflectivity at different  $\lambda$  and to the thickness and position of the depletion region into the Silicon bulk.

### 3.1. Gamma-ray detection with scintillators



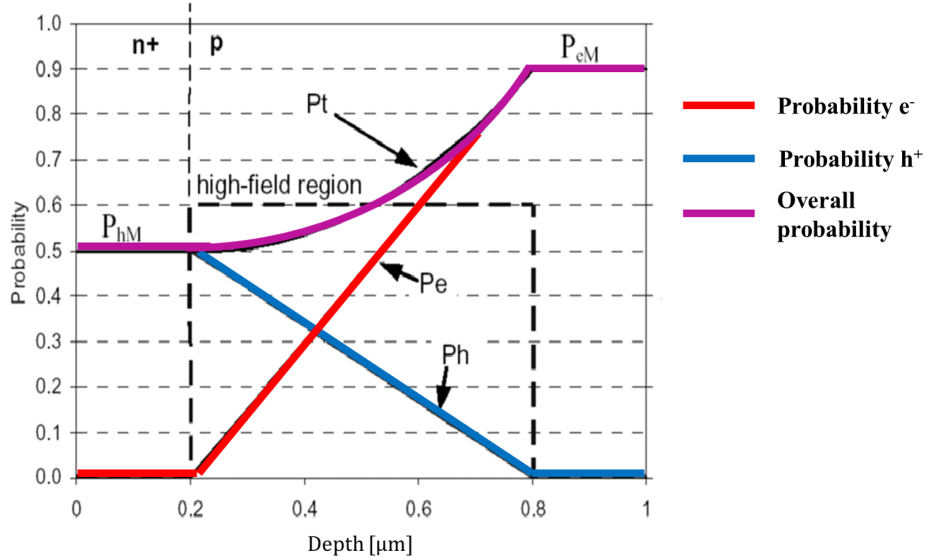
**Figure 3.10:** Quantum efficiency (QE) or External Quantum Efficiency (EQE) for the Silicon and as function of the light wavelength. Also the processes that contribute to EQE definition are depicted: reflectance on the external interface of the silicon detector and Internal Quantum Efficiency (IQE) of the material.

Also  $P_{ON}(\lambda)$  contributes to the general PDE( $\lambda$ ): Figure 3.11 depicts the  $P_{ON}$  (for both electrons and holes) as function of the depth of penetration. The doped profile produces variations in the electric field (E) inside the microcell volume and the avalanche region presents the high magnitudes for E. Since the electrons and holes have opposite polarization, they travel in different directions. Thus an hole will have chance to trigger an avalanche only if it has been generated before the limit of the avalanche region (vice versa for the electron).

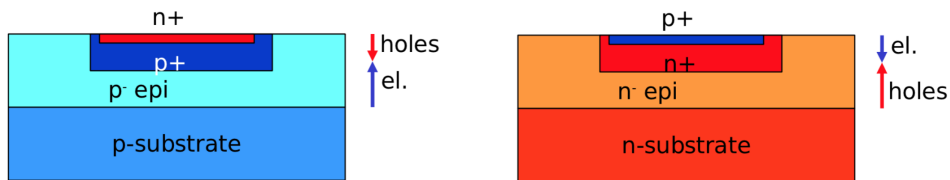
Photons absorbed in the first micrometers (low wavelengths) will have probability to trigger an avalanche only through the holes intervention, while photons absorbed more in depth (higher wavelengths) will have better chances to initiate an avalanche process, simply because the higher  $P_{ON}$  for electrons.

The example shown favors the medium-high wavelengths (around 450 - 500 nm), because the doping profile is  $N^+$  on P. A reverse structure of the device (Figure 3.12), will invert the diffusion direction of the carriers, endorsing the  $P_{ON}$  for lower wavelengths (around 350 - 400 nm).

### Chapter 3. Gamma-detection module design



**Figure 3.11:** Probability of avalanche trigger, for both electrons and holes, as function of the depth of absorption in the microcell volume. The high field area is highlighted with a black dotted line.

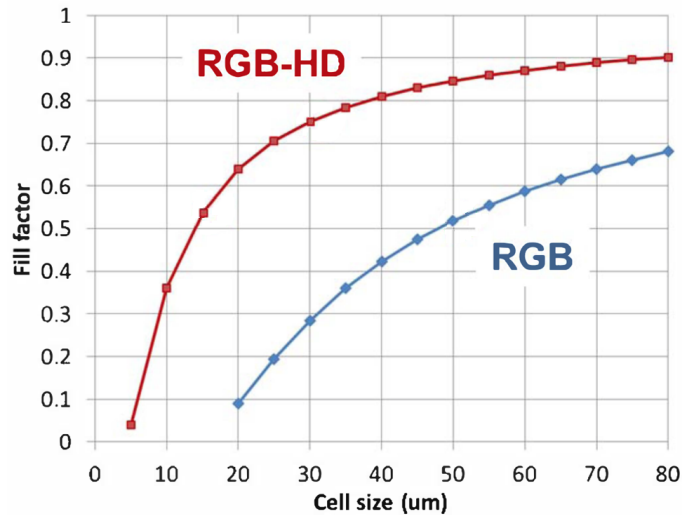


**Figure 3.12:** Variations in dopant configuration for two different SiPM microcells. The n/p profile is designed with regard to optimize the wavelength range to be detected by tuning the mean depth of interaction for the electrons, the carriers that bring higher trigger probability. (left) configuration with QE maximization for wavelengths between 500 - 700 nm. (right) configuration with QE optimization for wavelengths between 300 - 500 nm.

Figure 3.13, indirectly describes the proportion between fill factor and PDE: increasing the dimension of the microcells reduces (by a non-linear factor) the dead area surface, then fill factor, one of the main PDE components, augments with the microcell side.



### 3.1. Gamma-ray detection with scintillators



**Figure 3.13:** Fill factor as function of microcell size for two consecutive SiPM technologies adopted during the project. The absolute dimension for the single microcell remains almost constant independently from the active area dimension, thus their relative weight on fill factor raises with lower dimension microcells. Courtesy of FBK Trento, Italy.

**Dark Count Rate** - Photon ionization is not the only cause that determines the initiation of a breakdown process: the avalanche can be unleashed by means of thermal spontaneous electron-hole pair generation or by released carriers, previously trapped in the lattice. Every avalanche generation which is not related to the optical signal of interest, is considered as a disturb on the signal itself. In regular conditions, with no light stimulation of the SiPM, this noise is persisting and is then called *dark current* or, better, *Dark Count Rate (DCR)* for the impulsive nature of the spurious events. The wider the surface of the detector, the higher the number of dark events collected. DCR is measured in [Hz/mm<sup>2</sup>]. Unfortunately, also dark count events incur into multiplication by mean of avalanche process, thus this disturb source can not be reduced by enhancement of the SiPM gain. Dark current is mainly the result of three components addition:

1. Thermal generation of carriers in the depletion region, which is proportional to the temperature on the device ( $DCR \propto T$ ).
2. Spontaneous generation of e-h pairs in the multiplication region for *Trap Assisted Tunneling (TAT)* [90]. In high electric fields the bands bending allows the electrons to pass from the valence to conduction band with a lower energy. The process probability is improved by

### Chapter 3. Gamma-detection module design

the presence of impurities in the lattice. This component for the dark current is proportional to the effective depletion volume and by the  $P_{ON}$  probability. Thus,  $DCR \propto V_{OV}$ . For high values of  $V_{OV}$ , the dark current is additionally worsen by crosstalk effect, later described in the section.

3. Diffusion of minority carriers in the depletion region. This effect is predominant at very high temperatures, since it requires high activation energy. In the cases considered in the present work, this contribute can be considered negligible.

**Non-linearities** - Other phenomena affects the entity of the DCR and the multiplication process with uncertainties:

- **Optical crosstalk (OCT)** is related to the probability of secondary optical photons in the avalanche process. The secondary photons travel in neighbor microcells and give rise to spurious breakdown events. OCT is proportional to the square of  $V_{OV}$  and for this reason high values of biasing bring to a steep worsening of the DCR.
- **Afterpulsing (AP)** is a process correlated to the amount of impurities, and related traps, in the crystal lattice. Carriers that fall into these traps can be released after a short time interval and generate a new avalanche. The effect is obviously seen only if the carrier is released after the absolute refractory time. If the carrier is released during the relative refractory time, the gain on the microcell will be proportional to the amount of voltage bias restored on the microcell 3.14, as described above.

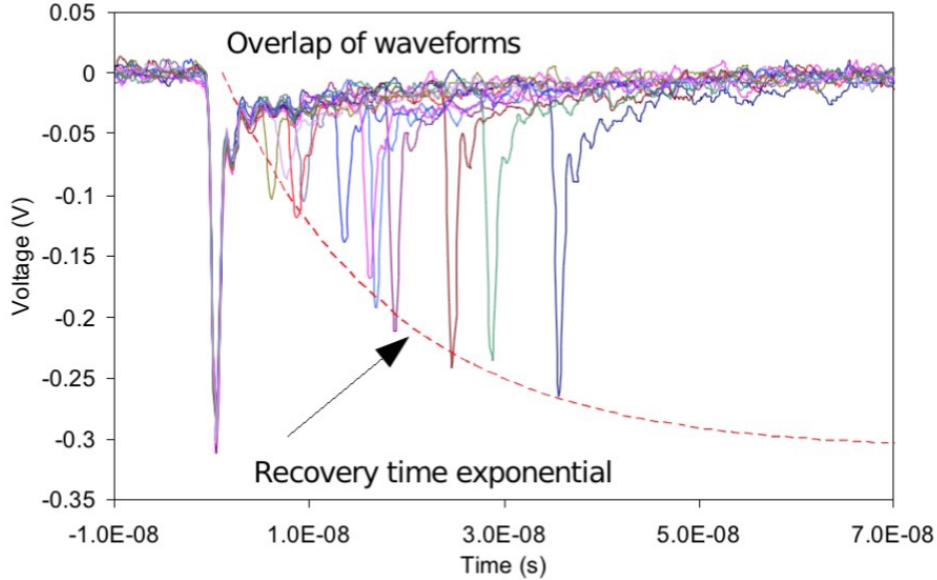
The Afterpulsing effect is proportional to the amount of impurities and to the  $P_{ON}$  of the carrier. Then,  $AP \propto V_{OV}$ .

The OCT and AP phenomena do not only affect DCR with the introduction of spurious events (even if time-correlated with the signal), but mostly introduce uncertainties on the number of events count. The presence of a charge excess due to non-linearities is considered by the ENF (Excess Noise Factor) parameter, experimentally measured as:

$$ENF = \frac{I_D}{q_{e^-} \cdot DCR \cdot A_{SiPM} \cdot M} \quad (3.9)$$

where  $I_D$  is the output dark current and  $A_{SiPM}$  is the active area of the

### 3.1. Gamma-ray detection with scintillators



**Figure 3.14:** Temporal distribution of a number of afterpulses after the primary avalanche. The amplitude of swift afterpulses is reduced due to the relative refractory time, when the  $V_{OV}$  is still not completely recovered. [91]

SiPM. For a detector that exhibit no OCT or AP, the ratio should be equal to the unity. The ENF is indirectly associated to the variance on the multiplication process.

#### Temperature dependence

The most evident consequence of temperature variation in SiPM is the variation of the breakdown voltage and of the dark count rate. The latter correlation has been already explored in a previous section. For what concerns the former effect, the linear relation between Breakdown voltage and temperature is approximately expressed by:

$$\frac{\Delta V_{BD}}{\Delta T} = 20 \div 80 \frac{mV}{K} \quad (3.10)$$

Given equation 3.5, it is possible to derive the over-voltage dependence from temperature, from which many other figures of merit are proportional (first of all the SiPM gain). From this perspective, temperature cooling and

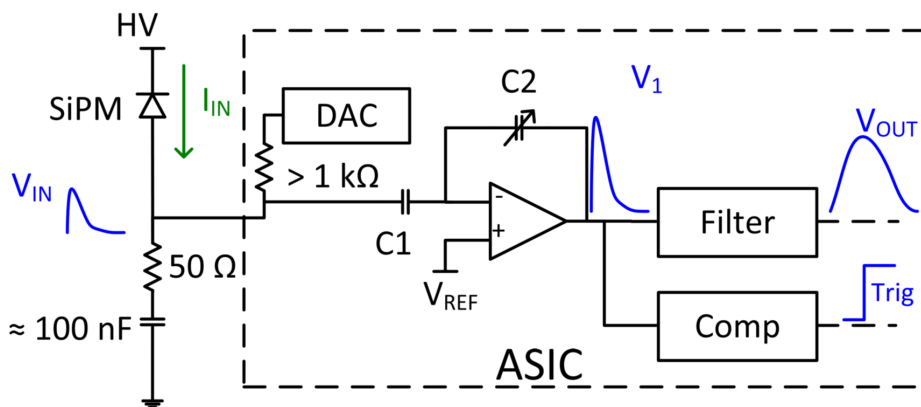
### Chapter 3. Gamma-detection module design

stabilization is a mandatory key for practical implementation of SiPMs: the former allows to reduce the DCR (dominant) component of noise; the latter reduces the variability of the gain, therefore on the output parameters of the gamma-detection module.

#### Electronic Readout Strategies

SiPM readout electronics presented in literature can be categorized depending on signal processing modality.

In **voltage mode approach**, the photodetector current is converted into a voltage by means of a small resistor (typically 50 ohms) [92,93]. A generic circuit for this modality is presented in Figure 3.15.

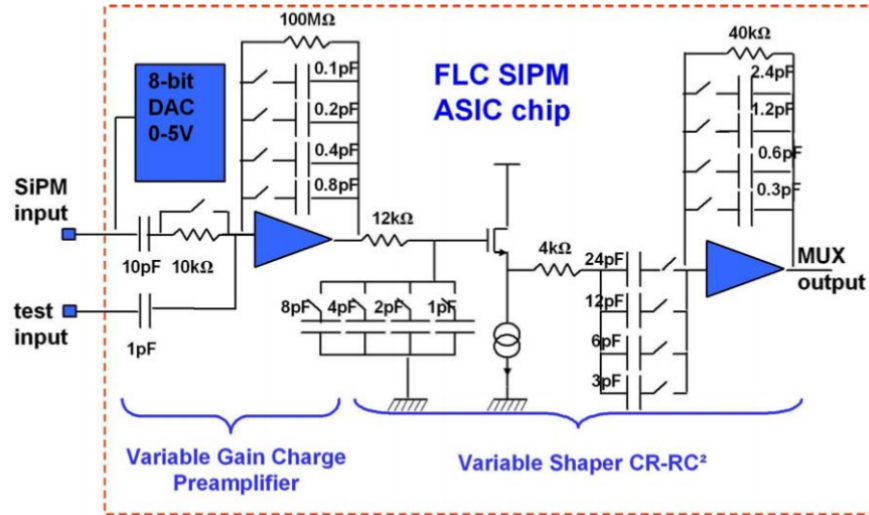


**Figure 3.15:** Schematic structure of a voltage mode approach for SiPM readout.

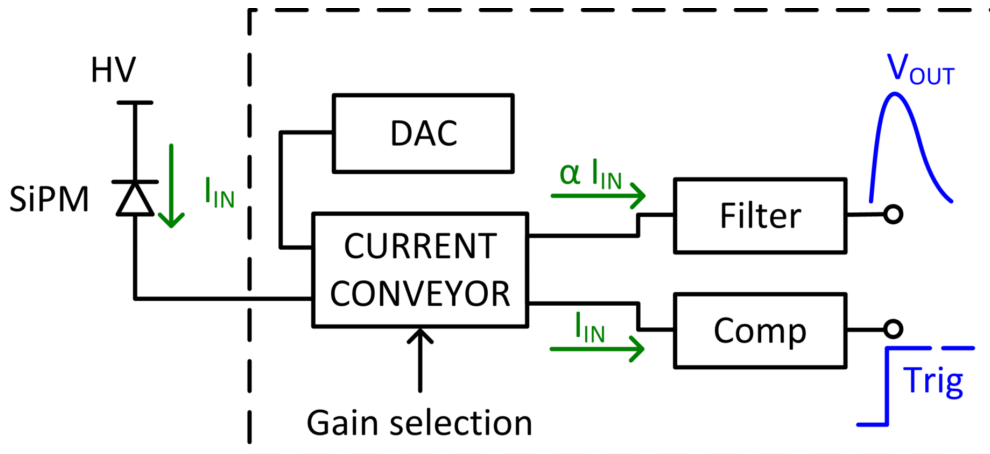
**Charge sensitive mode** (shown in Figure 3.16) take advantages by the easy biasing of the SiPM, an ideal null input impedance, and the possibility to realize directly the signal charge integration necessary for the following filtering [94]. Unfortunately, this approach is not well suited for managing high value capacitance (above 300 nF) for the SiPM, due to stability limits of the circuit [95].

On the other side, **current mode based circuits** (Figure 3.17) [97, 98] guarantee large bandwidth, thanks to the very low input impedance seen by the detector capacitance, a high dynamic range that allows to exploit the whole SiPM signal and to scale the signal to suit the voltage range.

### 3.1. Gamma-ray detection with scintillators



**Figure 3.16:** SPIROC structure, a charge mode based circuit for SiPM signal readout [96].



**Figure 3.17:** Principle scheme of a current mode approach with current conveyor that allows to read the SiPm at very low impedance.

#### 3.1.4 Signal elaboration

This section provides a brief description of the signal elaboration chain, from the SiPMs current, to the final image. For what concerns the electronics readout, a current mode circuit based on current conveyor is considered, since it is the general architecture for the final electronic readout channel. An imaging system requires the parallel acquisition of the signals from each

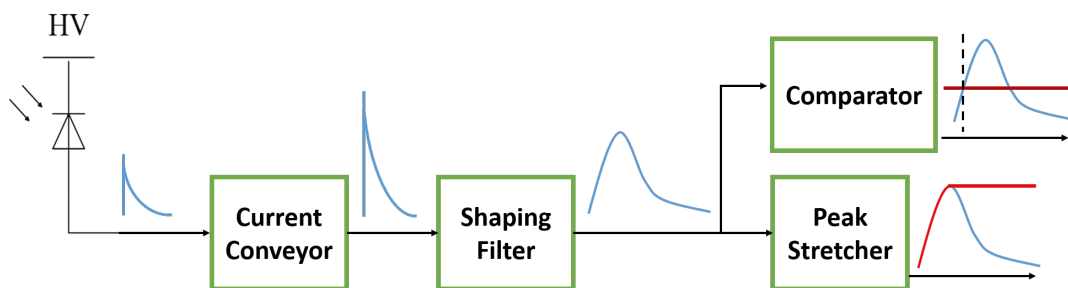
### Chapter 3. Gamma-detection module design

single imaging pixel (i.e. the SiPMs in a photodetector array). In an Anger camera, the overall light signal pulse is divided on the pixels that compose the photo-sensitive matrix. The readout approach requires to read all the channels synchronously when a scintillation event is detected. Then the information obtained for each different pixel is elaborated and recombined to produce the imaging and spectroscopic outcomes.

In literature, a number of works implements simple readout architectures with resistive networks in order to passively calculate the coordinates of gamma interaction and the amplitudes histogram from which the energy spectrum can be estimated [99, 100]. Despite the high reduction of signal elaboration complexity given by this approach, we estimated that resistive networks implementation could have brought to practical and not trivial difficulties. Without getting too much in detail:

- Tolerances on the components is a key role and must be extremely controlled.
- The calibration or correction for possible channels alteration would require a complex control on every resistor of the network.
- The output from resistive networks does not allow the application of analysis or sophisticate statistical algorithms that can improve the output performance

Figure 3.18 depicts the diagram blocks concept for a single readout channel. This structure is replicated for the number of channels needed to read all the photodetector array (typically one for each SiPM).



**Figure 3.18:** Conceptual diagram of the SiPM signal readout process in the case of a current mode circuit. The current, buffered and amplified by the current conveyor, is shaped into a voltage signal and the maximum amplitude is then hold by the peak stretcher. A comparator block has the function to provide a digital trigger associated to the arrival of one event.

### 3.1. Gamma-ray detection with scintillators

The current pulse signal from the SiPM is collected by a current conveyor (CC) block circuit: it offers practically null input impedance to the SiPM, avoiding issues such as bias variations on the detector. The CC configuration permits to read SiPMs with a correlated high capacitance (above 300 nF) with no stability issues. The block works as a current buffer, but can also amplify the current amplitude.


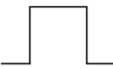

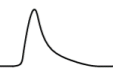

Signal from the SiPM present a temporal shape which is coherent with the scintillation decay of the crystal, if we assume negligible the SiPM contribute on time distribution. The *Shaping Filter* and the *Pike Stretcher* blocks have the function to filter the signal, optimize the SNR and, at the same time, provide an output proportional to the amount of photoelectron collected from the photodetector.

*Optimal filter theory* sentences that, if the time template of the signal is not known, the best possible SNR is achieved if the signal pulses are shaped to the form of an infinite cusp [57]. This filter is unpractical to be realized for several reasons, then other methods of pulse shaping are more commonly used that are inferior in SNR performance, but can be implemented in circuits. Figure 3.19 lists some of the common methods of pulse shaping generally found in linear pulse amplifiers.

On a parallel line to that of the Peak Stretcher, the shaped signal is sent to a *Discriminator* with the function to compare the input signal with a arbitrary defined threshold. If the pulse of one of the channels among all goes over threshold, a logic trigger is sent to the *Peak Stretcher* block to activate it. Once enabled, the *Peak Stretcher* works as a sample-and-hold circuit: it follows the signal until the maximum is reached and then it holds the voltage peak value has output. This analog value is proportional to the amount of charge collected by the photodetector and has to be digitized by an *Analog-to-Digital Conversion* (ADC) block. A digital value for every channel is transmitted and stored into a computer for further elaboration. Every single scintillation interaction is defined as *event*: in a generic acquisition, thousands or even millions of events are recorded and saved. For each event an array of  $N_{Channel}$  digital values is given. The basic information from a gamma-detection module measurement is a  $N_{Events} \times N_{Channel}$  matrix of digital values.

Finally the data can be elaborated in order to obtain the imaging and spectroscopic outcomes: the amplitudes histogram, is obtained by the summation of the  $N_{Channel}$  values for every event. The resulting array is plotted as an histogram and from this graph information on the energy spectrum of the radioactive source is retrieved.

### Chapter 3. Gamma-detection module design

Filter	Impulse response or weight function	$\tau$ definition	$A_3$
Triangular		Peaking time	0.335
Gated integrator		Gating time	0.5
RC		RC	0.25
CR-RC		Peaking time	0.923
CR-RC <sup>7</sup>		Peaking time	0.3372

**Figure 3.19:** Shape and properties ( $A_3$  and shaping definition) for commonly employed filters in radiation spectroscopy.

The output matrix is also elaborated by means of reconstruction algorithms in order to estimate the position of gamma-interaction in the scintillator for each event in the matrix. The output of such kind of algorithms (described in chapter 4) is an image that depicts the distribution of the gamma-events in the crystal coordinates.



## 3.2 Design tools

As seen so far, the design of a gamma-camera with constrained output performance requires the optimization of a multitude of geometrical and physical parameters, most of the times with respect to very delicate tradeoffs between output results. The development of the device can be represented as an iterative process: at the first iteration, a preliminary design is proposed and, by means of some predictive tool, its performance are estimated. The parameters domain is explored by selectively changing the values and estimating the related outcomes. This approach gives a tentative indication on the chief parameters that mostly influence the camera performance.

In a next phase, experimental trial on single components or emulating systems (i.e. gamma-cameras from other projects) are performed to verify the predicted behaviors and to set lower and upper limits to input parameters, but also to better define an hypothesis on the outcomes.

The system is then re-designed, with the new information on the parameters and on the tool model. After the production of the first prototype, if any discrepancy between the experimental results and the hypothesis is found, the predictive model is revised or practical system limits are underlined. The process passes to a new design phase and so on.

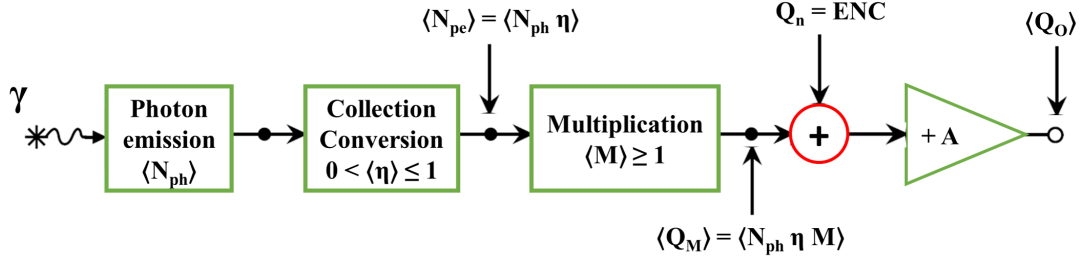
The present section presents the “predictive tools”, practically statistical models that we employed in the design and development process of the INSERT detection module.

### 3.2.1 Energy resolution theoretical model

The analytical models allow fast and continuous estimation of the output performance by defining a set of input parameters. The present section describes the model adopted for energy resolution forecast. Analytical model for the intrinsic spatial resolution has been also developed [101], but their description and application are not treated in the present work. The energy resolution of a gamma-camera can be estimated by means of a theoretical model based on error propagation statistics [102–104]. Figure 3.20 depicts the general model of a radiation spectroscopy system, practically a diagram cascade of blocks, each one representing a stochastic process of signal conversion, transport or elaboration in the gamma-detector chain. Every block operates a transformation to the signal and introduces uncertainties on the measurement.

The first block considers the photon emission in the scintillator:  $N_{ph}$

### Chapter 3. Gamma-detection module design



**Figure 3.20:** Conceptual diagram of the cascade of processes in gamma-ray detection with scintillator. Each process introduce a source of uncertainty which can be modeled with a stochastic distribution. Thus, the error on the measurement propagates through the blocks and determines the final signal variability.

(number of generated photons) is modeled to follow a Poisson distribution with average value  $\langle N_{ph} \rangle = E_{\gamma} \cdot \text{Yield}$ . The conversion block takes in consideration the effects of photon collection on the photodetector matrix and it is associated to a binomial distribution with frequency of positives  $\eta = \eta_{coll} \cdot \eta_{conv}$  (equal to PDE in the SiPM case). Multiplication block is present in SiPMs and it is source for additional fluctuation on the signal. It is generally modeled with a Gaussian distribution of mean  $\langle M \rangle$  and standard deviation  $\sigma_M$ . Relative variance is often use to define the variance on quadratic mean ratio ( $\nu_M = \sigma_M^2 / \langle M \rangle^2$ ). The cascade of this three main blocks produces the overall signal from the detectors array to the readout electronic, with its amplitude and fluctuation. Then a noise block, correlated to the electronics elaboration, is summed to take into account the contribute from the devices and electronics noise. The model for energy resolution estimation is built with the hypothesis of a scintillation pulses well separated in time (low count rate) and shaping time of the electronics filter longer than the pulses time length (no issues of incomplete charge collection).

The energy resolution, as defined in section 2.2.1, can be estimated through a Gaussian fitting on the energy peak of interest and it is equivalent to:

$$R_{En} = \frac{\Delta E}{E} = \frac{FWHM}{\langle E \rangle} = 2.35 \frac{\sigma_o}{\langle S_o \rangle} \quad (3.11)$$

where  $\langle S_o \rangle$  and  $\sigma_o$  are respectively the mean and the standard deviation of the signal output, considering a Gaussian distribution of the amplitudes. The signal at the output is the result of the cascade of process described

### 3.2. Design tools

in Figure 3.20 - scintillation, conversion and multiplication - plus the noise contribute. From error propagation theory and considering the probability distribution of each block in the model, the following equation is obtained:

$$\frac{\Delta E}{E} = 2.35 \sqrt{\left( \frac{\sigma_{N_{ph}}^2}{\langle N_{ph} \rangle^2} - \frac{1}{\langle N_{ph} \rangle} \right) + \frac{1 + \nu_M}{\langle N_{ph} \eta \rangle} + \left( \frac{ENC}{\langle N_{ph} \eta M \rangle} \right)^2} \quad (3.12)$$

where three main contributes under square root are underlined: the first term (between brackets) is equal to zero in the case of pure Poisson distribution for  $N_{ph}$ , since  $\sigma_{N_{ph}}^2 = \langle N_{ph} \rangle$ . Scintillation non-linearities actually bring to a broader distribution with respect to Poisson's. The effect is that the terms are no more symmetric and the net difference is expressed as intrinsic contribute energy resolution.

The second term,  $(1 + \nu_M)/\langle N_{ph} \eta \rangle$ , represent the contribute due to statistical fluctuation of the number of generated photons, the conversion and the multiplication processes.

The last term represents the noise contribution to energy resolution.

To summarize, the 3.12 can be expressed as the square root quadratic sum of the intrinsic, statistical and noise contribute:

$$R_{En} = \sqrt{R_{int}^2 + R_{stat}^2 + R_{noise}^2} \quad (3.13)$$

In the case of SiPM detectors, the equation takes the following form:

$$R_{En} = 2.35 \sqrt{\frac{\Delta E_{int}}{E_{int}} + \frac{ENF}{\langle N_{pe} \rangle} + \frac{ENC^2 N_{SiPM}}{\langle N_{pe} M \rangle^2}} \quad (3.14)$$

where  $\langle N_{pe} \rangle = \langle N_{ph} \eta \rangle$  ( $\eta = \langle \eta_{coll} \cdot PDE \rangle$ ),  $N_{SiPM}$  is the number of SiPMs in the array, while ENC is the *Equivalent Noise Charge* calculated at the output of the system chain. It consist of all the noise sources from the photodetectors and the electronic circuits. Since the SiPMs are considered, the multiplication factor has the effect to minimize the disturb of the electronics noise on the signal from the detectors. Unfortunately, dark count events are equally multiplied by means of avalanche process, then their contribute is the dominant component of the noise over signal.

The dependence of the ENC from the dark count rate (DCR) is give by the following:

### Chapter 3. Gamma-detection module design

---

$$ENC^2 = 2q_e \cdot I_{DC} \cdot A_3 \cdot \tau \cdot M^2 \cdot ENF \quad (3.15)$$

with  $I_{DC}$  the dark current and  $A_3$  a form factor given by the filter shape and by the definition of shaping time  $\tau$ .

$I_{DC}$  is defined as:

$$I_{DC} = q_{e^-} \cdot DCR \cdot A_{SiPM} \quad (3.16)$$

For definition and calculation sake, the ENC value obtained from 3.15 is divided by the electron charge ( $q_e$ ), in order to respect the unit of measure [number of charges].

Regarding the  $\langle PDE \rangle$ , it is the *effective PDE average* and it can be calculated from the emission spectrum ( $\epsilon(\lambda)$ ) of the scintillator employed and the  $PDE(\lambda)$  characteristic:

$$\langle PDE \rangle = \int PDE(\lambda) \cdot \epsilon(\lambda) d\lambda \quad (3.17)$$

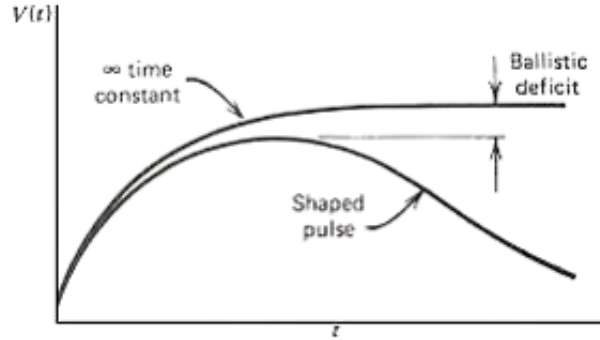
#### incomplete charge collection

Equation 3.14 well describes the energy resolution of a gamma-detection module as function of the system parameters and it is limited hypothesis domain (low count rate and no incomplete charge collection effects). The output signal from the shaper can be calculated as the convolution of the input signal (current signal from the SiPM) with the time function of the shaping filter.

Ideally, we would like to implement a very long shaping time to recover all the signal information (Figure 3.21). On the other hand, long  $\tau_{shaping}$  filters have the effect to collect more noise, with direct worsening effect on SNR. The shaping time requires a tradeoff between amount of signal and noise collected. The percentage of signal lost in the convolution process due to the shape and time length of the filter is called *Ballistic Deficit* (BD). BD can be calculated as:

$$BD = \frac{\max \langle h(t) \rangle - \max \langle f(t) * h(t) \rangle}{\max \langle h(t) \rangle} \times 100[\%] \quad (3.18)$$

### 3.2. Design tools



**Figure 3.21:** Definition of ballistic deficit: it is the degree to which the infinite time constant amplitude has been decreased by the shaping process (depending on time constants and shape).

with  $f(t)$  the signal time distribution and  $h(t)$  equal to the filter time function.

Unfortunately, the decay time of the CsI(Tl) scintillator chosen for INSERT and the shaping time of the filter differ only by one order of magnitude ( $\tau_{CsI} \approx 1 \mu s$  against  $\tau_{RC-shaping} = 10 \mu s$ ) and the consequence is that the system acquisition will suffer of incomplete charge collection due to Ballistic Deficit. To our knowledge, there is no literature on the analytical correction of 3.12 in the case of incomplete charge collection. The only modification that can be account for is the reduction of the total signal in the noise contribution of the formula, leading to the following:

$$R_{En} = 2.35 \sqrt{\frac{\Delta E_{int}}{E_{int}} + \frac{ENF}{\langle N_{pe} \rangle} + \frac{ENC^2 N_{SiPM}}{\langle N_{pe} M(1 - BD) \rangle^2}} \quad (3.19)$$

#### 3.2.2 Montecarlo simulator

Montecarlo simulations play an important role in the design of imaging systems based on gamma-detectors. Since every process of the cascade (scintillation, light transport, conversion into carriers by the photodetector array, etc.) has major influence on the detector performance, a general model that incorporates all the stochastic phenomena is needed.

A Montecarlo simulator receives as input all the geometrical and physical

### Chapter 3. Gamma-detection module design

---

parameters required by the models incorporated into the algorithm in order to well emulate the detector behavior, than an high number of gamma interactions are performed, with consideration of the physical models that simulate the different processes. The output result is a  $N_{Events} \times N_{Channel}$  matrix with the amount of electrons collected by every electronics channel (with added noise) and some statistical information on different processes (i.e. the number of photons lost in the light collection process).

The error on outcome prediction for a simulator is related to the accuracy on the physical models implemented. Generally, a good model requires a relatively high grade of complexity and this improves the number of parameters that define the model itself. Then, also the accuracy on the parameters is a fundamental requirement for having simulated results adherent with experimental ones.

Many works in literature show an upraising of simulation softwares based on GEANT4 or even the adoption of GATE platform for gamma-cameras simulation [105, 106]. The drawback of GATE software and algorithms implemented with GEANT4 is the relatively slow computational times for photon tracking in scintillation models. Moreover, the training for the management of these toolkits can require an important time effort, even though the high level of accuracy of the models has been validated for many gamma-detectors configurations and provide a reliable tool.

Although GATE software offers attractive advantages in terms of model accuracy and system update (since it is developed by an active international collaboration), the task density in the INSERT work plan required a temporal compromise that suggested, at the first steps of the project, a very limited amount of time for the training on a new simulation toolkit. Thus, for the design and study of the INSERT detection module, a ready and custom implemented simulator (Matlab based) has been adopted. During my master thesis and before the start of the INSERT project, I personally worked on the implementation of a new optical model for the custom simulator and on the optimization of the processing time [107, 108].

The advantage in employing a custom algorithm for simulation is the high level of control of all the system variables. The drawbacks are constituted mainly by the possible accuracy of the models and by the validation process, which is time and resource consuming and should be repeated for different configurations of gamma-cameras. In fact, if one specific simulated configuration gives results adherent with the experimental ones, it does not imply that the algorithm is capable to predict with the same accuracy the behavior of cameras with different configurations. This is mainly

### 3.2. Design tools

due to the fact that the models implemented approximate real process and different configurations can require different level of approximation.

As final note, it is of primary importance to remind that the results of a simulation are strictly dependent on the reliability of the input parameters: most of the physical characteristics of scintillators, reflectors and photodetectors can be retrieved only through complex experimental setup [ESEMPI]. A faster approach is to rely on the information provided by specific literature or manufacturers, even if this can lead to errors related to poor consideration on the properties variability in the materials employed. Hereafter the custom simulator is described in its parts.

#### General structure of the simulator

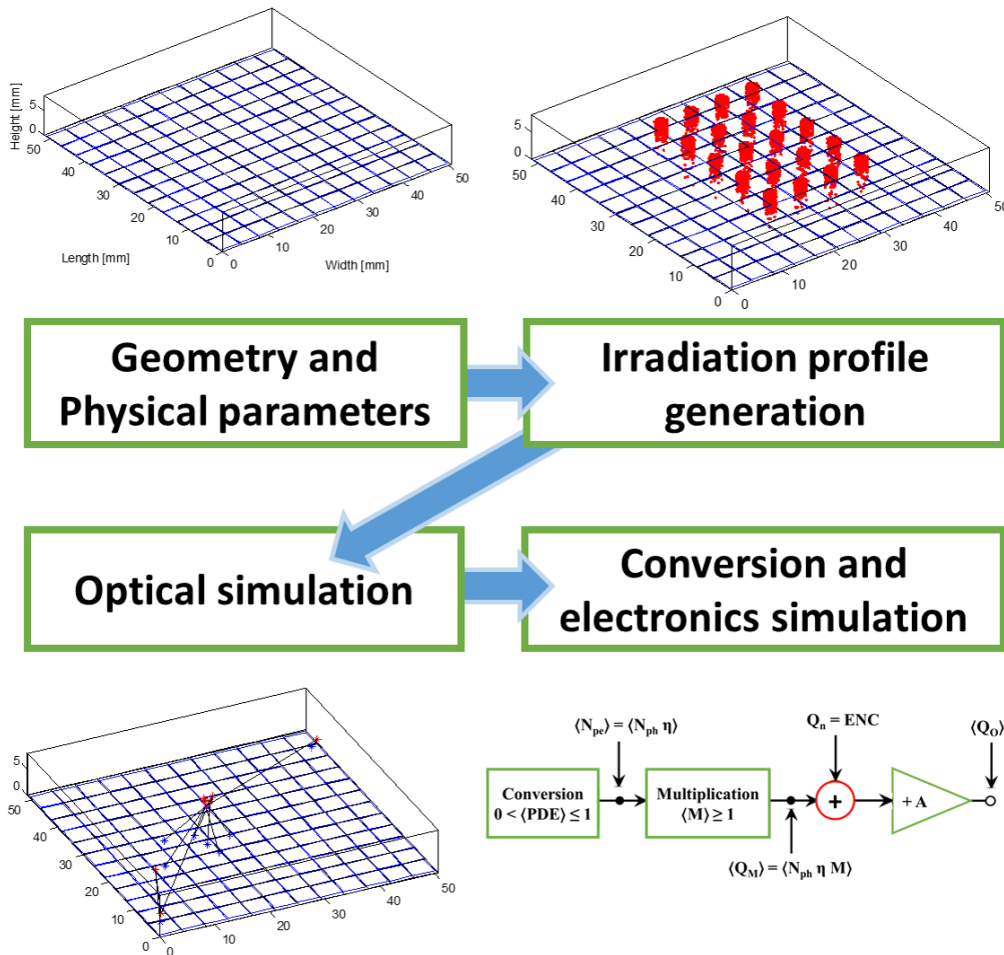
The structure of the custom simulator is presented with a block diagram in Figure 3.22. In a first step the user defines the geometrical and physical parameters for the gamma-detector and for the irradiation profile. Then a first block simulates an arbitrary number  $N_{Events}$  of gamma interaction in the crystal. Coordinates of interaction and energy absorbed are recorded for each event. This data are given as input to a second simulation block that implements the optical model for the scintillator. It computes the light transport into the crystal up to the photodetection matrix. The last block emulates the processes related to the detectors and the readout electronics (light conversion, filter, nonlinear effects, etc.).

#### Gamma-camera geometry

The first action required by the simulator is to create a file with the information on the gamma camera geometry and physics. A Graphic User Interface (GUI) is provided to fill all the information needed to complete the file. The required parameters for the scintillator are composition, shape (parallelepiped or cylinder) and dimensions. Once chosen the material of the crystal, the system retrieves the physical information from a database. The photodetector array geometry is generated by selecting the single device shape (square, circle or hexagon), its dimension and by adding information on the dead areas between adjacent detectors.

The transport model requires also information on the surface mechanical condition of the crystal (polished or rough) and the reflectivity parameters of the reflectors attached to the crystal faces.

### Chapter 3. Gamma-detection module design



**Figure 3.22:** Model blocks for the custom simulator implemented: the geometrical and physical parameters of the gamma camera are firstly defined, then the irradiation profile is designed and the gamma interactions are simulated. A third block provides the optical model for scintillation light collection into the crystal. Finally, a block model based on the error propagation from the previous section is implemented to simulate the fluctuations introduced by the electronic readout.

#### Irradiation Montecarlo simulation

A following GUI permits to apply a specific irradiation profile to a gamma-camera model previously created. The user selects a radioactive source from a list linked to the NIST database for retrieving the information on the peaks of emission. The geometrical distribution of the source is drawn typ-



### 3.2. Design tools

ically on the crystal face which is opposite to the photodetectors array (but also other entrances can be chosen) and is supported by geometrical patterns that the user can select and regulate. The number of events ( $N_{Events}$ ) to be processed has to be defined here.

When this information are given, the simulator randomly generates a set of data for each gamma interaction: for every event coordinates of interaction and energy absorbed. The absorption of the radiation in the crystal is simulated through a GEANT4 based model that considers the properties of the scintillator and includes physical processes such as photoelectric absorption, Compton effect, Pairs production and so on.

#### Optical models for light collection simulation

A second elaboration is performed by the algorithm block that implements the optical models for the light transport. The software takes as input the coordinates of interaction and the energy associated to each gamma event and gives as output the amount of optical photons collected on the active area of each photodetector. The model works on a single-photon-tracking principle: the path of each scintillation photon in to the crystal is computed from the interaction up to the absorption or lost of the photon. Given one gamma event, the amount of scintillation photons, produced in the interaction coordinates, is randomly generated following a Poisson distribution with mean value  $\langle N_{ph} \rangle = E_{\gamma} \cdot Y_{crystal}$  (yield of the scintillator).

Each photon generated is associated to a coordinate that identifies its position and to a vector that defines the direction of propagation. The initial values for the vectors are randomly generated in such a way to simulate an isotropic expansion of the light bundle.

The trajectory of each single photon is computed until one of the following stop conditions is satisfied:

- the photon is self-absorbed by the crystal.
- the photon is transmitted outside the simulated domain. In this case is considered as absorbed by external coverings or more generally lost.
- the photon collides onto the photodetection plane (either on active or dead area).

Self-absorption in CsI(Tl) is quite a unlikely event and it is modeled through a distance threshold  $SA_{th}$  expressed in [mm]. The cumulative path of the photon is monitored, while bouncing from the crystal faces for reflection; once the cumulative path overcomes  $SA_{th}$ , the photon is automatically

### Chapter 3. Gamma-detection module design

removed and considered self-absorbed. The  $SA_{th}$  parameter is useful also to speed up the algorithm in case of photons stuck in reflective loops.

A key element to determine the entire photon path is the optical model at the interface: when the photon reaches the boundaries of the crystal, the different electromagnetic properties of the external media surrounding the scintillator has the effect to deviate the radiation path. Such a class of phenomena is well described by the optic laws and includes light reflection and transmission at the interface.

The optical model implemented in the custom simulator takes inspiration from the UNIFIED model described by Levin and Moisan [109]: the two media interface is modeled as a rough surface by considering it composed by a multitude of *micro-facets*, or, better, microscopic plain surfaces with a normal vector  $\mathbf{N}'$  forming an angle  $\alpha$  with the overall surface normal  $\mathbf{N}$ . To emulate the random behavior of a rough surface, the  $\alpha$  value of the micro-facets follows a Gaussian distribution with null mean and standard deviation equal to  $\sigma$ . When the photon collides on the interface (on a micro-facet with normal  $\mathbf{N}'$ ) it can be reflected or transmitted into the other material, depending on the refractive indexes of the interface media. The probability of reflection and transmission are governed by the Fresnell equations and also depend on the photon incidence angle on the micro-facet:

$$T = 1 - R \quad (3.20a)$$

$$R = \frac{R_s + R_p}{2} \quad (3.20b)$$

$$R_s = \left[ \frac{\sin(\theta_t - \theta_i)}{\sin(\theta_t + \theta_i)} \right]^2 \quad (3.20c)$$

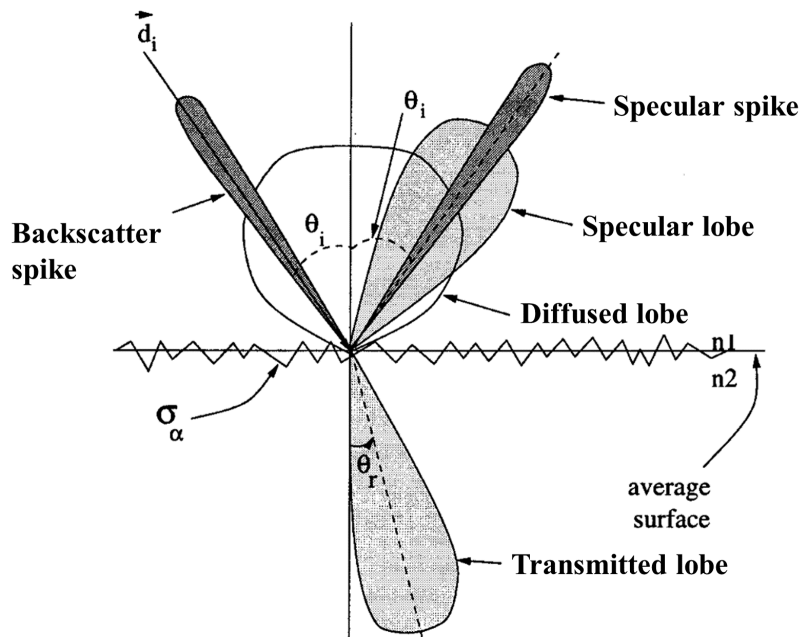
$$R_p = \left[ \frac{\tan(\theta_t - \theta_i)}{\tan(\theta_t + \theta_i)} \right]^2 \quad (3.20d)$$

where  $T$  and  $R$  are respectively the refraction and reflection probability for unpolarized light;  $R_s$  is the s-polarazide (electric field of the radiation perpendicular to the plane of incidence) reflection probability and  $R_p$  is the p-polarazide (magnetic field of the radiation perpendicular to the plane of incidence) reflection probability. The angle of transmission  $\theta_t$  is calculated knowing the angle of incidence  $\theta_i$  through the Snell law:

$$n_1 \sin(\theta_i) = n_2 \sin(\theta_t) \quad (3.21)$$

### 3.2. Design tools

with  $n_1$  and  $n_2$  respectively the refractive indexes of the material of photon origin and of the second material at the interface.



**Figure 3.23:** Polar plot of the radiant intensity in the UNIFIED model for the description of light reflection/refraction at the interface between two optical media. The different components of the total reflection and transmission are underlined. [109]

The refraction in the UNIFIED model is considered with respect to the normal  $\mathbf{N}'$  to the micro-facet. On the other hand, when reflection occurs, four optional behaviors are modeled (Figure 3.23) and can be tuned by defining their four correlated coefficients:

1. **Specular lobe** - the photon is reflected with an angle  $\theta_r = \theta_i$  and with respect to the normal  $\mathbf{N}'$  to the micro-facet.
2. **Specular spike** - the photon is reflected with an angle  $\theta_r = \theta_i$  and with respect to the normal  $\mathbf{N}$  to the average surface.
3. **Backscatter spike** - the photon is reflected backward with respect to the direction of incidence.

### Chapter 3. Gamma-detection module design

---

4. *Diffuse lobe* - the photon is reflected following a pure Lambertian distribution.

The reflection behavior of every surface can be modeled by means of a linear combination of these four contributes [110], even if an accurate tuning can be performed only through a specialized and sophisticated setup [111].

All the crystal faces implement the UNIFIED model. The faces that are not coupled to the photodetectors matrix are considered to have up to 2 interfaces for a maximum of 3 optical materials: the first one is the crystal itself (the most internal one), while the third is considered as the coating material (the external one). In the middle, a coupling material is considered, which is typically air or some kind of glue for crystal/coating adherence. Because of the difficulty to define the UNIFIED parameters for two interfaces, the second one between air and coating material is defined by the user by selecting either specular reflection or pure Lambertian diffusion and by fixing a value for the reflectivity parameter. The photons that are transmitted into the most external material are considered lost.

A limit of the current optical simulator is that it does not consider the contribute due to the coupling material between the crystal and the detector: the different refractive indexes between the interfaces can produce internal reflections. The dead areas could give contribute to this reflections, while in the case of the present simulator, every photon that collides on dead surface is considered absorbed and lost. The thickness of the coupling material can contribute to light divergence or convergence, depending on the refractive indexes. All these phenomena are neglected. The assumption made is that a very thin layer of coupling material (say 100  $\mu\text{m}$ ) like the one employed in INSERT (see section 3.3.1) it should not introduce a significant light dispersion.

In order to consider the transmission through the optical glue (or grease) and then through the optical resin covering the photodetectors array, an equivalent refractive index is calculated:  $T_{12}$  and  $T_{23}$  are the transmission probability respectively from the crystal to the optical glue and from the optical glue and the photodetector resin; then the overall transmission  $T_{13} = T_{12} \cdot T_{23}$ . The transmission factors can be easily calculated through equation 3.20a and considering  $\theta_t = \theta_i = 90^\circ$ , for which  $T_{12} = 1 - (n_1 - n_2)/(n_1 + n_2)$ , and so on. From this is possible to calculate the equivalent refractive index  $n_x$  for the description of the overall transmission  $T_{13}$ :

### 3.2. Design tools

$$n_x = \frac{n_1 \cdot T_{13}}{2 - T_{13}} \quad (3.22)$$

with  $n_1$  being the crystal refractive index.

The photons that stop on the detection plane are assigned to each single detector (or channel) depending on their coordinates of collision. All the photons ended on the dead areas are considered lost.

The percentage of the mean number of collected photons with respect to the generated ones is the simulated collection efficiency  $\eta_{coll}$ .

#### Signal elaboration

The last block of the simulator filters the number of photons collected on each channel considering all the main phenomena connected with photon-electron conversion and signal elaboration. The process considered in the filter block are:

- The **intrinsic resolution** of the scintillator, since its contribute on the scintillation light is not taken into account in the optical simulator. It is implemented by adding a random number of photons to each event (the photons are distributed on the channels proportionally to the percentage of light on the channel on the specific event). The number of photons to add follows a Gaussian distribution with mean equal to zero and standard deviation equal to  $(R_{int}/2.36) \langle N_{ph} \eta_{coll} \rangle$ .
- The **conversion efficiency** of the photodetector (the PDE for the SiPM). The amount of photons on every channel, per every event is reduced considering a binomial distribution with probability of success equal to QE (the PDE in the case of SiPMs).
- The **fluctuation on the multiplication process**. In the case of the SiPM it is derived by the ENF factor. As like for the intrinsic resolution, it is implemented by adding a random number of photon following a Gaussian distribution. The mean value for the distribution is zero, while the standard deviation is equal to  $\sqrt{ENF} \langle N_{ph} \eta_{coll} PDE \rangle$ .
- The overall **noise on signal**: practically the ENC overlapped to the photoelectron signal. The simulator takes into account of it by adding a normal distributed noise over the signal. The standard deviation for the distribution is equal to the ENC over the whole photodetector array  $(ENC \cdot \sqrt{N_{SiPM}})$ .

### Chapter 3. Gamma-detection module design

---

- The signal reduction given by **incomplete charge collection**. It is due to the ballistic deficit and it is related to the scintillator decay constant, to the collection time function of the photodetector and to the filter shape and shaping time. To simplify the filtering, the number of photoelectrons after ballistic deficit reduction are calculated through the application of a binomial distribution, with probability of success equal to  $(1-BD)$ .

The output data are now ready for the analysis, image reconstruction with the methods described in chapter 4 and eventually compared with experimental results.

### 3.3. Detection module design

### 3.3 Detection module design

In the present section, the design and development of the INSERT gamma-detection module is presented, with a summary of the analysis of the various components and the motivations that have brought to the final concept. The discussion explores the following points:

- Analysis of the scintillator to employ.
- Crystal wrapping and optical coupling media.
- Selection of the photodetector: comparison of SiPM and SDD solution and design of the photodetector array.
- Readout electronics and acquisition protocol
- Structure of the detection module and cooling strategy.
- Compatibility issues and strategies.

For what concerns the design of the crystal and the photodetector array, they are discussed separately for convenience' sake. However their optimizations are correlated and the decisions taken on the first influence the design of the second and vice versa. Typically, the other components or characteristics of the gamma-camera are designed following the choices taken on the crystal and on the detection matrix.

#### 3.3.1 Crystal design

The election of an optimal scintillator is a non-trivial problem since most of the output performance of the gamma-detector depends on the crystal properties and usually the maximization of one characteristic produces a deficit in another ones. The most important aspect to choose has been the scintillator composition, since it defines many of the chief properties.

#### Material comparison

As main strategy, the CsI(Tl) crystal has been elected as baseline for the project, then other possible materials have been compared with it to assess if one of those could bring to some kind of advantage. CsI(Tl) choice is related to the scientific history and experience of the Politecnico di Milano laboratory: the studies and development of a CsI(Tl) and SDD based gamma-camera for nuclear medicine (HICAM [32]) has provided a robust

### Chapter 3. Gamma-detection module design

---

base for the INSERT module development.

The CsI(Tl) is a bright scintillator with a peak wavelength around the green range of the visible spectrum ( $\approx 540$  nm) and a moderate density value ( $4.51$  g/cm<sup>3</sup>). Unfortunately is a rather slow scintillator, with two decay time constants ( $\tau_1 = 680$  ns,  $\tau_2 = 3.34$   $\mu$ s at room temperature) and there is evidence that the temporal distribution function of the scintillation photons delays with temperature cooling [112, 113]. The crystal is slightly hygroscopic, then a dry environment has to be provided during operations, however it does not require any encapsulation.

The yield of the scintillator is a key parameter since it defines the brightness, in other word the amount of light signal provided by the crystal. An high gamma energy/photons conversion factor is of primary importance in low gamma energy detection (between 100-200 keV) since the number of photons collected influences energy resolution (see equation 3.12), but also helps to improve spatial resolution since the reconstruction algorithms works better with higher SNR values. Optimization of the yield should not let unconscious regarding the necessity to optimize the effective PDE, which requires a good matching between the  $\epsilon(\lambda)$  of the scintillator and the absorption spectrum of the photodetector, and the reduction effect given by ballistic deficit when a slow crystal is chosen.

The crystals compared with the baseline are NaI(Tl) and GAGG(Ce). LaBr<sub>3</sub> and SrI<sub>2</sub>(Eu) were also considered in the comparison analysis for their competitive characteristics and because of encouraging results reported in literature [114]. Nevertheless they were discarded considering the economic effort required to fulfill the entire clinical SPECT.

**NaI(Tl)** (Sodium Iodide) is the most extensively used scintillator material in nuclear medicine. It is less bright ( $Y = 38$  ph/keV) and dense ( $3.67$  g/cm<sup>3</sup>) than the CsI(Tl), but presents a faster decay time ( $\tau \approx 20$  ns) then the ballistic deficit for a system implementing NaI(Tl) is negligible. The lattice is highly hygroscopic and for this reason a protective encapsulation is required. The light transmission is typically provided by a quartz window that introduces a further component of light dispersion in optical coupling. Since no NaI(Tl) crystals were available for experimental comparison with CsI(Tl). Simulated performance were evaluated and compared. Table 3.2 resumes the parameters adopted for the energy resolution evaluation with both CsI(Tl) and NaI(Tl) crystals and briefly describes their definition.



### 3.3. Detection module design

**Table 3.2:** Parameters for energy resolution estimation for two scintillators, CsI(Tl) and NaI(Tl).

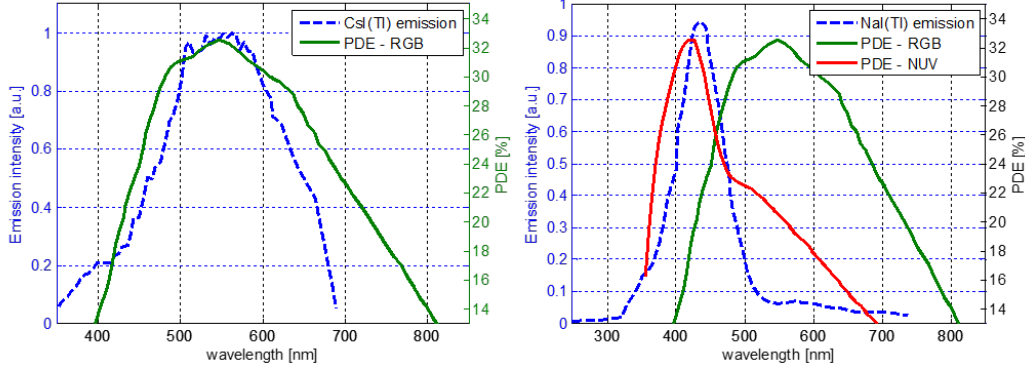
Crystal	CsI(Tl)		NaI(Tl)	
	value	note	value	note
<b>Yield</b>	65	see table 3.1	38	see table 3.1
<b>Eff. Coll.</b> ( $\eta_{coll}$ )		80 %		from optical simulation (dead areas are considered)
<b>QE (PDE)</b>	28.9 %	see eq. 3.17	27.1 %	see eq. 3.17
<b>ENC</b>	68 e <sup>-</sup>	gated integrator filter $\tau_{sh} = 10 \mu s$	26 e <sup>-</sup>	gated integrator filter $\tau_{sh} = 1.5 \mu s$
<b>BD</b>	2.37 %	""	0 %	""
<b>R<sub>int</sub> (at 140 keV)</b>	6 %	[115]	5 %	[116]

The  $\eta_{coll}$  is practically identical for both the crystals, considering an optical simulated collection (obtained through Montecarlo simulations. See section 3.2.2). This parameter also consider the light lost due to dead areas. Effective QE is calculated as described for equation 3.17: considering a photodetection matrix populated with SiPMs. The SiPM coupled to CsI(Tl) is an RGB (FBK, Trento), with  $\lambda_{max} = 540$  nm; on the other side, NUV SiPMs (FBK, Trento), with  $\lambda_{max} = 400$  nm, have been considered for the NaI(Tl). The ENF for both the SiPM technologies is set to 1.2 (from manufacturer). More detail over these SiPM technologies is going to be given later in the discussion on the SiPM array design.

The reason for coupling different SiPM technologies to different crystal is clearly understandable from Figure 3.24: the emission spectrum for distinct scintillator need to be overlapped as much as possible with the light absorption peak from the photodetector. Since CsI(Tl) and NaI(Tl) exhibit different emission centroids, specific and suited detectors need to be coupled.

For the calculation of the ENC (electronic noise) the same DCR has been considered (100 kHz/mm<sup>2</sup>), for a surface of approximately 50 mm × 50 mm. For the calculation of both ENC and Ballistic Deficit (BD), the signal is considered to be filtered by a gated integrator with different shaping times for the two crystals, mainly to respect the different scintillation decay times and reduce BD. The gated integrator has been chosen because an advanced version of the INSERT module electronics should implement this typology of filter and the simulation was intended to give a projection on the very last outcomes in term of energy resolution. All the parameters

### Chapter 3. Gamma-detection module design



**Figure 3.24:** (left) Emission spectrum of the CsI(Tl) compared with the PDE( $\lambda$ ) for the RGB SiPMs (green line). (right) Emission spectrum of the NaI(Tl) compared with the PDE( $\lambda$ ) for both the RGB SiPMs (green line) the NUV one (red line). The latter is more suited for NaI(Tl) because it better matches the emission curve.

**Table 3.3:** Energy resolution (and its components) estimated for CsI(Tl) and NaI(Tl) configurations.

	CsI(Tl)	NaI(Tl)
$R_{int}$	6 %	5 %
$R_{stat}$	5.62 %	7.59 %
$R_{noise}$	7.79 %	5.31 %
$R_{tot}$	11.33 %	10.53 %

have been tuned in order to consider a configuration cooled at 0 °C for dark count reduction.

The parameters from the two configurations have been elaborated through equation 3.19 and produced the results in table 3.3.

The CsI(Tl) crystal is brighter than the NaI(Tl) and this is directly reflected in the better statistical component for the resolution. However, the long scintillation decay of the former requires a longer shaping time, with consequently more noise collected and this aspect is directly observable from the noise contribution comparison. The expected energy resolution of the NaI(Tl) is just slightly inferior to that calculated for CsI(Tl).

Since the performance difference for the two options was quite negligible, the baseline configuration (with CsI(Tl)) was preferred for practical reason, for example NaI(Tl) is hygroscopic, then manufacturing and conservation

### 3.3. Detection module design

of the scintillator is more complex and expensive. Moreover, the CsI(Tl) offers a better density value, which is desirable for improve the gamma detection efficiency (then count rate).



**Figure 3.25:**  $Gd_3Al_2Ga_3O_{12}$  (GAGG(Ce)) scintillator block from Furokawa, Japan. [117]

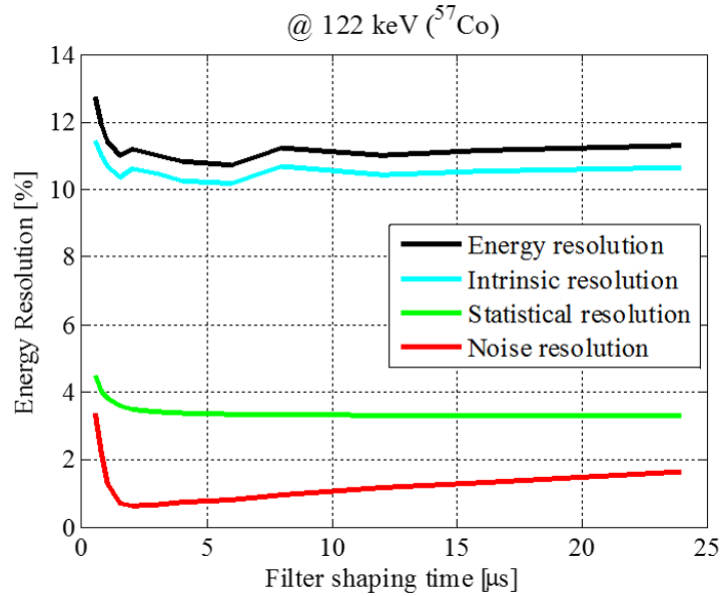
**GAGG(Ce)** ( $Gd_3Al_2Ga_3O_{12}$ ) is a Gadolinium based scintillator (Figure 3.25) from Furokawa (Japan) with good performance in terms of brightness and density (see table 3.1). It is not hygroscopic and it also present a scintillation decay time better than in the CsI(Tl) case. Nevertheless, measurements with a GAGG(Ce) crystal have underlined that the intrinsic resolution at low energies represents a limiting factor for this material. A value around 9-10 % at 140 keV for GAGG(Ce) intrinsic resolution is typically reported in literature [118]. We repeated the measurement irradiating with  $^{57}Co$  (122 keV) a cylindrical (diameter = 8 mm, height = 8 mm) crystal coupled to a squared 8 mm  $\times$  8mm SDD (FBK, Trento). Considering equation 3.13, it is possible to extrapolate  $R_{int}$  from overall experimental measured energy resolution ( $R_{tot}$ ):

$$R_{int} = \sqrt{R_{tot}^2 - R_{stat}^2 - R_{noise}^2} \quad (3.23)$$

where  $R_{stat}$  and  $R_{noise}$  have been estimated through the knowledge on the signal peak amplitude and on the ENC for the SiPM. The resulting components for the energy resolution obtained at different shaping times is depicted in Figure 3.26.

The value for the GAGG(Ce) intrinsic resolution has been considered a too risky lower limit for energy resolution (the overall resolution for the

### Chapter 3. Gamma-detection module design



**Figure 3.26:** Experimental measured energy resolution (and its component) for a GAGG(Ce) scintillator coupled to an SDD. The intrinsic contribute represents the main limit to energy resolution optimization.

system is required to be around 10-12 %), also considering the high noise contribute to resolution that should be added when the detection array is composed numerous photodetectors, as it is the case for the INSERT module. For this reason, GAGG(Ce) has been discarded.

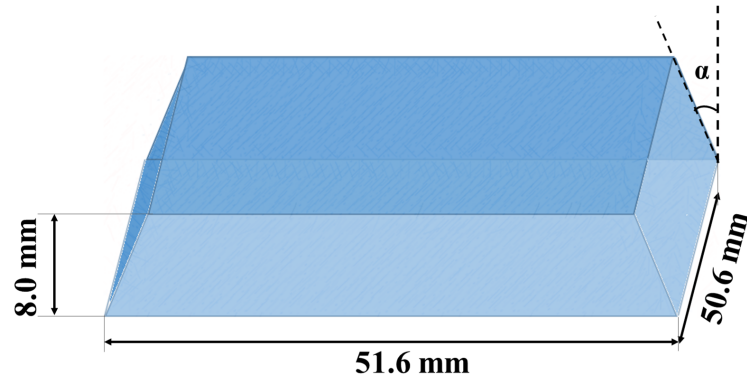
#### Crystal geometry

Crystal is a rectangular faces scintillator with two slanted edges to permit joints to adjacent detectors (Figure 3.27). The XY plane dimensions are related to the requirements for the FOV, then approximately 50 mm × 50 mm for the preclinical and 100 mm × 50 mm for the clinical system. The actual base size for the crystal is defined in order to cover the entire active area of the photodetectors matrix, which is better described in section 3.3.4.

The crystal thickness is a compromise between intrinsic spatial resolution and to the detection efficiency. The discussion regarding the relation between crystal geometry and image quality is described more in detail in section 4.1.

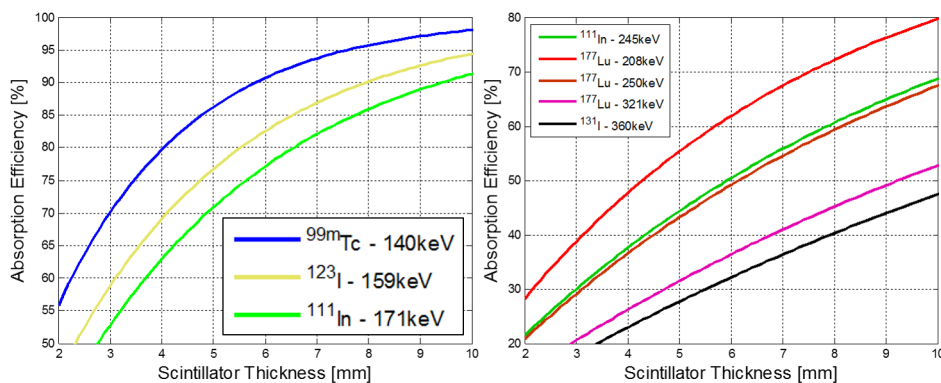
For the INSERT CsI(Tl) scintillator we basically decided to minimize the Z dimension as much as possible, but maintaining a sufficient detection

### 3.3. Detection module design



**Figure 3.27:** Geometrical description and dimensions for the (preclinical) INSERT crystal. The two slanted edges are required to structurally joint together the detectors in a ring shape. The angle  $\alpha$  depends on the number and architecture for the system (for the preclinical configuration, with 10 modules in a closed ring,  $\alpha = 18^\circ$ ).

efficiency value for the  $^{99m}\text{Tc}$  source.



**Figure 3.28:** Absorption probability for different SPECT radioisotopes as function of the crystal ( $\text{CsI(Tl)}$ ) thickness.

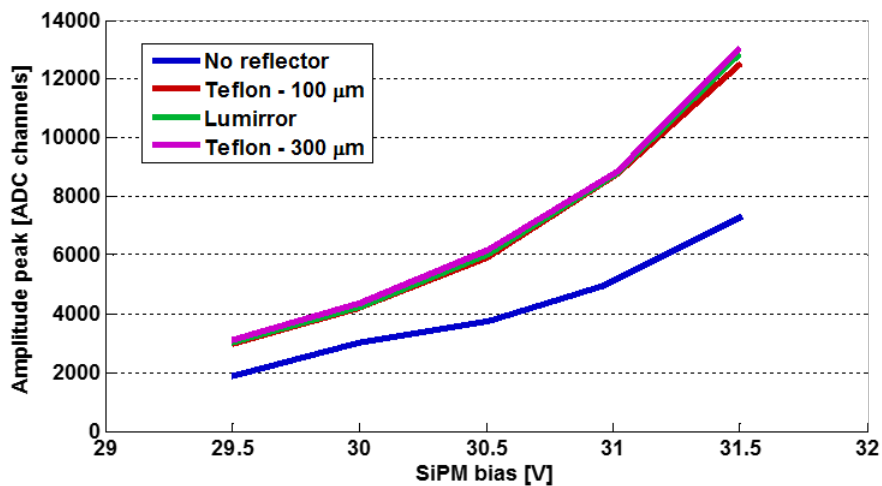
Since more than 95 % of the radiation for Technetium is absorbed in 8 mm of crystal section, this value has been chosen as baseline (Figure 3.28). The surface treatment is another property to consider for the  $\text{CsI(Tl)}$  geometry. Depending on the industrial technique employed, the smoothness of the surface can be described as *polished* or *rough*. Typically, the  $\text{CsI(Tl)}$  composition does not permit to obtain a perfectly polished crystal, however the term rough is generally used only for crystal with a very poor mechanic finish. Polished are more suited for imaging systems, since the light paths

### Chapter 3. Gamma-detection module design

maintain an high level of space coherency. It is noteworthy also that few studies demonstrated that polished CsI(Tl) crystal permits higher light collection [119], while our team experience with bulky CsI(Tl) crystals with different surface treatments brings to the opposite conclusion: rough faces facilitate a more efficient light collection [120]. Nevertheless, we decided to favor an imaging inclined solution, then the baseline treatment for the INSERT crystal is polished.

#### 3.3.2 Crystal wrapping and optical coupling media

Light collection efficiency is enhanced with the wrapping of the scintillator with 4-5 layers of Teflon: above all the material for crystal coating, Teflon layers exhibit one of the best value in terms of light reflectivity (around 94 %) [76,110,121]. We also performed simple light collection measurements by changing coatings to a 25 mm × 25 mm × 4 mm CsI(Tl) coupled to a matrix of 6 × 6 SiPMs (4 mm × 4 mm active area). Figure 3.29 depicts the light output for four configurations of crystal coating: the first one, no reflector, produces the lowest signal. Lumirror (Toray, Japan) is a thin diffusive material with high reflectivity. The Teflon performance are slightly better than Lumirror ones also depending on the number of layers applied.



**Figure 3.29:** Channel peak for four different coating strategies and as function of the SiPM array biasing. The reflector have been wrapped around a 25 mm × 25 mm × 4 mm CsI(Tl) crystal.

Teflon’s reflectivity benefits  $\eta_{coll}$  (collection efficiency), but, at the contrary, the diffusive behavior of such a material reduces the grade of light

### 3.3. Detection module design

distribution coherence with respect to the gamma interaction point. No studies have been completed yet to verify the light collection behavior when reflector is not applied on the lateral edges of the scintillator.

Optical coupling is provided through a transparent mounting media similar to a resin (Meltmount, Cargille). It is provided with different refractive indexes, namely 1.539, 1.605, 1.662 and 1.704. Considering the CsI(Tl) refractive index ( $n_{CsI} = 1.80$ ) and the one from the optical resin that covers the SiPM employed ( $n_{op.res.} = 1.51$ ), in order to protect them, the best matching media coupling the two components is found through equation 3.4. The optimal geometrical mean for the resin would be 1.649. Thus the first choice fell on Meltmount 1.662, since it is the most proximal in value. Unfortunately, the different resin presented quite variable viscosity behavior: 1.662 it is structurally hard, which represent a benefit for mechanical rigidity, but it is difficult to be handle and, in the deposition phase, bubbles generation is practically unavoidable and undesired; 1.605 and 1.704, at the contrary, have proven to be too melted and did not provide an adequate crystal stability on the SiPM matrix. For this reason, Meltmount 1.539 has been adopted.

#### 3.3.3 Photodetector selection

The earliest step in the design of the INSERT module demanded the resolution of a crucial aspect, that is the selection of the optimal photodetector. Our laboratory expertise towards Silicon Drift Detectors (SDDs), together with the related hardware platforms from previous projects, has provided a pole position for this technology in the list of considered detectors. On a parallel trail, the Silicon PhotoMultiplier (SiPM) is a relatively new technology, with a promising innovation range in the future years. Many works, cited in the first chapter and in section 3.1.3, have proven the validity of implementing SiPM in high magnetic fields, in PET inserts for MR scanners and other works of the last years reports the development of SPECT system employing SiPMs.

The present section will cover the main analysis performed in order to compare the two photodetectors, make an hypothesis on the possible outcome from a gamma-camera implementing either SDDs or SiPMs and finally discuss the reasons for the SiPM choice. Table 3.4 summarizes the main characteristic of the two kind of photodetectors, with their significant properties and their drawbacks.

On one side, SDD provide better QE, which is fundamental to retrieve

### Chapter 3. Gamma-detection module design

**Table 3.4:** *Characteristics comparison between SDD and SiPM.*

	<b>SDD</b>	<b>SiPM</b>
<b>Quantum Efficiency</b>	>80 %	(PDE) <30 %
<b>Multiplication</b>	1	$\approx 10^6$
<b>Excess Noise Factor</b>	1	1.1 - 1.6
<b>Leakage current</b>	0.4-2 nA/cm <sup>2</sup>	3-10 pA/cm <sup>2</sup>
<b>Electronic Frontend</b>	Yes (near SDD)	No
<b>Electronic Readout</b>	Complex (semigaussian)	Simple (RC or gated integrator)
<b>Cooling</b>	Moderate (-20 °C)	Soft (0-5 °C)

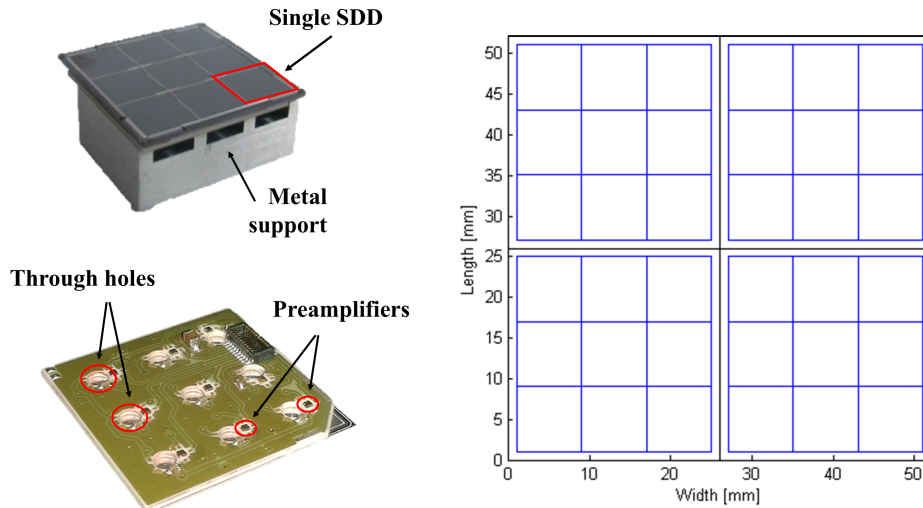
a strong light signal. Moreover the absence of multiplication factor brings to a null fluctuation due to internal gain. On the other side, SiPMs have internal multiplication (and related excess noise factor as drawback) which benefits many aspects: the only electronic noise that influences the SNR in SiPM is the dark current of the device itself, then there is no necessity for electronic frontend to minimize the contributes to noise from the electronic components. In addition the filter block can be designed maintaining a relatively low level of simplicity (RC filter or Gated Integrator filter). The SDD frontend, at the contrary, is required to be as proximal as possible to the device in order to minimize parasitic capacitance. The lower leakage current density of the SiPM brings to the conclusion that cooling for noise reduction can be softer than in SDD case, where usually the system is chilled to temperature of approximately -20 °C.

The SDDs considered for INSERT are 8 mm × 8 mm (active area) square detectors, organized in a monolithic 3 × 3 matrix depicted in Figure 3.30 (FBK, Trento).

The overall surface is 26 mm × 26 mm and is couple to a FR4 board with one through-hole in correspondence of each detector collecting anode. A preamplifier ASIC is mounted near each hole and a wire bonding provides short connection between the SDD anode and the electronic frontend input. The FOV required is covered by joining side by side 4 matrices in a 2 × 2 geometry, for a total of 36 electronic channels.



### 3.3. Detection module design

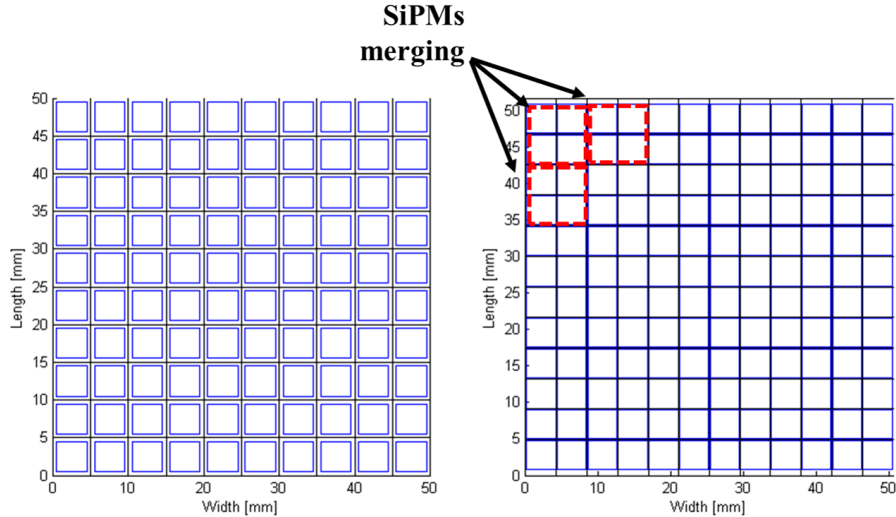


**Figure 3.30:** SDD matrix employed for the photodetectors comparison: (top-left) top view of a  $3 \times 3$  array of  $8 \text{ mm} \times 8 \text{ mm}$  square SDDs (FBK, Trento); (bottom-left) bottom side of the SDD array, with the preamplifiers positioned as close as possible to each SDD anode. (right) Simulated geometry of the overall matrix covering the FOV for the preclinical gamma-detection module.

The SiPM unit considered for the array is a  $4 \text{ mm} \times 4 \text{ mm}$  RGB (FBK, Trento). RGB is a technology that defines a class of SiPMs with the absorption spectrum range centered around  $540 \text{ nm}$ , as depicted previously in Figure 3.24. The choice for this kind of device is related to the baseline crystal, the CsI(Tl), emission spectrum. The RGB SiPM is composed by 9340 microcells, with an active area of  $40 \mu\text{m} \times 40 \mu\text{m}$  each. The single microcell fill factor (FF) is approximately 60 %. The PDE range is approximately 20-30 % and effective PDE when coupled to CsI(Tl) has been estimated around 29 % at 3 V overvoltage ( $V_{OV}$ ). The DCR is inferior to  $200 \text{ kHz/mm}^2$  at room temperature ( $+20 \text{ }^\circ\text{C}$ ).

The SDD/SiPM comparison required a preliminary definition of the SiPM array, which was initially designed as depicted in Figure 3.31 (left), with  $10 \times 10$  SiPMs populating a square array, with 1 mm of dead space between adjacent detectors. The first solution needed an optimization of the detection surface, since the dead area reached the 36 % of the overall surface and tremendously affecting light collection. In collaboration with Fondazione Bruno Kesler (FKB), we designed and optimized the array geometry, reducing the death space to only 11.8 % (Figure 3.31 - right). The new geometry

### Chapter 3. Gamma-detection module design



**Figure 3.31:** Top view of the simulated SiPM arrays considered for the comparison with the SDD: (left) original geometry with single SiPM aligned with 1 mm of dead area between each detector (conservative design); (right) novel approach with single SiPMs aligned on a common host board and with reduced dead area (see section 3.3.4). Because of the necessity to reduce the electronics complexity, the number of readout channel has been reduced by merging the output signal from groups of  $2 \times 2$  neighbor SiPMs (red square).

is composed by  $12 \times 12$  SiPMs. In order to reduce the number of readout channels, thus the electronics complexity, the SiPM outputs have been merged in groups of 4 neighbor elements ( $2 \times 2$ ), creating virtual detection areas for each channel of  $8 \text{ mm} \times 8 \text{ mm}$ , like in the case of SDDs.

The SDD and SiPM array configurations were both evaluated by means of analytical and Montecarlo simulations. The following points list briefly summarizes the simulation parameters adopted:

- **Radioactive source** -  $^{99m}\text{Tc}$ , 140 keV.
- **Scintillator** - CsI(Tl), rectangular shape ( $52 \text{ mm} \times 52 \text{ mm} \times 8 \text{ mm}$  for the SDD array and  $50 \text{ mm} \times 50 \text{ mm} \times 8 \text{ mm}$  for the SiPM array). The crystal surface is considered polished.
- **Crystal coating** - Lambertian, pure diffusive reflection on all the faces that are not optically coupled to the detection matrix. The reflectivity index is set to 94 % [76].

### 3.3. Detection module design

**Table 3.5:** Simulated results for two gamma-cameras implementing either SDDs or SiPMs.

	SDD	SiPM
<i>Analytical model</i>		
<b>Energy resolution</b>	11.7 %	10.4 %
<i>Simulation</i>		
<b>Energy resolution</b>	12.8 %	12.1 %
<b>Intrinsic spatial resolution (center of FOV)</b>	0.80 mm	0.85 mm
<b>CFOV (&lt;1 mm FWHM)</b>	40 mm × 40 mm	

- **Optical coupling** - A value of  $n = 1.515$  is considered for the material at the interface with the optically coupled crystal surface.

The overall collection efficiency  $\eta_{coll}$  for these preliminary simulations was found to be around 80 % (also considering dead areas). For the shaping filter a gated integrator with  $\tau_{shaping} = 8 \mu s$  has been adopted. Regarding the procedure for energy and spatial resolution retrieval, the reader can refer to a detailed description in chapter 5. Table 3.5 reports the final results obtained from the simulation performed: the outcome was analyzed to finalize a decision over the INSERT photodetector to adopt.

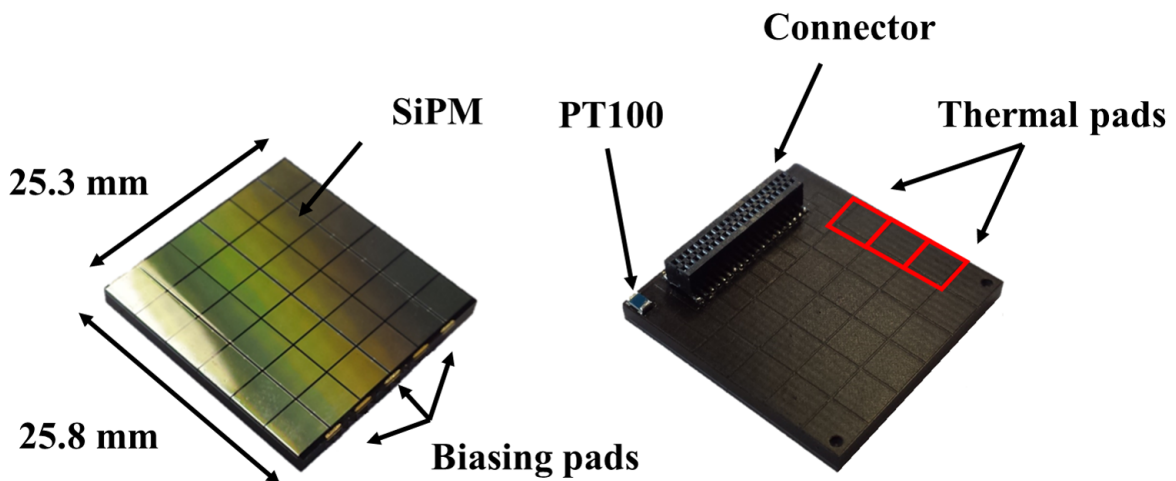
The expected performance from SDD and SiPM arrays are considerably similar, both for spatial and energy resolution. The choice for the photodetector to implement has been then translated to a more practical level of considerations: SiPM devices were finally elected for the following technical reasons:

- **Cooling** - SiPMs require a moderate cooling with respect to SDD that should be chilled to at least  $-20 \text{ }^\circ\text{C}$  to reach an adequate SNR. As experienced along the project development, the technical implementation of a cooling strategy presents many challenging aspect, like liquid leakages, fluid pumping and distribution, cooling uniformity and so on. The main trend is that the cooler the temperature to be reached, the more complex the cooling system to be implemented.
- **Robustness** - SiPM arrays are, by direct experience, more robust and less fragile than the SDD ones.

### Chapter 3. Gamma-detection module design

- **Expectancy of technological improvements** - The SiPM is a relatively new technology, with applications that goes far beyond implementation in scintillation gamma detector for nuclear medicine. A trend of performance development was expected for this devices during the same period of occurrence of the INSERT project. Indeed, the initial baseline for the SiPM were the mentioned RGB technology. In the present time a new family of devices under the name of RGB-HD is under production from FBK. The RGB-HD present lower DCR at room temperature and higher PDE value, thanks to a redesign of the SiPM microcell that allowed to increase the internal fill factor.

#### 3.3.4 SiPMs array design

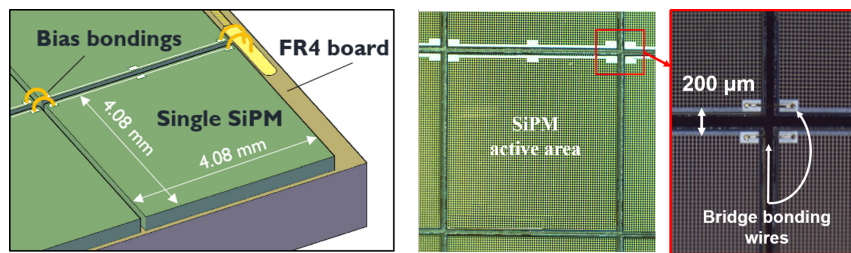


**Figure 3.32:** *SiPMs tile. top (left) and bottom (view) of the  $6 \times 6$  SiPMs array mounted on a 1.6 mm thick FR4 board. On the bottom side, 36 thermal metal pads are covered with a thin layer of black insulator.*

The present section describes the basic unit of the SiPM preclinical and clinical array: the *SiPM tile*. The SiPM tile (Figure 3.32) is composed by  $6 \times 6$  single RGB SiPMs, mounted on a compact  $25.3 \times 25.8 \times 2.1 \text{ mm}^3$  FR4 board and covered with a  $300 \mu\text{m}$  layer of optical resin ( $n = 1.51$ ) for the protection of the detectors and of the bias bonding wires that connect the cathodes among the top of each SiPM. The wires origin from few pads positioned on one of the lateral edges of the FR4 board, as shown in

### 3.3. Detection module design

Figure 3.33. The current signals from SiPMs are collected independently through the soldering pad below each detector. The tile provides a PT100 sensor (PTS0805, Vishay) soldered on a corner of the FR4 board, for temperature measurement. A 40 pins socket connector (CLE-120-01-G-DV-A, Samtec) on the bottom of the module carries the current signals from individual SiPMs, the resistance value of the PT100 and the biasing voltage for detector polarization.

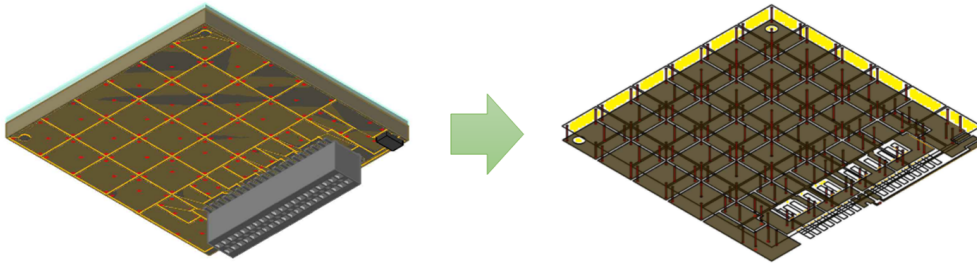


**Figure 3.33:** Details on the SiPMs alignment in the tile structure, over the FR4 board: (left) description of the SiPMs disposition, with the bias pads (yellow) from which the bias bondings origin. The bias is directly carried to all the SiPMs cathodes through bridge bondings between neighbor detectors. (right) The mechanical cut for each SiPM starts 40  $\mu\text{m}$  from the edge microcells, then 120  $\mu\text{m}$  separates adjacent SiPMs (200  $\mu\text{m}$  overall). Courtesy of FBK Trento, Italy.

Three strategies have been adopted in order to keep the dead areas low: a thin bonding routing for the biasing, the precision in the mechanical cut of the wafer and the alignment of the SiPMs. The biasing for all the detectors is provided through a sequence of bridge bondings that connect the cathodes among the top of every SiPM. The bondings origin from five pads positioned on one of the lateral edges of the FR4 board, as shown in Figure 3.33. The current signals from the SiPMs are collected independently through the soldering pad below each detector. Moreover, the precision of the mechanical cut and of the alignment on the FR4 board leads to the an insensitive thickness, between adjacent SiPMs, of only 200  $\mu\text{m}$ . The gamma-ray detection module has an overall area of 25.30 mm  $\times$  25.85 mm, characterized by only the 11.8 % of dead areas. Finally the surface of the module is covered with a thin layer of optical resin for detectors and bondings for mechanical protection.

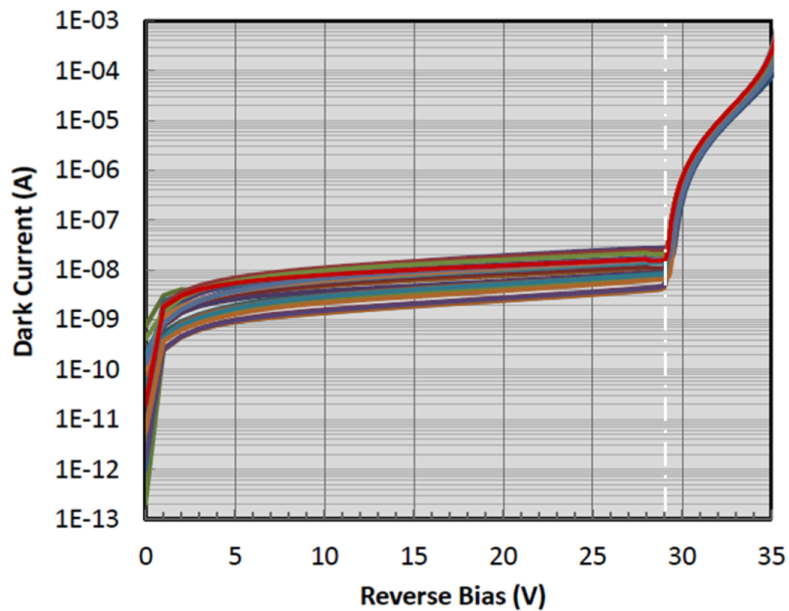
The module design has been optimized also for cooling: the metallic pads, on which the SiPM anodes are soldered, are thermally connected to other metallic pads placed at the bottom of the FR4 board through conductive vias that cross the insulating board material (Figure 3.34). The bottom

### Chapter 3. Gamma-detection module design



**Figure 3.34:** (left) bottom view of the SiPM array. (right) same view: x-ray description of the internal structure of the FR4 board, with the thermal vias (lined with red color) thermally connecting the pads on the top of the board, where the SiPM anodes are soldered, with the thermal pads on the bottom of the board.

side of the board is then covered by a thin layer of electric insulator to avoid short circuits. The thermal pads allow to create a thermal path from the SiPMs to the bottom of the tile unit. An heat sink can then placed below the board to cool down the devices.



**Figure 3.35:** I-V characteristics for 36 single RGB SiPM soldered on a single array. The breakdown voltage is approximately 29 V. Courtesy of FBK Trento, Italy.

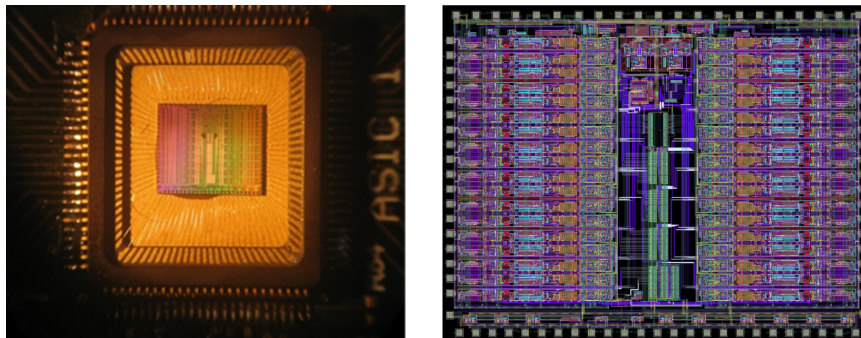


### 3.3. Detection module design

The dark current as function of the reverse bias voltage has been measured for every SiPM of each one of the arrays under test. Figure 3.35 depicts the I-V characteristics of the 36 SiPMs of one array. All the detectors present a breakdown voltage centered on 29 V, with just little variation in the order of few tens of mV. The SiPM array offers high modularity: it can be aligned with other arrays (3-side-tileable) in order to compose larger photo-detector matrices and keeping the overall dead area value low at the same time. The conceptual idea for the tile is then to provide a basic array unit that can populate different crystal surfaces, for example the two different FOV required in the preclinical and clinical INSERT gamma-modules.

#### 3.3.5 Readout electronics

The current signal produced by each SiPMs collectively represent the information related to energy and position of gamma-ray interaction. This information is conveniently elaborated by the electronics, providing an analog signal with an amplitude proportional to the number of photo-electrons collected. The analog values are then digitized by means of ADCs and then transferred to a proper elaboration unit. Reconstruction algorithms (the reader can refer to chapter 4) elaborate the collected data in order to produce a final planar image of the radiotracer distribution acquired by gamma-detection module.

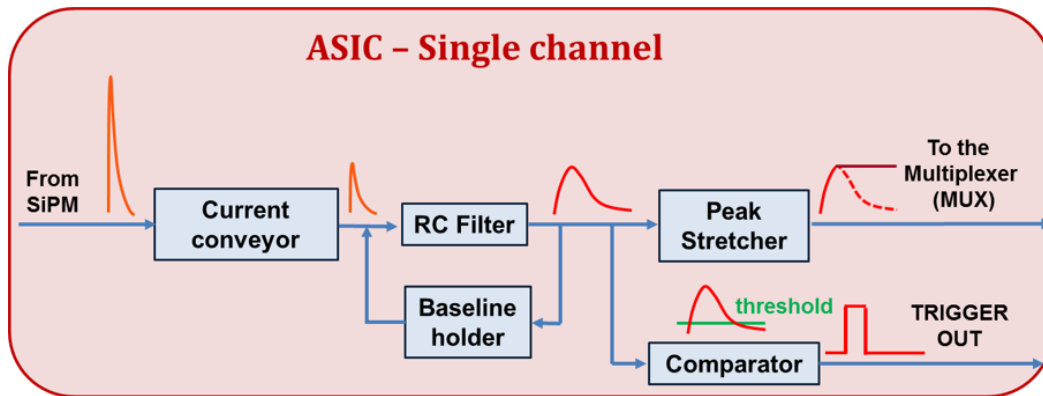


**Figure 3.36:** (left) Top view of a magnified photograph of the “Angus” chip, an 36 channel ASIC implementing a current mode readout with current conveyor and RC filter. (right) layout of the 6.1 mm × 4.9 mm chip, with the 36 readout channels.

The current signal from SiPMs is read by a front-end electronics, implemented into a compact 36-channels ASIC (“Angus”, designed by Paolo Trigilio and depicted in Figure 3.36). Primary attention has been paid into compactness of the chip, considering the high number of channels required

### Chapter 3. Gamma-detection module design

for both the preclinical and clinical instruments, thus VLSI technology has been adopted. The ASIC is mounted on a board (“ASIC board”) described in the next section. Each ASIC channel reads the current signal provided by the sum of four neighbor SiPMs, collectively called *merged channel*, as better described later.



**Figure 3.37:** Diagram of a single readout channel for signal processing in the Angus ASIC.

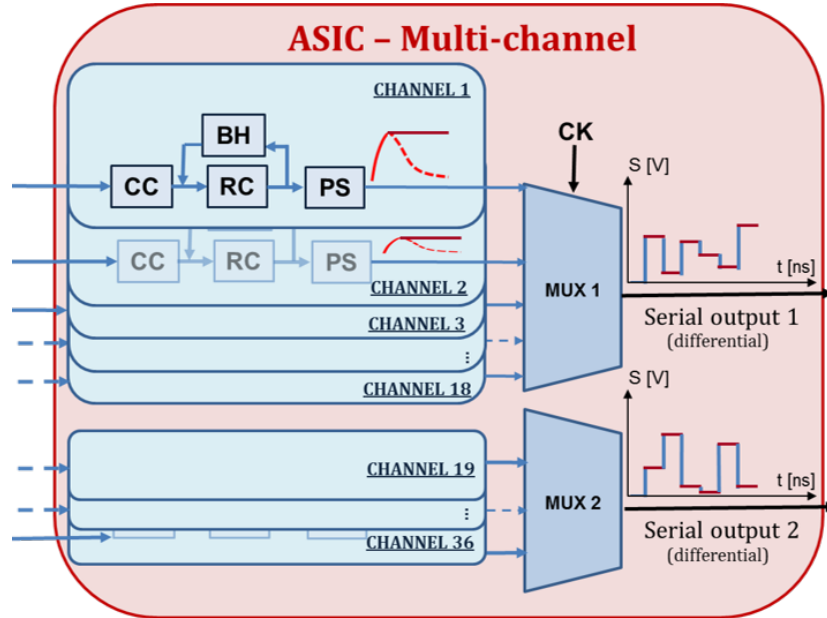
Figure 3.37 shows the conceptual scheme of the single readout channel. The input current signal is buffered and amplified by a current conveyor circuit that provides an approximately null input impedance and is capable to sustain current signal from high capacitance SiPMs ( $>200 \text{ pF/mm}^2$ ) [122]. The signal is then fed to a programmable RC filter (the selectable shaping time are 2.5, 5, 7.5 and  $10 \mu\text{s}$ ) with baseline holder (shaping of the signal is needed to optimize SNR). RC filter was initially selected as baseline for the shaping filter, however an alternative multi-channel ASIC implementing a gated integrator filter with improved SNR performance is under study and development for the final version of the INSERT SPECT systems [123]. The shaped pulse is given to a peak stretcher circuit which holds the maximum pulse value.

The pulse generated by the RC filter is also driven into a comparator that provides an output trigger every time a scintillation event is verified, that is when the pulse overcomes a user defined threshold.

Signals from each channel converge into two independent multiplexers (18 channels per each MUX) that serialize them in a stream of analog values (Figure 3.38). The frequency of the clock (CK), that controls the MUX



### 3.3. Detection module design



**Figure 3.38:** Diagram describing the overall readout strategy for the 36 channels in Angus ASIC: the signal is readout in parallel by the channels and then serialized through two MUX.

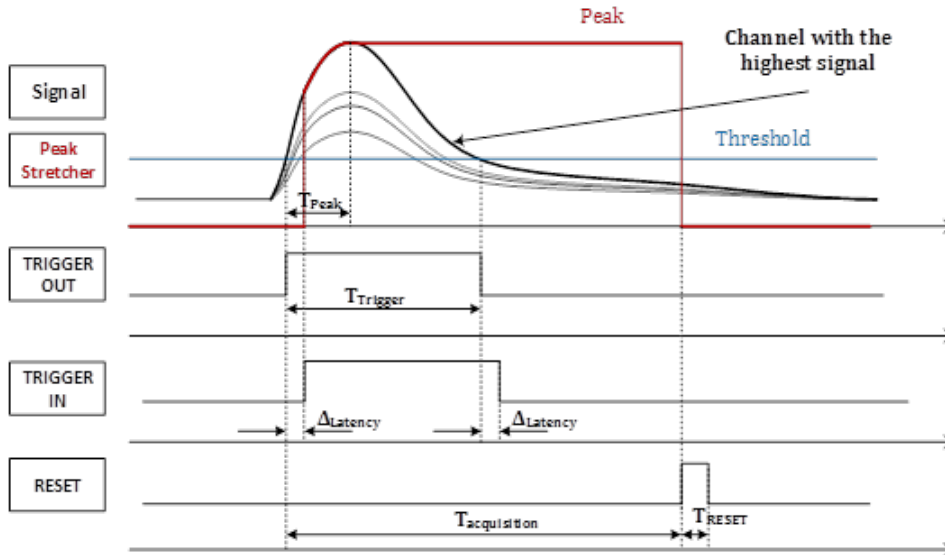
input channel switch, can be regulated by the user among 2.5, 5 or 10 MHz. The streams are finally driven by differential ASIC output buffers.

#### acquisition protocol

The acquisition protocol for one generic gamma event is briefly described in Figure 3.39. The diagram depicts a subset of the 36 signal pulses, outputs from the RC filter and whose amplitude is proportional to the amount of photo-electrons collected by each channel. The channel with the highest signal is also the first one to overcome the comparator threshold, then to fire an output trigger.

This logic signal is sent to a global OR block where the trigger outputs from all the ASIC channel convey (please notice that the OR logic is physically implemented outside the chip in order to provide a global trigger for multiple ASICs in case of clinical system, which requires two ASICs for the readout of all the matrix channels). The OR output is named TRIGGER IN and is a logic signal that enables the peak stretcher block for all the channels. The peak stretchers follow the pulse curve up to the maximum value, then hold it and give it as output to the MUX for parallel-to-serial

### Chapter 3. Gamma-detection module design



**Figure 3.39:** Timeline plot of the fundamental signals involved in single event pulse acquisition. The scintillation event is read by each channel, generating a shaped pulse at the output of each channel RC filter. The pulse with higher amplitude is the first to be detected by the comparator and activate an automatic process for the enabling of the peak stretcher on all the ASIC channels.

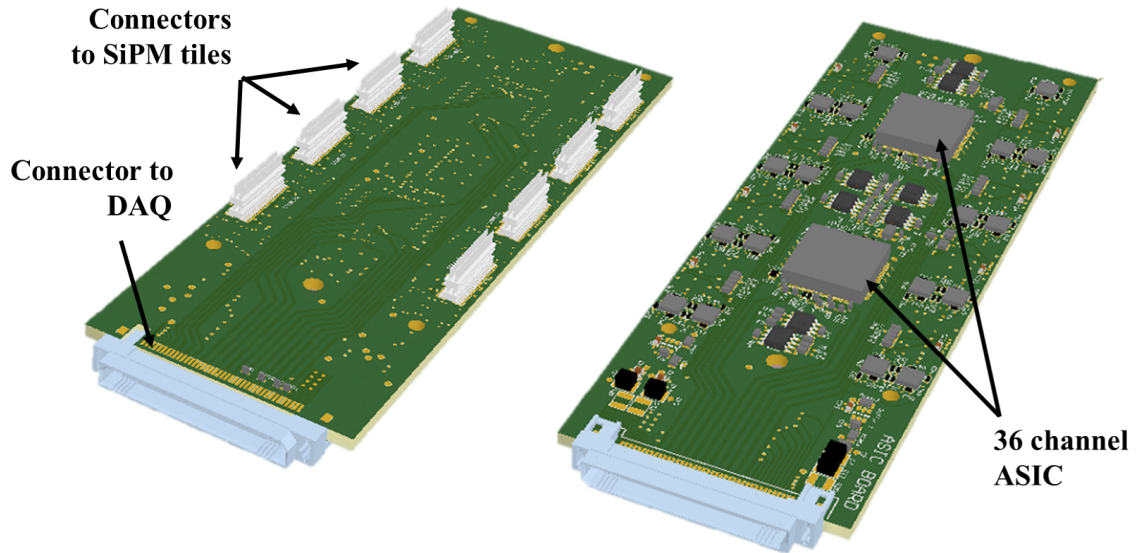
sequencing of the channels analog values. After an adequate time lapse, depending on the MUX switching frequency, a RESET signal is sent to all the peak stretcher to make them return from hold to disabled state.

Analog-to-digital conversion is performed on a separate board (DAQ board) described in the next section. Then the digital data are sent to an elaboration system (PC) and stored in an arrayal form. Then data are fed to a software for energy and image reconstruction (see chapter 4).

#### 3.3.6 Structure of the gamma-detection module and cooling strategy.

The present section describes the ASIC board geometry and functions and completes the depiction of the overall gamma-module, with a particular regard also to the cooling strategy adopted.

### 3.3. Detection module design



**Figure 3.40:** (left) top and (right) bottom view of the INSERT ASIC board.

#### ASIC board

The ASIC board is an FR4 electronic board with dimension  $150 \text{ mm} \times 53 \text{ mm} \times 1.6 \text{ mm}$  (Figure 3.40) and supporting the following functions:

1. from the top side of the board, 8 plug connectors (AW-20-03-G-D-185-115-A, Samtec) allow the mechanical mounting and electrical connection for the SiPM tiles. Only 4 tiles are installed in case of preclinical modules ( $50 \text{ mm} \times 50 \text{ mm}$  FOV), otherwise all the 8 positions are populated in case of clinical modules ( $100 \text{ mm} \times 50 \text{ mm}$  FOV). The ASIC board also provides the power lines for SiPMs biasing.
2. The board offers mechanical support not only to the SiPM tiles and coupled crystal, but also to the heat sink for cooling. Moreover it is the component that provide stability due to mechanical coupling to the SPECT support structure.
3. The board hosts up to a number of 2 ASICs (from which the name *ASIC board*), the integrated electronic chips with 36 channels each one for the SiPMs readout (the reader can refer to section 3.3.5). In case of preclinical system, only 36 channels are required, then one

### Chapter 3. Gamma-detection module design

---

ASIC is mounted or enabled. On the other hand, when the board is converted to clinical usage, both the ASIC are installed and activated.

4. The output lines of 4 ( $2 \times 2$ ) neighbor SiPMs are connected together or *merged* at the ASIC board level, before carrying the signal to the ASIC inputs. The total signal from each merged channel is the sum of the original four and this operation is performed to reduce the order of complexity of the electronic readout. The virtual detector thus created are  $6 \times 6$  with a  $8 \text{ mm} \times 8 \text{ mm}$  active area.
5. Two main ancillary circuits are present on board: 8 independent circuits for the readout of the tile mounted PT100 sensors (Weathstone bridge architecture) and a pulsing circuit that provides controlled current pulses to all the ASIC channel inputs when commanded from the user. The pulsing circuit has been designed for electronic channels equalization.

#### DAQ board

The DAQ board (Figure 3.41, designed in MEDISO, Budapest) is directly connected through a pair of 80 pins connectors (ERF8-ERM8, Samtec) to the ASIC board.

This board supplies power required for the ASIC, the ASIC board and the high voltage for SiPMs biasing.

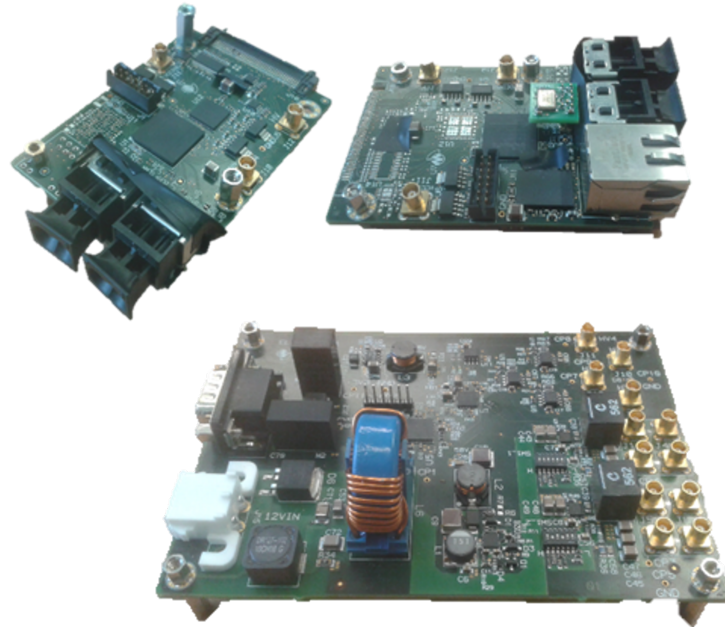
The main tasks of DAQ board are:

1. to configure the ASICs register (e.g. for shaping time or clock frequency definition).
2. collection of the analog data from the ASIC/s and their digitization through ADC.
3. communication with a twin board for data transmission via optical interface.

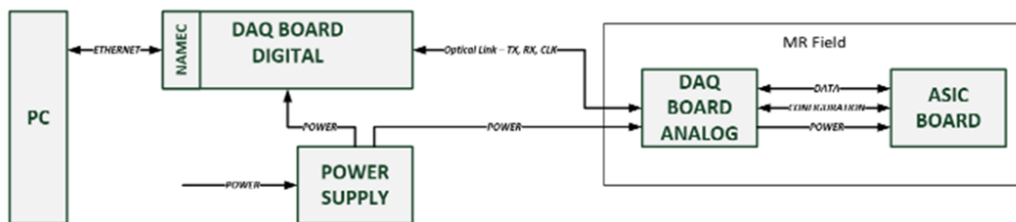
An overall description of the data transmission system and the power supply line for the electronic system is depicted in Figure 3.42. PC for post elaboration and power supplier are physically placed far from the ASIC board, in order to avoid interference with the high MR field where the gamma module should work.

Communication of data and configuration setting is provided through a couple of twin DAQ boards, organized as transceivers and transmitting

### 3.3. Detection module design



**Figure 3.41:** DAQ System: (left) DAQ board, directly connected to the ASIC board, has been designed by MEDISO (Hungary) following magnetic compatibility criteria. (right) gateway board for the optical communication, twin of the DAQ board. (bottom) power supply board, generating the required bias for the SiPMs and the whole system. Courtesy of Mediso Kft., Hungary.



**Figure 3.42:** Data communication and power supply architecture for the single gamma-detection module. The ASIC board is connected to the DAQ board and placed in the MR bore, while the elaboration system (PC) and power supply generator are far away and shielded from magnetic field. Optical fibers and coaxial cables provide the necessary connection between components.

through long optical fibers to avoid signal corruption from the RF coils or the magnetic gradient switching. Power supply is delivered in parallel through shielded coaxial cables.

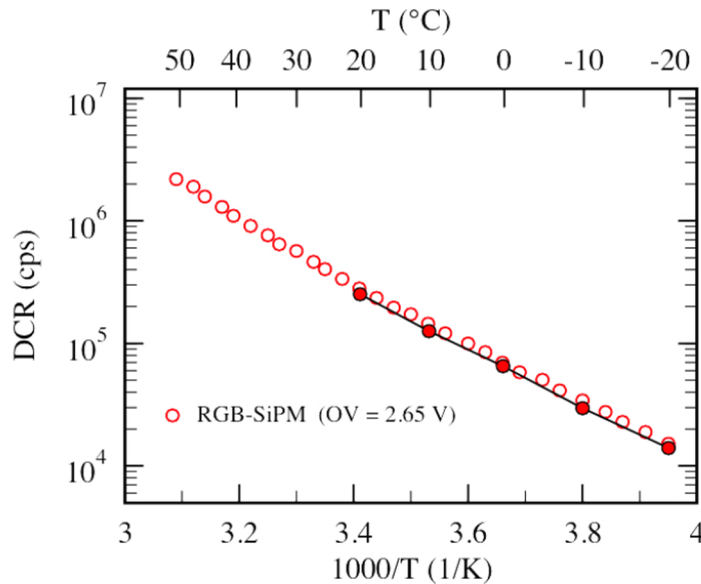
### Chapter 3. Gamma-detection module design

#### Cooling strategy

The key parameter that establishes the SiPMs performances and, as direct consequence, the overall gamma-detection outcomes is temperature. Dark count rate is the main factor for energy resolution degradation and also plays an important role in defecting spatial resolution. Indeed, a imaging system requires a wide detection surface for achieving the FOV requirement, then the overall intrinsic noise from SiPM is dependent on the number of devices populating the matrix. This is reflected in to the fact that the dominant component for energy resolution broadening is the noise contribute. The problem can be visualized in formulas:

$$R_{noise} \propto ENC \cdot \sqrt{N_{SiPM}} \propto \sqrt{DCR(T) \cdot A_{Matrix}} \quad (3.24)$$

Where  $A_{Matrix}$  is the overall active area of the SiPM matrix. DCR is temperature dependent and in RGB detectors its absolute value is halved every  $\Delta T = 8 \text{ }^\circ\text{C}$  of temperature reduction (Figure 3.43).

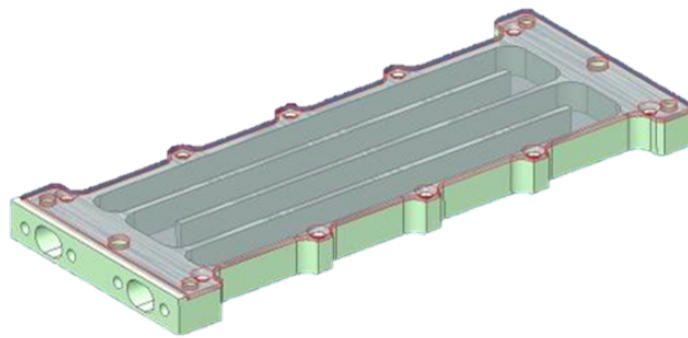


**Figure 3.43:** DAQ System: (Dark Count Rate (DCR) as function of absolute temperature when considering RGB SiPMs (FBK, Trento). DCR is halved approximately every  $\Delta T = 8 \text{ }^\circ\text{C}$  of temperature reduction. Courtesy of FBK Trento, Italy.

### 3.3. Detection module design

Energy resolution variation with absolute temperature has been explored by means of simulated estimations and experimental tests on prototypical detection modules and the results lead to the conclusion that a SiPMs cooling at approximately 0 °C is mandatory for address the spectroscopic requirements.

The cooling strategy is based on the heat extraction from the SiPMs thermal pads on the tile bottom by means of an heat sink (Figure 3.44).



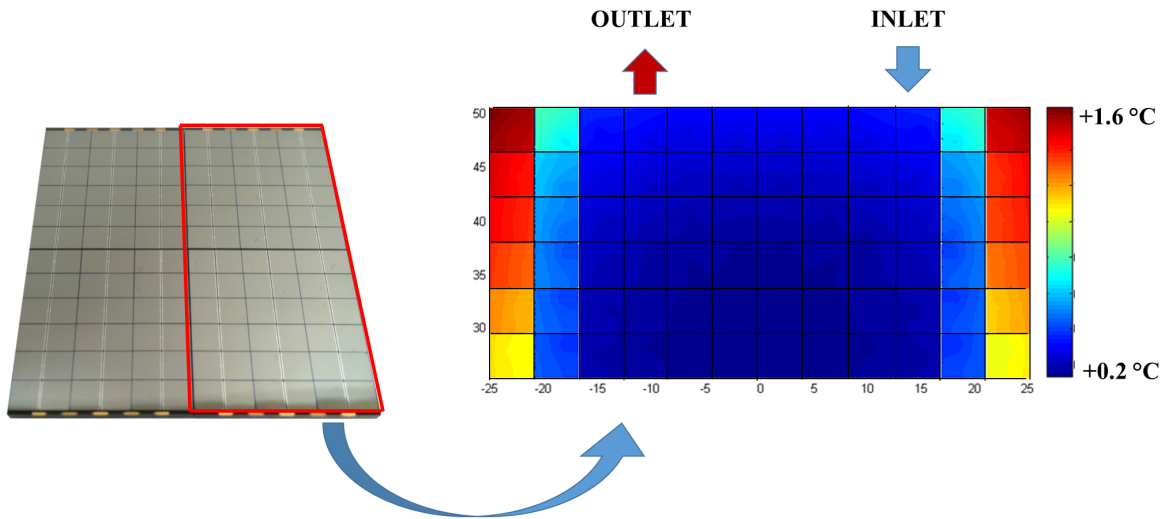
**Figure 3.44:** Rendered model of the 8 mm thick cooling block. The internal pipes are shown by removing the top lid. Courtesy of Mediso Kft., Hungary.

This is a bulky block of thermal conductive material with an internal dug cooling coil (serpentine) where a cooling fluid flows and exploits heat transport. For MR compatibility issues, commonly employed copper heat exchangers (which exhibit very good thermal conductivity 401 W/mK) can not be implemented. To overcome this limitation, we investigate different materials and solutions to build an MRI compatible cooling unit. These include thermally conductive non-metallic materials, like ceramic material SHAPAL (Precision Ceramics, UK - thermal conductivity 92 W/mK) and a thermally conductive plastic Coolpoly D5506 (Cool Polymers, USA - thermal conductivity 10 W/mK) as possible choices for the cooling block material. SHAPAL have been discarded during the study phase due to its fragility, difficulty in manufacturing and relatively high costs. Coolpoly, at the contrary, is cheaper and can be easily modeled in complex forms with robust and reliable outcome.

Effort has been dedicated by project partners also on the study of the fluid to employ for heat extraction: air cooling proved a considerable level of difficulty in flow stabilization and was thus discarded as option. The current baseline solution is the employment of a water + glycol mixture (40 % - 60%) that should allow to reach 0 °C. The remaining concerns in using

### Chapter 3. Gamma-detection module design

a liquid are related to preventing leakages and possible spurious signals in MR images due to water flow.



**Figure 3.45:** Temperature gradient simulated through Comsol physic software. The estimation has been performed only on the two SiPM tiles mounted on the heat sink in the position most proximal to pipes inlet (cold refrigerator) and outlet (warm refrigerator), where the gradient temperature is expected to be maximal.

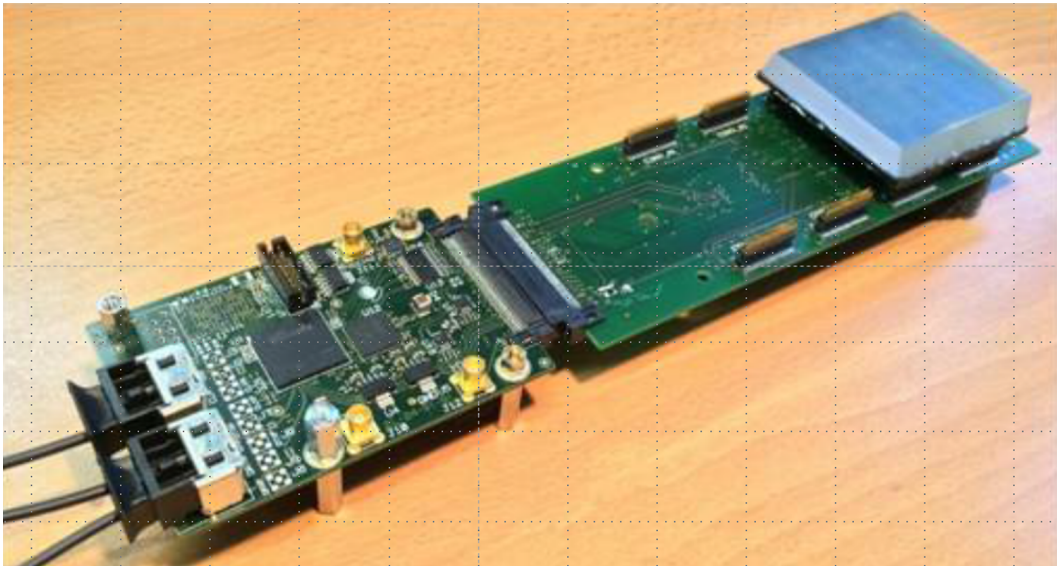
Physical simulation (Comsol software) of the cooling configuration chosen have been performed and the resulting temperature gradient (Figure 3.45) on the SiPM matrix has been analyzed: The maximum temperature difference expected is  $\Delta T = 1.6 \text{ }^\circ\text{C}$ . Temperature gradient brings to a spatial-dependent modification of the breakdown voltage ( $V_{BD}$ ) which entails a variation of the SiPMs gain with temperature,  $dG/dT = 27 \text{ mV}/^\circ\text{C}$  (for RGBs). The relative gain variation for the SiPM  $dG/G$  is then estimated inferior to 2 %, considering a 3 V overvoltage ( $V_{OV}$ ) on the SiPMs. The gain variation among the detectors surface for temperature gradient is then supposed to minimally affect reconstruction and energy resolution. Nevertheless, the temperature dependence of the multiplication factor raise the problem of temperature stabilization, for which the cooling system should not only provide an absolute temperature value for the SiPMs, but also time stability to limit gain fluctuation that can worsen the imaging and spectroscopic performance. The pumping and cooling strategy for the refrigerated liquid is still under investigation and development.



### 3.3. Detection module design

#### INSERT module

Figure 3.46 shows the current global design for the INSERT gamma-detection module.



**Figure 3.46:** *INSERT gamma-detection module (preclinical configuration). The CsI(Tl) crystal is coupled to 8 SiPM tiles, covering a surface of slightly more than 100 mm × 50 mm. The 8 mm connectors stack separates the tiles from the ASIC board (two ASICs are mounted below, not depicted in the picture) and provides internal volume for the heat sink slot. The DAQ board is connected to the ASIC board via 80 pins, edge mounted connectors.*

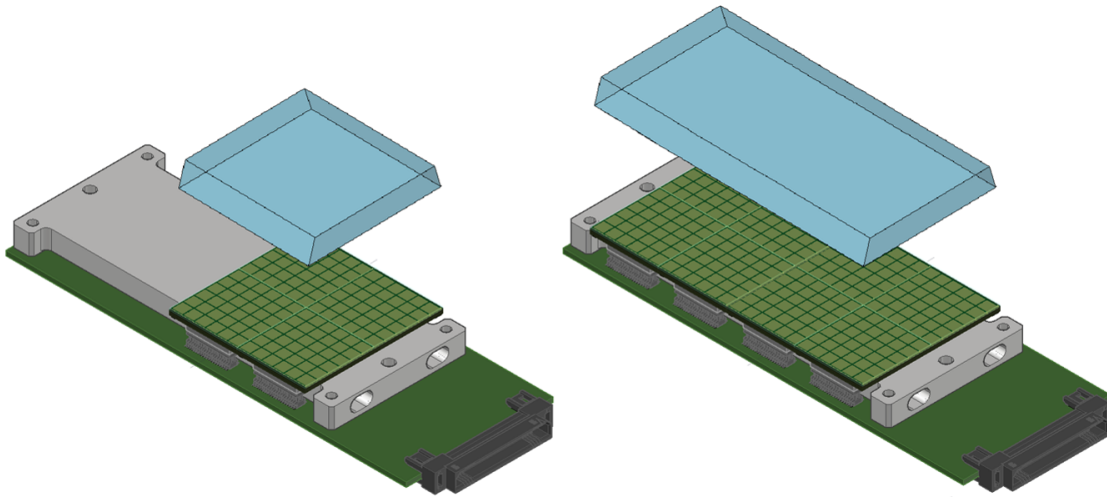
The system is practically a stack of the components that provide gamma conversion into electrical signal and then elaboration. The cooling block is placed in between the SiPM tiles and the ASIC boards, forming a *sandwich* architecture. In this geometry, cooling is provided not only to the SiPMs, but also to the ASICs on board.

The result is a compact geometry approximately 23 mm in thickness, width determined by the photodetector array and crystal (53 mm) and length dominated by the ASIC board plus DAQ board sizes (150 mm + 80 mm).

The INSERT module has been developed with the precaution to limit the design modifications when translating from preclinical to clinical configuration: The ASIC board is the common support for both the systems (only the number of ASICs and related ancillary systems varies); The FOV re-

### Chapter 3. Gamma-detection module design

quirements are satisfied by adding or removing SiPM tiles and coupling the overall matrix with a monolithic scintillator adequate in dimensions (Figure 3.47).



**Figure 3.47:** *Gamma-detector module modularity: with few design modifications it is easily possible to translate preclinical module (left) into a clinical one (right).*

#### 3.3.7 Compatibility issues and strategies.

The design of the whole gamma-detection module required, due to the intrinsic nature of the project, to pay particular attention to the issue of mutual compatibility between the SPECT modules we developed and the MR scanner.

From the point of view of the detection module, we discussed with the project partners some guidelines to protect the device from the following harmful effects:

1. Magnetic force attraction on the system or its components by the static field of the MR scanner. This issue is related to the presence of material with not negligible magnetic susceptibility in the detection module that can be attracted by the magnetic field and then cause mechanical instability in the SPECT ring. Ferromagnetic materials like Iron and Nickel are thus theoretically banned, also for the disturbance they introduce in the uniform  $B_0$  field in the MR system, which causes image artifacts and distortion.

### 3.3. Detection module design

2. Bulky, electrically conductive objects should be avoided since they are typically affected by eddy currents when the module has to be inserted into the MR bore and when the gradient switchers change the local magnitude of magnetic field in the scanner. This eddy current can be damaging for the gamma-detector, but also introduce spurious signal in both SPECT electronics and MR image because of the generation of induced electromagnetic fields.
3. The RF signal and the gradient switching activity from the MR can interfere with the gamma-detector electronics by means of electromagnetic field coupling. In that sense, all the possible cares in the design of the ASIC and DAQ board should be considered.
4. The activity of the analog and (mostly) digital circuits from the gamma-detector could affect the RF signal in the generation of the MR image. This effect is not well documented in literature and requires experimental tests.

The issues presented in the first two points were treated by a scrupulous selection of the components for the detection module: all the electronics devices and mechanical parts have been chosen by selecting only ferromagnetic-free elements. In few cases (i.e. the SiPM tile/ASIC board connector) traces of Nickel in the electronics components were unavoidable. For what concerns eddy currents, the most evident example of heavy impact on the system design is given by the material choice for the heat sink.

Once selected the components, they were sent to MRI.Tools (Berlin), the German partners involved in the design of the RF coils and project guidance for the compatibility aspects: the object under analysis was placed on a MR bed (either 3 or 7 T) and moved inside the bore to check possible limitations due to magnetic attractions or eddy currents generation. All the component chosen for the INSERT prototype received a first approval from the compatibility tests.

Unfortunately, the measurements on single components can not provide neither a picture on the final SPECT mechanical response to static attraction and induced currents, nor a forecast for the possible issue that could arise when both gamma-detection electronics and MR system are active (the two last points discussed in the previous list).

To protect and strengthen the electronic signals on ASIC and ASIC board, all the digital and most of the analog signal have been designed

### Chapter 3. Gamma-detection module design

---

differential, following the LVDS technical standard. The signal transmitted from/to the ASIC board to the DAQ board travel in the most internal layers of the former and are shielded by ground planes built on more external layers.

The mutual interference between RF coils and gamma-camera electronics is furthermore hampered by the introduction of shielding material (e.g. thin copper film) around the SPECT hosting structure. To minimize error in signal transmission from inside of the the MR bore to the nearby operator room, the technical consortium has decided to implement the ADC directly on board into the magnetic field, in order to minimize the analog signal path, since it is the most difficult to be recovered in case of interferences. The signals from and to the DAQ board are carried by optical fibers that are insensitive to magnetic fields.

A first informal test on the system electronics compatibility has been performed in Berlin by introducing the active gamma-detection prototype presented in the previous section into a 7 T human MR scanner (MAGNETOM, Siemens). The experiment were supposed to give a first iteration feedback on the compatibility aspects of the system with the devices enabled.

No test with radioactive sources could be performed because of lack of authorization in the test facilities. The ASIC channels were stimulated by the pulse circuit on ASIC board (with the SiPM tiles mounted on) and the output signal was recorded. Also the supply voltage on board was monitored along the tests. The protocol have been was repeated in different activity condition for the MR system:

1. Only the  $B_0$  field active.
2. The  $B_0$  field and RF signal (different stimulation patterns) active.
3. The  $B_0$  field and gradients switching (different timing and magnitudes) active.
4. Simulated MR sequences, with both RF signal and gradient switching enabled.

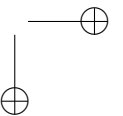
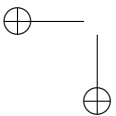
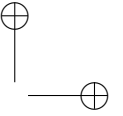
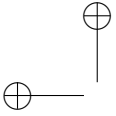
The tests with the  $B_0$  field and the RF pulses resulted in negligible mutual compatibility issues both in mechanic structure and electronics signal. On the other side the effects of the gradient switching were experienced to introduce sensible signal degradation on the ASIC output, most probably correlated to induced spurious effect observed on the biasing voltages.

---

### 3.3. Detection module design

The information obtained from this first experiments have been employed for a revision of the ASIC and ASIC board, with a focus on the bias distribution and stability.

In conclusion, the compatibility issues for the INSERT module are engaged by following an iterative protocol of design, test in MR scanner, analysis of the results and generation of new hypothesis for solving the problem and then redesign of the system on the base of the promoted considerations.



---

## CHAPTER 4

---

### Reconstruction algorithms

---

Nowadays, planar image reconstruction in gamma-cameras is typically performed through analytical or numerical algorithms implemented on software platforms. These methods are required to retrieve the coordinates of the gamma-rays interactions with minimal error and starting from the detected light distribution on the photodetectors plane. The position of a scintillation event can be estimated as the centroid of the signals from the photodetectors: although its ease in implementation, it is a method that suffers of non-linear response and requires channels calibration to avoid image distortions. An alternative approach to event position reconstruction is to use statistical reconstruction techniques (such as Maximum Likelihood Estimation or Weighted Least Square Error method), based on finding the best match between the observed and expected photodetector signals. The advantages of these methods over the centroid reconstruction are:

- Potentially smaller distortions
- Larger useful field of view
- Better filtering of noise events

However, statistical reconstruction requires detailed knowledge of the

## Chapter 4. Reconstruction algorithms

---

average signal amplitude as function of the scintillation event position for each photodetector, referred to as *Light Response Function*, or LRF. Retrieving the spatial response of the detectors with a sufficient precision is a non-trivial task and this constitutes the main obstacle for implementation of statistical position reconstruction methods for medical gamma cameras. One general approach is to directly measure it with complex setup systems (involving robotics controls). This solution gives a result specific to the properties of the real gamma-camera and it has an high level of reliability, even if the measurements are extremely time consuming. A second approach is based on the estimation of the response based on numerical simulations. Unfortunately, as already mentioned in section 3.2.2, accurate simulations require knowledge of a high number of optical parameters.

Other approaches are based on the choice of a suitable parametric model for the LRF and adjust the parameters in such a way to minimize the mean sum of squared residuals in the WLS method for a population of calibration events [124]. There are also alternative methods proposed with respect to the ones relying on the LRF: the coordinates of interaction are directly estimated through an iterative algorithm that minimize the weighted least squares difference between the experimental light distribution on the photodetectors and a parametric function for the PSF that models the light distribution in a specific crystal configuration [125].

In the present work we propose an adaptive method for LRF estimation: it only requires data from a flood field irradiation (uniform irradiation of the entrance plane of the scintillator), then the spatial response is obtained by means of an iterative technique. There is no strict requirement on the irradiation uniformity, making acquisition of such data straightforward and quick.

This method is well suited for practical medical applications, since it only requires a fast experimental calibration measurement.

### 4.1 Centroid methods

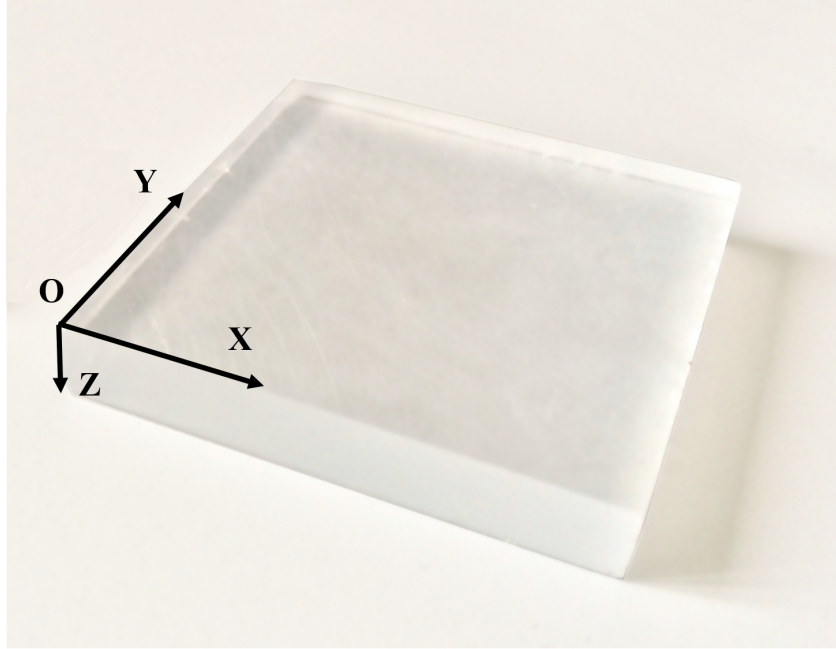
---

The *Centroid Method* (CM), or also *Center of Gravity* (CoG) algorithm, is a widely diffused approach for coordinates of interaction reconstruction thanks to the ease of implementation and to the very limited computational time required to process also huge amount of data. The approach requires the definition of the center position  $(x_i, y_i)$  for the  $i$ -th photodetector among  $M$  in the detection array. The coordinates of the centers are related to the reference space of the scintillator XY plane, parallel to the photodetectors



#### 4.1. Centroid methods

plane (Figure 4.1).



**Figure 4.1:** Reference coordinates and directions for a rectangular scintillator with the photodetector array (below) parallel to the XY plane.

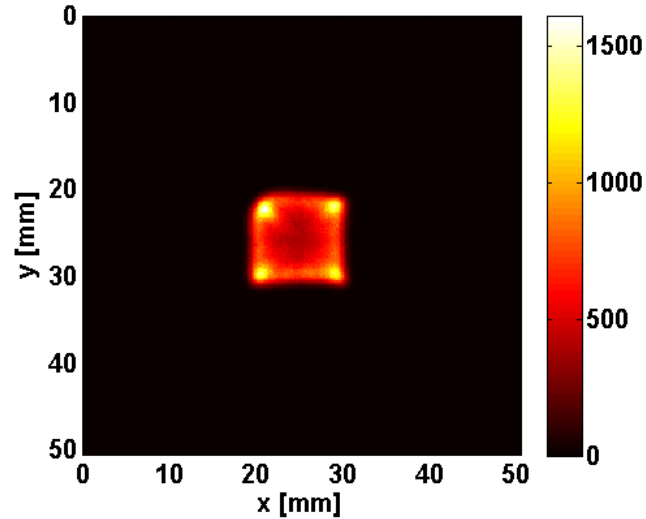
Considering one single event  $j$ ,  $N_{ji}$  represent the number of photoelectrons (signal plus noise) collected by the  $i$ -th photodetector. The reconstructed position  $(X_j, Y_j)$  for the  $j$ -th event is thus computed:

$$X_j = \frac{\sum_i^M x_i \cdot N_{ji}}{\sum_i^M N_{ji}}; Y_j = \frac{\sum_i^M y_i \cdot N_{ji}}{\sum_i^M N_{ji}} \quad (4.1)$$

When all the events coordinates are reconstructed, they are plotted on a bi-dimensional histogram that can be visualized and represent the *reconstruction image*. One example of uniformly distributed irradiation over an Anger camera, reconstructed with the *centroid method* is depicted in Figure 4.2.

An intrinsic limit of the Centroid method is that the FOV reconstruction is penned inside a region delimited by the centers of the edge detectors. This is consequence of the fact that there is no configuration of  $N_i$  in an

## Chapter 4. Reconstruction algorithms



**Figure 4.2:** Flood field irradiation of the INSERT preclinical module: the event positions are reconstructed with a simple Centroid Method.

event that could bring the center of gravity outside this region.

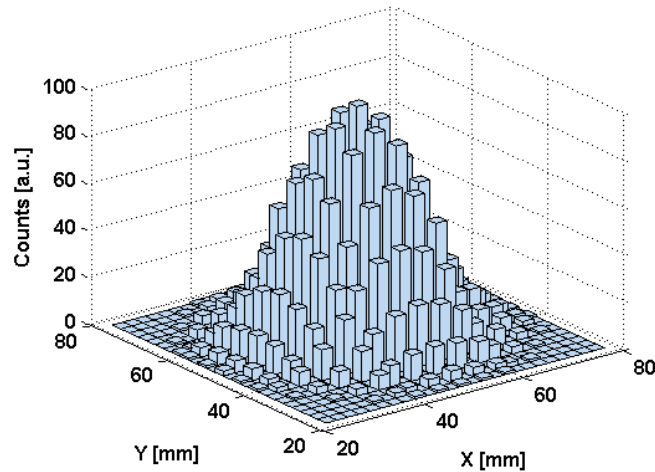
The principle on which the method works, lies in the distribution of the photoelectrons on the detection array. Let us consider, as example a perfect uniform distribution of charges collected: each photodetector has measured  $N_i = cost.$  number of electrons. The algorithm retrieve the center of gravity of the system, which is, for a uniform plane, the exact center of the plane itself. On the other hand, if all the light is collected and read by only one photodetector, the  $N_i$  value for the other detectors will be equal to zero, then the point of reconstruction will be the central coordinates of the photodetector that received the light.

Now, the actual light distribution on the photodetectors array is typically different from the previous cases: there is a correlation between the amount of light seen by one detector and the position of the event interaction approximately defined by the solid angle subtended by the latter on the active surface of the former. These coherence results into the typical *bell shape* of the light distribution on the matrix (Figure 4.3). The peak position of the bell represents the center of gravity, that is the reconstructed coordinates.

This assumptions brings to several interesting consequences:

1. A series of flat bell-light distribution (verging on a uniform distribu-

#### 4.1. Centroid methods



**Figure 4.3:** Bivariate histogram representing a fictional bell light distribution on a photodetectors array: each square pixel represent a photodetector, while the height of the pillars is the amount of photons collected by the detectors. The light distribution depends on many different parameters: crystal thickness and surface treatment, reflecting wrappings, refractive indices of the components, etc.

tion) will produce an image with all the events collapsed in a limited amount of space around the center of the photodetector matrix. So, uniform distributions produce poor spatial information, even if all the detectors have read some sort of signal.

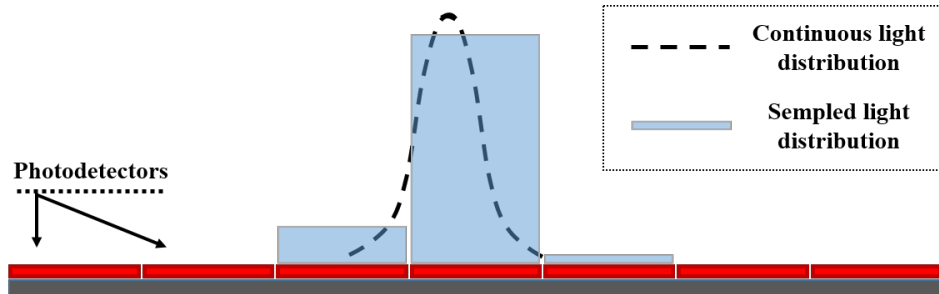
2. On the opposite case with respect to the previous point, a too peaked bell shape will suffer for undersampling condition due to the fix dimension of the photodetector (Figure 4.4). Then the error in the reconstruction is proportional to the shape of the bell function and to the dimension of the detectors.

In the centroid method, peaked distributions typically activate few detectors and the reconstruction coordinates tend to the center of the detector that received more signal.

3. In order to form a well-defined bell shape, an high number of counts (number of photoelectrons  $N_{pe}$ ) is required. A poor statistic of  $N_{pe}$  will produce a bell distribution with an high fluctuation on the shape, then worse reconstruction error.

Thus, in order to have better image resolution, it is fundamental to maximise all the parameters that improve  $N_{pe}$  ( $E_\gamma$ , crystal yield, col-

## Chapter 4. Reconstruction algorithms



**Figure 4.4:** *Undersampling effect of a photodetector array on a very steep light distribution. The photons bundle is collected by few detectors, with a correlated, limited spatial information.*

lection efficiency, conversion efficiency).

4. On the other way round, the fluctuation on the bell shape due to statistical and electronics noise do produce a limit in the reconstruction accuracy (for the same reason a low number of  $N_{pe}$  gives the same effect). The overall information given by point 3 and 4 together is that the reconstruction error, then the image spatial resolution, directly depends from the SNR on each detection channel.

This considerations have been shown in the case of the centroid method, but their principles are still valid also for other reconstruction algorithm. This is because all the methods for image reconstruction estimated the interaction coordinates from the light distribution on the detection matrix.

A general conclusion can be extrapolated from the previous points: a steep bell light distribution gives better reconstruction performance, provided that the distribution profile is well sampled (a little dimension of the photodetectors). Unfortunately, while the reduction of the detectors size helps the sampling on one side, on the other one the same amount of scintillation light is distributed on an higher number of channels (considering a fixed detection surface). Thus the SNR on the detection channels is worsened and the reconstruction is affected (as described in point 4).

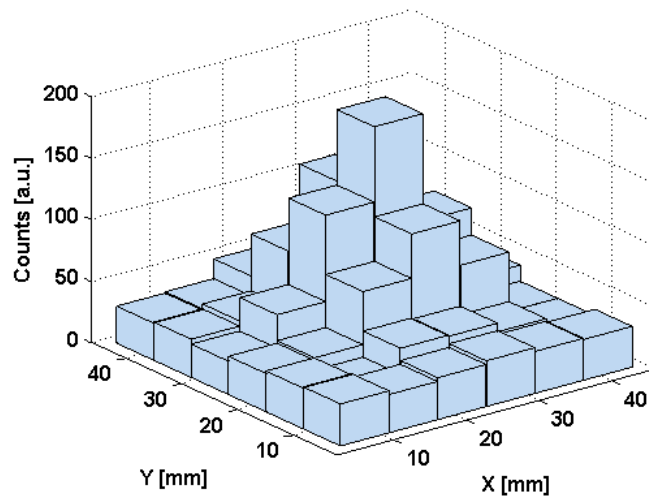
The photodetectors dimension is then a very important parameter to be optimized, also with respect to the mean light distribution, which is in part related to the thickness of the scintillator and for the rest to the light collection configuration (crystal shape, wrapping materials, optical parameters, etc.). A thumb rule typically employed in imaging system is to choose a photodetector size equal to the thickness of the scintillator coupled.

## 4.1. Centroid methods

### 4.1.1 Modified centroid method

As seen in the previous section, the mean light distribution on the detectors array depends on the coordinates of gamma interaction and by the optical properties that determine the way light travels in the crystal. The requirements for the INSERT module specified that a system with hybrid (imaging and spectroscopy) properties was needed. The strength of light signal is important since it defines the SNR which affects both imaging and energy resolution. Then a maximization of light collection was a primary aim and the most reflective material, based on literature, Teflon, was elected as wrapping material for the crystal.

Teflon reflects light following a diffusive behavior, which has the effect to spread the scintillation light all over the matrix with low spatial coherence. A typical distribution function (Figure 4.5) presents a bell shape in the region of interaction, due to direct light collection on the photodetectors and to the fraction of reflected light that preserved spatial coherence. The other component is a baseline of light, approximately constant on all the detectors: this part is related to highly diffused light and contains no spatial information.



**Figure 4.5:** Example of the bivariate distribution of the light on the preclinical INSERT module: a constant amount of light (due to diffusive reflections) is added to the typical bell distribution.

The effect of a almost uniform light distribution is to collapse the entire image in the central region of the crystal. Thus, to restore the FOV, the

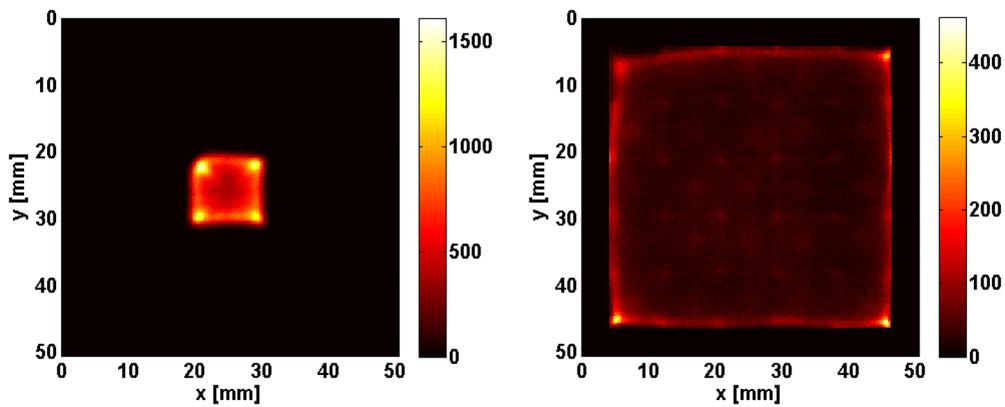
## Chapter 4. Reconstruction algorithms

constant component can be cut by subtracting a baseline value to the data [126]:

$$X_j = \frac{\sum_i^M x_i \cdot (N_{ji} - B)}{\sum_i^M N_{ji}}; Y_j = \frac{\sum_i^M y_i \cdot (N_{ji} - B)}{\sum_i^M N_{ji}} \quad (4.2)$$

where  $B$  is the baseline subtracted. This method is here referred to as *Modified Centroid Method* and it is currently implemented in most of the available commercial systems.

Figure 4.6 depicts the same dataset reconstructed with either a regular centroid method and a modified centroid method. The subtraction of the baseline allows to restore the FOV of the image.



**Figure 4.6:** (left) - flood field irradiation of the INSERT preclinical module, reconstructed with the Centroid Method; (right) - the same dataset, reconstructed with a Modified Centroid Method (arbitrary baseline subtraction).

## 4.2 Statistical methods

Statistical methods give access to better imaging reconstruction. The main mechanism on which statistical methods rely on the knowledge of the LRF for all the photodetectors in the array: since the LRF is dependent from the coordinates of gamma interaction, reconstructing the event position from an experimental light distribution means to find the best matching between the experimental data and the LRFs.

## 4.2. Statistical methods

### 4.2.1 Light Response Function - LRF

The mean overall number of photons generated in a scintillation event, in coordinates  $\vec{r}=(X, Y)$ , is  $N_{ph}$ . The probability for the  $i$ -th detector to collect  $n_i$  photons can be approximated by the Poisson distribution [127]:

$$P_i(n_i) = \frac{\mu_i^{n_i} e^{-\mu_i}}{n_i!} \quad (4.3)$$

where  $\mu_i = N_{ph}\eta_i(\vec{r})$  is the expectation for a number of photons detected by the  $i$ -th detector out of the  $N_{ph}$  initial ones and  $\eta_i(\vec{r})$  being the LRF, thus the fraction of photons emitted by scintillation event in position  $\vec{r}$  and collected on the  $i$ -th detector.

The stochastic phenomena that affects the light signal after collection (conversion into electrons, electronics filter, etc.) are supposed linear and introduce a gain factor  $G_i$  on the  $i$ -th signal. High variability in the detectors  $G_i$  values can lead to image deformation in centroid method reconstruction, then in this case an equalization of the channels is required.

#### LRF extrapolation methods

The Light Response Function can be obtained by an operation of experimental characterization of the crystal [127–129]. A highly collimated radiation beam is used to scan the entire scintillator detecting surface: the beam is moved by a robotic mechanism and sequentially hits the crystal in different  $(X, Y)$  coordinates; thus an average light distribution on the detection surface is measured for every beam position. The LRF values are then extrapolated for the coordinates stimulated, then the continuous LRF is obtained through interpolation. The accuracy of the LRF is correlated to the spatial sampling frequency of the beam scanning. The benefit of such approach is the reliability of the light response, because it is estimated by experimental data extrapolated by the real system, considering the complex and non-linear effects given by light collection and conversion on a photodetector array which is always presenting some kind of non-uniformity. On the other hand, the scanning system requires a bulky, complex setup with robotic arms, which can barely be fitted in SPECT gantries for LRF retrieve on the single gamma-detection modules. Moreover this technique is characterized by very long acquisition time, thus its practicability is further compromised.

## Chapter 4. Reconstruction algorithms

LRF can also be estimated through optical simulation, adopting analytical optical models [130], Montecarlo algorithms like the one presented in section 3.2.2. The simulated LRF can be practically implemented for all the imaging modules in a SPECT ring and allow direct estimation also of the Z coordinate of interaction (the depth of interaction), even if it does not consider the inter-module variations in the light response. Beyond that, the accuracy of the model is related to the knowledge of dozen of simulation parameters.

The LRF estimation method proposed in the present doctoral work is based on an iterative method proposed by Solovov and Morozov [131–133]. This technique requires a population of calibration events obtained through a flood field irradiation of the scintillator. The acquisition of such a dataset benefits from ease in the setup implementation (a non-collimated monoenergetic gamma source is required) and by the overall recording time. The LRF is iteratively extrapolated by the calibration data in the following manner. A large dataset of N events is acquired for all the M photodetectors; then the interaction coordinates  $(X_j, Y_j)$  for each j-th event are estimated, at a first step, employing either a Centroid or a Modified Centroid Method. Let us consider  $Q_j$  the total signal on the M channels for the j-th event and  $q_{ij}$  the amount of signal on each channel, in order to have:

$$Q_j = \sum_i^M q_{ij} \quad (4.4)$$

then the fraction of signal  $f_{ij} = q_{ij}/Q_j$  for each channel and event is computed. Considering a fixed i-th,  $f_{ij}$  present a spatial distribution given by the approximated reconstruction with the (modified) centroid method:

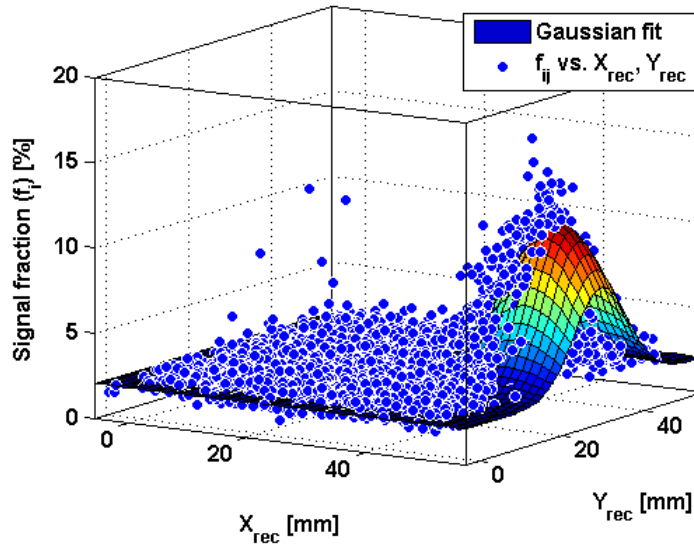
$$f_{ij} \leftrightarrow (X_j, Y_j) \quad (4.5)$$

If one considers that LRF smoothly depends on  $\vec{r}$  and assuming that all the events produce the same amount of light, it is possible to obtain the first approximation for the LRF  ${}^1\eta_i(\vec{r})$  by fitting every i-th photodetector dataset  $(X_j, Y_j, f_{ij})$  by a smooth function of  $\vec{r}$ . An example of LRF data fitting for a single photodetector is depicted in Figure 4.7.

This first approximation can be used to obtain a second dataset of reconstructed coordinates  $(X_j, Y_j)$  employing a statistical method (i.e. maximum likelihood). If compared to the centroid estimates, these new estimates are



## 4.2. Statistical methods



**Figure 4.7:** 2D Gaussian fitting of a  $(X_j, Y_j, f_{ij})$  dataset for one photodetector positioned at the edge of the detection matrix. The bidimensional interpolation result represents the Light Response Function (LRF) for the  $i$ -th photodetector.

less biased, especially in the case of events on the edge of the UFOV. Every photodetector response as a function of coordinates is fitted again and a second approximation  ${}^2\eta_i(\vec{r})$  is thus generated.

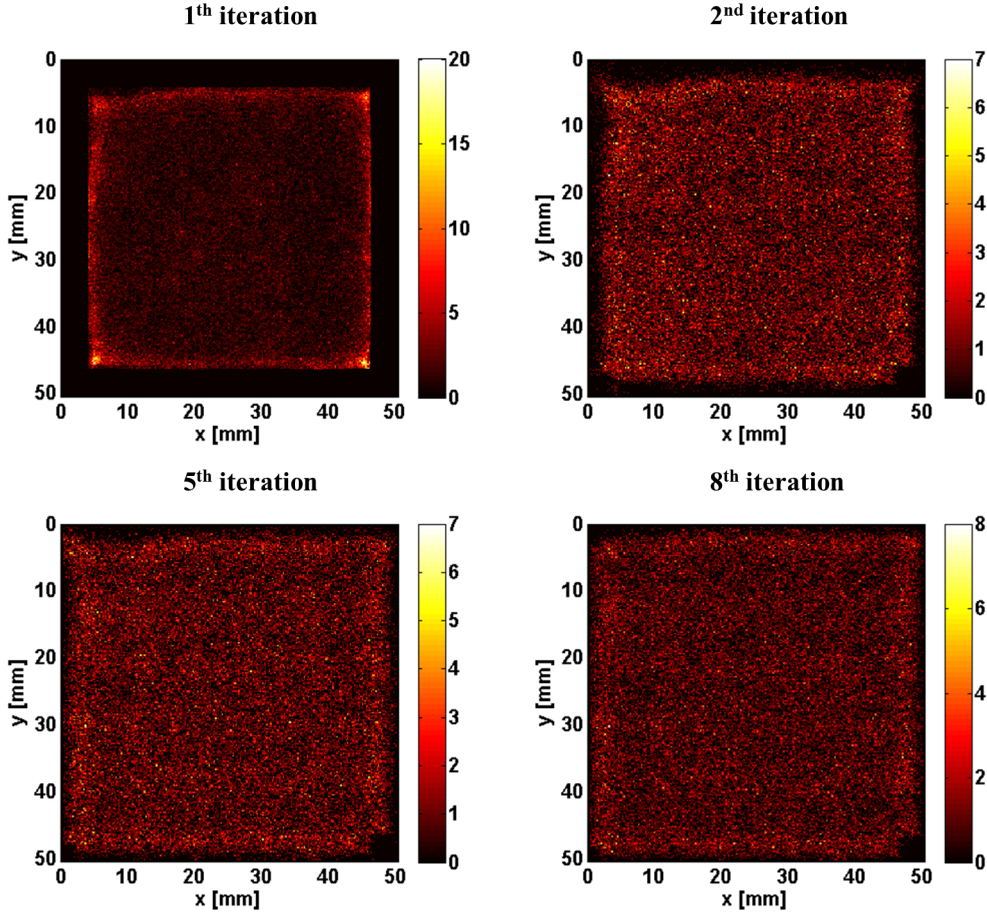
Figure 4.8 shows the enlargement of the UFOV for the flood field irradiation at different algorithm iterations.

The previous steps are iteratively repeated until any stop condition or convergence criterion is reached. For example, the spatial events distribution should exhibit a uniformity controlled by a density threshold. Another option is to iterate until the change in the LRFs on the next step falls below a pre-defined tolerance.

The algorithm also requires some additional tuning and regularization to force the iteration to converge: the initial spatial distribution of the reconstructed interactions should present the lower level of non-linearities and a sufficiently large FOV. Light distributions light the one tested with the INSERT module bring to compressed FOV if simple centroid method is employed, then modified centroid method is preferred.

The convergence to a more uniform distribution of the non-collimated events is supported by adding some arbitrary noise on the interaction coordinates

## Chapter 4. Reconstruction algorithms



**Figure 4.8:** *Progressive enlargement of the FOV in the reconstructed image at different iteration of the algorithm for Light Response Function (LRF) extrapolation. The first iteration (top-left) is obtained through a Modified Centroid Method. The 2<sup>nd</sup>, 5<sup>th</sup> and 8<sup>th</sup> iterations (top-right and bottom) are reconstructed with the Maximum Likelihood algorithm. 50000 events have been reconstructed.*

at every iterative cycle.

Last remark is on the choice of the smooth function: Solovov and Morozov suggested the assumption that the LRF function for the photodetectors (in their case PMTs) exhibit axial symmetry  $\eta_i(\vec{r}) = \eta_i(\rho)$ , where  $\rho$  is the distance from the PMT axis. Under this condition, the LRF can be well fitted through a cubic spline. The distribution of the calibration events in the XY space of the i-th photodetector suggested that the previous approxima-

## 4.2. Statistical methods

tion was non adequate for the INSERT imaging module. For these reason bidimensional fitting function have been considered.

The 2D Gaussian function has given the best results in terms of homogeneity and LRF model generation time:

$$f_{unc} = A \cdot \exp(-[b(x - x_0)^2 + c(y - y_0)^2]) + \Phi \quad (4.6)$$

where  $(A, b, c, x_0, y_0, \Phi)$  are the parameters to optimize for the fitting.  $A$  is the amplitude of the Gaussian height;  $b$  and  $c$  are parameters inversely proportional to the Gaussian bell variance and respectively for the  $x$  and  $y$  directions;  $(x_0, y_0)$  are the coordinates of the Gaussian center;  $\Phi$  is an offset proportional to the baseline threshold  $B$  in the modified centroid method.

A second function implemented is suggested in [131]:

$$f_{unc} = A \cdot \exp\left(-\frac{\alpha\rho}{1 + \rho^{1-\alpha}} - \frac{b}{1 + \rho^{-\alpha}}\right) + \Phi \quad (4.7)$$

where  $\rho$  is the distance from the central axis of the photodetector.

The iterative method for LRF extrapolation is fast and requires calibration data from experimental measurements easy to be repeated also in clinical practice. With the same calibration it is possible to set the LRF of all the gamma-detectors in the SPECT ring, each one adapted to the specific conditions of the camera. The algorithm is automatic, but requires a moderate tuning of few variables (modified centroid baseline threshold, fitting curve model, noise on the data for convergence, etc.) to help it to converge to solution. Since the method relies on the knowledge of planar coordinates retrieval from experimental data, it does not possess intrinsic information for the discrimination of the depth of interaction (DOI).

### 4.2.2 Maximum likelihood method

The *Maximum Likelihood* (ML) method for the reconstruction problem consists in finding the set of parameters ( $\hat{X}$  and  $\hat{Y}$  coordinates of interaction and the energy of the gamma event  $\hat{N}$  expressed as number of photoelectrons or signal intensity) that maximizes the likelihood of obtaining the experimentally measured result. When the signals  $n_i$  are known for each photodetector, the likelihood function can be easily calculated from

## Chapter 4. Reconstruction algorithms

---

the Poisson distribution 4.3 as:

$$L = \prod_i^M P(n_i|\mu_i) \quad (4.8)$$

where  $M$  is the number of photodetectors in the array and  $P(n_i|\mu_i)$  is the *joint density function* which represents the probability to detect a signal  $n_i$ , given an average  $\mu_i$  value which is a function of the parameters to be optimized ( $\mu_i = \hat{N}\eta_i(\hat{r})$ ). Equation 4.8 is true if the  $n_i$  are independent and identically distributed. The equation can be simplified in:

$$\ln(L) = \sum_i^M P(n_i|\mu_i) = \sum_i^M (n_i \ln(\mu_i) - \mu_i) - \sum_i^M (n_i!) \quad (4.9)$$

where the last term is a constant and can be neglected in the optimization phase. The equation is better expressed as:

$$\ln(L(\hat{r}, \hat{N})) = \sum_i^M (n_i \ln(\hat{N}\eta_i(\hat{r})) - \hat{N}\eta_i(\hat{r})) + Cost \quad (4.10)$$

Given  $\hat{N}\eta_i(\hat{r})$ , the LRF for all the  $M$  detectors, then the best estimates for the system parameters can be found by maximizing function 4.10.  $\hat{N}$  can be found analytically as a function of the interaction position:

$$\hat{N}(\vec{r}) = \frac{\sum_i^M n_i}{\sum_i^M \eta_i(\vec{r})} \quad (4.11)$$

Now, by substituting  $\hat{N}(\vec{r})$  on  $\hat{N}$  into 4.10, the likelihood factor is only dependent on  $\vec{r}$ . The final step is to find the coordinates that maximize  $\ln(L(\vec{r}))$ , in the present thesis executed through a numerical method.

### 4.3 Implementation of the statistical method

---

The iterative algorithm for LRF extrapolation and all the reconstruction methods previously described have been implemented in Matlab (R2011b).

### 4.3. Implementation of the statistical method

#### 4.3.1 Light Response Function generator

The blocks diagram depicted in Figure 4.9 describes the protocol for LRF calculation through the iterative method.

The starting dataset is constituted by a  $N$  (events)  $\times$   $M$  (detector channels) matrix, with each cell defining  $Q_{ij}$ , the amount of signal recorded by the  $i$ -th event in the  $j$ -th event. Dataset can be originated from either Monte-carlo simulations or experimental measurements. A first filter block is required to eliminate those events that lies outside a user-defined *energy*<sup>1</sup> range: the amplitude of a single event  $Q_j$  is calculated as  $\sum_i^M Q_{ij}$  and depends on the gamma-ray energy released in the scintillation event. Scattering events, Compton effects, escape phenomena, cosmic background and other non-idealities can occur depending on the measurement conditions and the setup configuration. The result is an amplitude histogram (correlated with the energy spectrum) corrupted with typically lower energy counts with respect to the photoelectric events that compose the main source energy peak (Figure 4.10).

These non-idealities do not carry useful imaging information and can be removed by defining an acceptance range in the amplitudes histogram.

$N_{SiPM,min}$  represents the minimum number of activated photodetectors per event required to image that very event: with reference to section 4.1, if the scintillation light is collected by only few photodetectors (approximately below 4) the spatial reconstruction capability of the system is impoverished by sampling limits. These events typically produce reconstruction accumulation artifacts in the image that can be removed by setting a threshold for  $N_{SiPM,min}$ .

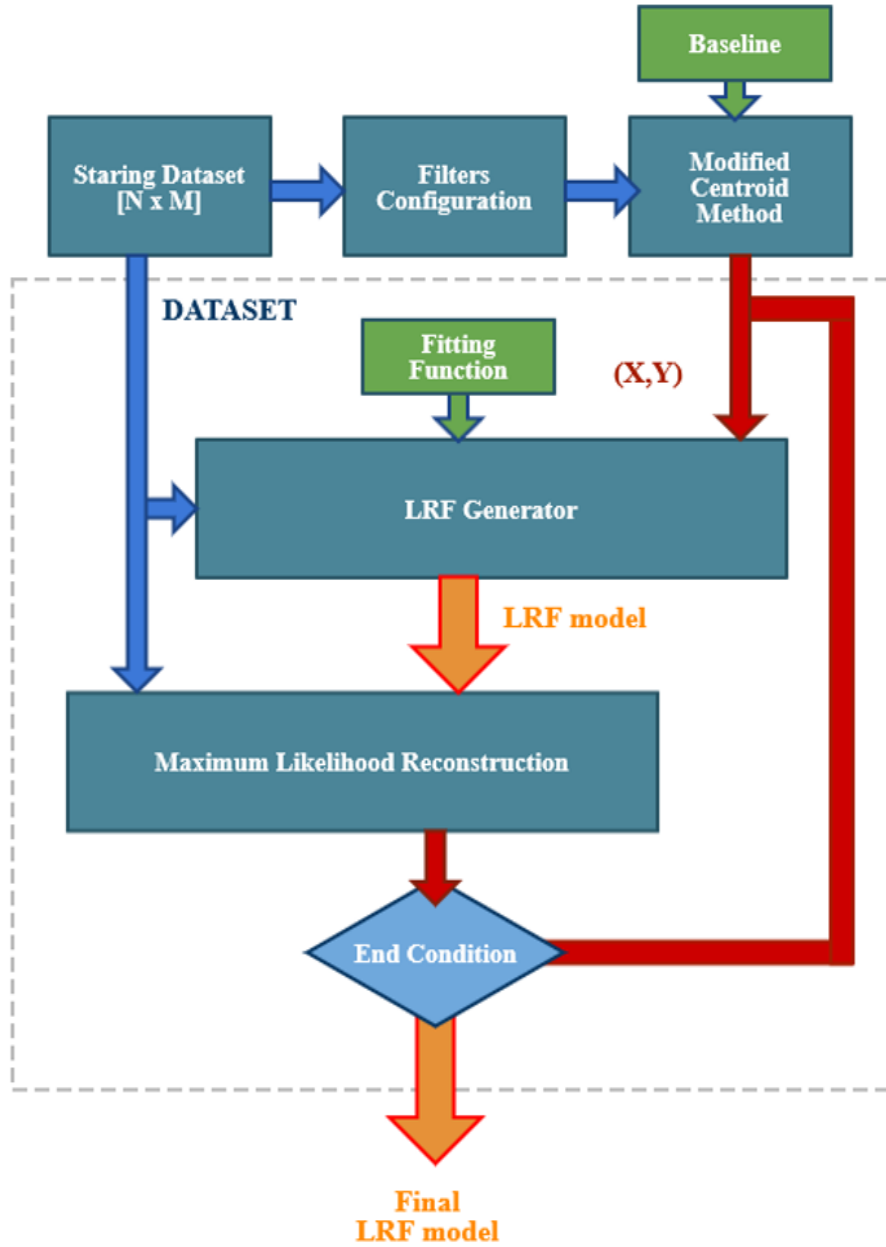
Proceeding with the elaboration, the filtered data are fed to a modified centroid algorithm that reconstructs the coordinates of interaction  ${}^1(X_j, Y_j)$  for all the  $N$  events and for the first iteration of the algorithm.

The LRF is than calculated with the following procedure:

- If set by the user, a Gaussian random noise (null mean, arbitrary standard deviation) is added on the  ${}^1(X_j, Y_j)$ .
- Considering the  $i$ -th photodetecting channel, a scatter plot of the points  ${}^1(X_j, Y_j, Q_{ij})$  is generated. The operation is repeated for all the  $M$  channels.
- A custom defined 2D function (usually a bidimensional Gaussian bell) is fitted to each one of the scatter plots. The ensemble of all the  $M$  fitting functions constitutes the  ${}^1$ LRF of the system (first iteration).

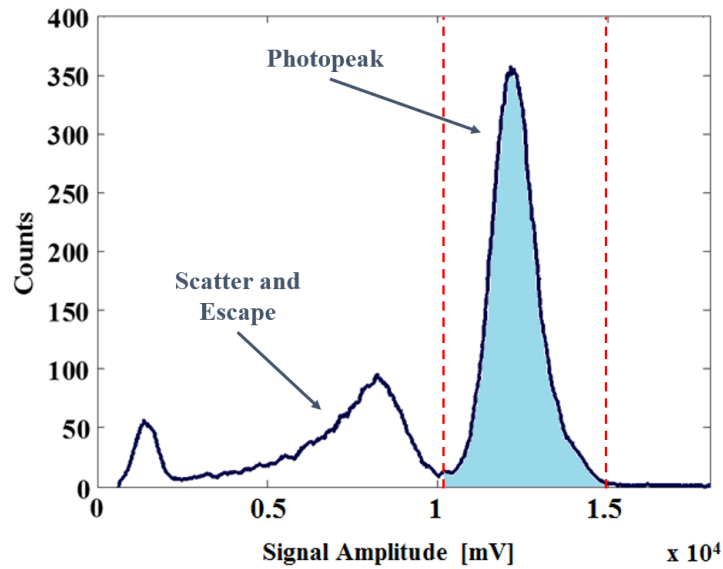
<sup>1</sup>The term *energy* is here improperly employed since it actually refers to the single event signal amplitude

Chapter 4. Reconstruction algorithms



**Figure 4.9:** Flowchart of the LRF extrapolation procedure through iterative algorithm. The starting dataset is a  $[N_{events} \times M_{channels}]$  matrix obtained from a flood irradiation measurement.

### 4.3. Implementation of the statistical method



**Figure 4.10:** Amplitude ( $Q_j$ ) histogram for a generic flood irradiation measurement on a custom Anger camera. The photopeak contains all the events that bring coherent spatial information, that is useful for image reconstruction. The “lower energy” events are consequence of scattering, escape effects or others and do affect image quality. An acceptance range is set (two red dotted lines) to consider only the events in the photopeak and discard the others.

The filtered data are now given as input to the statistical method (maximum likelihood) that relies on the <sup>1</sup>LRF model. The new set of reconstructed coordinates <sup>2</sup>( $X_j, Y_j$ ) is then generated. At this point the algorithm passes through a conditional block to verify if the convergence threshold has been reached. At the present time, the stop condition is defined only by a maximum number of iterations: the user is provided of all the reconstructed images, one for each iteration, and can choose the LRF model which qualitatively procure the better result. If no stop condition is verified, the new set of reconstructed coordinates is given to the LRF generator and a new iteration starts.

#### 4.3.2 Maximum Likelihood algorithm optimization

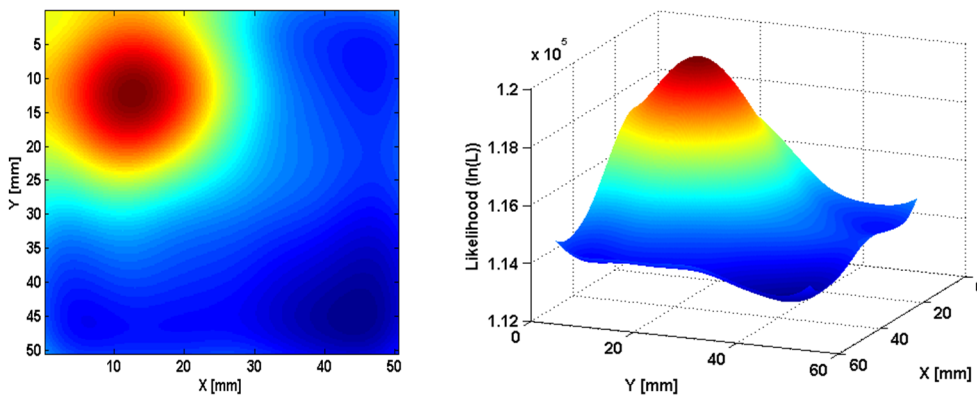
The major issue with statistical reconstruction methods, then also of maximum likelihood estimation, is the computational time required for estima-

## Chapter 4. Reconstruction algorithms

tion of the interaction position. Analytical approach for solving the ML problem has been discarded since it represents a too heavy solution for Likelihood optimization. Instead, a numerical method has been adopted and implemented.

Given  $\rho$  the lateral dimension of a single square pixel ( $\rho = 0.05 - 0.4$  mm),  $L$  and  $W$  respectively the length and width of the crystal, the crystal is divided in a number  $L/\rho \times W/\rho$  of pixels (the Z dimension of the crystal is compressed). Each pixel is defined by its dimension and by the coordinates of the center.

For each one of the  $N$  events, the likelihood value is calculated on all the pixels by solving equation 4.11 and then 4.10. An illustrative representation of likelihood distribution for a generic event is depicted in Figure 4.11.



**Figure 4.11:** Likelihood map as function of the crystal XY plane coordinates for one single gamma event.

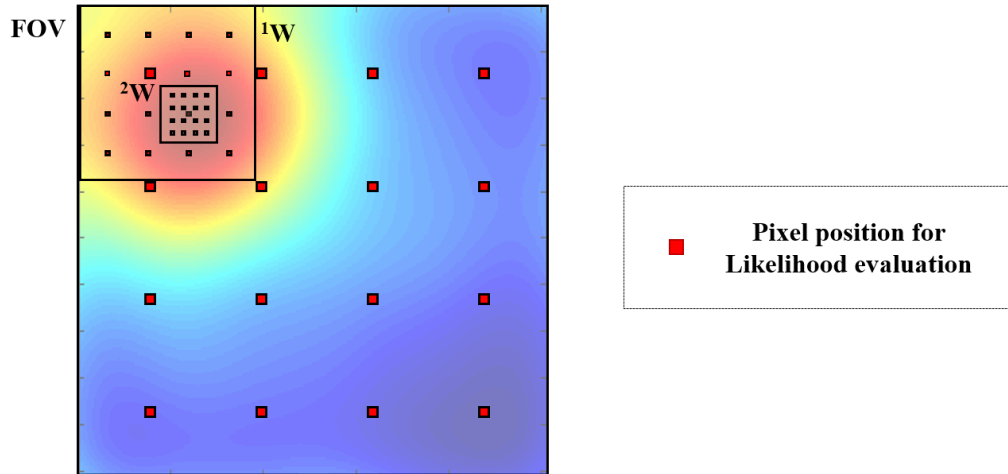
The absolute maximum is computed and the related coordinates are saved and considered as the reconstructed position for that event.

Unfortunately, this approach is still affected by slowness, since it requires heavy computation on a very high number of pixels for all the events. For this reason an alternative optimization protocol has been implemented, based on two main strategies:

1. Implementation of multi-core processing for parallel calculation: the computation burden is divided on more than one processor to speed up the overall algorithm.
2. The research of the maximum value for the likelihood is temporally optimized through a procedure takes inspiration from the *successive*



### 4.3. Implementation of the statistical method



**Figure 4.12:** Description of the successive approximation algorithm implemented to optimize the maximum likelihood factor for a single event reconstruction. The method starts from few positions (image pixels) and iteratively repeats the research of the absolute maximum is progressively reduced areas of the FOV.

*approximation algorithm:* the likelihood value is initially computed only for few pixels in a grid that covers all the crystal surface; the maximum value for this subset of data is found and then a focused window  $^1W$  around the maximum is defined (Figure 4.12). Later, a new set of points is created inside  $W$  for which likelihood is calculated and the maximum value is found and consequently a new smaller window  $^2W$  is created. The procedure stops when the grid resolution has reached the dimension of the single pixel.

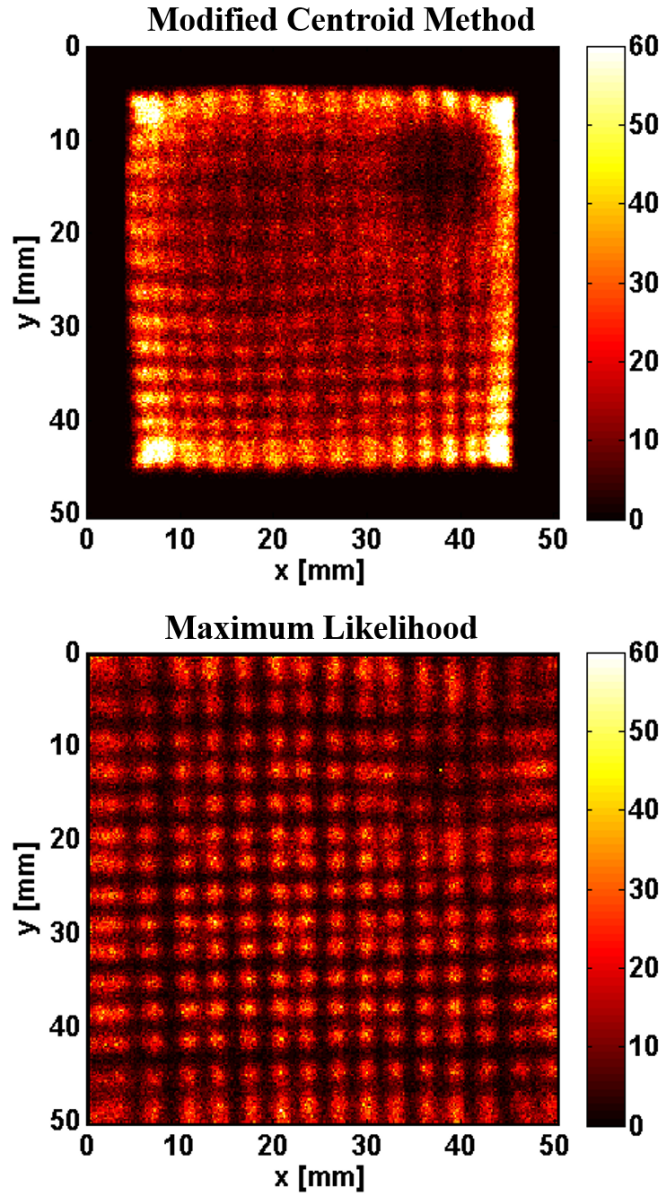
In this way the overall algorithm is tremendously hasten.

#### 4.3.3 Reconstruction performance

The reconstruction capability of the ML algorithm, with LRF based on experimental calibration data from flood irradiation acquisition, is summarized through an example in Figure 4.13: a grid of collimated gamma beams is reconstructed with both modified centroid method and maximum likelihood.

The protocol for the acquisition of the data related to the image showed will be discussed in chapter 5. The baseline for the modified centroid algorithm has been chosen in order to optimize the tradeoff between FOV recovery and linearity in reconstruction. Edge effects on the modified centroid method are clearly visible as like non-uniformity and non-linearities

## Chapter 4. Reconstruction algorithms



**Figure 4.13:** Reconstructed image representing a grid distribution of collimated gamma-ray beams from a  $^{57}\text{Co}$  source (distance between every couple of neighbor spots is 3 mm). Both modified centroid (top) and maximum likelihood (bottom) methods have been adopted for comparison. In the modified centroid reconstructed image the artifact produced by a broken channel is clearly visible.

### 4.3. Implementation of the statistical method

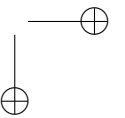
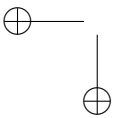
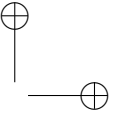
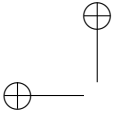
---

related to the lack of readout channel calibration. Moreover, for this particular acquisition, one electronic channel was broken and then muted (all the data for that channel have been set to zero).

The ML reconstruction implementing the flood-calibration-based LRF present the following advantages:

- better reconstruction performance at the borders, with complete crystal FOV recovery.
- increased reconstruction linearity.
- increased reconstruction uniformity, even with uncalibrated channels: this benefit is provided by the extraction of the LRF from experimental data (with respect to a simulated model) which automatically calibrates the channel signal and compensate for different average channel gain.
- the compensation effect is particularly visible in the broken channel area, where the spots are partially reconstructed (even if with some reduction in linearity and uniformity is still present). This is possible since the ML can overlook the information from the broken channel and complete the reconstruction with the data from the neighbor channels.

The algorithm has been developed in Matlab R2013a and run, for performance evaluation on a Intel(R) Core(TM) i7 CPU (2.93 GHz, quad core). Every image is composed by  $250 \times 250$  pixels, which represents also the overall dimension of the LRF model. The average computational frequency recorded for the reconstruction of an image with ML method is approximately **1670 events/s**.



---

## CHAPTER 5

---

### Detection module performance and results

---

#### 5.1 Introduction

---

The design and study phase described in the previous chapters have paved the way for the development of a first prototype for the gamma-detection module. This detector does not reflect the complete final design foreseen for INSERT, since it implements a SiPM technology (RGB, FBK) that still presents some parameter limitations to the final performances of the gamma camera, first of all an high Dark Count Rate (400 - 800 kHz/mm<sup>2</sup> from manufacturer datasheet). Moreover, the electronic readout channels of the Angus ASIC implement a simple RC filter, developed mainly to advantage a fast design and realization of a prototype chip: this choice was well motivated by several practical factors like observance of project deadlines and development, but also the possibility to have a baseline for the electronic channels for an optimization plan. Nevertheless, gated integrator filters can provide better performances, mainly due to the reduced ballistic deficit produced on the slow CsI(Tl) scintillation signal. The final INSERT detection module has being designed also starting from the information and indications obtained by the experimental results on the first prototype: it is mandatory to reduce the DCR of the SiPM and, at the same time, increase

## Chapter 5. Detection module performance and results

---

the PDE in order to maximize the SNR. The actual development plan foresees the production of a new line of SiPM tiles, implementing RGB-HD technology, with improved microcell fill factor (then PDE) and with reduced intrinsic noise.

In the present chapter the expected performance for the state of the art INSERT prototype (implementing RGB SiPMs and RC filter for the readout channels) and the final detection module design (with RGB-HD SiPMs and gated integrator readout) will be computed and compared, also with the project requirements defined in chapter 2.

Experimental measurements, obtained with different irradiation profiles on the prototype gamma-detection module, are also described and discussed. A comparison between the simulated and experimental results lead to an analysis on the models adopted for the gamma-camera design.

All the evaluations have been performed considering a preclinical INSERT gamma-detection module. The outcomes for a clinical module are not reported, but can be derived from the results retrieved with the experimental session on the preclinical one.

### 5.2 Theoretical and simulated expectations

---

The theoretical and simulated performance computation for the prototype system and the final foreseen version of the gamma-detection module is hereafter presented and described. In a first section, the simulation parameters are listed and justified.

#### 5.2.1 Model parameters

The following parameters have been considered for either the energy resolution analytical equation and the optical simulation.

##### Scintillator:

- **Material** - Cesium Iodide, CsI(Tl). Physical parameters from table 3.1. The time parameters to model the scintillation decay and calculate the ballistic deficit are based on the measurements by Valentine [72]. For the emission spectrum, the one from Figure 3.24 [112] has been considered for effective PDE calculation. Intrinsic energy resolution ( $R_{int}$ ) is equal to 6 % [115].

## 5.2. Theoretical and simulated expectations

- **Geometry** - Parallelepiped, 50.6 mm × 51.7 mm × 8 mm. The inclination of the slanted faces is not simulated.
- **Optical reflections** - UNIFIED model is considered: the surface roughness is modeled with a standard deviation for the micro-facet angle  $\alpha$  equal to  $1^\circ$ . This value is arbitrarily defined in order to consider a smooth CsI(Tl) surface by emulating other literature works setting the roughness parameter for polished crystals [121]. The coating material is Teflon, for which pure Lambertian diffusion is considered, with a reflectivity probability of 94 % (please, refer to section 3.3.2). Between crystal and Teflon, a thin layer of air ( $n_{air} = 1$ ) is simulated. Thus the interface between crystal and air is simulated by means of the UNIFIED model, with  $\sigma_\alpha = 1^\circ$  and considering only specular lobe among all the possible reflection components.
- **Optical coupling** - The coupling window is simulated by defining the equivalent refractive index seen by the crystal and described in section 3.2.2. Given a refractive index for the Meltmount optical glue and for the optical resin covering the SiPMs respectively equal to  $n_{glue} = 1.539$  and  $n_{resin} = 1.51$ , then the equivalent refractive index for the model is approximately  $n_{eq} = 1.514$ .

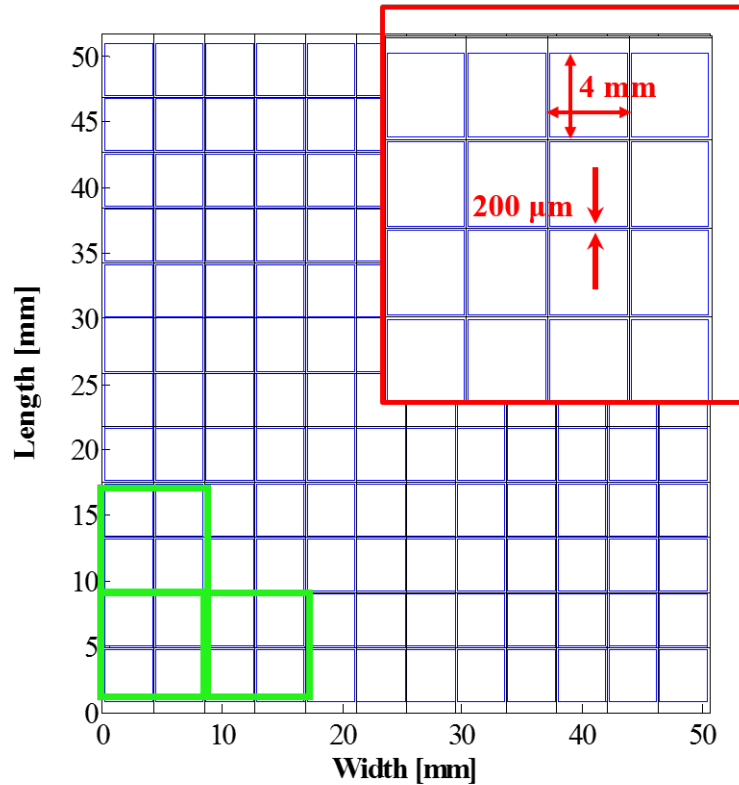
### SiPMs array:

- **Geometry** - The SiPMs matrix is geometrically defined considering all the mechanical dimensions of four tiles aligned in a  $2 \times 2$  configuration (Figure 5.1). The same array geometry is considered for both RBG and RBG-HD devices.
- **Technical parameters** - Table 5.1 reports the technical parameters for the two different SiPM technologies considered: RGB (state of the art and RGB-HD (future implementation).

Both RGB and RGB-HD present an average breakdown voltage of approximately 29 V at room temperature. The above properties are considered for an optimal working overvoltage of approximately 3 V. This value has been found to maximize the SNR value (than optimizes the energy resolution) since competitive effects act as function of the biasing voltage over breakdown. PDE increases with the  $V_{OV}$  following an approximately bi-linear curve behavior, while  $DCR(V_{OV})$  augments exponentially (Figure 5.2).

Also the ENF increases following a linear trend. The overall effect of this main components have been experimentally observed through

## Chapter 5. Detection module performance and results



**Figure 5.1:** Simulated geometry for the SiPM array (top view). The distance between active areas is  $200\ \mu\text{m}$ . In correspondence of conjunction of two tiles, additional  $100\ \mu\text{m}$  have been added to consider mechanical alignment. The collected light simulated on  $2 \times 2$  neighbor SiPMs is summed together to consider the channel merging (green squares).

energy resolution measurements at different overvoltages and the optimal value ( $V_{OV} = 3\ \text{V}$ ) has been adopted as reference for the simulations and measurements.)

**Shaping filter:** Two different shaping strategies are considered: the RC filter (state of the art for the prototype) and the gated integrator (future implementation).

The  $A_3$  shaping factor for the filters have been already reported in Figure 3.19 (for the RC filter  $A_3 = 0.25$ , while for the gated integrator  $A_3 = 0.5$ ). The shaping time is left as free variable to explore ENC and ballistic deficit dependencies for both the strategies.



## 5.2. Theoretical and simulated expectations

**Table 5.1:** *Technical parameters for RGB and RGB-HD SiPMs (FBK, Trento).*

	RGB	RGB-HD
<b>microcell size</b>	40 $\mu\text{m}$	25 $\mu\text{m}$
<b>SiPM active area</b>	4 $\text{mm}^2$	
<b>PDE (effective)</b>	28.9 %	35.0 %
<b>DCR (at 20 °C)</b>	400 $\text{kHz}/\text{mm}^2$	200 $\text{kHz}/\text{mm}^2$
<b>ENF</b>	1.6	1.2
<b>Cooling Temperature</b>	0 °C	

**Radioactive source:** almost all estimations have been performed considering a  $^{99m}\text{Tc}$  source (140.5 keV).

### 5.2.2 Energy resolution from analytical model

Equation 3.19 is applied to the two configurations considered, with  $\langle N_{pe} \rangle = \langle N_{ph} \eta_{coll} \cdot \text{PDE} \rangle$  and  $\eta_{coll}$  estimated through optical simulation output as the ratio of the mean number of photons collected over the average of the scintillation generated photons (the simulation is performed with the same parameters described in the previous section and considering a flood irradiation of the crystal). The collection efficiency adopted for the simulation is  $\eta_{coll} = 54.5 \%$ .

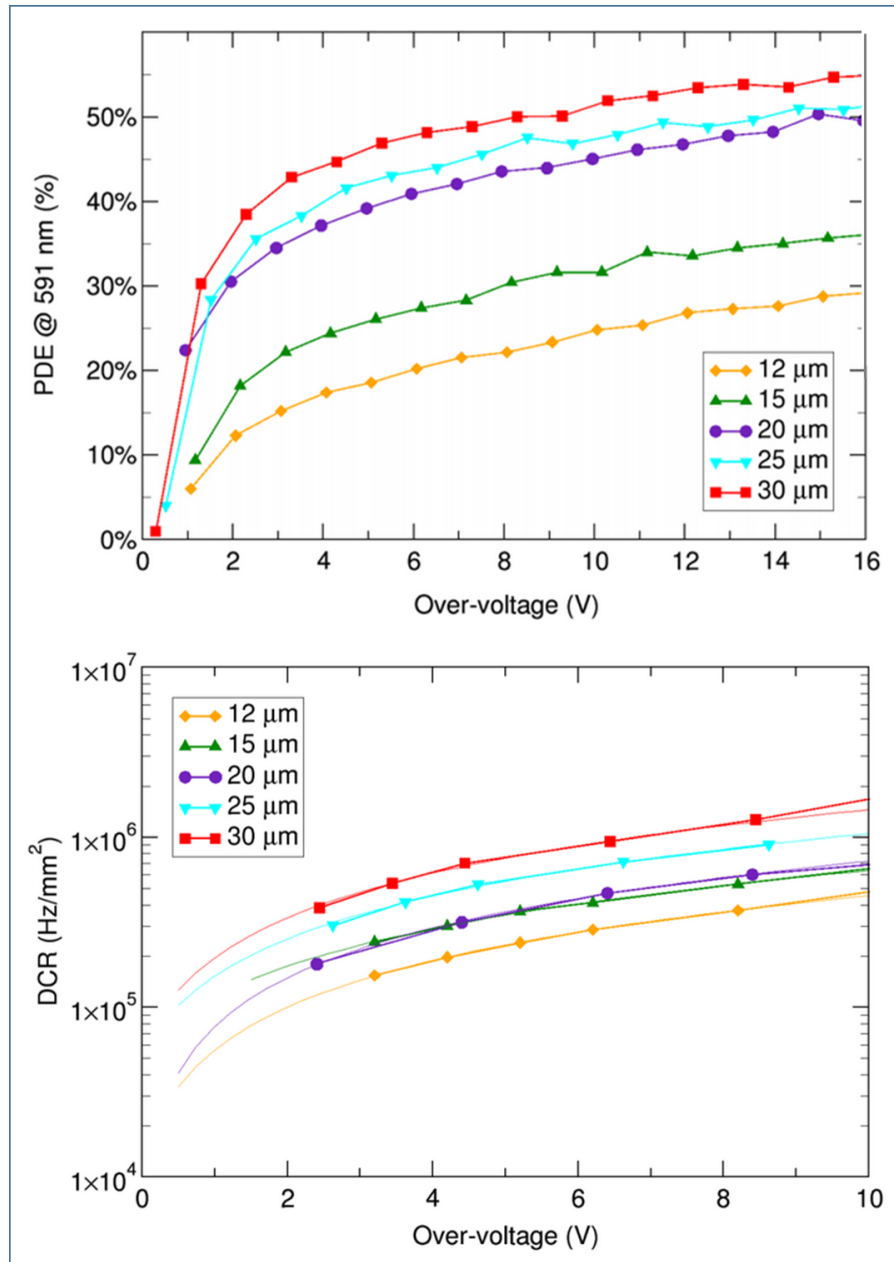
The ENC for the two configurations is estimated in Figure 5.3. The DCR at 0 °C has been calculated considering that, starting from ambient temperature  $T_{amb}$ , it is halved every  $T_{1/2} = 8 \text{ }^\circ\text{C}$ :

$$DCR(T) = DCR(T_{amb}) \cdot 2^{\frac{T - T_{amb}}{T_{1/2}}} \quad (5.1)$$

from which, considering also equation 3.15, ENC at 0 °C is slightly inferior to half of the same at 20 . If we consider the noise charge for the future INSERT module, the improvement in DCR is compensated by the worsening in the  $A_3$  factor for the gated integrator, which collects more tail dark counts because of its shape. The parameter that gives further benefit to ENC is the ENF reduced from 1.6 to 1.2.

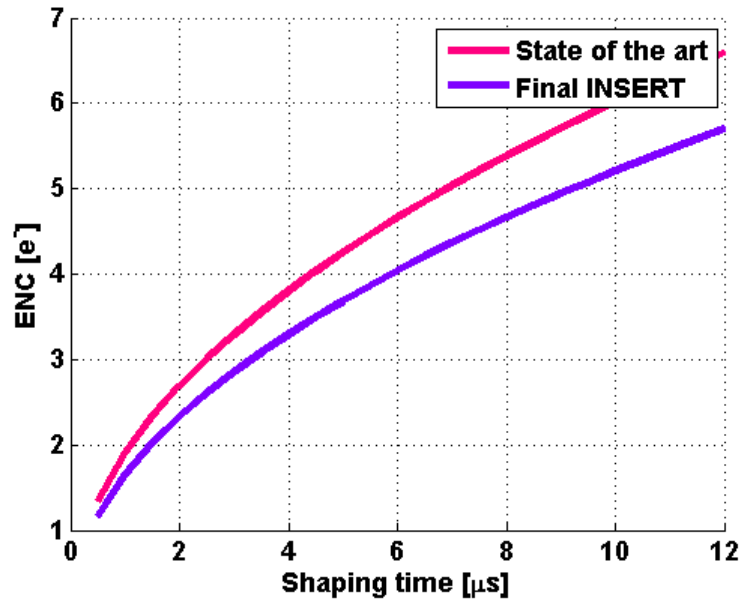
On the other side, the huge difference between the RC and gated integrator filters is clearly visible in the expected ballistic deficit trends (Figure

**Chapter 5. Detection module performance and results**



**Figure 5.2:** (top) PDE and (bottom) DCR as function of the overvoltage for different microcell dimensions in a RGB-HD SiPM (FBK-IRST). The PDE plot is in linear scale, while the DCR y axis is logarithmic. Courtesy of FBK Trento, Italy.

## 5.2. Theoretical and simulated expectations



**Figure 5.3:** ENC estimated for a single merged channel (2 times 2 SiPM for a  $64 \text{ mm}^2$  active area). The parameter is given for the two configurations under analysis and as function of the filter shaping time.

5.4).

The gated integrator is definitely capable to collect more photoelectron signal, then favoring SNR.

This aspects have a direct consequence on the estimated energy resolution. Figure 5.5 depicts the contributes to resolution calculated for the state of the art configuration (simulating a  $0 \text{ }^\circ\text{C}$  temperature on the system): the noise component is the dominant one and rises with the shaping time, which means that the DCR is a key factor for resolution at the present time and thus cooling is a mandatory condition to limit energy resolution broadening. An optimum energy resolution of 13.4 % is obtained at a shaping time of approximately  $1.5 \mu\text{s}$ , which is a too short time estimation with respect to the experimental condition, as it is going to be described in the next sections.

In Figure 5.6 the energy contributes analysis is repeated for the detection module implementing new RGB-HD SiPMs and gated integrator filter. The effect of reduced ballistic deficit and increased PDE, together with significantly reduced ENF, brings to a sensible improvement in the statistical

Chapter 5. Detection module performance and results

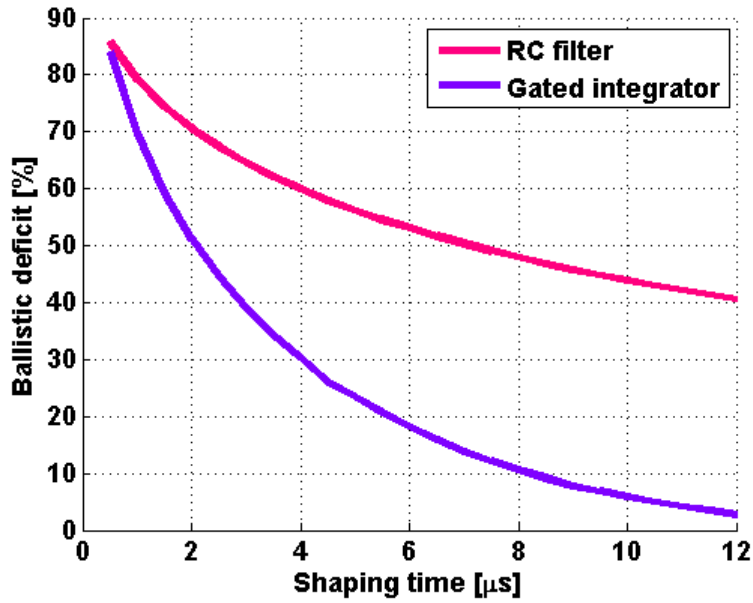


Figure 5.4: Estimated ballistic deficit (BD) when shaping with either RC or gated integrator filter the scintillation decay signal from a CsI(Tl) cooled at 0 °C.

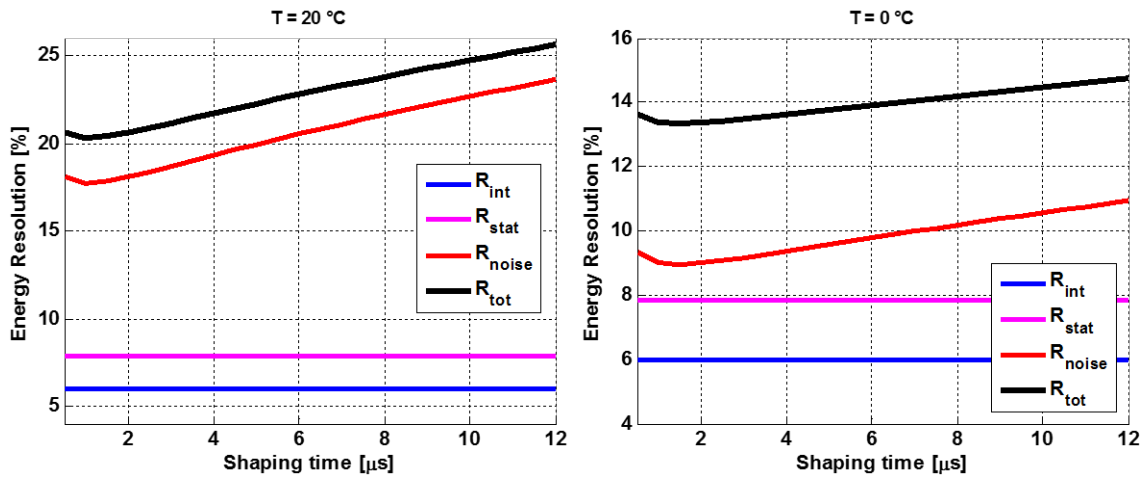
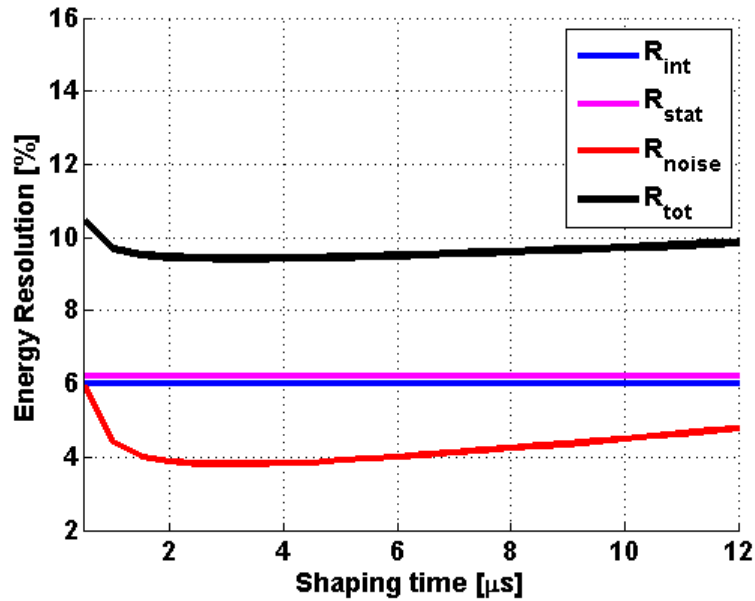


Figure 5.5: Energy resolution and its components for the state of the art INSERT prototype, estimated through the analytical model described in equation 3.19 and considering ambient temperature (left) or 0 °C cooling (right). The noise component results the dominant one for energy resolution. Data are plot as function of the filter shaping time.

## 5.2. Theoretical and simulated expectations

and noise resolution components. The resolution worsening at long shaping time is particularly reduced due to the fact that the noise contribution is no more a dominant effect.

In this case an optimum energy resolution of 9.5 % has been estimated at 3  $\mu\text{s}$  shaping time.



**Figure 5.6:** Energy resolution and its components for the final INSERT detection module. The improvements in SiPM technology and readout filtering should significantly reduce the noise contribute and attenuate also the statistical one. Data are plot as function of the filter shaping time.

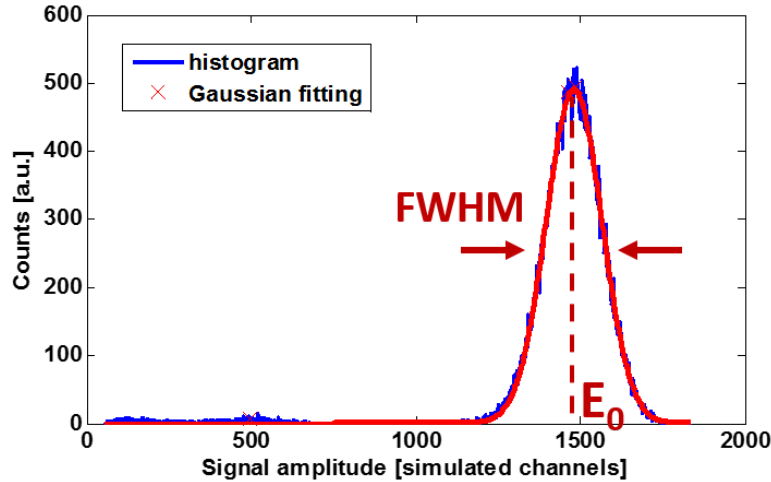
### 5.2.3 Simulation results

#### Energy resolution simulations

For a further estimation of the system energy resolution, the Montecarlo simulator has been adopted: the simulated gamma-camera has been irradiated with an uniform XY distribution of events (the Z of interaction is computed by the GEANT4 routines embedded in the absorption physics model). 100 thousand events have been elaborated with the optical simulator, in order to have sufficient statistics but also limit the overall computational time (approximately 11 events/sec with the current configuration). Then optical data have been filtered considering the SiPMs and electronics

## Chapter 5. Detection module performance and results

parameters.



**Figure 5.7:** Simulated signal amplitude histogram, fitted by means of a Gaussian curve. The energy resolution is estimated from the FWHM and  $E_0$  of the interpolation function.

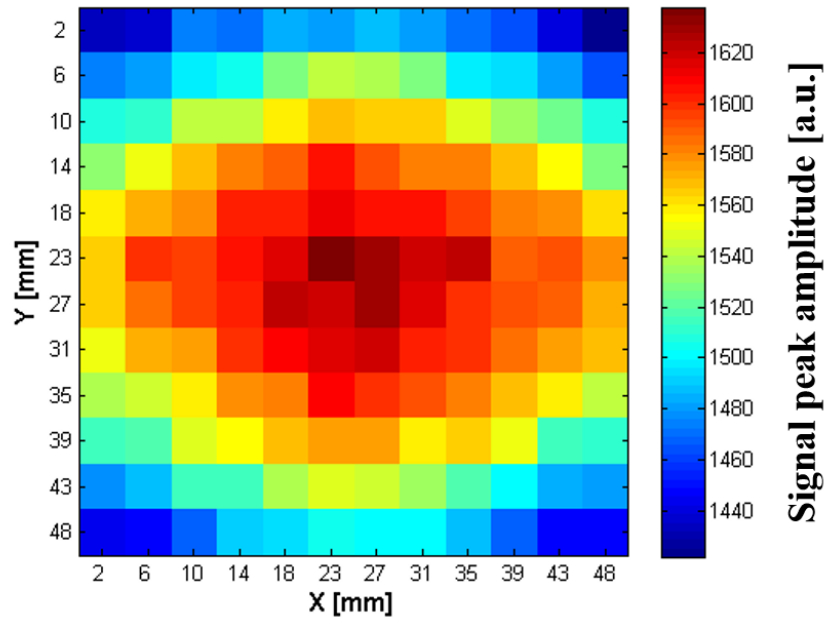
The elaboration has been repeated considering four different shaping time for the filters (2.5, 5, 7.5 and 10  $\mu\text{s}$ ) and also with the distinct configurations for the state of the art prototype and the final INSERT gamma-camera.

Given the output matrix ( $[N_{events} \times N_{channels}]$ ) the signal amplitude histogram is computed (Figure 5.7) and the resolution is obtained by fitting the peak curve with a Gaussian function. The energy resolution estimated is equal to the FWHM over the peak position of the Gaussian curve.

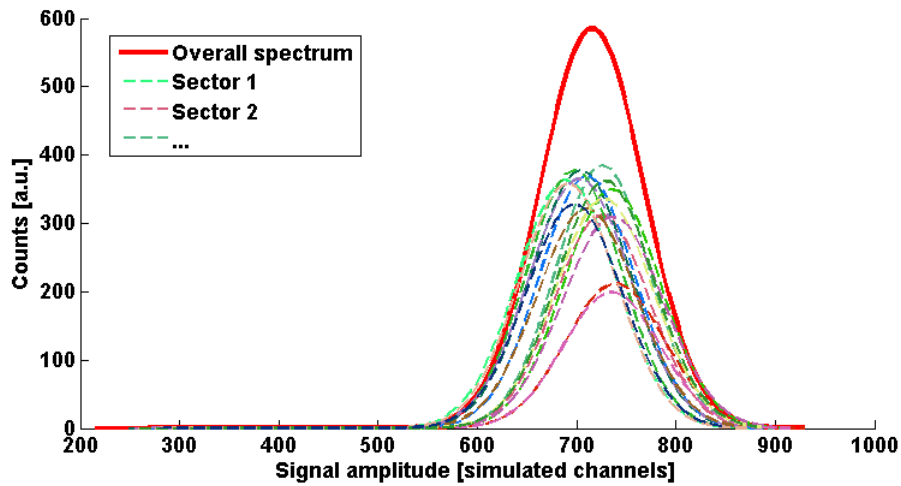
Figure 5.8 depicts the peak position of the amplitude histogram as function of the position in the XY reconstruction plane: this distribution has been calculated by evaluating the energy resolution only in a limited sector of the XY plane (considering the energy of the events which fall into that area) and then repeating the operation for all the sectors covering the overall detection plane.

The amplitude histograms for the gamma-rays absorbed in the central area of the crystal present an higher peak position with respect to those which interacted at the edges and at the corners: this non-uniformity in energy response produces a broadening in the overall spectrum (Figure 5.9). The information from matrix in Figure 5.8 can be employed to spatially

## 5.2. Theoretical and simulated expectations



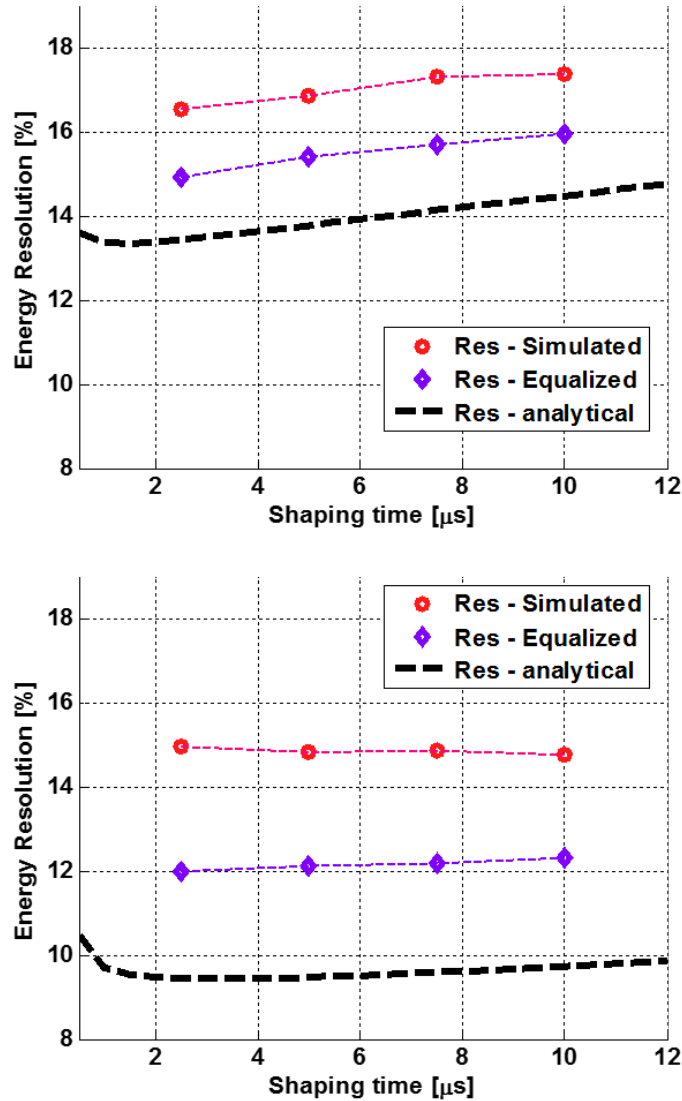
**Figure 5.8:** Spatial distribution of the amplitude peaks ( $E_0$ ) for a sampled number of regions in the scintillator XY plane. The collection efficiency  $\eta_{coll}$  varies with the crystal position and produces local modifications to the energy spectrum.



**Figure 5.9:** Effect of overall energy spectrum broadening due to the different energy peak distribution in the crystal XY space.

## Chapter 5. Detection module performance and results

equalize the energy resolution and reduce the total energy resolution.



**Figure 5.10:** Simulated energy resolution as function of the filter shaping time for the state of the art prototype (top) and for the final INSERT module (bottom). The energy resolution has also been corrected through the energy equalization map. Estimated resolution estimated with the analytical model is plot for comparison.

Figure 5.10 presents the results for the simulated energy resolutions in the two cases under analysis. Considering the equalized resolutions, the



## 5.2. Theoretical and simulated expectations

---

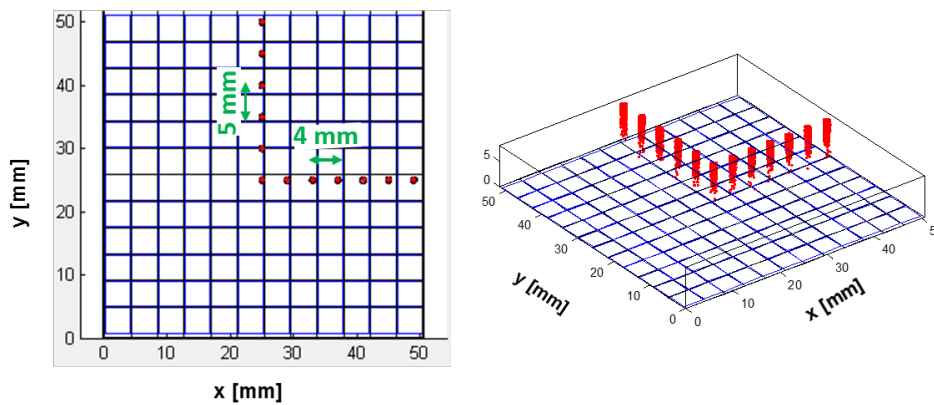
estimation for the state of the art prototype does not fit with the project requirements, while, for the final INSERT configuration, the simulator forecasts an approximately 12 % in energy resolution, which is practically the upper boundary limit for the spectroscopic requirements.

The simulated curves are parallel to the analytical trend for the overall resolution and this relies on the common statistical bases shared by the two models. Nonetheless the simulated curve suggests a worse estimation for the resolution since the simulator also considers the space as a further component for parameter fluctuation: the energy peak gradient described in Figure 5.8 demonstrate that the number of photons collected in the crystal depends on the coordinates of interaction, thus  $\eta_{coll} = \eta_{coll}(X,Y,Z)$ , which was not considered into the analytical model.

## Chapter 5. Detection module performance and results

### Simulated image reconstruction

The Montecarlo simulator is the only tool that could allow us an estimation of the imaging performance of the detection modules. The irradiation profile has been designed in order to retrieve information on the expected spatial resolution and to assess some preliminary reconstruction performance for the *Modified Centroid Method* (MCM) and the *Maximum Likelihood* (ML) algorithm based on the experimentally extrapolated *Light Response Function* (LRF).



**Figure 5.11:** Simulated irradiation profile for the study of the intrinsic spatial resolution for the detection module. A sequence of point-size collimated beams collide on two perpendicular lines with origin in the crystal centroid. The 7 points in the X axis are separated by 4 mm, while the 6 points in Y axis by 5 mm.

Figure 5.11 shows the simulated irradiation strategy: two perpendicular rows of point-like collimated beams cover the central X and Y positions in the crystal. The points are separated by 4 mm in the X direction and by 5 mm in the Y direction. The central point is irradiating the crystal centroid. The reconstructed images will thus give an idea of the imaging performance of the gamma camera as function of the distance of the gamma interactions from the center of the scintillator.

The data are elaborated as like in the previous simulation, then the distribution image is reconstructed using either a MCM with optimized baseline subtraction or ML algorithm. For the latter, the LRF model is obtained from the simulated flood irradiation already generated for the energy resolution estimation.

The *Point Spread Functions* (PSFs) of the events distributions have been interpolated with a Gaussian function (for both X and Y directions) and

## 5.2. Theoretical and simulated expectations

an average spatial intrinsic resolution is thus obtained from the FWHM, as function of the distribution from the crystal center.

Figure 5.12 depicts the reconstructed image for the INSERT prototype, obtained with both MCM and ML algorithms.

No uniformity corrections have been applied to the image since the statistic on the number of flood data in the correction map pixels was too limited.

The Modified Centroid Method reconstruction suffers of non-linearity at the edge of the FOV, which is reduced of 4 mm on each boarder because of algorithm limits. The position of the reconstructed PSFs is then not adherent with the irradiation profile, when the distance with from the center of the crystal is relatively high. The point distributions at the edges are slightly overlapped and it is difficult to resolve them. On the other side, the ML reconstruction, based on the flood retrieved LRF model, performs better linearity. On this point, it is noteworthy that the choice on the baseline subtraction on the flood image as starting point for the LRF model extraction plays quite an important role in the final linearity performance of the ML method. The baselines referred in the images presented from now on has been arbitrarily optimize in order to obtain a good level of linearity in the ML reconstructed images. However an automatic algorithm for optimal baseline subtraction is under design. The FOV is restored to the entire crystal plane.

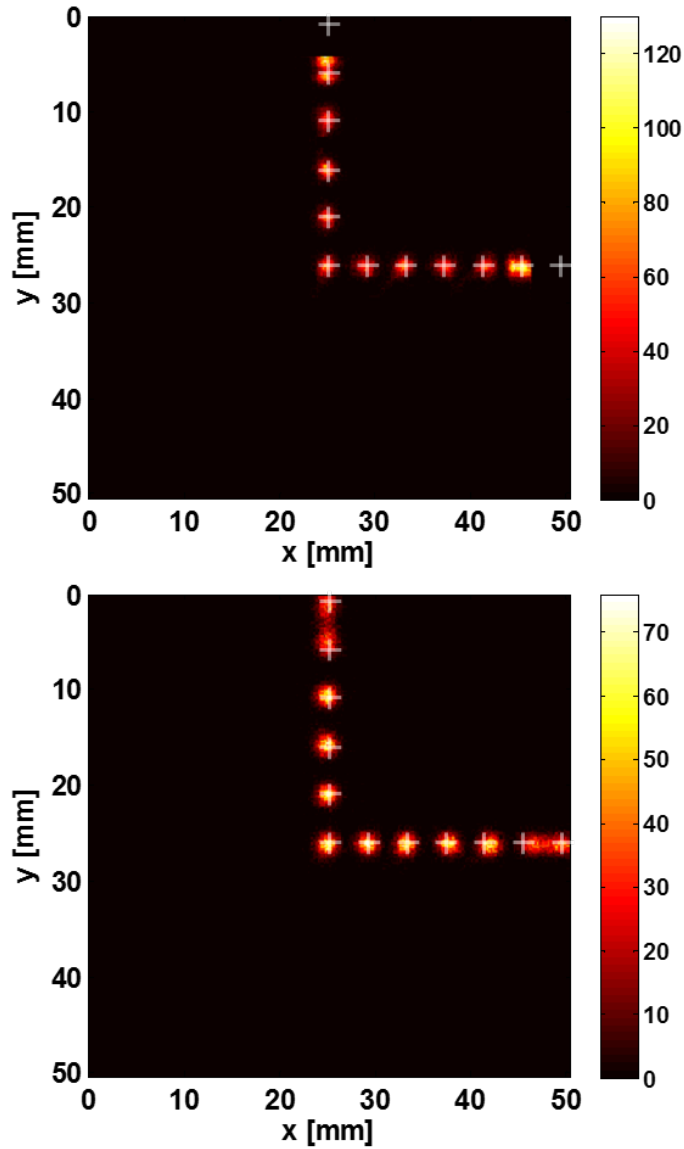
Figure 5.13 depicts the reconstructed image for the final INSERT detection module. The improvement of the PDE, thus pulse signal, and the reduction in DCR, ballistic deficit and ENF produce a sensibly better outcome in intrinsic spatial resolution.

This has been estimated for both the configurations by measuring the FWHM of the PSF for the point distributions in the ML reconstructed image (with better linearity), then the dataset of intrinsic resolutions as function of the distance from the center of the FOV has been fitted by means of spline interpolation (with low smoothing factor,  $< 0.02$ ) in order to define an average trend for the spatial resolution.

Thus, intrinsic spatial resolution (Figure 5.14) has been estimated as function of the distance from the crystal centroid (the results on the X and Y lines have been mixed considering geometrical symmetry of the detection module).

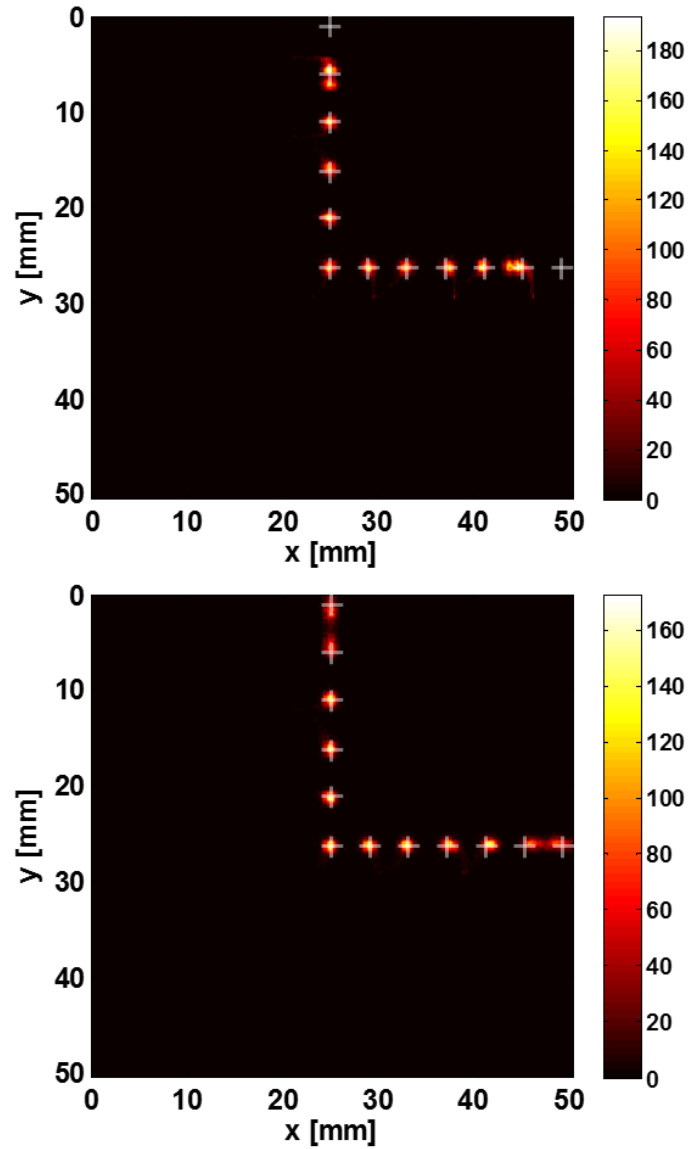
The intrinsic resolution estimated for the prototype presents a minimum in the center of the FOV between 1.5 and 1.75 mm FWHM, rapidly in-

Chapter 5. Detection module performance and results



**Figure 5.12:** *Modified Centroid Method (MCM - top) and Maximum Likelihood (ML - bottom) image reconstruction of the simulated grid profile for the state of the art prototype. The baseline for the MCM subtraction has been optimized for linearity. The ML reconstruction achieves better linearity and recover the entire crystal FOV. In transparency two perpendicular series of crosses define the expected positions for the spots correct localization.*

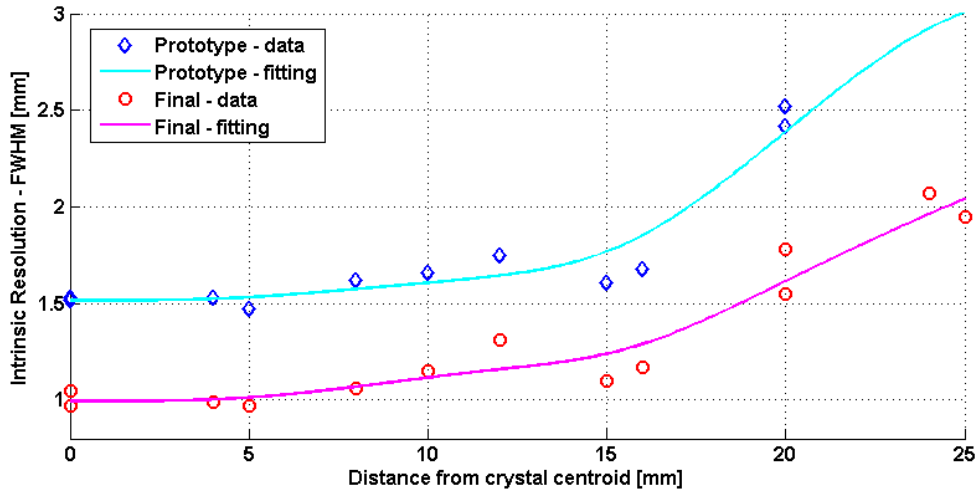
## 5.2. Theoretical and simulated expectations



**Figure 5.13:** MCM (top) and ML (bottom) image reconstruction of the final INSERT module. The spatial resolution for this configuration is sensibly upgraded with respect to the prototype performance. In transparency two perpendicular series of crosses define the expected positions for the spots correct localization.

creasing at the edge of the crystal geometry because of the limited spatial information related to the scintillator coating strategy. the estimation of spatial resolution at the edge of the FOV is more difficult and often unprac-

## Chapter 5. Detection module performance and results



**Figure 5.14:** Estimation of the intrinsic spatial resolution as function of the distance from the crystal centroid: the evaluation is performed from the simulation data for both, state of the art prototype (blue) and final INSERT module (red). The datasets have been fitted by means of smoothing spline interpolation.

tical, then reliability of the interpolation for high distance from the crystal center is quite poor. The simulated performance for the first configuration are far from the INSERT requirements ( $< 1$  mm FWHM resolution on a  $40 \text{ mm} \times 40 \text{ mm}$  CFOV area). With the final INSERT module, we expect definitely better results: approximately 1 mm FWHM resolution in a  $10 \text{ mm} \times 10 \text{ mm}$  central FOV and also good resolving capability up to the edges of the FOV. However, these results somehow warn that imaging performances, also in the best latter case, are foreseen to stay at the upper boundaries of the project requirements, then some conservative measurement should be taken into account: one possible solution is to redefine with the project partners the requirements and try to find out if these can be relaxed, in an overall system logic and strategy. Otherwise, the final design needs some redesign considerations that will probably compromise one of the module performance in order to advantage the others. This discussion is postponed after the presentation of the experimental results.

### 5.3. Experimental setup: INSERT detection module prototype

## 5.3 Experimental setup: INSERT detection module prototype

The prototype gamma-detection module for the preclinical INSERT SPECT has been characterized by means of experimental tests. The present section describes the setup implemented for the measurements.

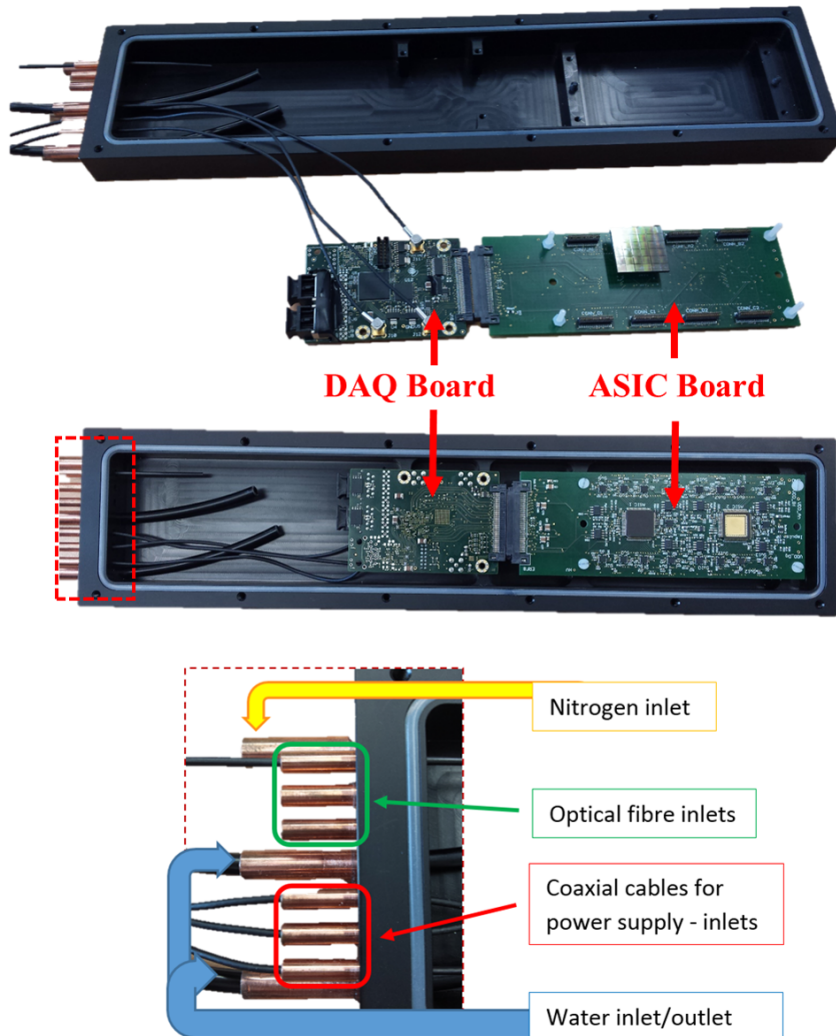
The prototype is constituted by the gamma-ray detector (CsI(Tl) crystal and SiPMs tiles) with the ASIC and DAQ boards connected together. For this particular measurements, the rectangular base crystal (CsI(Tl), Scionix) has been covered with a property diffusive material, with characteristics similar to the Teflon, but thinner in geometry. The Coolpoly heat sink is placed in between the tiles and the ASIC board and flexible, black plastic pipes provide inlet and outlet for the cooling liquid. A thermal-cryostat (CF31, Julabo) has been employed to pump refrigerated oil into the cooling circuit. The temperature on the SiPMs arrays is monitored through the PT100 sensor on the tile board bottom.

The complete module is protected by a black, MR compatible plastic box (Figure 5.15), composed by a base with edges and a cover and designed in order to also perform compatibility tests in the commercial MR scanners. In this latter case the box also requires an external shielding provided by a thin layer of sprayed copper. For our scintigraphy measurement the box is needed due to the followings:

- to provide visible light shielding, since it would interfere with the SiPM detection.
- to thermally insulate the crystal and SiPM tiles from the external world and optimize and stabilize the cooling strategy.
- to create a dry environment for the crystal and the electronics. In facts, when the system is cooled down, the dew point of the air inside the box is reached and the water particles suspended start to condensate, with dangerous consequences for the crystal and the electronics. For this reason the atmosphere around the detector is saturated with dry Nitrogen.

One humidity sensor (HIH-4000, Honeywell) is placed inside the box to monitor the Nitrogen flow. A number of copper pass-through holes on one of the box sides. Two of them are for the cooling pipes, one for the Nitrogen inlet and the other are reserved to all the optical fibers and coaxial cables for signal and power supply transmission in and outside the box. The

## Chapter 5. Detection module performance and results



**Figure 5.15:** Details on the setup system and box for the experimental campaign: the black plastic box provide stability, light shielding and an insulated environment for the INSERT prototype. A number of passing through copper pipes allow the in/out signal transmission, power supply, cooling and Nitrogen inflation.

communication and biasing system is the same described in section 3.3.6.

All the measurements have been performed at approximately 0 °C (for every test, the exact temperature recorded is reported). The experimental



## 5.4. Experimental results

session for testing of the INSERT detection module prototype have been performed at the research department of nuclear medicine in *ospedale San Raffaele* (Milano). The measurements have been performed with  $^{99m}\text{Tc}$  (140.5 keV, activity between 0.1 - 1.2 mCi) source and, for energy calibration purposes, have been repeated with  $^{57}\text{Co}$  (122 keV, activity approximately 0.1 mCi).

### 5.4 Experimental results

The performance of the INSERT prototype described in the previous chapters have been tested through different experimental measurements. In the following sections the measure protocol is briefly described and then the results are reported. The experimental measurements have been compared to the simulated forecasts and thus a discussion on the outcomes obtained and on the model validity is proposed.

#### Energy resolution measurements

The energy resolution has been retrieved through a flood irradiation of the scintillator: the radioactive source (either  $^{99m}\text{Tc}$  or  $^{57}\text{Co}$ ) has been placed at a distance of approximately 60 cm above the entrance crystal plane, in order to assess a uniform gamma-ray distribution over the XY scintillator plane. Temperature have been monitored on only one PT100 sensor and, for cooling stability reasons, the measurements were performed with the SiPM matrix refrigerated at approximately  $+3\text{ }^{\circ}\text{C}$ . The time window required for each measurement is rather short, since no collimation is required: with a 3 minutes acquisition, more than 500000 gamma events were collected for each trial.

Two main test sections have been performed for energy resolution analysis:

1. Flood irradiation with fixed RC shaping time ( $7.5\ \mu\text{s}$ ) and varying the bias voltage ( $V_{bias}$ ). These measurements allowed to define the optimum working condition for the system.
2. Flood irradiation with fixed, optimal  $V_{bias}$ , and exploring different shaping time for the RC filter.

Each measurement has been repeated with  $^{99m}\text{Tc}$  and  $^{57}\text{Co}$ . The energy peak position for both the radiosources has been estimated through Gaussian fitting of the main peak in the amplitudes histogram. Then, the peak

Chapter 5. Detection module performance and results

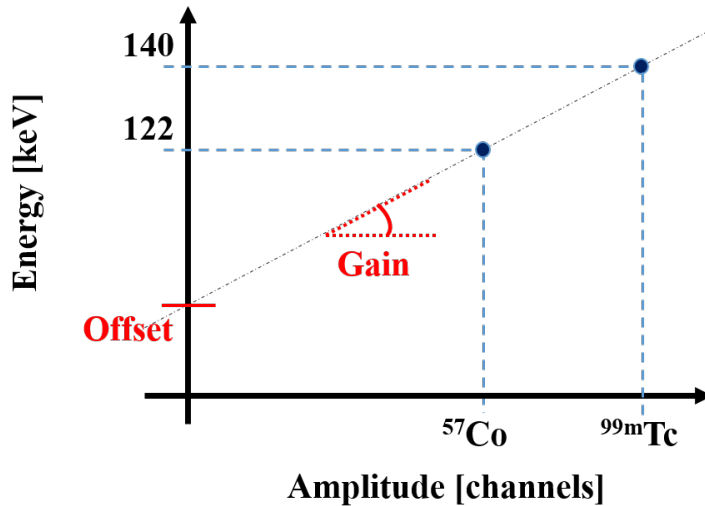


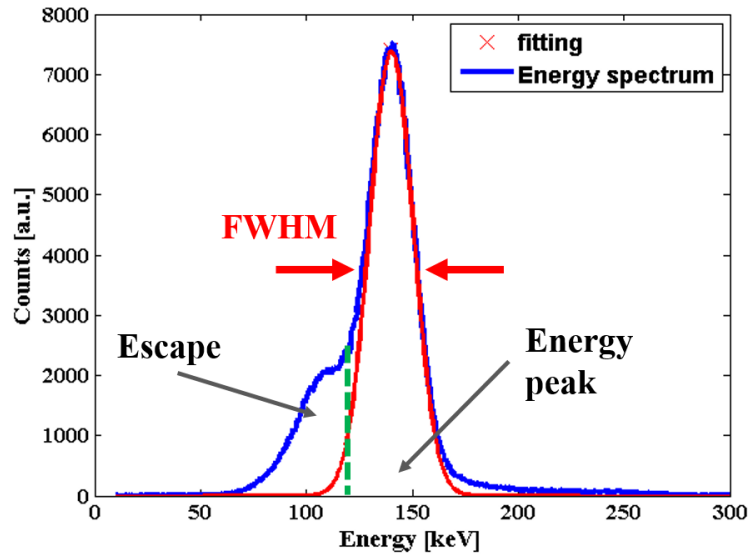
Figure 5.16: Energy calibration curve employed to correct the experimental data and obtain the measured energy spectrum.

values have been employed to linearly calibrate the system for the energies (Figure 5.16): *Gain* and *Offset* are calculated and applied as correction coefficients to the data in the amplitude histogram. The result is a calibrated energy spectrum for each radioactive source, as depicted in Figure 5.17, from which energy resolution can be properly estimated by means of Gaussian fitting.

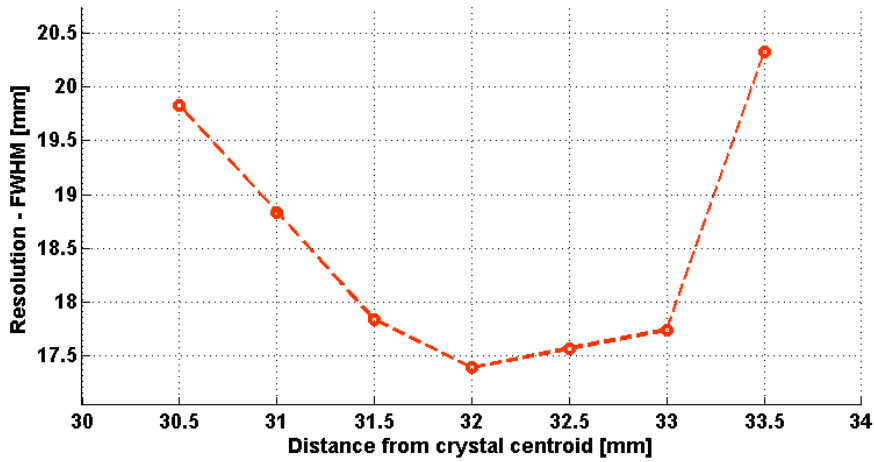
Figure 5.18 reports the energy resolution as function of the bias voltage, for which the optimum is found for  $V_{bias} = 32$  V. As previously described, the presence of an optimal value depends on the dependence of parameters like PDE, ENF and DCR from the  $V_{OV}$ : Figure 5.19 depicts the curve of the PDE normalized for the ENF value as function of the overvoltage (for RGB-HD SiPMs), which is connected directly to the statistical contribute for energy resolution. For low  $V_{OV}$  the PDE rises faster than ENF, then the trend is overturned and an optimal value is found in the two parameters ratio.

Figure 5.20 describes the measured energy resolution with  $^{99m}\text{Tc}$ , for different shaping times (the bias voltage is fixed at the optimal overvoltage). The results are also compared with the simulations previously obtained.

### 5.4. Experimental results



**Figure 5.17:** Energy spectrum for  $^{99m}\text{Tc}$  obtained through a flood irradiation of the prototype crystal (shaping time equal to  $7.5 \mu\text{s}$ ). The energy resolution is estimated from the parameters of a Gaussian curve fitting the energy peak. The energy spectrum is also employed to subtract the gamma-events that contain no useful imaging information (see escape peak).



**Figure 5.18:** Measured energy resolution as function of the bias voltage ( $\tau_{shaping} = 7.5 \mu\text{s}$ ). The breakdown voltage for the SiPMs is approximately 29 V at room temperature, but is reduced to 28.5 V at  $0^\circ\text{C}$ . A optimum is found at  $V_{bias} = 32 \text{ V}$ .

Chapter 5. Detection module performance and results

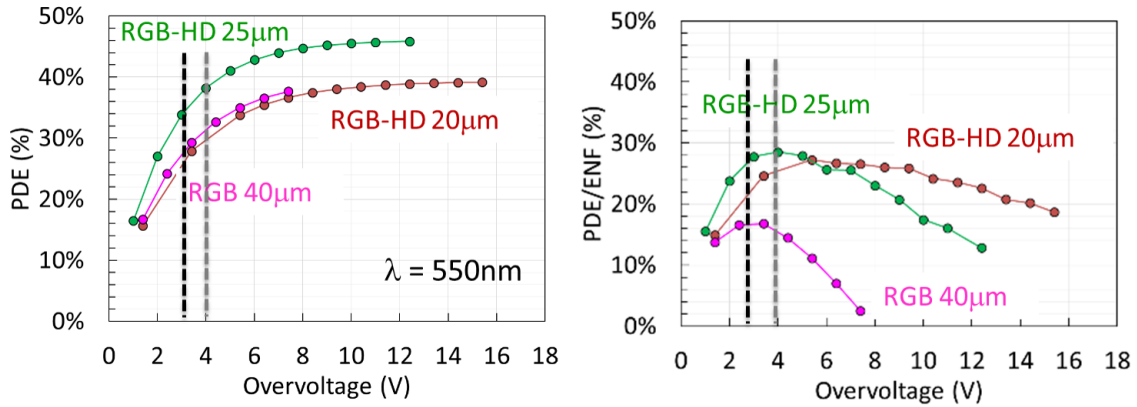


Figure 5.19: PDE (left) and PDE/ENF (right) as function of the overvoltage for  $\lambda = 550$  nm and for RGB-HD technology. The parameters ratio presents a maximum value for an optimal overvoltage around 3-4 V. Courtesy of FBK Trento, Italy.

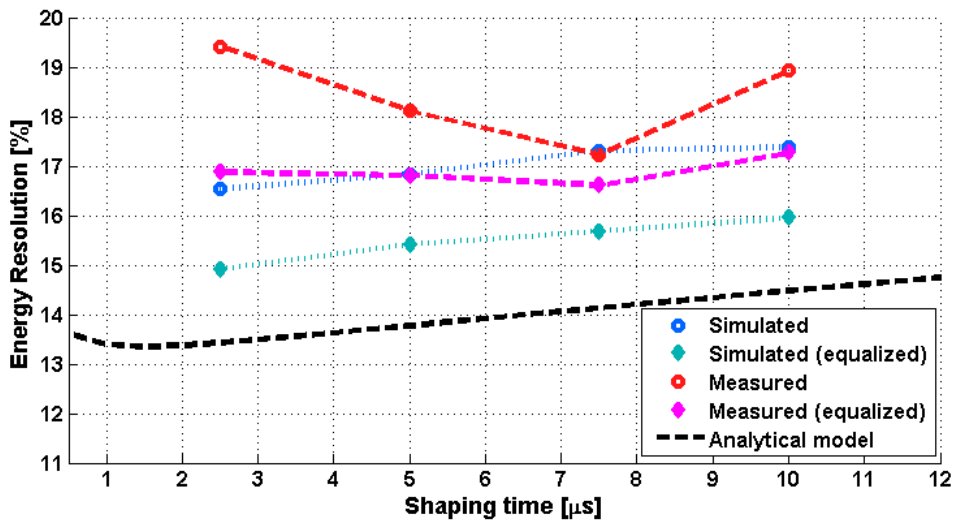


Figure 5.20: Measured energy resolution at different filter shaping times for the INSERT prototype ( $V_{bias} = 32$  V). The energy has been also equalized by means of correction map. The results are compared with the simulated outcomes.

The measured resolution presents an optimal value of approximately 17.2 % ( $\tau_{shaping} = 7.5 \mu s$ ), while the model and simulations predict a minimum for the energy resolution at lower shaping times. The profile is quite smoother after energy equalization of the curve, however the trend profile

## 5.4. Experimental results

remains the same, with a best resolution of 16.6 %. The experimental and simulated results are quite in accordance for the optimal values, but diverge at different shaping times, mostly for the shorter ones.

This difference it is probably to be related to the limit in the model for the incomplete charge collection, then ballistic deficit effect. Equation 3.12 typically describes well the energy performance for those systems that implements fast scintillators. On the contrary, the slow CsI(Tl) is more difficult to be modeled and particularly when the scintillation is delayed by crystal cooling: a temperature pattern should be considered and simulated in the crystal volume and decay time fluctuations accounted in the overall estimation.

Possible variation to the analytical formula (then to the simulation model) can be proposed to better fit the experimental trend, however the intimate physical and systems phenomena involving charge collection requires a further in-depth analysis. One model proposed considers a dependence from BD of the statistical contribute to energy resolution:

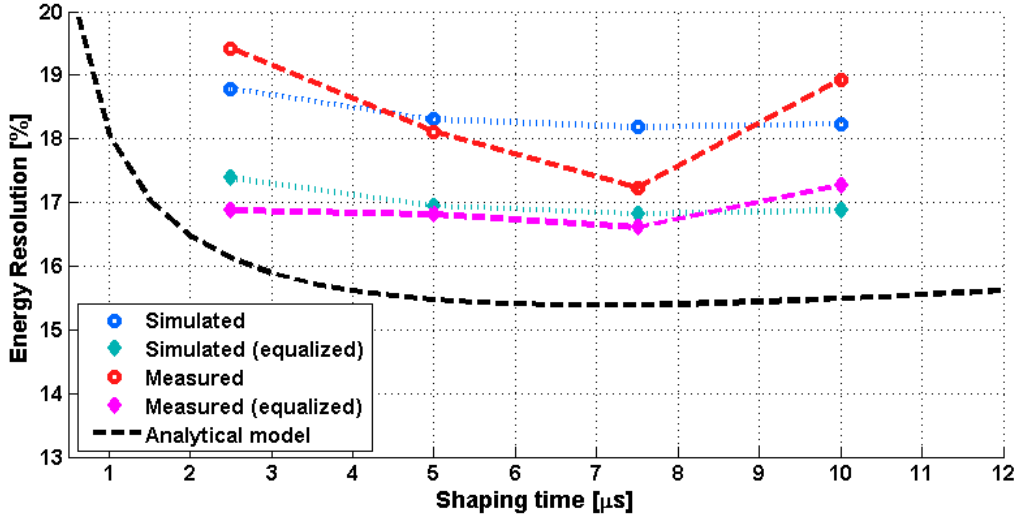
$$R_{En} = 2.35 \sqrt{\frac{\Delta E_{int}}{E_{int}} + \frac{ENF}{\langle N_{pe}(1 - BD) \rangle} + \frac{ENC^2 N_{SiPM}}{\langle N_{pe} M(1 - BD) \rangle^2}} \quad (5.2)$$

which is obtained by considering the effect of ballistic deficit as an efficiency factor acting also on the mean signal in the statistical contribute to energy resolution (but with no modifications on the variance). This obviously represents a simplification, since the convolution between the light signal and the shaping filter involves more complex correlations between the terms on the different contributes in the formula. Nevertheless it is a starting hypothesis to handily verify the implications of the defects in charge collection into the overall energy estimation.

Figure 5.21 shows the comparison between the energy resolution simulated with the modified equation 5.3 and the experimental results: the better adherence of the matching does not give absolute validity to the new formulation, but gives evidence that the original model for charge collection was underestimating the energy resolution for short shaping times.

The energy distribution on different regions of the XY plane for the experimental case (Figure 5.22) exhibits a less uniform pattern if compared to the simulated one (previously proposed in Figure 5.8). The causes for this effect have to be found in non-uniformities in the coating adherence on the crystal, micro-bubbles in the optical glue coupling scintillator and

## Chapter 5. Detection module performance and results



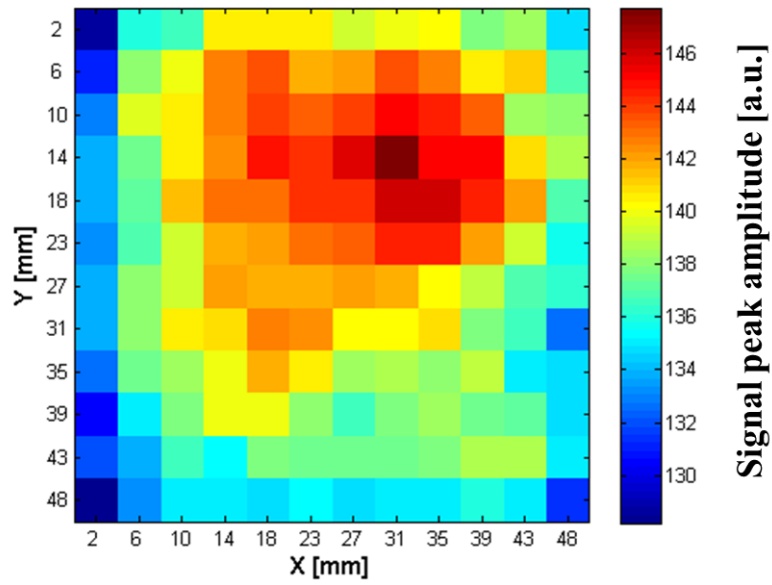
**Figure 5.21:** Comparison with the measured energy resolution and the analytical model result considering a different model for the ballistic deficit (equation 5.3).

SiPMs array and mostly on the thermal gradient on the photodetectors array, that locally modifies the SiPMs multiplication gains and DCR. The relative variation of energy resolution in the plane  $E(x,y)$  can be estimated as:

$$\langle \Delta E(x,y) \rangle = \frac{\max(E(x,y)) - \min(E(x,y))}{\langle E(x,y) \rangle} \quad (5.3)$$

This can be used to compare the simulated and experimental variations, which respectively score  $\Delta E(x,y) = 13 \%$  and  $\Delta E(x,y) = 14 \%$ . The energy distribution follows slightly different distribution, but the average variation is practically the same for the simulated and experimental case.

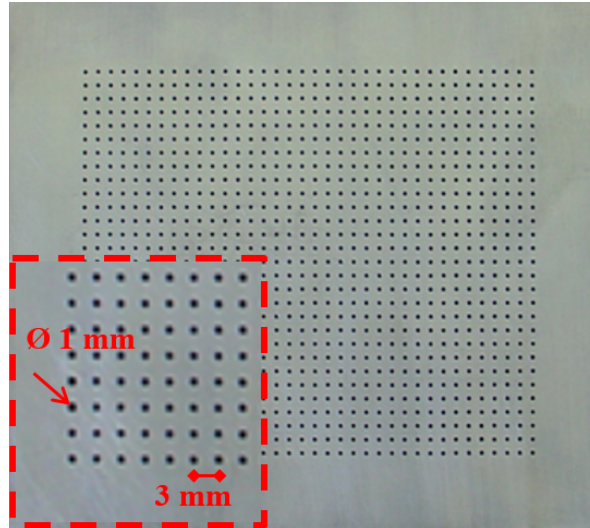
## 5.4. Experimental results



**Figure 5.22:** Signal peak distribution (from which energy equalization map is retrieved) for the experimental case: the asymmetries are most probably related to a temperature gradient in the SiPM matrix, due to non-uniformities in the cooling strategy.

## Chapter 5. Detection module performance and results

### Image reconstruction from experimental data



**Figure 5.23:** top view of the 4 mm thick, lead grid of holes employed for the estimation of the INSERT prototype intrinsic resolution.

The intrinsic spatial resolution and the FOV performance of the prototype have been tested through the following experimental protocol.

A 4 mm thick lead grid (Figure 5.23), with 1 mm diameter holes separated by 3 mm space one from others, is placed above the crystal entrance plane outside the plastic box. The  $^{99m}\text{Tc}$  has been placed at a distance of 60 cm above the lead grid with the intent to produce an irradiation profile constituted by a square matrix of collimated spots. As referred in section 2.2.1 (equation 2.2) the spatial resolution of the spots is the result of two contributions, the spatial resolution from the collimator, which is considered equal to the hole dimension, and the intrinsic spatial resolution of the gamma-detection module. Thus, the intrinsic resolution is calculated as:

$$R_{intrinsic} = \sqrt{R_{extrinsic}^2 - R_{collimator}^2} \quad (5.4)$$

The box cover introduces an approximately 3 mm gap between the lead grid and the scintillator, but its effect on the overall resolution is considered negligible.

As general comment, these kind of protocol is not the most appropriate for intrinsic resolution retrieval: the holes should be at least two or three times smaller than the intrinsic resolution value to be measured in order to avoid



## 5.4. Experimental results

high error introduced by the variability on  $R_{collimator}$  in formula 5.4. A better solution would be to scan the whole crystal surface with a single hole collimator and digitize the image with less than 0.1 mm/pixel resolution. However this procedure would have required a complex characterization setup to be manufactured and installed and a relatively higher time amount for the system to be defined in its imaging performance.

SiPM matrix was refrigerated at approximately +3 °C. The time required for each measurement is approximately 15 minutes acquisition, more than 2 millions gamma events collected. The biasing voltage has been set to 32 V and the RC shaping time is  $\tau_{shaping} = 7.5 \mu s$ .

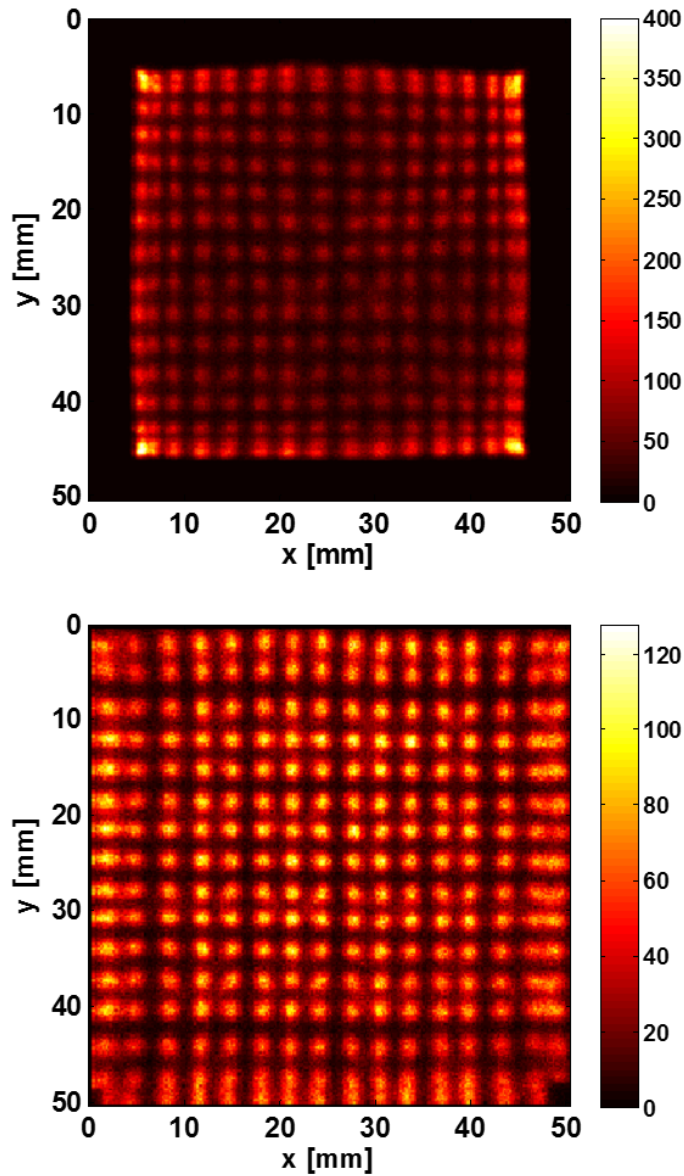
The reconstructed profile of the gamma distribution collimated on the prototype through the lead collimator is presented in Figure 5.24. The images have been generated with both Modified Centroid Method (optimal baseline has been arbitrary defined in order to enlarge the original FOV and maintain good linearity at the same time) and Maximum likelihood algorithm. The LRF model for the ML method has been obtained elaborating the data from the flood irradiation measurement with the iterative algorithm for light response function retrieval. The LRF has been defined through 2D Gaussian functions, the standard deviation for the Gaussian noise applied on the reconstruction data for algorithm convergence to solution is equal to  $\sigma_{noise} = 3 \text{ mm}$ . The algorithm has been stopped when the flood distribution reached an arbitrary uniformity level (5 iterations).

The ML reconstruction, as already mentioned in the simulation section, gives a more uniform imaging result among all the FOV which is restored to the crystal surface dimension. The most remarkable result is the improvement of the imaging capability at the edges.

From the spots matrix reconstruction with ML, the X and Y profiles of the spots on different lines are obtained just by integrating the counts profile on a limited number of rows or columns (Figure 5.25). Since the profile distribution of each spot partially overlaps with the one of the neighbors, a multiple-Gaussian fitting has been adopted for FWHM resolution estimation. The spatial resolution has been evaluated for the most of the spots in the central rows and columns: as like for the simulated case, a dataset of intrinsic spatial resolution as function of the distance from the crystal center is fitted by means of smoothing spline interpolation. Results are depicted in Figure 5.26 and compared with the previously analyzed simulations.

The estimation of the resolution for the spots at the edge of the field of view is much more difficult because of higher superimposition of proxi-

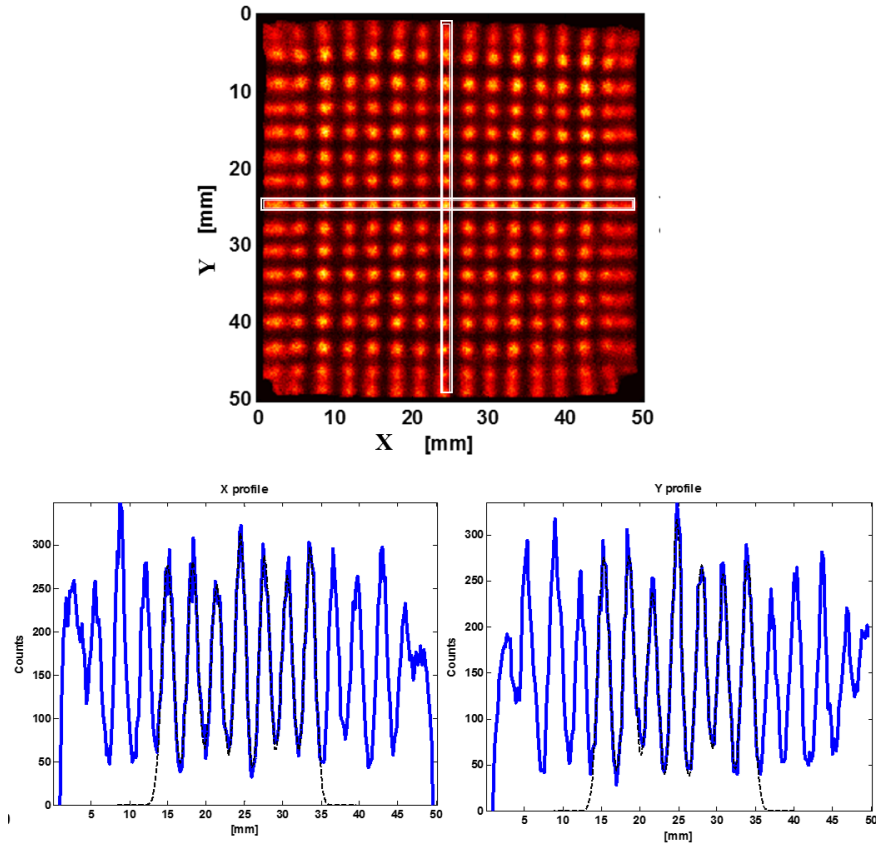
## Chapter 5. Detection module performance and results



**Figure 5.24:** Reconstructed images (MCM on top and ML on bottom) of the experimental grid irradiation ( $V_{bias} = 32$  V,  $\tau_{shaping} = 7.5$   $\mu$ s).

mal spots. For this reason the estimation error on the fitting curve can be very high. The standard deviation error on the intrinsic spatial resolution measured is 0.1 mm. The experimental resolution (1.4 mm FWHM in the center) is slightly inferior to the simulated prediction and presents a consid-

## 5.4. Experimental results

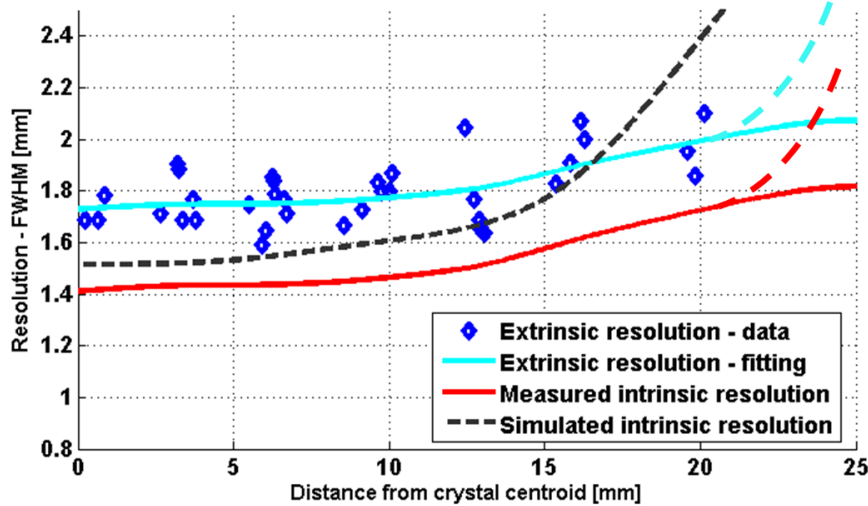


**Figure 5.25:** Description of the protocol for extrinsic resolution estimation: every linear sequence of spots lies on a set of rows or columns in the image; the counts on a limited number of either few rows or columns are integrated and the X (bottom-left) and Y (bottom-right) profiles for the spot sequences are retrieved. By means of multi-Gaussian fitting, the FWHM of each spot is estimated and collected in a dataset.

erably smoother behavior at the edge of the FOV, which represents a welcome outcome for the project objectives. The reason for this discrepancy is probably related to a limited accuracy of the simulator optical model to reproduce the exact light collection and distribution as in the experimental condition. This effect is generally more prominent at the edge of the FOV, where inaccuracies in the model can lead to more sensible differences in light response.

However, the difference between the model and the experimental result is quite limited and the divergence of outcomes far from the detector center

## Chapter 5. Detection module performance and results



**Figure 5.26:** Experimental extrinsic and intrinsic spatial resolution for the INSERT gamma-detection module as function of the distance from the crystal centroid ( $V_{bias} = 32$  V,  $\tau_{shaping} = 7.5$   $\mu$ s). The simulated interpolation for the prototype is plotted for comparison. Data interpolation in the last 5 mm (edge of the FOV) are poor and the actual resolution is probably worsen by side effects.

it is most probably due to the poor number of data employed in the simulated evaluation, correlated to the estimation variance for resolution.

One other possible reason for the measured resolution to show a better result than the simulation is due to the way ENF is modeled: the excess noise factor in a SiPM is caused by optical cross-talk and afterpusing effects, which are phenomena that introduce fluctuation on the signal and worsen the SNR, but their temporal distribution is correlated with the signal itself and, somehow, they also reinforce the amount of charge (it is not only a white noise on signal). The analytical model and the simulator considers only the fluctuations related to ENF, but not its contribute to the signal, which most likely should be accounted for a more accurate forecast on spatial resolution. No other models have been explored for ENF contribute, up to the current development of the simulators.

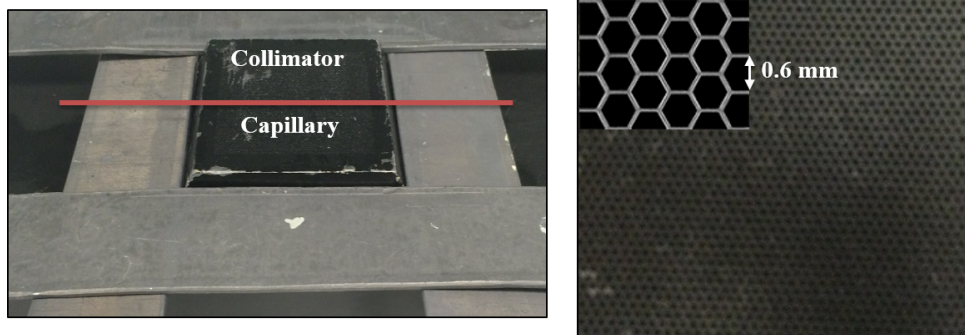
The experimental resolution of the prototype is nevertheless out of the INSERT requirements, then no specifications on the CFOV can be derived, since, by definition, it is the extension of the detector surface for which intrinsic spatial resolution is inferior to a threshold value, given as require-

## 5.4. Experimental results

ment (1 mm).

### Other imaging measurements

Further tests have been performed to assess the preliminary capability of the INSERT detection module prototype: an other typical measurement for the spatial resolution definition is performed by acquiring the irradiation profile of a  $^{99m}\text{Tc}$ -filled capillary tube (0.6 mm) located on a parallel holes collimator composed by hexagonal holes of 0.6 mm in diameter (Figure 5.27).



**Figure 5.27:** Experimental setup with glass  $^{99m}\text{Tc}$ -filled capillary (concept) laying perpendicular to one of the axis of a Tungsten parallel holes collimator (0.6 mm hole diameter).

The capillary has been positioned along both X and Y axis of the crystal plane. The resulting reconstructed image for the Y direction is presented in Figure 5.28: the resolution is measured by selecting a slice of events along few rows or columns, depending on the capillary direction, and integrating the number of interaction counted as function of the perpendicular to the integration axis.

The extrinsic resolution measured are 1.70 mm FWHM for the Y direction and 1.53 mm FWHM. Subtracting the collimator contribute to resolution, the intrinsic one is found ( $R_{int,X} = 1.47$  mm,  $R_{int,Y} = 1.27$  mm).

Finally, the detector was employed to retrieve scintigraphy images from immunodepressed rodents, for a first qualitative evaluation of the project state of the art, but also for motivational act addresses for all the project partners. The measurements were performed taking profit from parallel study activities on mice by our partners in Ospedale San Raffaele.

One laboratory mouse have been injected from the tail with 2.5 mCi of [ $^{99m}\text{Tc}$ ]MDP (Methylene DiPhosphonate), an agent widely employed in

## Chapter 5. Detection module performance and results

---

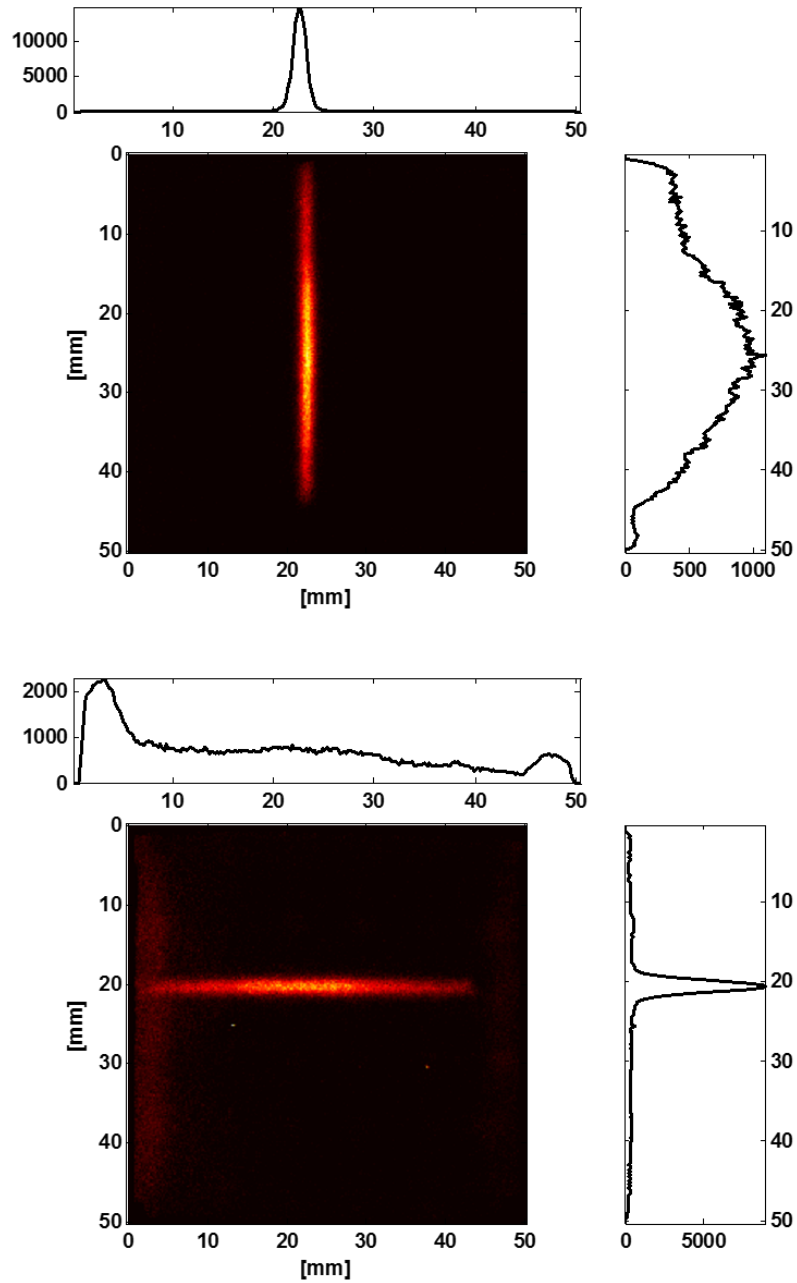
nuclear medicine to detect bone abnormalities, including metastases. After 120 minutes, the subject has been anesthetized with an injection of 1.7 % tribromoethanol and then positioned above the parallel hole collimator (Figure 5.29), taking care to shield all the body compartments which were outside the camera FOV. The mouse have been acquired for approximately 45 minutes.

The collimator is partially translated with respect to the crystal exact position, then the superior part of FOV appears completely black.

A second mouse has been treated with 2.3 mCi of [ $^{99m}\text{Tc}$ ]Tetrofosmin, a drug used in nuclear medicine cardiac imaging. The same acquisition protocol has been followed as the previous mentioned, but with only 60 minutes of time lapse in order to respect hearth uptake dynamic.

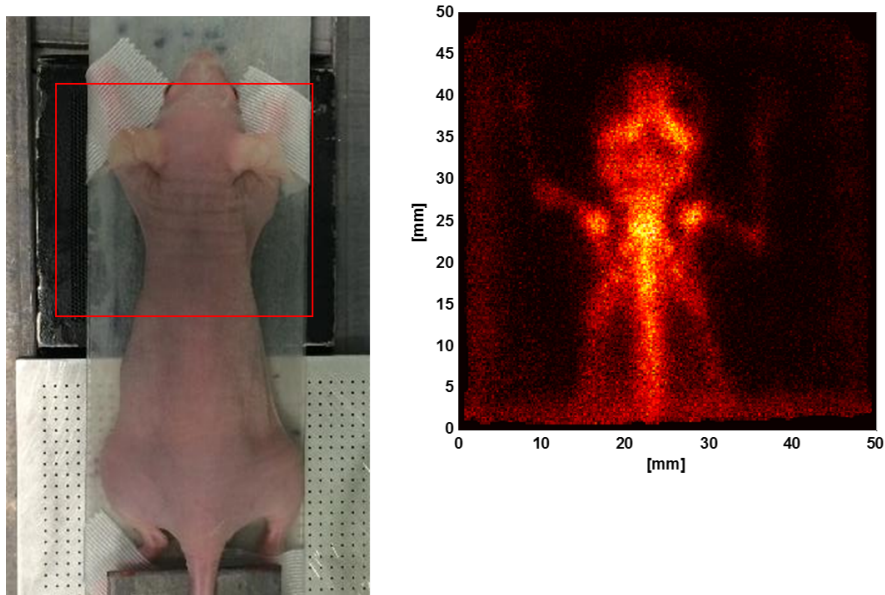
The resulting image is showed in Figure 5.30: the hearth is completely covered by the gamma emission deriving from the cholecyst (the bright element in the center of the FOV). This organ can usually provide image artifacts when [ $^{99m}\text{Tc}$ ]Tetrofosmin or other cardiac agents are employed. To remedy this issue, human patients are fed with a fats-based meal (typically ham) before the scintigraphy acquisition.

### 5.4. Experimental results

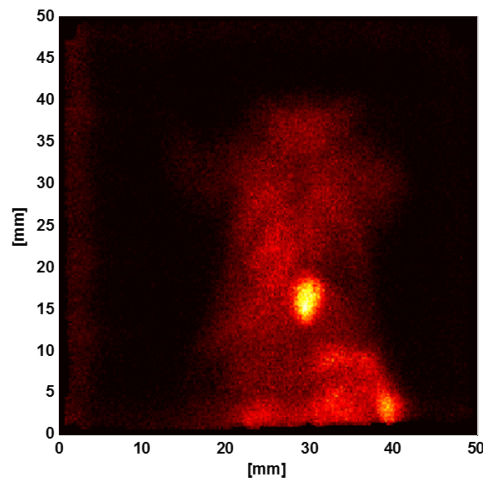


**Figure 5.28:** Reconstruction with ML algorithm of the  $^{99m}\text{Tc}$ -filled capillary (0.6 mm width) positioned along two different directions: parallel to the Y axis (top) and to the X axis (bottom) of the crystal.

## Chapter 5. Detection module performance and results



**Figure 5.29:** (right)  $[^{99m}\text{Tc}]\text{MDP}$  scintigraphy of the upper-body skeletal system of a laboratory mouse positioned above the Tungsten collimator (left). The data have been obtained through the INSERT detection module prototype and elaborated with ML method.



**Figure 5.30:**  $[^{99m}\text{Tc}]\text{Tetrofosmin}$  scintigraphy of the trunk of a laboratory mouse for hearth definition. The uptake from the cholecyst (bright in the center) produces a covering artifact on the image. The data have been obtained through the INSERT detection module prototype and elaborated with ML method.



## 5.5 Final discussion

The INSERT prototype implements RGB SiPM technology for the scintillation light conversion from a monolithic CsI(Tl) crystal covered with 4 layers of white Teflon. The signal from 36 merged ( $2 \times 2$  SiPMs) channels is read by an equivalent number of current mode readout channels with RC filter implemented for pulse shaping ( $\tau_{optimal} = 7.5 \mu\text{s}$ ).

The image reconstruction is performed by both a modified version of the most typical Center of Gravity (CoG) and a Maximum Likelihood (ML) methods applied on the data centered on the main energy peak. A dedicated iterative algorithm allows to retrieve the Light Response Function (LRF) required from the ML method from calibration data acquired through a simple flood irradiation of the system. The algorithm also requires minor tuning of a very limited number of parameters for convergence to solution. The combination of experimental based LRF with ML produces an improved reconstruction method, with automatic calibration of the channels signal and complete recovery of the crystal FOV dimension.

The experimental results, obtained irradiating the prototype with proper collimated patterns of  $^{99m}\text{Tc}$  (140.5 keV), show an optimal energy resolution equal to 16.6 % (equalized through energy correction map) and an intrinsic spatial resolution approximately equal to 1.4 mm FWHM in the center of the FOV, which is extended to crystal surface dimension thanks to a statistical reconstruction method based on maximum likelihood.

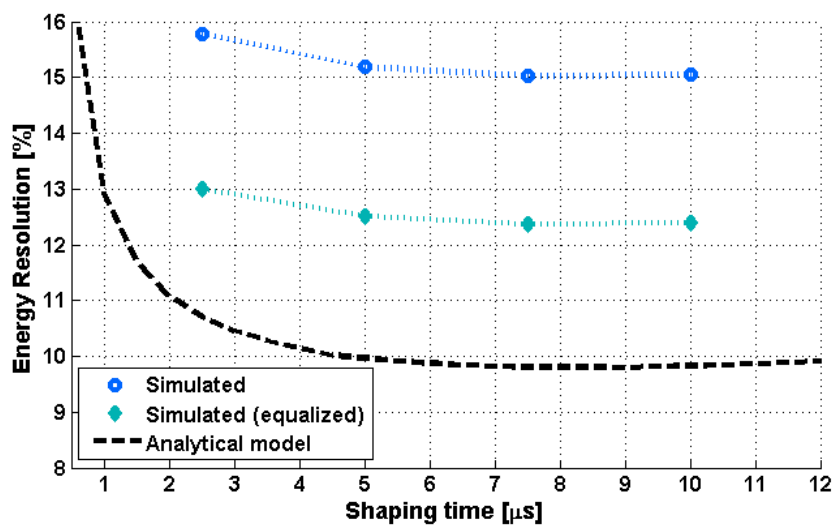
These results have been achieved with a preliminary configuration of the detection system, particularly with a SiPM technology not optimized towards project requirements. However the comparison of these first measurements with the complete system and the simulation performed has made possible to better address the redesign of the gamma camera and to reduce the forecast error on the expected performance from a system with optimized components.

Our intent is to address the development of the final design for the detection module towards the project requirements. On this regard, an advanced RGB-HD technology with better PDE and limited DCR and ENF has been selected. Moreover the next version of the readout ASIC would implement a gated integrator filter which should sensibly reduce the ballistic deficit effect, thus enhancing the SNR of the device and the output performance.

The performance of both the systems, the state of the art prototype and the future version of the INSERT module, have been evaluated by means of analytical model and Montecarlo simulations. The simulated outcomes

## Chapter 5. Detection module performance and results

for the energy resolution show good adherence with the experimental results, particularly for higher filter shaping time. The analytical model do not completely explains all the fluctuations on the signal average, but the absolute energy foreseen by this method is still consistent and correlated with the measured results. An hypothesis of limited description for the incomplete charge collection phenomena into the model has been speculated to explain the lower convergence of the curves for short shaping time.



**Figure 5.31:** Theoretical and simulated energy resolution expected for the final INSERT detection module, considering a different model for the ballistic deficit (equation 5.3).

An alternative model has been proposed just to support a quest for a re-design of the analytical formula to better include the ballistic deficit effect also on other contributes for the energy resolution. The results obtained with the new formula do minimally change the outcome for longer shaping times, which are the ones for which we found experimental optimum. The forecasts for the final INSERT module, in terms of energy resolution, are summarized in Figure 5.31: the best predictor is the simulated curve, corrected with energy equalization among the XY reconstruction plane. The best energy resolution estimated is 12.3 % at 7.5  $\mu\text{s}$ .

The estimated intrinsic resolution has been calculated and reported in Figure 5.14. A resolution of 1 mm in an approximately 10 mm  $\times$  10 mm CFOV is expected, with a progressive degradation up to 2 mm at the very

## 5.5. Final discussion

edge of the FOV. The estimated intrinsic resolutions obtained from the measurements were quite adherent with the simulated expectations (see Figure 5.26), even if the average absolute value was slightly better (0.1 mm FWHM) than the value foreseen. This result gives us an indication that the simulation with the parameters presented can be considered as a conservative forecast and the possible experimental result can present better outcomes.

Although encouraging, the previsions on the final INSERT module, supported by the validation of the simulation tools with the experimental data, suggest a scenario where the best performance obtainable give not too much safety margin for unexpected behavior in the experimental case, otherwise the project requirements would not be respected.

The good matching between experimental and simulated outcomes does not automatically validate anyone of the simulation parameters described in section 5.2.1: the performance comparison can give an address not only to the prediction on further versions of the gamma-camera, but also relevant information on the reliability of some aspects of the custom simulator, which is one of the tools primarily adopted in the design and in the decision process related with the development of the INSERT detection module.

First, above all, the simulated value for the collection efficiency has been found to be around 54.5 % (also considering the 11.8 % of dead areas on the SiPM array) which represents a dominant component in light signal degradation and is also quite a different value from that evaluated at the very beginning of the design phase of the project ( $\eta_{coll} = 80\%$ ). This preliminary parameter was estimated adopting a different optical model with respect to the one described in chapter 3 and was adopted for all the evaluations made up to the realization of the INSERT detection module. The consequence of this sensible difference, beyond the gap in the estimated performance, is the question regarding the reliability on the parameter value itself, then on the optical model adopted.

The quest for better optical parameters accuracy in the model requires considerable effort without the experimental setup necessary to measure each single characteristic of the materials, like crystal roughness, Teflon reflectivity and so on. Desuming single parameter reliability from output results is tricky and can bring to misleading conclusions.

The information provided from the simulator can then be used as preliminary hypothesis that provide a work baseline. This hypothesis can be later

## Chapter 5. Detection module performance and results

---

supported or dismissed by means of experimental tests aimed to verify its reliability. Whether the parameter or the configuration of parameters is no longer reliable, a new one is proposed (also with the support of the experimental information previously collected). This discussion on the reliability of the parameters value can be extended also to the SiPM and electronics filter ones. By the way, the accuracy on this components characteristic is definitely much easier to be controlled.

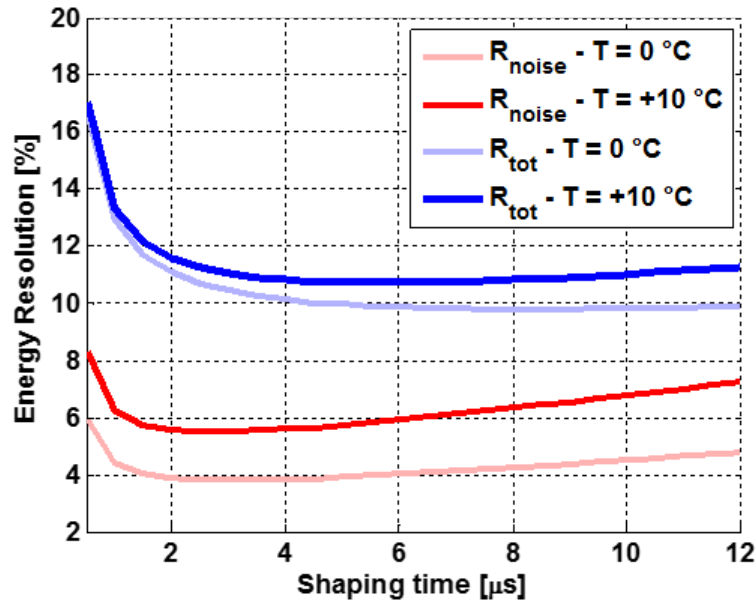
The  $\eta_{coll} = 54.5\%$  have been confirmed by the simulator also by coarsely changing some optical parameters in the simulation (i.e.  $\sigma_{roughness} = 10^\circ$  instead of  $1^\circ$ ). The next step in the redesign of the detection module will be related to the investigation of this parameter: if the value can be confirmed, primary interest for the performance optimization task is to better understand if there is any margin for better light collection with a different configuration of optical parameters (and also if this is physically implementable).

One tool for the further comparison of simulated and experimental results is the LRF extracted and employed for maximum likelihood reconstruction. From the LRF model it is possible to study the average light distribution over the SiPM matrix. It is noteworthy that the LRF also include the effects from light conversion and electrical signal elaboration, however the average spatial distribution of the signal is, for the INSERT configuration, minimally affected by the fluctuations of the stochastic processes that occur after like collection.

A major technical remark is addressed to the cooling strategy. The simulations and measurements performed along the project development have underlined not only the necessity of SiPMs (and also ASIC) cooling, but also thermal stability in time and uniformity in spatial distribution of the temperature in the photodetectors array. One of the success key of the project will be the achievement of a cooling system that provides the performances required from the detectors.

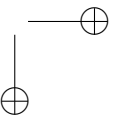
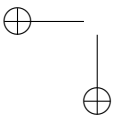
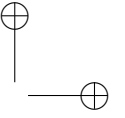
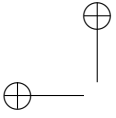
On the other way round, it can also be considered to relax some working condition, for example absolute temperature, in which the cooling system can properly and most efficiently operate. For example, the introduction of lower dark count SiPMs (RGB-HD) together with the employment of gated integrator filter can jointly reduce the supremacy of the noise contribution for the SNR, then a redefinition of the cooling temperature can be supported with minimal difference in the performance. Figure 5.32 depict

## 5.5. Final discussion



**Figure 5.32:** Energy resolution estimated with the analytical model (modified with ballistic deficit also on the statistical component) for the final version of the INSERT module, with RGB-HD and gated integrator filter. The resolution is presented for two different working temperatures.

the estimated energy resolution for the final version of the INSERT module at 0 and +10 °C: the higher DCR for the second condition is mitigated by the faster scintillation decay time of the CsI(Tl) at higher temperatures, which slightly reduces the ballistic deficit effect.



---

## CHAPTER 6

---

### Conclusions

---

In the first part of the dissertation, the INSERT project has been presented: its objective is the design and development of a combined SPECT/MR, both in a preclinical and clinical architecture, with the final aim to provide a stratified and multimodal information useful for glioma and other brain tumors diagnosis, radio/chemotherapy planning and follow up of the disease treatment. The main strategy of the project is to realize a SPECT ring populated with a multitude of identical gamma cameras and to design it as an insert for commercial available MR scanners.

A rationale for a SPECT/MRI development has been reported and it directly justifies the project technical requirements described in the second chapter. The main dimensions and geometry for the two SPECT rings and related collimators has been briefly described, with also the magnetic compatibility issues considered and the actions promoted to avoid undesired interference between the MR and the SPECT scanners. The main requirements for the basic detection module are at most 12 % in energy resolution at 140 keV ( $^{99m}\text{Tc}$ ) and an intrinsic spatial resolution of 1 mm over 40 mm  $\times$  40 mm of central FOV.

A second section has been dedicated to the very core of the present doc-

## Chapter 6. Conclusions

---

toral work: the design and development of the gamma camera unit, the fundamental block for the realization of the preclinical and clinical SPECT systems. The main architecture follows the Anger concept of monolithic inorganic scintillator optically coupled to a photodetectors array read by a multichannel custom electronic. The detection module mechanics and electronics have been designed in such a way to minimize the modifications required to translate from the preclinical to the clinical configuration.

The theoretical and statistic models employed to support the design and optimization of the detector have been presented. In particular, a custom Montecarlo simulator has been implemented and its main advantages and limitations have been underlined.

The motivations for the compound and geometry choices over the CsI(Tl) crystal for gamma-rays absorption have been exposed and supported with simulated and experimental data. The scintillator has been covered with 4 Teflon layers to maximize the light collection on the detection array. The study over the wide range of possible MR compatible solid-state photodetectors has brought to the election of the Silicon photomultiplier (SiPM), which is suited for its insensitivity to magnetic fields, compactness and for the swift progress in detection performance, since it is a relatively new technology. The RGB-SiPMs have been chosen, with  $4\text{ mm} \times 4\text{ mm}$  active area and have been then organized in modular tiles of  $6 \times 6$  SiPMs each, with minimized dead area between the detectors and optimized mechanical structure for better thermal exchange from the photodetectors.

An overall crystal FOV of  $50\text{ mm} \times 50\text{ mm}$  for the preclinical and  $100\text{ mm} \times 50\text{ mm}$  for the clinical system has been covered with respectively  $4 \times 4$  and  $8 \times 4$  SiPM tiles. The optical coupling is made possible through a thin layer of transparent resin optically matched between the scintillator and SiPMs refractive index.

A 36 channels ASIC (CMOS technology,  $0.35\ \mu\text{m}$ ) provides the electronic readout for an equivalent number of photodetection pixel, each one constituted by 4 neighbor SiPMs with the output anodes connected together to form a merged channel, with a virtual active area of  $8\text{ mm} \times 8\text{ mm}$ . The overall number of merged channels is  $6 \times 6$  (1 ASIC) and  $12 \times 6$  (2 ASICs) respectively for the preclinical and the clinical. Every electronic channel implements a current mode circuit for readout, with current conveyor, RC shaping filter together with baseline holder, comparator and peak stretcher. An ASIC board holds the electronics on one side, with few ancillary systems for calibration and temperature control, while, on the other side, it hosts a thermoplastic  $8\text{ mm}$  thick heat sink on which the SiPM tiles



**Table 6.1:** *Results summary*

	<b>Theoretical</b>	<b>Simulated</b>	<b>Experimental</b>
Energy resolution (equalized)	14.1 %	15.8 %	16.6 %
Intrinsic spatial resolution (in the center)	-	$1.52 \pm 0.1$ mm	$1.41 \pm 0.1$ mm
Maximum spatial resolution (in 40 mm $\times$ 40 mm)	-	$2.40 \pm 0.5$ mm	$1.72 \pm 0.2$ mm

are aligned and mounted. The analog signal is digitized on a DAQ board connected to the ASIC one. From the DAQ board optical fibers for data transmission and shielded coaxial cables for power supply depart to an external control systems. The parts described are supposed to be the ones inserted in the magnetic field and thus they have been developed considering the MR compatibility issue debated in the dissertation.

The thermal strategy for cooling and temperature stabilization and the simulations performed to check the expected performance have been described.

A fast maximum likelihood (ML) algorithm for interaction coordinates reconstruction has been implemented in Matlab R2013a. The light response function (LRF) required from the likelihood method is provided by acquiring a simple uncollimated irradiation of the crystal. The method is capable to fully recover the original crystal FOV and, thanks to the LRF originating from experimental calibration data, the reconstruction appears more uniform and linear than an equivalent image elaborated with the most typical (modified) centroid method.

The performance of a prototype for the preclinical system have been experimentally measured and compared with the theoretical and simulated expectations. A brief summary of the results is reported in table 6.1, considering a  $^{99m}\text{Tc}$  source and an RC filter shaping time of  $7.5 \mu\text{s}$  for which the best experimental result is obtained.

The models fit quite well the measurements, especially for longer shaping times. On the other hand, for shorter ones, it has been demonstrated that the model for incomplete charge collection requires theoretical revision.

## Chapter 6. Conclusions

---

The spatial resolution obtained is slightly better than the simulated. Thus a check on the light distribution model is required to provide better forecasts. Nevertheless, the tools adopted have demonstrated to provide, together with the experimental results, fundamental indications for the further optimization of the system.

The study on a future version of the INSERT detection module, implementing new RGB-HD SiPMs and gated integrator filter in the electronic channels, has foreseen an energy resolution proximal to 12 % (at 140.5 keV) and an intrinsic spatial resolution slightly better than 1 mm in the very center of the FOV. The models do not provide an adequate level of precision in the prevision of the CFOV, at least considering the protocol presented in the dissertation: a new simulation protocol has to be designed to reduce the uncertainties on the estimation of the spatial resolution at the edge of the FOV, which is fundamental for an accurate forecast on the CFOV.

Future actions aim to the realization of the new version of detection module and its optimization to fit the project requirements. The reconstruction algorithm requires a further optimization and a fast hardware support for real time reconstruction. A method for depth of interaction discrimination, not discussed in the present thesis, has to be designed and implemented.

The detection module have to be tested for MR compatibility and then mounted in the preclinical and clinical SPECT rings and further technical and biological measurements will be required in the next months.

---

## Bibliography

---

- [1] S.N. Histed et al. Review of functional/ anatomic imaging in oncology. *Nuclear Medicine Communications*, 33(4):349–361, 2012.
- [2] D.A. Chesler. Positron tomography and three-dimensional reconstruction technique. *Tomographic imaging in nuclear medicine*, pages 176–183, 1973.
- [3] H.N. Wagner. *A Personal History of Nuclear Medicine*. Springer-Verlag London, 2006.
- [4] S.R. Cherry. Multimodality imaging: beyond PET/CT and SPECT/CT. *Seminars in nuclear medicine*, 39(5):348–353, 2009.
- [5] D.W. Townsend. Multimodality imaging of structure and function. *Physics in Medicine and Biology*, 53(4):R1, 2008.
- [6] T. Beyer O. Ratib. Whole-body hybrid PET/MRI: ready for clinical use? *European Journal of Nuclear Medicine and Molecular Imaging*, 38(6):992–995, 2011.
- [7] MRI and Medical Imaging blog. <http://mriandmedicalimaging.blogspot.it/>. Accessed: 2015-05-01.
- [8] L. Marti’-Bonmati’ et al. Multimodality imaging techniques. *Contrast Media and Molecular Imaging*, 5(4):180–189, 2010.
- [9] S.R. Cherry et al. The integration of positron emission tomography with magnetic resonance imaging. *Proceedings of the IEEE*, 96(3):416–438, 2008.
- [10] C. Catana et al. Simultaneous Acquisition of Multislice PET and MR Images: Initial Results with a MR-Compatible PET Scanner. *Journal of Nuclear Medicine*, 47(12):1968–1976, 2006.
- [11] B.J. Pichler et al. Performance Test of an LSO-APD Detector in a 7-T MRI Scanner for Simultaneous PET/MRI. *Journal of Nuclear Medicine*, 47(4):639–647, 2006.
- [12] D.P. McElroy et al. Evaluation of silicon photomultipliers: A promising new detector for MR compatible PET. *Nuclear Instruments and Methods in Physics Research A*, 571:106–109, 2007.
- [13] P. Despres et al. Evaluation of a MR-compatible CZT detector. In *Nuclear Science Symposium Conference Record, 2007. NSS ’07. IEEE*, volume 6, pages 4324–4326, 2007.

## Bibliography

---

- [14] L. Cai et al. First imaging result with an ultrahigh resolution stationary MR compatible SPECT system. In *Nuclear Science Symposium and Medical Imaging Conference (NSS/MIC), 2012 IEEE*, pages 3568–3571, 2012.
- [15] J.E. Mackewn et al. Performance Evaluation of an MRI-Compatible Pre-Clinical PET System Using Long Optical Fibers. *Nuclear Science, IEEE Transactions on*, 57(3):1052–1062, 2010.
- [16] B.E. Hammer and N.L. Christensen. Measurement of positron range in matter in strong magnetic fields. *Nuclear Science, IEEE Transactions on*, 42(4):1371–1376, 1995.
- [17] N.L. Christensen et al. Positron emission tomography within a magnetic field using photo-multiplier tubes and lightguides. *Physics in Medicine and Biology*, 40(4):691, 1995.
- [18] Y. Shao et al. Development of a PET detector system compatible with MRI/NMR systems. *Nuclear Science, IEEE Transactions*, 44(3):1167–1171, 1997.
- [19] Y. Shao et al. Simultaneous PET and MR imaging. *Physics in Medicine and Biology*, 42(10):1965, 1997.
- [20] H.P. Schlemmer et al. Simultaneous MR/PET for brain imaging: First patient scans. *Journal of Nuclear Medicine, Meeting Abstracts*, 48(MeetingAbstracts 2):45P a, 2007.
- [21] M. Schmand et al. BrainPET: First human tomograph for simultaneous (functional) PET and MR imaging. *Journal of Nuclear Medicine, Meeting Abstracts*, 48(MeetingAbstract 2):45P, 2007.
- [22] J. Pichler. Antiangiogenic therapy in malignant gliomas. *MEMO - Magazine of European Medical Oncology*, 2(3):10–12, 2009.
- [23] N.U. Schramm et al. High-resolution SPECT using multipinhole collimation. *Nuclear Science, IEEE Transactions on*, 50(3):315–320, 2003.
- [24] B.M.W. Tsui et al. Design and development of MR-compatible SPECT systems for simultaneous SPECT-MR imaging of small animals. volume 7961, pages 79611Y–79611Y 7, 2011.
- [25] F. Van Der Haveet al. U-SPECT-II: An Ultra-High-Resolution Device for Molecular Small-Animal Imaging. 50(4):599–605, 2009.
- [26] R. Pani et al. Multi-crystal YAP:Ce detector system for position sensitive measurements. *Nuclear Instruments and Methods in Physics Research Section A: Accelerators, Spectrometers, Detectors and Associated Equipment*, 348(2–3):551–558, 1994.
- [27] L.H. Barone et al. Toward a nuclear medicine with sub-millimeter spatial resolution. *Nuclear Instruments and Methods in Physics Research Section A: Accelerators, Spectrometers, Detectors and Associated Equipment*, 360(1–2):302–306, 1995.
- [28] M.M. Khalil et al. Molecular SPECT Imaging: An Overview. *International Journal of Molecular Imaging*, (796025):15, 2011.
- [29] D.J. Burdette. *A study of the effects of strong magnetic fields on the image resolution of PET scanners*. PhD thesis, The Ohio State University, 2009.
- [30] S.S. Gambhir et al. A novel high-sensitivity rapid-acquisition single-photon cardiac imaging camera. 50(4):635–643, 2009.
- [31] S. Yamamoto et al. Development of a high-resolution SiPM-based gamma camera system. *Physics in Medicine and Biology*, 56(23):7555, 2011.
- [32] C. Fiorini et al. The HICAM Gamma Camera. *Nuclear Science, IEEE Transactions on*, 59(3):537–544, 2012.
- [33] Y. Zhang et al. Joint estimation for incorporating MRI anatomic images into SPECT reconstruction. In *Nuclear Science Symposium and Medical Imaging Conference, 1994., 1994 IEEE Conference Record*, volume 3, pages 1256–1260, Oct 1994.

## Bibliography

- [34] A. Colin and J.Y. Boire. MRI-SPECT fusion for the synthesis of high resolution 3D functional brain images: a preliminary study. *Computer Methods and Programs in Biomedicine*, 60(2):107–116, 1999.
- [35] C.B. Goetz et al. SPECT Low-Field MRI System for Small-Animal Imaging. 49(1):88–93, 2008.
- [36] M.J. Hamamura et al. Development of an MR-compatible SPECT system (MRSPECT) for simultaneous data acquisition. *Physics in Medicine and Biology*, 55(6):1563, 2010.
- [37] B.M.W. Tsui et al. A completed SPECT/MR insert for simultaneous SPECT/MR imaging of small animals. *J NUCL MED MEETING ABSTRACTS*, 54(MeetingAbstracts 2):595, 2013.
- [38] L. Cai et al. Hybrid pixel-waveform CdTe/CZT detector for use in an ultrahigh resolution MRI compatible SPECT system . *Nuclear Instruments and Methods in Physics Research Section A: Accelerators, Spectrometers, Detectors and Associated Equipment*, 702(0):101–103, 2013.
- [39] L. Cai et al. MRC-SPECT: A sub-500  $\mu\text{m}$  resolution MR-compatible SPECT system for simultaneous dual-modality study of small animals . *Nuclear Instruments and Methods in Physics Research Section A: Accelerators, Spectrometers, Detectors and Associated Equipment*, 734, Part B(0):147–151, 2014.
- [40] X. Lai et al. MRC-SPECT-DF: an MR-Compatible SPECT system with Dual-FOV collimation design for microscopic SPECT imaging. *EJNMMI Physics*, 2(Suppl 1):A48, 2015.
- [41] C. Bouckaert et al. Evaluation of a compact, high-resolution SPECT detector based on digital silicon photomultipliers. *Physics in Medicine and Biology*, 59(23):7521, 2014.
- [42] N. Dinu et al. SiPM arrays and miniaturized readout electronics for compact gamma camera. *Nuclear Instruments and Methods in Physics Research Section A: Accelerators, Spectrometers, Detectors and Associated Equipment*, 787(0):367–372, 2015.
- [43] S. Yamamoto et al. Development of an Optical Fiber-Based MR Compatible Gamma Camera for SPECT/MRI Systems. *Nuclear Science, IEEE Transactions on*, 62(1):76–81, 2015.
- [44] P. Bouziotis and C. Fiorini. SPECT/MRI: dreams or reality? *Clinical and Translational Imaging*, 2(6):571–573, 2014.
- [45] R. Pani et al. LaBr<sub>3</sub>:Ce small FOV gamma camera with excellent energy resolution for multi-isotope imaging. *Journal of Instrumentation*, 10(06):C06002, 2015.
- [46] H.H. Coenen et al. Recent radiochemical developments for authentically labelled bi-modal PET(SPECT)/MR-probes. 3rd Conference on PET/MR and SPECT/MR, Kos Island (Greece), 05/19/2014 - 05/21/2014, 2014.
- [47] D. Hoffman et al. Intrinsically radiolabelled [(59)Fe]-SPIONs for dual MRI/radionuclide detection. *American Journal of Nuclear Medicine and Molecular Imaging*, 4(6):548–560, 2014.
- [48] R. Madru et al. <sup>99m</sup>Tc-Labeled Superparamagnetic Iron Oxide Nanoparticles for Multimodality SPECT/MRI of Sentinel Lymph Nodes. *Journal of Nuclear Medicine*, 53(3):459–463, 2012.
- [49] M.R. Bernsen et al. The role of preclinical SPECT in oncological and neurological research in combination with either CT or MRI. *European Journal of Nuclear Medicine and Molecular Imaging*, 41(1):36–49, 2014.
- [50] F.J. Beekman et al. U-SPECT-I: A Novel System for Submillimeter-Resolution Tomography with Radiolabeled Molecules in Mice. *Journal of Nuclear Medicine*, 46(7):1194–1200, 2005.
- [51] H. Zaidi. *Molecular Imaging of Small Animals: Instrumentation and applications*. Springer New York, 2014.

## Bibliography

---

- [52] H. Ito et al. Cerebral blood flow measurement using [123I]-IMP SPECT and venous blood sampling: A calibrated standard input function. *Nucl Med*, 36:2339–2342, 1995.
- [53] T. Fritz-Hansen. Measurement of the arterial concentration of Gd-DTPA using MRI: A step toward quantitative perfusion imaging. *Magnetic Resonance in Medicine*, 36(2):225–231, 1996.
- [54] L. Knutsson et al. Absolute quantification of cerebral blood flow in normal volunteers: Correlation between Xe-133 SPECT and dynamic susceptibility contrast MRI. *Journal of Magnetic Resonance Imaging*, 26(4):913–920, 2007.
- [55] Johns Hopkins Medicine. *What is a Glioma?*, [http://www.hopkinsmedicine.org/neurology\\_neurosurgery/centers\\_clinics/brain\\_tumor/center/glioma/glioma-brain-tumor.html](http://www.hopkinsmedicine.org/neurology_neurosurgery/centers_clinics/brain_tumor/center/glioma/glioma-brain-tumor.html).
- [56] S. Genna and A.P. Smith. The development of ASPECT, an annular single crystal brain camera for high efficiency SPECT. *Nuclear Science, IEEE Transactions on*, 35(1):654–658, 1988.
- [57] G.F. Knoll. *Radiation detection and measurement*. Wiley - Third edition, 2000.
- [58] L. Abbene et al. Direct measurement of mammographic x-ray spectra with a digital CdTe detection system. *Sensors*, 12(6):8390, 2012.
- [59] E.E. Ermis and C. Celiktas. Timing applications to improve the energy resolution of NaI (Tl) scintillation detectors. *International Journal of Instrumentation Science*, 1(5):54–62, 2012.
- [60] E.G DePuey. Advances in SPECT camera software and hardware: Currently available and new on the horizon. *Journal of Nuclear Cardiology*, 19(3):551–581, 2012.
- [61] Medical Imaging. <http://oftankonyv.reak.bme.hu/tiki-index.php?page=Collimators>. Accessed: 2015-05-05.
- [62] J.P. Islamian et al. Advances in pinhole and multi-pinhole collimators for single photon emission computed tomography imaging. *World Journal of Nuclear Medicine*, 14(1):3–9, 2015.
- [63] S.D. Metzler et al. On-axis sensitivity and resolution of a slit-slat collimator. *Journal of Nuclear Medicine*, 47(11):1884–1890, 2006.
- [64] R. Accorsi S. Metzler and R.M. Lewitt. Slit-slat collimation, 2010. US Patent 7,831,024.
- [65] M. Lyra and A. Ploussi. Filtering in SPECT image reconstruction. *Journal of Biomedical Imaging*, 2011(10):1–14, 2011.
- [66] H.P. Floris. Comparison of 3D-OP-OSEM and 3D-FBP reconstruction algorithms for high-resolution research tomograph studies: effects of randoms estimation methods. *Physics in Medicine and Biology*, 53(12):3217, 2008.
- [67] L. Zhi-Pei and P.C. Lauterbur. *Principles of Magnetic Resonance Imaging: A Signal Processing Perspective*. Wiley - IEEE press, 1999.
- [68] Top 10 Invention. <http://internal.champaignschools.org/central/business/johnson/5thfa2007/acarter/inventions.html>. Accessed: 2015-05-05.
- [69] S.T. Mahmood et al. Design of a novel slit-slat collimator system for SPECT imaging of the human brain. *Physics in Medicine and Biology*, 54(11):3433, 2009.
- [70] D. Salvado et al. Collimator design for a clinical brain SPECT/MRI insert. *EJNMMI Physics*, 1(1), 2014.
- [71] W. Mengesha et al. Light yield nonproportionality of csi(tl), csi(na), and yap. *Nuclear Science, IEEE Transactions on*, 45(3):456–461, 1998.

## Bibliography

- [72] J. Valentine et al. Temperature dependence of absolute CsI(Tl) scintillation yield. In *Nuclear Science Symposium and Medical Imaging Conference, 1991., Conference Record of the 1991 IEEE*, volume 1, pages 176–182, 1991.
- [73] Furukawa. *Ce:GAGG scintillator crystal*, 2014. <http://www.furukawa-denshi.co.jp/cgi-bin/pdfdata/20140428162950.pdf>.
- [74] Saint Gobain. *BrilLanCe380*, 2014. [http://www.crystals.saint-gobain.com/BrilLanCe\\_380\\_Scintillator.aspx](http://www.crystals.saint-gobain.com/BrilLanCe_380_Scintillator.aspx).
- [75] Light Scattering. [https://en.wikipedia.org/wiki/Light\\_scattering](https://en.wikipedia.org/wiki/Light_scattering). Accessed: 2015-07-05.
- [76] M. Janecek and W.W. Moses. Measuring light reflectance of BGO crystal surfaces. *Nuclear Science, IEEE Transactions on*, 55(5):2443–2449, 2008.
- [77] Wai-Hoi Wong, Hongdi Li, Yuxuan Zhang, Hossain Baghaei, Rocio Ramirez-Jaramillo, Shitao Liu, Chao Wang, and Shaohui An. Development and NEMA imaging performance of a lower-cost higher-resolution animal PET-CT using PMT-quadrant-sharing technology. *Journal of Nuclear Medicine*, 52(supplement 1):376, 2011.
- [78] F. Sanchez et al. ALBIRA: A small animal PET/SPECT/CT imaging system. *Medical Physics*, 40(5), 2013.
- [79] J.J. Vaquero et al. MRI compatibility of position-sensitive photomultiplier depth-of-interaction PET detectors modules for in-line multimodality preclinical studies. *Nuclear Instruments and Methods in Physics Research Section A: Accelerators, Spectrometers, Detectors and Associated Equipment*, 702(0):83–87, 2013.
- [80] J.E. Mackewn et al. Performance Evaluation of an MRI-Compatible Pre-Clinical PET System Using Long Optical Fibers. *Nuclear Science, IEEE Transactions on*, 57(3):1052–1062, 2010.
- [81] M. Imaizumi et al. Simultaneous imaging of magnetic resonance imaging and positron emission tomography by means of MRI-compatible optic fiber-based PET: a validation study in ex vivo rat brain. *Japanese Journal of Radiology*, 27(6):252–256, 2009.
- [82] P. R. Mendes et al. A detector insert based on continuous scintillators for hybrid MR-PET imaging of the human brain. *Nuclear Instruments and Methods in Physics Research Section A: Accelerators, Spectrometers, Detectors and Associated Equipment*, 702(0):80–82, 2013.
- [83] J.L. Corbeil, N. Zhang, and M.J. Schmand. Magnetic resonance imaging compatible positron emission tomography detector, 2013.
- [84] An Introduction to Silicon Drift Detectors. <http://www.azom.com/article.aspx?ArticleID=11973>. Accessed: 2015-07-05.
- [85] C. Fiorini et al. Study of Compatibility of a Silicon Drift Detector With a MRI System. *Nuclear Science, IEEE Transactions on*, 58(2):559–568, 2011.
- [86] S. Yamamoto et al. Development of an ultrahigh resolution Si-PM based PET system for small animals. *Physics in Medicine and Biology*, 58(21):7875, 2013.
- [87] Evaluation of a SiPM array coupled to a Gd<sub>3</sub>Al<sub>2</sub>Ga<sub>3</sub>O<sub>12</sub>:Ce (GAGG:Ce) discrete scintillator. *Physica Medica*, (0):–, 2015.
- [88] D. Philippov et al. SiPM-MAROC gamma-camera prototype with monolithic NaI(Tl) scintillator. *EJNMMI Physics*, 2(Suppl 1):A49, 2015.
- [89] W. Oldham et al. Triggering phenomena in avalanche diodes. *Electron Devices, IEEE Transactions on*, 19(9):1056–1060, 1972.
- [90] N. Serra et al. Characterization of new fbk sipm technology for visible light detection. *Journal of Instrumentation*, 8(03):P03019, 2013.

## Bibliography

---

- [91] C. Piemonte et al. Characterization of the first prototypes of silicon photomultiplier fabricated at ITC-irst. *Nuclear Science, IEEE Transactions on*, 54(1):236–244, 2007.
- [92] M. Bouchel et al. SPIROC (SiPM Integrated Read-Out Chip): Dedicated very front-end electronics for an ILC prototype hadronic calorimeter with SiPM read-out. In *Nuclear Science Symposium Conference Record, 2007. NSS '07. IEEE*, volume 3, pages 1857–1860, 2007.
- [93] L. Raux et al. SPIROC: Design and performance of a dedicated very front-end for an ILC prototype Hadronic Calorimeter with SiPM. In *Nuclear Science Symposium and Medical Imaging Conference (NSS/MIC), 2012 IEEE*, pages 557–561, 2012.
- [94] M.G. Bagliesi et al. A custom front-end ASIC for the readout and timing of 64 SiPM photosensors. *Nuclear Physics B - Proceedings Supplements*, 215(1):344–348, 2011.
- [95] D. Meier et al. An ASIC for SiPM/MPPC readout. In *Nuclear Science Symposium Conference Record (NSS/MIC), 2010 IEEE*, pages 1653–1657, 2010.
- [96] S. Blin et al. Dedicated very front-end electronics for an ILC prototype hadronic calorimeter with SiPM readout. *Report-No: LC-DET-2006-007*, 12, 2006.
- [97] F. Corsi et al. ASIC development for SiPM readout. *Journal of Instrumentation*, 4(03):P03004, 2009.
- [98] F. Ciciriello et al. BASIC32 ADC, a front-end ASIC for SiPM detectors. In *Nuclear Science Symposium and Medical Imaging Conference (NSS/MIC), 2013 IEEE*, pages 1–6, Oct 2013.
- [99] Y.C. Shih et al. An 8x8 row-column summing readout electronics for preclinical positron emission tomography scanners. In *Nuclear Science Symposium Conference Record (NSS/MIC), 2009 IEEE*, pages 2376–2380, 2009.
- [100] D. Stratos et al. Comparison of three resistor network division circuits for the readout of 4x4 pixel SiPM arrays. *Nuclear Instruments and Methods in Physics Research Section A: Accelerators, Spectrometers, Detectors and Associated Equipment*, 702(0):121–125, 2013.
- [101] R. Pani et al. Revisited position arithmetics for LaBr3:Ce continuous crystals. *Nuclear Physics B-Proceedings Supplements*, 197(1):383–386, 2009.
- [102] E. Breitenberger. Scintillation spectrometer statistics. *Progress in nuclear physics*, 4:56, 1955.
- [103] J.F. Loude. Energy resolution in nuclear spectroscopy. In *LPHE notes and conferences*, pages IPHE 2000–22, 2000.
- [104] S. Naydenov and V. Ryzhikov. Energy Resolution Improvement of Scintillation detectors: Priorities and Prospects. *ArXiv Physics e-prints*, 2002.
- [105] D. Lazaro et al. Validation of the GATE Monte Carlo simulation platform for modelling a CsI(Tl) scintillation camera dedicated to small-animal imaging. *Physics in Medicine and Biology*, 49(2):271, 2004.
- [106] D.J. van der Laan et al. Optical simulation of monolithic scintillator detectors using GATE/GEANT4. *Physics in Medicine and Biology*, 55(6):1659, 2010.
- [107] M. Occhipinti et al. A new optical simulator for light collection estimation in scintillation detectors. In *Nuclear Science Symposium and Medical Imaging Conference (NSS/MIC), 2012 IEEE*, pages 343–346, 2012.
- [108] M. Occhipinti. Sviluppo di un simulatore ottico per la progettazione di una gamma camera in medicina nucleare. Master’s thesis, Politecnico di Milano, 2012.
- [109] A. Levin and C. Moisan. A more physical approach to model the surface treatment of scintillation counters and its implementation into DETECT. In *Nuclear Science Symposium, 1996. Conference Record., 1996 IEEE*, volume 2, pages 702–706, Nov 1996.



## Bibliography

- [110] M. Janecek and W.W. Moses. Optical reflectance measurements for commonly used reflectors. *Nuclear Science, IEEE Transactions on*, 55(4):2432–2437, 2008.
- [111] M. Janecek and W.W. Moses. Design of an instrument to measure optical reflectance of scintillating crystal surfaces. *Nuclear Science, IEEE Transactions on*, 55(3):1381–1386, 2008.
- [112] J.D. Valentine et al. Temperature dependence of CsI(Tl) gamma-ray excited scintillation characteristics. *Nuclear Instruments and Methods in Physics Research Section A: Accelerators, Spectrometers, Detectors and Associated Equipment*, 325(1–2):147–157, 19933.
- [113] M. Grodzicka et al. Characterization of CsI:Tl at a wide temperature range ( $\hat{a}$ 40 °C to +22 °C). *Nuclear Instruments and Methods in Physics Research Section A: Accelerators, Spectrometers, Detectors and Associated Equipment*, 707(0):73–79, 2013.
- [114] R. Pani et al. LaBr3:Ce crystal: The latest advance for scintillation cameras. *Nuclear Instruments and Methods in Physics Research Section A: Accelerators, Spectrometers, Detectors and Associated Equipment*, 572(1):268–269, 2007.
- [115] A. Syntfeld-Kazuch et al. Non-proportionality and energy resolution of CsI(Tl). *Nuclear Science, IEEE Transactions on*, 54(5):1836–1841, 2007.
- [116] L. Swiderski et al. Non-proportionality and energy resolution of NaI(Tl) at wide temperature range (-40 °c to +23 °c). In *Nuclear Science Symposium Conference Record, 2006. IEEE*, volume 2, pages 1122–1128, 2006.
- [117] Ce:GAGG Scintillator Crystal. <http://www.furukawa-denshi.co.jp/cgi-bin/pdfdata/20140428162950.pdf>. Accessed: 2015-07-05.
- [118] P. Siczynski et al. Characterization of GAGG:Ce scintillators with various Al-to-Ga ratio. *Nuclear Instruments and Methods in Physics Research Section A: Accelerators, Spectrometers, Detectors and Associated Equipment*, 772(0):112–117, 2015.
- [119] I.V. Kilimchuk et al. Study of surface roughness of CsI:Tl crystals treated by various abrasives. In *Nuclear Science Symposium Conference Record, 2008. NSS '08. IEEE*, pages 1134–1137, 2008.
- [120] P. Busca. *Development of a gamma camera for medical and nuclear physics applications*. PhD thesis, Politecnico di Milano, 2013.
- [121] M. Janecek and W.W. Moses. Simulating scintillator light collection using measured optical reflectance. *Nuclear Science, IEEE Transactions on*, 57(3):964–970, 2010.
- [122] P. Trigilio et al. ANGUS: a multichannel CMOS circuit for large capacitance silicon photomultiplier detectors for SPECT applications. In *Nuclear Science Symposium and Medical Imaging Conference (NSS/MIC), 2014 IEEE*, volume N19-5, 2014.
- [123] M. Gerosa. Sviluppo di un circuito integrato con filtro a gated integrator per lettura di silicon photomultiplier per applicazioni SPECT. Master’s thesis, Politecnico di Milano, 2015.
- [124] T Ling et al. Parametric positioning of a continuous crystal PET detector with depth of interaction decoding. *Physics in Medicine and Biology*, 53(7):1843, 2008.
- [125] A. Fabbri et al. A new iterative algorithm for pixilated and continuous scintillating crystal. *Nuclear Instruments and Methods in Physics Research Section A: Accelerators, Spectrometers, Detectors and Associated Equipment*, 648, Supplement 1:S79–S84, 2011.
- [126] A. Fabbri et al. Study of position reconstruction of a LaBr3:Ce continuous scintillation crystal for medical applications. *Journal of Instrumentation*, 8(12):P12010, 2013.
- [127] H.H. Barrett et al. Maximum-likelihood methods for processing signals from gamma-ray detectors. *IEEE Transactions on Nuclear Science*, 56(3):725–735, 2009.

## Bibliography

---

- [128] G. Borghi, V. Tabacchini, S. Seifert, and D.R. Schaart. Experimental validation of an efficient fan-beam calibration procedure for k -nearest neighbor position estimation in monolithic scintillator detectors. *Nuclear Science, IEEE Transactions on*, 62(1):57–67, 2015.
- [129] R.S. Miyaoka et al. Resolution properties of a prototype continuous miniature crystal element (cMiCE) scanner. *Nuclear Science, IEEE Transactions on*, 58(5):2244–2249, 2011.
- [130] Z. Li et al. Nonlinear least-squares modeling of 3D interaction position in a monolithic scintillator block. *Physics in Medicine and Biology*, 55(21):6515, 2010.
- [131] V.N. Solovov et al. Position reconstruction in a dual phase Xenon scintillation detector. *Nuclear Science, IEEE Transactions on*, 59(6):3286–3293, 2012.
- [132] A. Morozov et al. Adaptive algorithms of position and energy reconstruction in Anger-camera type detectors: experimental data processing in ANTS. *Journal of Instrumentation*, 8(05):P05002, 2013.
- [133] A. Morozov et al. Iterative reconstruction of detector response of an Anger gamma camera. *Physics in Medicine and Biology*, 60(10), 2015.